Composition Dependence of Structure, Properties and Crystallization in Three Series of Oxide Glasses

Zheng, Qiuju

Publication date:
2012

Document Version
Publisher's PDF, also known as Version of record

Composition Dependence of Structure, Properties and Crystallization in Three Series of Oxide Glasses

Qiuju Zheng

Section of Chemistry
Aalborg University
Ph.D. Dissertation, 2012

AALBORG UNIVERSITY

Ph.D. Dissertation

Composition Dependence of Structure, Properties and Crystallization in Three Series of Oxide Glasses

by

Qiuju Zheng

Section of Chemistry
Department of Biotechnology, Chemistry,
and Environmental Engineering
Aalborg University, Denmark

Date of Defense
August 24th, 2012

Assessment committee

Thorkild Hvitved-Jacobsen
Professor Emeritus
Aalborg University, Denmark

Himanshu Jain
Professor
Lehigh University, USA

Karsten Agersted Nielsen
Senior Scientist
Technical University of Denmark, Denmark

Supervisor

Yuanzheng Yue
Professor
Aalborg University, Denmark

Co-supervisor

John C. Mauro
Research associate
Corning Incorporated, USA

Preface and Acknowledgements

This dissertation is submitted to the Faculties of Engineering and Science, Aalborg University in partial fulfillment of the requirements for obtaining the Ph.D. degree. The Ph.D. study was carried out from September 2009 to July 2012. The work was primarily done at the Section of Chemistry at Aalborg University with external stays at Corning Incorporated for four months. The study was financed by both China Scholarship Council and Aalborg University.

I would like to thank my supervisor Yuanzheng Yue for his dedicated supervision, insightful ideas, commitment and encouragement throughout the project. I have learned the importance of scientific rigor and enthusiasm in doing research. I have truly enjoyed our collaboration and also wish future long term collaboration on glass science and other topics. Appreciation also goes to my co-supervisor John C. Mauro from Corning Incorporated. During my internship in Corning Incorporated, his great supervision and encouragement lead to fruitful results and accelerated progress in my PhD study. I also look forward to keep this collaboration in the future.

My kind acknowledgements also go to other colleagues from Corning Incorporated. Thanks to Marcel Potuzak (Corning Inc.) for providing me access to his research laboratory, as well as his practical assistance and many valuable discussions. Randall E. Youngman (Corning Inc.) deserves special mentioning for always performing NMR spectroscopy measurements in addition to evaluation of the results and valuable discussion. Thanks also to Carrie L. Hogue (Corning Inc.) for performing NMR spectroscopy measurements. I would also like to thank Adam J. Ellison (Corning Inc.) for offering viscosity data and valuable discussion. Furthermore, I owe special thanks to the Advanced Materials Processing Laboratory and Characterization Sciences and Services Directorate at Corning for preparing and characterize the glass samples.

I would also like to express my appreciation to the present and former members of the glass group for the assistance and discussions during my study. Morten Mattrup Smedskjær deserves a special credit for his support in paper and thesis writing, as well as his help in the lab and valuable discussions. In addition, my warm thanks go to Ralf Keding, Martin Jensen, Mette Moesgaard, and Xiaoju Guo at Aalborg and Mette Solvang from Rockwool International. Finally, special recognition goes to all the colleagues at Aalborg University and Corning Incorporated for creating great working and social environments.

Abstract

In order to predict the composition dependence of glass properties we first need to understand the atomic structure of glass, since glass properties are correlated to glass structure. We study the structure of three glass series: soda lime borate, soda lime aluminosilicate, and sodium boroaluminosilicate. All these glass series contain abundant structural features, e.g., the "boron anomaly" effect and mixed network former effect, which both yield nonmonotonic variations of physical properties with composition. It is critical to explore the structural roles of the network-modifying cations in different glass systems. In order to access different regimes of sodium behavior, we design glass compositions with varying the ratio of network former and network modifier or the ratio of different network formers. Multinuclear NMR experiments on ^{11}B, ^{27}Al, ^{29}Si and ^{23}Na were performed to determine the network former speciation and modifier environments as a function of glass composition. The different roles of sodium in relation with the network-forming cations (Si, B, and Al) have been clarified and quantified. In addition, we predict the fractions of various network species by using a recently proposed model (two-state model) and the values obtained from modeling are in agreement with the NMR data.

The composition and temperature dependence of viscosity is an important aspect for controlling glass production process, and for tailoring physical properties of glass products. Moreover, it is also critical for understanding the liquid and glass dynamics. With the assumption of a universal high temperature limit of viscosity, Angell proposed that the non-Arrhenius character of the temperature dependence of viscosity is described by the kinetic fragility index. However, the existence of a universal high-temperature viscosity limit has not been validated until now. In the present thesis, we investigate the high temperature limit of liquid viscosity by analyzing measured viscosity curves for 977 liquids including oxide, metallic, molecular, and ionic systems. Based on the Mauro–Yue–Ellison–Gupta–Allan (MYEGA) model of liquid viscosity, the high temperature viscosity limit of silicate liquids is determined to be $10^{-2.93}$ Pa·s. This result simplifies the modeling process of the compositional dependence of viscosity and indicates a common underlying physics of silicate liquids at the high temperature limit. In addition, we find that there is a parallel relationship between the kinetic fragility and the thermodynamic fragility (e.g., the jump of the isobaric heat capacity in the glass transition region) for the three studied glass series.

The physical and chemical properties of glasses can be controlled and designed by varying the mixing ratio of different structure units. The mixed network former effect leads to nonlinear variation in many macroscopic properties as a function of chemical composition. The prediction of glass properties from first principles calculations is often impossible due to the long time scales involved with glass transition and relaxation phenomena. We thus use the temperature-dependent constraint theory to explain the composition dependence of glass properties. According to this theory, glass properties are related to the number of constraints since the atomic structure of a glass-forming liquid could be regarded as a network of bond constraints. In this work we investigate the composition-structure-property relationships of the three model glass series. The determined properties include dynamic properties (glass transition temperature T_g and fragility), thermodynamic properties (e.g., heat capacity) and mechanical properties (elastic moduli and hardness). We also explore how the addition of 1 mol% Fe_2O_3 affects the measured properties of the boroaluminosilicate glasses.

Any liquids can vitrify if it is cooled fast enough to prevent crystallization of a specified volume fraction. The slowest cooling rate, at which a liquid is vitrified at a given critical amount of crystals, is defined as the critical cooling rate. This rate is used to quantify the glass forming ability (GFA) of different liquids. GFA is an important property in the glass production process. However, it is difficult to accurately measure the *critical cooling rate*. GFA is often quantified by glass stability (GS), which is the glass resistance against devitrification upon heating. It has been found that these two parameters show direct relationship. Therefore GS is in this work used to represent GFA. The GS is derived from the characteristic temperatures such as T_g, onset crystallization temperature and liquidus temperature, which are determined using a differential scanning calorimeter. In general there is no clear correlation between GS and fragility for the studied glass series. We have found that GS of the soda-lime-borate series can be enhanced by lowering the cooling rate from the melt to the glassy state, and the possible structural origin of this enhancement has been clarified. Finally we have discovered that GS of soda lime aluminosilicate glasses dramatically drops when Al_2O_3 content surpasses a critical value. This phenomenon is found to be related to the appearance of five-fold coordinated aluminum species.

Resume (Danish Abstract)

For at kunne forudsige effekten af kemisk sammensætning på egenskaberne af glas, er det nødvendigt først at forstå den atomare struktur af glas. Det skyldes, at glasmaterialers egenskaber er direkte bestemt af glassets struktur. I denne afhandling undersøger vi strukturen af tre glasserier: natrium calcium borat, natrium calcium aluminium-silikat og natrium bor-aluminium-silikat glas. Alle disse glasserier besidder en række interessante strukturelle fænomener, som eksempelvis "bor anomali" effekten og blandet netværks-danner effekten. Begge disse effekter resulterer i ikke-monotoniske variationer i de fysiske egenskaber som funktion af sammensætning. Det er vigtigt at udforske de strukturelle roller af de netværks-modificerende kationer i forskellige glassystemer. For at kunne studere de forskellige roller som natrium kan have, har vi designet glassammensætninger med varierende forhold mellem netværks-danner og netværk-modificerende kationer eller varierende forhold mellem forskellige netværks-dannere. Vi har udført multikerne NMR eksperimenter med ^{11}B, ^{27}Al, ^{29}Si og ^{23}Na for at bestemme netværks-danner speciering og de lokale miljøer for de netværks-modificerende kationer som funktion af glas sammensætning. De forskellige strukturelle roller af natrium i forbindelse med de netværks-dannende kationer (Si, B og Al) er blevet klarlagt og kvantificeret. Derudover har vi anvendt en ny model (to-tilstandsmodellen) til at forudsige fraktionerne af forskellig netværks speciering. De modellerede resultater er i god overensstemmelse med de eksperimentelle NMR data.

Afhængigheden af viskositet af kemisk sammensætning og temperatur er et vigtigt aspekt for at kunne kontrollere glasproduktionen og for at kunne skræddersy de fysiske egenskaber af glasprodukter. Desuden er det også kritisk for at kunne forstå dynamikken for væsker og glas. Baseret på antagelsen om en universel høj-temperatur grænseværdi for viskositet foreslog Angell, at væskers ikke-Arrhenius temperaturafhængighed af viskositet kan beskrives ved væskens kinetiske skrøbelighedsindeks. Hvorvidt der eksisterer en universel høj-temperatur grænseværdi for viskositet er dog stadig ikke blevet valideret. I denne afhandling undersøger vi høj-temperatur grænseværdien for viskositet ved at analysere målte viskositetskurver for 977 væsker, herunder oxider, metalliske, molekylære og ioniske systemer. Baseret på Mauro–Yue–Ellison–Gupta–Allan (MYEGA) modellen for væske viskositet har vi bestemt høj-temperatur græseværdien for viskositet af silikat væsker til at være $10^{-2.93}$ Pa·s. Dette resultat simplificerer modelleringen af viskositet vs. kemisk sammensætning og indikerer en fælles underliggende fysik for silikat væsker ved høj-temperatur grænseværdien. Derudover har vi vist, at der eksister en parallel relation mellem den kinetiske skrøbelighed og den termodynamiske skrøbelighed (f.eks. springet i isobarisk varmekapacitet ved glasovergangen) for de tre undersøgte glassystemer.

De fysiske og kemiske egenskaber af glas kan designes og kontrolleres ved at variere forholdet mellem de forskellige strukturelle enheder. Den blandede netværks-danner effekt resulterer i ikke-lineære variationer i mange makroskopiske egenskaber som funktion af kemisk sammensætning. Beregningen af glasegenskaber ud fra grundprincipper er ofte umuligt på grund af de lange tidsskalaer involveret i glasovergangen og relaksationsfænomener. Vi har derfor anvendt temperaturafhængig begrænsningsteori til at forstå og forklare afhængigheden af glasegenskaber af kemisk sammensætning. I henhold til denne teori afhænger glasegenskaber af antallet af bindingsbegrænsninger, da den atomare struktur af en glasdannende væske kan betragtes som et netværk af bindingsbegrænsninger. Vi har i dette arbejde undersøgt sammenhænge mellem sammensætning, struktur og egenskaber for de tre modelsystemer. Egenskaberne, som vi har studeret i denne afhandling,

inkluderer dynamiske egenskaber (glasovergangstemperatur T_g og skrøbelighed), termodynamiske egenskaber (f.eks. varmekapacitet) og mekaniske egenskaber (elasticitetsmodul og hårdhed). Vi har også klarlagt effekten af tilsætningen af 1 mol% Fe_2O_3 på de målte egenskaber for bor-aluminium-silikat glasmaterialerne.

Enhver væske kan omdannes til glas, hvis den nedkøles tilstrækkeligt hurtigt til at undgå krystallisation til en given volumenfraktion. Den langsomste nedkølingsrate, der giver et glas med en given kritisk mængde krystaller, defineres som den kritiske nedkølingsrate. Denne rate anvendes til at kvantificere glasdannelsesevnen (GFA) af forskellige væsker. GFA er en vigtig egenskab i forbindelse med glasproduktion, men det er svært præcist at bestemme værdien af den kritiske nedkølingsrate. GFA kvantificeres ofte ved glasstabiliteten (GS), der er glassets modstand mod krystallisation under opvarmning. Det er tidligere vist, at disse to parametre er direkte relateret. Derfor bruger vi i dette arbejde GS til at repræsentere GFA. Glasstabiliteten er udledt fra de karakteristiske temperaturer, såsom T_g, begyndelsestemperaturen for krystallisation og liquidus temperaturen, der er bestemt ved brug af et differentiel skanning kalorimeter. Der er generelt ingen klar sammenhæng mellem GS og skrøbelighed for de undersøgte glasserier. Vi har vist, at GS for natrium calcium borat serien kan forbedres ved først langsomt at nedkøle smelten til glastilstanden. Vi har diskuteret den mulige strukturelle årsag til forbedringen af glasstabilitet. Endelig har vi opdaget et dramatisk tab af GS, når koncentrationen af Al_2O_3 overskrider en kritisk værdi i natrium calcium aluminium-silikat glasserien. Dette fænomen hænger sammen med fremkomsten af fem-koordinerede aluminium ioner.

Table of Contents

1. Introduction **1**
1.1. Background and Challenges 1
1.2. Objectives 3
1.3. Thesis Content 3

2. Glass Structure **4**
2.1. Soda-Lime Borate System 5
2.2. Soda-Lime Aluminosilicate System 7
2.3. Sodium Boroaluminosilicate System 9
2.4. Summary 18

3. Dynamics of Oxide Liquids **19**
3.1. High-temperature Limit of Viscosity 19
3.2. Liquid Fragility 26
3.3. Summary 35

4. Structure-Physical Property Correlations **36**
4.1. Temperature-Dependent Constraint Theory 36
4.2. Soda-Lime Borate Glasses 38
4.3. Soda-Lime Aluminosilicates Glasses 40
4.4. Sodium Boroaluminosilicate Glasses 42
4.5. Summary 46

5. Glass-Forming Ability **47**
5.1. Soda-Lime Borate Liquids 49
5.2. Soda-Lime Aluminosilicate Liquids 52
5.3. Summary 53

6. General Discussion and Perspectives **54**

7. Conclusions **58**

8. Bibliography **60**

List of Publications **65**

1. Introduction

Glass is a wonderful material that has found widespread application in our daily life, such as container glass, window glass, liquid crystal display substrate, and optical fiber. Silica is found to be the major constituent of many of these glasses and also of the early man-made glass materials. The importance of a variety of non-silicate glasses has also been recognized, such as chalcogenide glasses. Moreover, polymers and metals can also be formed as glasses. In principal any liquid can be turned into a glass, provided that it can be cooled from the liquid state at a sufficiently fast rate.

A glass is defined as "an amorphous solid completely lacking in long range, periodic atomic structure, and exhibiting a region of glass transformation behavior." Any material exhibits glass transformation behavior is a glass [Shelby 2005]. We can form glasses by, e.g., chemical vapor deposition and sol–gel methods [Angell 1995; Varshneya 2006]. However, oxide glasses are most commonly made by cooling a liquid fast enough to avoid crystallization. The atomic structure of the resulting glass is representative of that of its frozen-in parent liquid at the temperature at which the liquid equilibrated for the last time. This temperature is defined as the fictive temperature T_f [Mauro *et al*. 2009b]. The glass is therefore a solid with a non-crystalline structure, which is unstable with respect to the supercooled liquid. The supercooled liquid is itself metastable with respect to the corresponding crystal [Varshneya & Mauro 2010].

Since the publication of the classic paper by W. H. Zachariasen in 1932 entitled "The Atomic Arrangement in Glass" [Zachariasen 1932], understanding of glass structure has been one of the most important topics in glass science, and also been improved significantly due to advancement of structural characterization techniques, computer simulation [Cormack & Cao 1996] and structure theories such as modified random network theory [Greaves & Sen 2007] and network constraint theory [Phillips 1979]. Recently, the first direct image of a two dimensional silica glass has been obtained [Huang *et al.* 2012]. However, even today glass structure is still far from fully understanding. From glass technology point of view, it is crucial to understand the atomic structure of glass which determines its properties. Revealing the connection between composition and properties is essential for predicting physical and chemical properties of glasses as a function of chemical composition and mechanical and thermal histories. However, unlike crystalline materials, no universal structural model exists for glassy materials. There are still many challenging problems in terms of glass structure and properties.

1.1 Background and Challenges

By use of the partial ionic character model of Pauling, the chemical components of oxide glasses can be classified into three groups on the basis of the electronegativity of the cation [Stanworth 1971]. The *network formers* are the cations used to create the structural network of oxide glasses. While the *network modifiers* are the cations used to modify the network structure. *Intermediates* are the cations behave intermediate between that of cations which do form glasses and those which never form glasses [Shelby 2005]. The network-modifying cations possess various structural roles in different glass systems. In silicate glasses, they disrupt the connectivity of the silicate network. In borate glasses, due to the "boron anomaly" effect, the role of network-modifiers becomes more complicated. In aluminosilicate glasses, Al_2O_3 has a dual structural role depending on the glass composition. Moreover, the addition of Al_2O_3 to borosilicate glasses causes changes of network speciation depending on the ratio

of the network-formers and the content of the network-modifier. The different structural roles of network modifiers in boroaluminosilicate glasses are complicated due to the mixed network-former effect. The extent and nature of the mixing of the network-forming cations (Si, B, and Al) is not yet well-understood. In the present Ph.D. work, we study the structure of three different model glass series: soda lime borate, soda lime aluminosilicate, and sodium boroaluminosilicate. The three glass series are all of industrial importance since the PhD work is carried out in close collaboration with Corning Incorporated. The properties, which we are interested in,include dynamic properties, glass-forming ability (GFA) and mechanical properties.

Adequate control of flow behavior is essential for all steps of industrial glass production and hence it is necessary to study the rheological and dynamic behaviors of glass-forming liquid. Moreover, the glass forming ability and physical properties of glasses are closely related to rheological and thermodynamic properties. However, although there has been considerable progress in recent years, our understanding of the mechanisms of viscous flow remains incomplete [Debenedetti & Stillinger 2001; Mauro *et al.* 2009b]. In this work, we investigate the dynamic behaviors (glass transition temperature T_g and liquid fragility index m) in terms of kinetics and thermodynamics. In particular, we answer the important question about whether the high-temperature viscosity limit of glass-forming liquids is universal. In Angell plot, the logarithmic viscosity (log η) is plotted against the T_g-scaled inverse temperature (T_g/T) [Angell 1985]. The slope of the log $\eta \sim T_g/T$ curve at T_g is defined as the liquid fragility index m. In general, there is a connection between the kinetic fragility index m and thermodynamic fragility despite several exceptions [Martinez and Angell, Nature 2001]. In this work we answer the question of how the two kinds of fragilities are interconnected for the chosen three model glass series.

The ability of substances to vitrify on cooling from the melt is known as glass-forming ability (GFA) [Avramov *et al.* 2003]. The GFA is important in the industrial glass-formation process. Moreover, it is also linked to the fundamental question of what physical factors control a liquid-glass transition [Tanaka 2005]. GFA has been the object of theoretical and experimental investigations for decades. Despite progress in understanding in the last few years, it is still a major challenge to quantify the GFA of many glass systems, in particular, good glass formers. There are still several puzzles about why some systems can be vitrfied while others cannot, and why certain composition ranges have good GFA while others do not. In this work, we attempt to determine and understand the GFA of soda-lime-borate glasses and soda lime aluminosilicate systems. The derived results will be beneficial to a general understanding GFA of liquids. We evaluate the GFA and the glass stability of these glasses by measuring their crystallization tendency and viscous flow behavior.

Substantial progress has been made over the past decade in the development of new glasses with improved mechanical properties. The understanding of composition dependence of elastic moduli is of importance since it is instructive to other mechanical properties which are closely associated with the elastic moduli, e.g., tensile strength. Hardness is another important mechanical property of materials for both advanced glass applications and for revealing underlying fracture mechanisms, e.g., touch screen displays require high hardness and scratch resistance [Varshneya 2010]. Deeper understanding of the mechanical properties is essential to optimize compositions that possess both high mechanical resistance and the economically favorable processing conditions. Some complicated glass systems, such as mixed network glasses, show nonlinear variation in many macroscopic properties, which is

due to the mixed network former effect. Although many previous attempts have been made to predict glass properties based on structural information, it is still challenging. In this thesis, we apply the temperature-dependent constraint theory [Mauro 2011a] to understand the composition dependence of their glass properties. This theory has been proved to be a powerful tool to predict the composition dependence of glass properties; moreover, it provides insight into the structural origins of that dependence.

1.2 Objectives

Based on the above introductions, the objectives of the present Ph.D. thesis are to

1. establish the high temperature limit of liquid viscosity by a systematic analysis of experimental data,
2. clarify the glass forming ability of a series of soda-lime borate glass,
3. detect the link between the kinetic fragility determined from viscosity measurements and various thermodynamic fragility indices,
4. clarify the structural role of sodium and the composition-structure-property relationships in boroaluminosilicate glasses, and
5. clarify the influence of aluminum speciation on the stability of aluminosilicate glasses.

1.3 Thesis Content

The thesis is presented as a plurality, including an introductory overview followed by papers. The thesis is based on the following publications (in the text these papers will be referred to by roman numerals):

I. Q. J. Zheng, R. E. Youngman, C. L. Hogue, J. C. Mauro, M. Potuzak, M. M. Smedskjaer, A. J. Ellison, Y. Z. Yue, "Structure of Boroaluminosilicate Glasses: Impact of $[Al_2O_3]/[SiO_2]$ Ratio on the Structural Role of Sodium," *Physical Review B*, **86**, 054203,(2012).

II. Q. J. Zheng, J. C. Mauro, A. J. Ellison, M. Potuzak, and Y. Z. Yue, "Universality of the high-temperature viscosity limit of silicate liquids," *Physical Review B* **83**, 212202 (2011).

III. Q. J. Zheng, M. Potuzak, J. C. Mauro, M. M. Smedskjaer, R. E. Youngman, Y. Z. Yue, "Composition-Structure-Property Relationships in Boroaluminosilicate Glasses," *Journal of Non-Crystalline Solids* **358**, 993-1002 (2012).

IV. Q. J. Zheng, J. C. Mauro, M. M. Smedskjaer, R. E. Youngman, M. Potuzak, and Y. Z. Yue, "Glass-Forming Ability of Soda Lime Borate Liquids," *Journal of Non-Crystalline Solids* **358** , 658-665 (2012).

V. Q. J. Zheng, M. M. Smedskjaer, R. E. Youngman, M. Potuzak, J. C. Mauro, Y. Z. Yue, "Influence of Aluminum Speciation on the Stability of Aluminosilicate Glasses against Crystallization," *Applied Physics Letters,* **101,** 041906 (2012).

2. Glass Structure

The prediction of physical and chemical properties of glasses as a function of chemical composition and thermal history relies on a detailed understanding of the glass structure. The structural models of complex multicomponent glasses rely on the combination of experimental data with atomistic modeling. However, due to lack of long-range order in glass, it is not possible to characterize the glass structure by the application of conventional techniques such as x-ray diffraction. Alternative techniques such as nuclear magnetic resonance (NMR) spectroscopy have been proved to be a powerful tool to characterize both the short- and intermediate-range structural order in glass. For example, ^{11}B NMR spectroscopy [Yun & Bray 1978; Zhong & Bray 1989] has successfully captured the composition dependence of the fraction of tetrahedral and trigonal boron species (B^{IV} and B^{III}) in B_2O_3-containing glasses.

In earlier studies, the low-field, static NMR provided some structural information; however, the resolution is not sufficient to determine the presence of different sites [Emerson *et al.*1989]. Moreover, the accurate determination of the isotropic chemical shifts is not allowed due to the dipolar broadening and anisotropic shifts. The magic angle spinning (MAS) NMR spectroscopy has been developed afterwards. This technique effectively reduces dipolar broadening and anisotropies, which enables the measurement of the isotropic chemical shift [Emerson *et al.*1989]. While conventional (MAS) NMR often cannot yield highly resolved spectra due to residual second order quadrupolar broadening, triple quantum (3Q) magic angle spinning (MAS) NMR spectroscopy has recently shown to generate better resolution on network speciation and modifier cation environment, particularly at relatively high-magnetic fields [Lee *et al.* 2006]. In this thesis, we have applied multinuclear NMR experiments including (MAS) NMR and (3Q) (MAS) NMR on ^{11}B, ^{27}Al, ^{29}Si and ^{23}Na to characterize the structure of different glass systems.

The chemical components of oxide glasses can be divided into different categories according to their role in the atomic arrangement of the glass network [Stanworth 1971]. The so-called network-forming cations (such as Si^{4+}) create the structural network of oxide glasses. These cations are defined as those having a fractional ionic bond with oxygen near or below 50%. On the other hand, the network-modifying cations (e.g., Na^+ and Ca^{2+}) form highly ionic bonds with oxygen. These cations modify and interfere with the primary network structure without becoming a part of it.

The network-modifying cations possess various structural roles in different glass systems. In silicate glasses, they disrupt the connectivity of the silicate network and create non-bridging oxygens (NBOs) that are linked to only one network-forming cation. In borate glasses, the role of network-modifiers is more complicate due to the so-called "boron anomaly" effect. The initial addition of modifier oxides to pure B_2O_3 results in the conversion of B^{III} to B^{IV}, with the network modifier cations acting as charge compensators for B^{IV}. The fraction of tetrahedral to total boron (N_4) reaches a maximum with further modifier addition, and then decreases due to formation of NBOs on B^{III} [Bray & O'Keefe 1963; Zhong & Bray 1989].

In aluminosilicate glasses, Al^{3+} is stabilized in tetrahedral coordination (Al^{IV}) when associated with charge balancing cations [Mysen & Richet 2005]. However, when the concentration of Al_2O_3 exceeds that of the network modifiers, higher coordinated aluminum

(e.g., five-fold coordination) species form. Hence, Al_2O_3 has a dual structural role depending on the glass composition, Therefore, the addition of Al_2O_3 to borosilicate glasses causes changes of network speciation depending on the ratio of the network-formers and the content of the network-modifier. This is because both aluminum and boron require network modifiers for charge compensation for stabilization in a tetrahedral configuration. However, it has been found that there is a preference in the formation of Al^{IV} over than of B^{IV}, since the addition of Al_2O_3 in these glasses results in an observed decrease in N_4 [Chan *et al.* 1999]. Five- and six-fold coordinated aluminum species (Al^{V} and Al^{VI}) may start to form if the molar ratio of modifier cation to Al is smaller than one [Chan *et al.* 1999; Züchner *et al.* 1998; Bunker *et al.* 1991]. The different structural roles of network modifiers in boroaluminosilicate glasses are therefore more complicated than the well-modeled borosilicate glasses.

Despite the large amount of reliable experimental data on glass structure that has been obtained in the last decades, none of the currently known structural models can be used to determine which type of structural units are responsible for changes in glass properties. In this chapter, we study the structure of three different model systems: soda lime borate, soda lime aluminosilicate, and sodium boroaluminosilicate glasses. The obtained knowledge will be applied in the subsequent chapters, where the different properties of these systems will be investigated.

2.1 Soda-Lime Borate System

Due to their poor chemical durability, pure borate glasses (i.e., without the addition of silica) have only found limited applications However, it has recently been discovered that nanofibers made from borate glass possess bioactivity, since they promote the healing of flesh wounds [Wray 2011]. The poor chemical durability of the borate glass is an advantage in this case, since it promotes soft-tissue regeneration and has an antimicrobial effect.

From a scientific point of view, borate glasses are interesting to study, since they contain an abundance of structural features, e.g., the "boron anomaly" effect, which yields nonmonotonic variations of physical properties. In borate glasses, boron can form both BO_3 triangles and BO_4 tetrahedra, whereas oxygen atoms can adopt both bridging (BO) and non-bridging (NBO) configurations. When alkali or alkaline earth oxides are added to B_2O_3, they will either be used to create NBO or to convert boron from a three-coordinated (B^{III}) to a four-coordinated (B^{4}) state depending on the molar ratio between B_2O_3 and the alkali and alkaline earth oxides [Smedskjaer *et al.* 2010a; Smedskjaer 2011]. Moreover, the random pair model of Gupta [Gupta 1986] establishes three rules for network formation: (i) BO_4 tetrahedra occur in corner-sharing pairs, where the B-O-B angle within a pair is random; (ii) pairs of BO_4 tetrahedra cannot be bound to each other; and (iii) NBOs occur in BO_3 groups only.

The structure of alkali and alkaline earth binary borate glasses has been studied widely [Stebbins & Ellsworth 1996]. However, the structure of ternary soda lime borate (Na_2O-CaO-B_2O_3) glasses has not drawn much attention. Smedskjaer *et al*. have investigated the structure of a series soda lime borate glass ((89-*x*)B_2O_3-*x*Na_2O-10CaO-1Fe_2O_3 system with x = 5, 10, 15, 20, 25, 30, and 35) [Smedskjaer *et al.* 2010a]. This is the same series of glasses that will be investigated in the subsequent chapters. Table 2.1 shows the chemical compositions and selected properties of this system. For x < 23 mol%, BO_3 units are converted into BO_4 unit as the Na_2O content increases. For x > 23 mol%, NBOs start to form [Smedskjaer *et al.* 2010a]. It should be noticed that some of the glasses contain 1 mol% Fe_2O_3 for investigating the

impact of boron speciation on the so-called inward diffusion, which requires the presence of a polyvalent oxide [Smedskjaer *et al.* 2010a].

Table 2.1 Nominal compositions and properties of investigated glass samples. Data taken from [Smedskjaer *et al.* 2010a].

Glass ID	Composition (mol%)				N_4 (±1%)	T_g (K)	m (-)
	B_2O_3	CaO	Na_2O	Fe_2O_3			
Ca10-Na5	84.85	10.1	5.05	-	-	708	-
Ca10-Na15	74.75	10.1	15.15	-	37	775	-
Ca10-Na25	64.65	10.1	25.25	-	46	764	-
Ca10-Na35	54.55	10.1	35.35	-	41.3	716	-
Ca10-Na5-Fe1	84	10	5	1	16	693	45±2
Ca10-Na10-Fe1	79	10	10	1	24	756	49±2
Ca10-Na15-Fe1	74	10	15	1	36	771	54±3
Ca10-Na20-Fe1	69	10	20	1	40	768	58±4
Ca10-Na25-Fe1	64	10	25	1	46	756	65±5
Ca10-Na30-Fe1	59	10	30	1	43	740	56±6
Ca10-Na35-Fe1	54	10	35	1	42	711	53±3

The inset of Fig. 2.1 shows the ^{11}B MAS NMR spectra with (dashed lines) and without (solid lines) 1 mol% Fe_2O_3 of glasses with 35, 25, and 15 mol% Na_2O. These spectra are characterized by a broad, nearly symmetric peak centered at ~16 ppm corresponding to the B^3 sites and a relatively narrow symmetric peak centered at ~ 1 ppm corresponding to the B^4 sites. The relative fractions of B^3 and B^4 sites can be obtained from the areas under the corresponding peaks in the ^{11}B MAS NMR spectra [Smedskjaer *et al.* 2010a]. Using Gupta's random pair model for network formation, Smedskjaer *et al.* have calculated the fractions tetrahedral to total boron (N_4) as a function of composition. As shown in Fig. 2.1, there is good agreement between these calculated fractions and those determined using ^{11}B MAS NMR spectroscopy [Smedskjaer 2011].

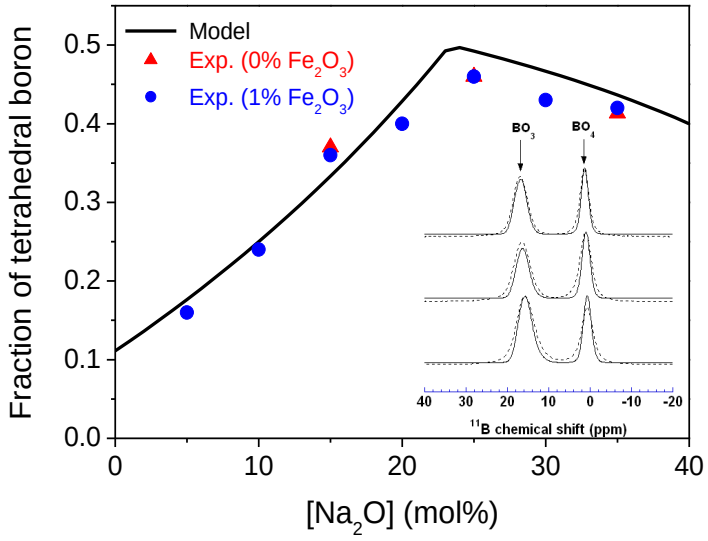

Figure 2.1 Fraction of tetrahedral to total boron in (90-*x*)B_2O_3-*x*Na_2O-10CaO glasses with and without 1 mol% Fe_2O_3 calculated using the random pair model of Gupta or determined experimentally using ^{11}B MAS NMR spectroscopy. Inset: corresponding ^{11}B MAS NMR spectra with (dashed lines) and without (solid lines) 1 mol% Fe_2O_3. The spectra from top to bottom correspond to glasses with 35, 25, and 15 mol% Na_2O. Data taken from [Smedskjaer 2011].

2.2 Soda-Lime Aluminosilicate System

Aluminosilicate glasses have many applications [Varshneya 2006], such as substrate glass for liquid crystal displays [Ellison & Cornejo 2010] and chemically strengthened cover glass for personal electronic devices [Varshneya 2010, Tandia *et al.* 2012]. However, better understanding of the relationship between glass composition, structure, and properties is of crucial importance. For example, the glass stability (GS) of these glasses is found to be closely related to the formation of five-coordinated Al species [Yu *et al.* 2010].

In aluminosilicate glasses aluminum plays mainly two different structure roles, viz., it can act either as a network-former in tetrahedral coordination or in a charge compensating role in five- or six-fold coordination [Bottinga & Weill 1972]. Generally, when the concentration of network modifiers is higher than that of alumina, Al^{3+} is stabilized in tetrahedral coordination (Al^{IV}) [Mysen & Richet 2005, Chan *et al.* 1999]. When there are insufficient network modifiers available, higher coordinated aluminum (e.g., five-fold coordination, Al^{V}) will exist as charge compensator. However, higher coordinated aluminum species have been experimentally detected in peralkaline alkali and alkaline earth aluminosilicate glasses [Toplis *et al.* 2000]. This indicates that the structure of aluminosilicate glasses is more complicated than the simple structural model.

Here we study the structure of a series of soda lime aluminosilicate glasses with compositions (in mol%) of (76-*x*)SiO_2–*x*Al_2O_3–16Na_2O–8CaO with *x* = 0, 2.7, 5.3, 8, 10.7, 13.3, 16, 18.7, 21.3, and 24. The atomic structural evolution of the glassy network is quantified through ^{27}Al magic-angle spinning nuclear magnetic resonance (MAS NMR) measurements. This is also

the same series of glasses that will be investigated in the subsequent chapters. Table 2.2 shows the chemical compositions and structure properties of this system.

Table 2.2 Nominal compositions and properties of investigated glass samples

Glass ID	Composition (mol%)				Al^V (at%)	NBO/T
	Na_2O	CaO	SiO_2	Al_2O_3		
Ca-Al0	15.7	8.1	75.9	0.0	0	0.627
Ca-Al2.7	15.8	8.1	73.2	2.7	0	0.538
Ca-Al5.3	15.8	7.9	70.7	5.3	0	0.452
Ca-Al8	15.7	7.9	68.1	8.0	0	0.371
Ca-Al10.7	15.8	8.0	65.2	10.7	0	0.302
Ca-Al13.3	15.8	8.1	62.6	13.3	8	0.267
Ca-Al16	15.8	8.1	59.8	16.0	12	0.222
Ca-Al18.7	15.7	8.1	57.2	18.7	13	0.168
Ca-Al21.3	15.7	8.4	54.3	21.3	18	0.148
Ca-Al24	15.8	8.1	51.8	24.0	26	0.142

The ^{27}Al MAS NMR results in Fig. 2.2a show that when $[Na_2O]>[Al_2O_3]$, the spectra primarily consist of a narrow peak centered at around +50 ppm, which corresponds to Al^{IV}[Smedskjaer *et al.* 2012; Risbud *et al.*1987]. For the glasses with $[Al_2O_3]\geq[Na_2O]$, the MAS NMR lineshape broadens asymmetrically on the more shielded side (lower shift), which is due to the presence of Al in 5-fold coordination [Risbud *et al.*1987]. Since calcium is not as effective as sodium in stabilizing Al tetrahedral, 5-fold coordinated aluminum species are formed for $[Al_2O_3]\geq[Na_2O]$, providing another means for charge-compensation. The fraction of Al^V increases with increasing Al_2O_3 content (Fig. 2.2b). The number of non-bridging oxygen per tetrahedron (NBO/T) can be calculated based on the Al^V fractions. NBO/T decreases as the sodium and calcium ions are used for charge-compensating tetrahedral aluminum instead of forming non-bridging oxygens (Fig. 2.3). It indicates that the network connectivity increases with the increase of $[Al_2O_3]$.

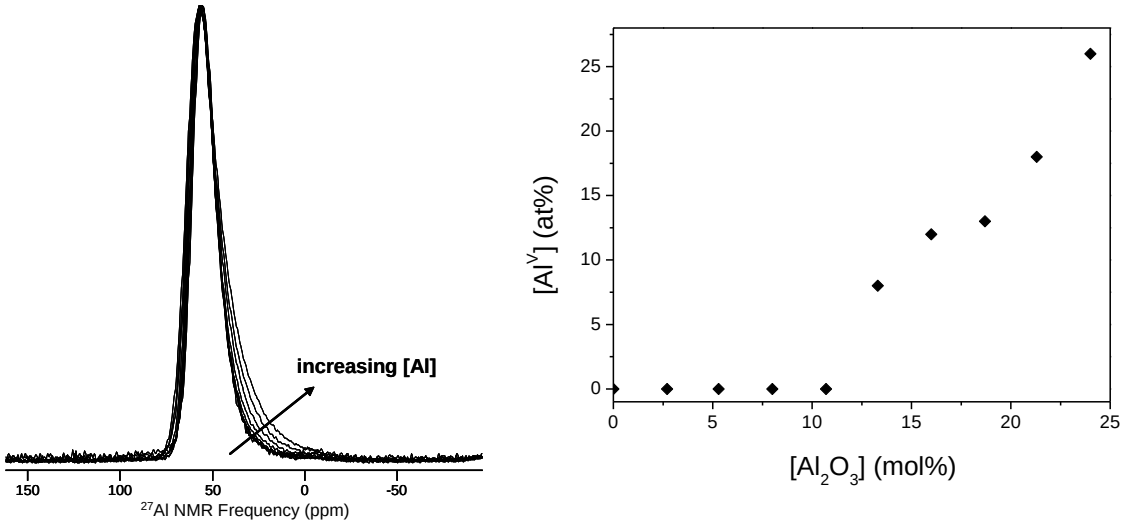

(a) (b)

Figure 2.2 (a) ^{27}Al MAS NMR spectra of the aluminosilicate glasses [Smedskjaer *et al.* 2012]. The spectra show unchanging lineshape for glasses having $[Al_2O_3]<[Na_2O]$ and asymmetrical broadening for glasses with $[Al_2O_3]\geq[Na_2O]$. Reproduced from Paper V. (b) The fraction of Al^V, i.e.,$Al^V/Al^{IV} + Al^V$) vs. $[Al_2O_3]$.

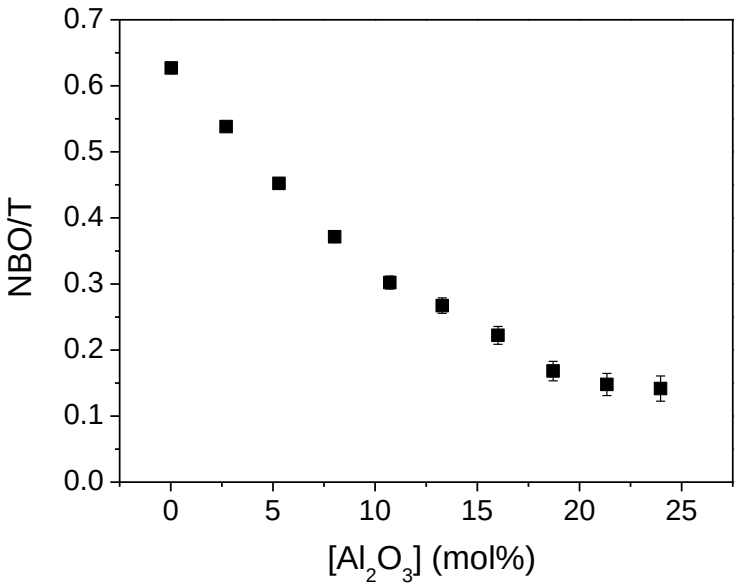

Figure 2.3 Composition dependence of the number of non-bridging oxygen per tetrahedron (NBO/T) calculated based on the analyzed compositions and the fraction of tetrahedral aluminum from ^{27}Al MAS NMR. Reproduced from Paper V.

2.3 Sodium Boroaluminosilicate System

Boroaluminosilicate glasses have found applications in many fields, such as crystal display substrates [Ellison & Cornejo 2010], glass fibers for reinforcement [Varshneya 2006],

thermal shock-resistant glass containers [Varshneya 2006], and radioactive waste glasses [Jantzen *et al.* 2010]. Therefore, it is important to understand the structure of this glass system. However, this is a complicated task due to the mixed network-former effect, which leads to nonlinear variation in many macroscopic properties [Ingram 1987; Martin 1991; Schuch *et al.* 2009]. The extent and nature of the mixing of the network-forming cations (Si, B, and Al) play an important role in controlling the macroscopic properties. However, it is not yet well-understood. Particularly, it is important to better understand the composition dependence of N_4, since boron speciation is a very important parameter controlling several glass properties [Saini *et al.* 2009].

In Paper I, we have investigated the structure of ten sodium boroaluminosilicate (Na_2O-B_2O_3-Al_2O_3-SiO_2) glasses with varying [Al_2O_3]/[SiO_2] ratio. The glasses are designed in a way to access different regimes of sodium behavior. Figure 2.4 shows the designed composition of the ten glasses in a ternary B_2O_3-Al_2O_3-SiO_2 phase diagram.

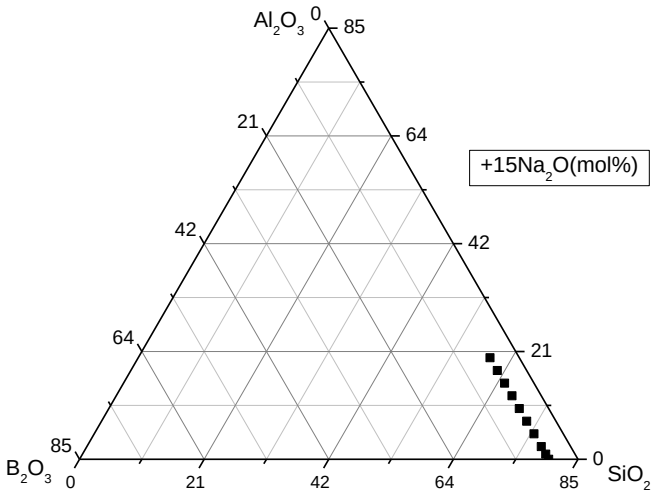

Figure 2.4 Ternary B_2O_3-Al_2O_3-SiO_2 phase diagram (mol%) plus 15% Na_2O. We mark the designed glass compositions under investigation in Paper I downward the composition triangle.

The analyzed compositions of the glasses are slightly different from the batched compositions, but we have retained the original naming convention based on $x$$Al_2O_3$, as listed in Table 2.3.

There are mainly three different regimes of sodium behavior in sodium boroaluminosilicate glasses: 1) Na^+ to stabilize aluminum in a tetrahedral configuration; 2) Na^+ to convert boron from trigonal to tetrahedral coordination; and 3) Na^+ to form nonbridging oxygens on silicon or trigonal boron. In Paper I, we have performed multinuclear NMR experiments on ^{11}B, ^{27}Al, ^{29}Si and ^{23}Na to determine the complicated network former speciation and modifier environments as a function of glass composition. We summarize these results in the following, where we also evaluate the ability of several models to predict the network former speciation.

Table 2.3 Analyzed chemical compositions, melting temperature (T_h), glass transition temperature (T_g), and fraction of tetrahedral to total boron (N_4) of the boroaluminosilicate glasses. Reproduced from Paper I.

Glass ID	Compositions (mol%)					T_h	T_g	N_4
	SiO_2	Al_2O_3	B_2O_3	Na_2O	Fining agent	(°C)	(K)	(at%)
Al0	80.08	0.16	4.84	14.77	0.15	1450	809	94.9
Al1	79.38	1.16	4.85	14.60	0.14	1450	814	93.2
Al2.5	78.80	2.00	4.70	14.40	0.08	1450	822	94.6
Al5	78.10	4.00	4.20	13.60	0.07	1500	837	91.6
Al7.5	76.90	5.70	4.30	13.00	0.06	1550	851	83.1
Al10	75.90	7.50	4.30	12.30	0.07	1600	871	74.4
Al12.5	72.00	10.40	4.40	13.10	0.07	1650	887	43.6
Al15	69.20	12.70	4.60	13.50	0.07	1650	899	19.9
Al17.5	62.97	17.18	4.99	14.73	0.13	1650	956	1.0
Al20	60.52	19.61	5.00	14.73	0.14	1650	966	0.8

[a]T_g was obtained by fitting viscosity data with MYEGA equation [Mauro *et al.* 2009b] and determined as the temperature at which equilibrium viscosity is 10^{12} Pa s [Paper III]. The uncertainty of T_g is approximately ±5 K. Al0, Al1, Al17.5 and Al20 used SnO_2 as fining agent while the rest of these glasses used As_2O_3 as a fining agent.

2.3.1 Aluminum Speciation

The ^{27}Al MAS NMR spectra of the ten mixed network-former glasses confirm the association between Na^+ and tetrahedral aluminum groups (Fig. 2.5). When $[Na_2O] \geq [Al_2O_3]$, the spectra all consist of the Al^{IV} peak centered at around +50 ppm and the spectra are similar to one another [Risbud *et al.* 1987]. This implies that there is no significant difference in the Al^{IV} environment as a function of glass composition. For the two peraluminous glasses (Al17.5 and Al20), the ^{27}Al MAS NMR spectra have become asymmetrically broader, which indicates the presence of both Al^{IV} and Al^{V} [Risbud *et al.* 1987]. 3QMAS NMR spectroscopy provides higher resolution for quadrupolar nuclei such as ^{27}Al, enabling better resolution of different coordination environments in the isotropic dimension. We have therefore also obtained two-dimensional ^{27}Al 3QMAS NMR spectra of representative glasses containing low (Al2.5) and high (Al17.5) $[Al_2O_3]$. As described in Paper I, these data are consistent with the ^{27}Al MAS NMR data.

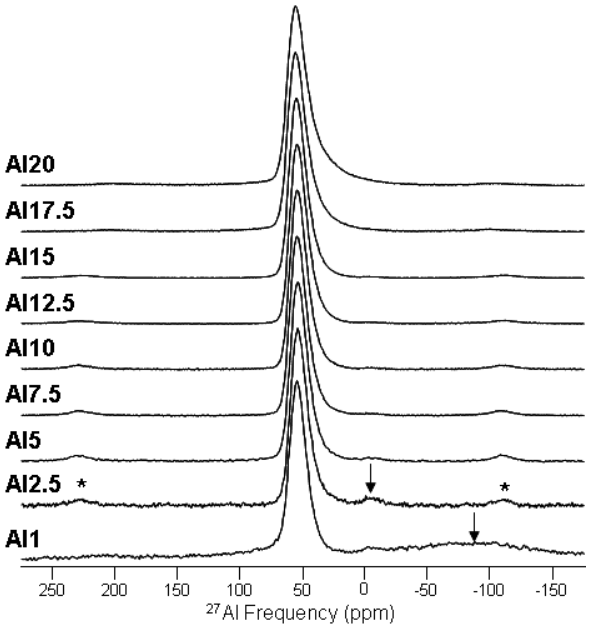

Figure 2.5 ^{27}Al MAS NMR spectra of the boroaluminosilicate glasses as described and labeled in Table 2.3. The asterisks mark spinning sidebands and the arrows denote background signal from rotor components, which is only seen at the lowest [Al_2O_3]. Reproduced from Paper I.

The ^{27}Al MAS and 3QMAS NMR results indicate that the aluminum-to-sodium ratio controls the Al speciation. For the peralkaline compositions, there is sufficient Na^+ available to stabilize all aluminum in four-fold coordination. Thus, only the Al^{IV} peak is detected and the Al^{IV} environments are mostly unchanged with composition. For the peraluminous compositions, a small fraction of Al^V is detected in both the ^{27}Al MAS and 3QMAS NMR data. The presence of Al^V is due to the insufficient amount of charge-balancing modifier cations (Na^+) to stabilize all Al in four-fold coordination. Therefor,e some higher coordination Al species are formed and believed to provide an additional source of charge compensation in these networks [Risbud *et al.* 1987; Sen & Youngman 2004]. Based on these results, we can confidently use the value of [Na_2O]-[Al_2O_3] to calculate an "effective" modifier concentration. This concentration corresponds to the amount of modifier left to act in other roles, including stabilization of B^{IV} and creation of NBOs in a pseudo-ternary sodium borosilicate glass.

2.3.2 Boron Speciation

The ^{11}B MAS NMR spectra are characterized by a broad peak centered at +10 ppm, corresponding to B^{III} sites, and a relatively narrow peak centered around -2 ppm, corresponding to B^{IV} sites (Fig. 2.6). When [Al_2O_3] ≤ [Na_2O], both B^{III} and B^{IV} are detected. When [Al_2O_3] > [Na_2O], most of the boron atoms exist in B^{III}, with little evidence for the B^{IV} resonance. The fraction of B^{IV} (N_4) decreases with increasing [Al_2O_3] for the entire series of glasses as reported in Table 2.3.

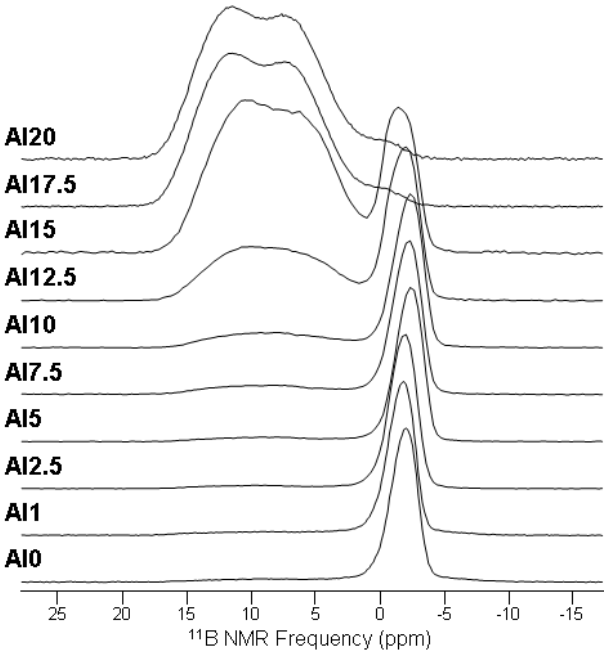

Figure 2.6 ^{11}B MAS NMR spectra of the boroaluminosilicate glasses as described and labeled in Table 2.3. Reproduced from Paper I.

^{11}B 3QMAS NMR spectra of representative glasses containing low (Al2.5) and high (Al17.5) [Al_2O_3] confirm the presence of both B^{III} and B^{IV} sites [Paper I]. Moreover, the spectra show that the high-[Al_2O_3] glasses contain a small quantity of B^{IV} units. At low [Al_2O_3], the boron are predominantly in four-fold coordination since there is sufficient sodium available to convert boron from B^{III} to B^{IV}. As [Al_2O_3] increases, the effective modifier content decreases, i.e., N_4 decreases.

2.3.3 Non-Bridging Oxygen Formation

As described above, N_4 never reaches 100% even when there theoretically is sufficient "effective modifier" available to charge compensate all boron atoms in four-fold configuration. Hence, after charge compensating Al^{IV}, not all of the excess Na^+ ions are used in converting B^{III} to B^{IV}. Instead, some of the excess modifier is used for formation of NBOs. The NBOs can be formed on both boron and silicon.

Both ^{11}B MAS NMR spectra and ^{11}B 3QMAS NMR spectra contain evidence for formation of NBOs on B^{III} [Paper I]. However, the quantification of NBOs on boron is difficult due to the small amount of boron. As the amount of excess modifier increases, the ^{11}B MAS NMR lineshape for B^{III} is changing from one comprised of all symmetric B^{III} units, to one with at least some fraction of B^{III} with NBOs (Fig. 2.6).

^{29}Si MAS NMR spectra of the ten boroaluminosilicate glasses show that the silicon shifts to higher chemical shift as [Al_2O_3] increases (Fig. 2.7). The spectra at lower values of [Al_2O_3] appear to be comprised of at least two separate resonances, whereas the peak narrows and becomes more symmetric at higher alumina concentrations. This indicates that the Si speciation changes with the variation of the [Al_2O_3]/[SiO_2] ratio.

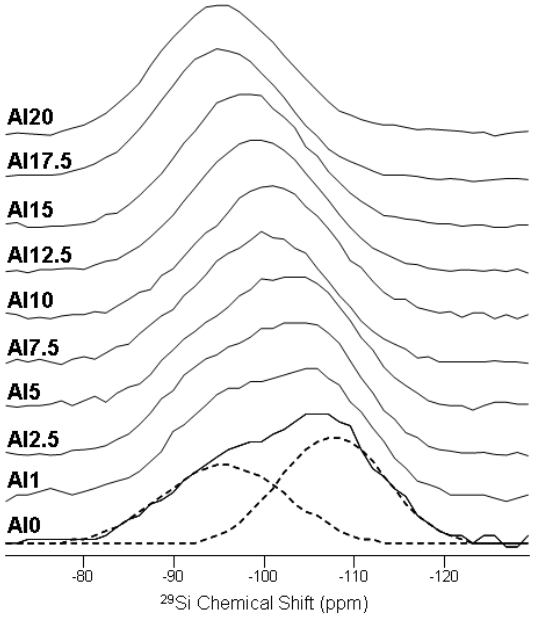

Figure 2.7 ^{29}Si MAS NMR spectra of the boroaluminosilicate glasses. The spectra are labeled as in Table 2.3. The spectrum of Al0 includes a Gaussian deconvolution into two distinct resonances (dashed lines). Reproduced from Paper I.

The quantification of non-bridging oxygen on silicon can be achieved by analysis of ^{29}Si wideline (static) NMR spectral lineshapes (Fig. 2.8). The ^{29}Si wideline NMR spectra for low [Al_2O_3] glasses are highly asymmetric, reflecting the existence of NBOs, which is consistent with the ^{29}Si MAS NMR data.

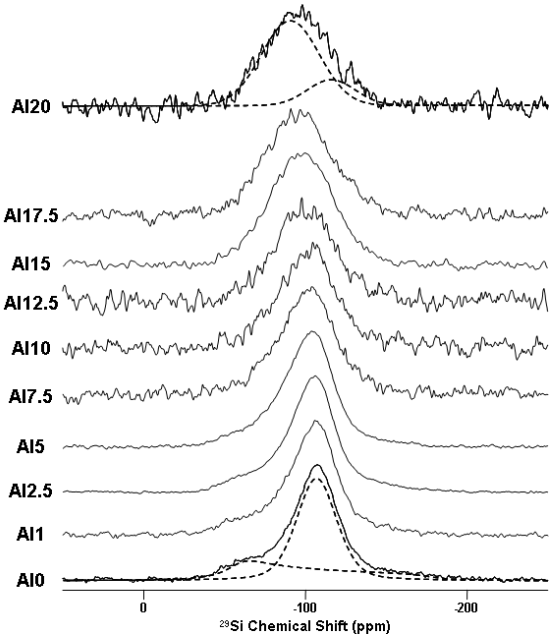

Figure 2.8 Wideline ^{29}Si NMR spectra of the boroaluminosilicate glasses. The spectra are labeled using the naming convention in Table 2.3. Dashed lines denote lineshape simulations. Reproduced from Paper I.

The wideline ^{29}Si NMR spectra were deconvoluted and fit with DMFit [Massiot *et al.* 2002] in order to provide quantitative estimates of the relative amounts of silicon with three BOs

and one NBO (Q^3) and silicon with four BOs (Q^4) (Table 2.4). The Q^3 concentration decreases with increasing $[Al_2O_3]$ and become zero for $[Al_2O_3] \geq \sim 12$ mol. Despite the complications in determining the Q^3 populations, the ^{29}Si NMR data do show the presence and compositional dependence of NBO on the $[Al_2O_3]/[SiO_2]$ ratio. The various NMR data confirm that the "effective modifiers" are used not only for converting B^{III} to B^{IV}, but also for creating Si-NBO and B-NBO. Hence, there is a competition between converting B^{III} to B^{IV} and creating NBO.

Table 2.4 Q^n units calculated by the random model and measured by NMR for the boroaluminosilicate glasses as described and labeled in Table 2.3. $Q^{3'}$ is estimated for comparision to the NMR results by assuming $Q^2=2Q^3$ and ignoring the minor contributions from Q^1 in the random model. Reproduced from Paper I.

Glass ID	Random model						NMR
	Q^4(%)	Q^3(%)	Q^2(%)	Q^1(%)	Q^0(%)	$Q^{3'}$(%)	Q^3 (%)
Al0	77.28	20.57	2.05	0.09	0.00	24.68	33
Al1	79.41	18.85	1.68	0.07	0.00	22.20	24
Al2.5	81.33	17.25	1.37	0.05	0.00	19.99	18
Al5	86.11	13.12	0.75	0.02	0.00	14.62	12
Al7.5	90.72	8.95	0.33	0.01	0.00	9.61	5
Al10	95.89	4.04	0.06	0.00	0.00	4.17	2
Al12.5	97.90	2.08	0.02	0.00	0.00	2.12	0
Al15	100	0	0	0	0	0	0
Al17.5	100	0	0	0	0	0	0
Al20	100	0	0	0	0	0	0

2.3.4 Structural Modeling

In the following section, we attempt to predict the fraction of tetrahedral to total boron (N_4) and the fraction of silicon atoms with one NBO (Q^3). In sodium borosilicates, the Dell and Bray model [Dell *et al.* 1983; DeGuire & Brown 1984; Yun & Bray 1978; Zhong & Bray 1989] is a frequently used empirical model to predict the composition dependence of N_4. To apply this model to the boroaluminosilicate glasses, we use $[Na_2O]$-$[Al_2O_3]$ as the "effective" modifier concentration, since Al_2O_3 is not considered in this model. The values of N_4 predicted using this model are all larger than the values obtained from the ^{11}B NMR data (Fig. 2.9). Du and Stebbins [Du & Stebbins 2005] have developed a modified Dell-Bray model for boroaluminosilicate glasses. This model groups Al and B as a single type of cation based on the consideration that the mixing behavior for Al^{IV} is similar to that of B^{IV} and the variation of N_4 is related to avoidance among B^{IV} and Al^{IV} species. The N_4 values predicted by this model also exhibit a certain degree of discrepancy with the experimental NMR data (Fig. 2.9). However, according to Du and Stebbins [Du & Stebbins 2005], the model is not expected to precisely predict N_4 in our glass system with the composition range of Al>>B. Despite of the discrepancy, the Du-Stebbins model gives a good prediction of the N_4 variation with composition.

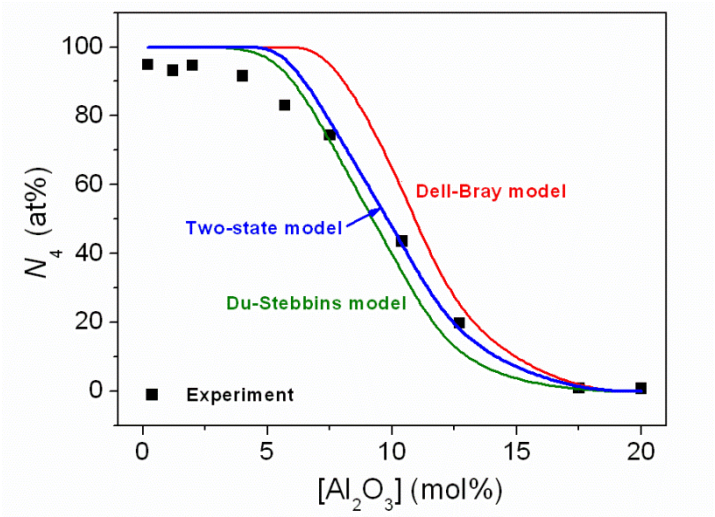

Figure 2.9 Comparison of the N_4 data obtained from NMR and the three different models. The errors of the experimental N_4 values are smaller than the size of the symbols. Reproduced from Paper I.

As noted above, there is a competition between converting B^{III} to B^{IV} and creating NBO. This has not been considered in any of the previous models for boron speciation. To quantify this effect, we consider the two-state statistical mechanical model of boron speciation recently introduced by Smedskjaer *et al.* [Smedskjaer *et al.* 2011a]. In this model, the addition of network modifiers leads to a thermodynamic competition between the formation of NBO and the conversion of boron from trigonal to tetrahedral configuration.

According to the two-state model, the free energy associated with NBO formation on Si^{IV} takes an intermediate value compared to those of the B^{III} to B^{IV} conversion and NBO-on-B^{III} formation [Smedskjaer *et al.* 2011a; Araujo 1980; Araujo 1983; Araujo 1986]. This value appears to be close to the energy associated with B^{III} to B^{IV} conversion. ΔH is defined as the enthalpy difference between NBO formation and B^{III} to B^{IV} conversion. When $[Na_2O]<[Al_2O_3]$, we state that $N_4=0$, which is close to the values determined from ^{11}B MAS NMR. When $[Na_2O]>[Al_2O_3]$, N_4 can be calculated as [Paper I]

$$N_4 = \frac{[Na_2O]-[Al_2O_3]}{[B_2O_3]+[SiO_2]\exp[-\Delta H / kT_f]}, \tag{2.1}$$

where k is Boltzmann's constant. The fictive temperature T_f is taken as equal to the glass transition temperature (cooled at 10 K/s), i.e., $T_f = T_g$ [Yue 2008]. The N_4 value is governed by the enthalpy difference between the two states (ΔH) and the number of available boron vs. silicon sites. If ΔH is large, the modifiers are more likely to be used for charge-balancing B^{IV}, so N_4 will be large. With higher fictive temperatures and high SiO_2 concentrations, N_4 attains a lower value due to the effect of entropy. The model predictions are in good agreement with the experimnetal NMR results (Fig. 2.9). However, this model has its limitation, i.e., the fictive temperature effect on N_4 applies only to silicate and boroaluminosilicate glasses, and N_4 is predicted to increase monotonically with Na_2O content. Despite several limitations of the two-state model, it gives the best prediction of boron speciation compared to the Dell-Bray model and the Du-Stebbins model.

Next, we attempt to also predict the Si speciation. To do so, we apply the random model which is used to describe the distribution of Q^n units in silicate glasses. The Q^n values are calculated as

$$Q^n = \frac{4!}{n!(4-n)!}(1-p)^n p^{4-n}, \qquad (2.2)$$

where p is the probability that a randomly chosen Si-O bond includes a NBO. For our aluminoborosilicate glasses, p=NBO/(4[Si^{IV}]+3[B^{III}]). Figure 2.10 shows that the values of Q^3 calculated by the random model agree well with the values obtained from fitting the wideline ^{29}Si NMR spectra, viz., Q^3 decreases as [Al_2O_3] increases.

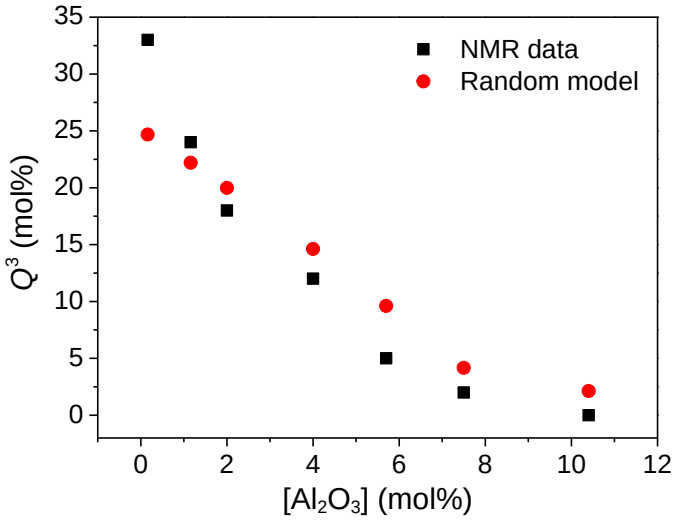

Figure 2.10 Comparison of Q^3 data calculated by the random model and measured by NMR of the boroaluminosilicate glasses as described and labeled in Table 1. The error range of the NMR data is ±5%. Reproduced from Paper I.

2.3.5 Structural Role of Sodium

The NMR spectra of the network-formers presented in the previous sections give information about the structural role of sodium in these glasses. To further investigate the role of sodium, we consider the ^{23}Na MAS NMR spectra. As shown in Fig. 2.11, the spectra exhibit a single, asymmetric resonance for all of the ten glasses. As [Al_2O_3] increases, the resonance becomes narrower and less asymmetric. At low [Al_2O_3], the broad ^{23}Na MAS lineshapes suggests multiple or at least a large distribution of sodium environments. They are likely from Na^+ as a charge-balancing cation for B^{IV}, NBO on boron and/or silicon, as well as a small fraction of Al^{IV}. At higher [Al_2O_3], the narrow ^{23}Na MAS lineshapes suggests a more uniform environment (and role) of Na^+ ions, i.e., they are mostly used to charge-balance Al^{IV} at the higher [Al_2O_3]. As described in Paper I, the ^{23}Na 3QMAS NMR spectra confirm these changes in the ^{23}Na resonance with increasing [Al_2O_3]. Hence, the ^{23}Na NMR data are consistent with the NMR data for the network formers and thus confirm our previous structural analysis.

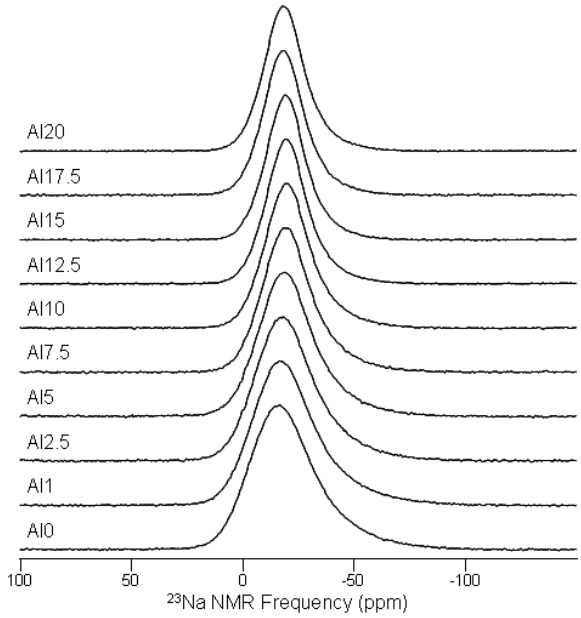

Figure 2.11 ^{23}Na MAS NMR spectra of the boroaluminosilicate glasses. The spectra are labeled using the naming convention in Table 2.3. Reproduced from Paper I.

2.4 Summary

We have investigated the structure of three different glass systems: soda lime borate, soda lime aluminosilicate, and sodium boroaluminosilicate glasses. For the series of the soda-lime borate glass, using Gupta's random pair model for network formation, Smedskjaer *et al.* have calculated N_4 and it shows good agreement with the ^{11}B MAS NMR data. For the series of soda-lime aluminosilicate glasses, we investigate the influence of the Al_2O_3 content on the structure. Al^V starts to form for $[Al_2O_3] \geq [Na_2O]$, and the fraction of Al^V increases with increasing Al_2O_3 content. The network connectivity increases as the increase of $[Al_2O_3]$. For the ten Na_2O-B_2O_3-Al_2O_3-SiO_2 glasses, we confirm that when $[Na_2O] < [Al_2O_3]$, almost all sodium is used to charge compensate Al^{IV}. When $[Na_2O] > [Al_2O_3]$, sodium first charge compensates Al^{IV}, after charge compensating Al^{IV}, not all of the excess Na^+ ions are used for converting B^{III} to B^{IV}, since some are used to create NBOs on both Si and B. We found the N_4 predicted by the two-state model shows best agreement with the measured values compared to Dell-Bray and Du-Stebbins models.

3. Dynamics of Oxide Liquids

Accurate knowledge of the temperature and composition dependence of shear viscosity is of critical importance for all stages of industrial glass production. Furthermore, it is crucial for the fundamental understanding of glass transition and relaxation phenomena. However, after many decades of research, our understanding of the mechanisms of viscous flow remains substantially incomplete [Debenedetti & Stillinger 2001; Mauro *et al.* 2009b]. Ideally, a comprehensive theory should explain all thermodynamic and kinetic properties of glass-forming systems, both at the microscopic and macroscopic levels.

In this section, we discuss the dynamic properties from both kinetic and thermodynamic points of view. Particularly, we address the important question about whether there exist universal dynamics of silicate liquids at the high-temperature limit. In other words, we investigate whether the high-temperature viscosity limit is composition dependent or not. We analyze this by using a large amount of viscosity data from Corning Incorporated to obtain a statistically significant result.

One of the remaining puzzles of the glass transition is the origin of a glass-forming liquid's "fragility," which quantifies the departure of its relaxation time from Arrhenius activated kinetics. Many studies have attempted to find the link between the kinetic fragility index *m* determined from viscosity measurements and various thermodynamic fragility indices [Stebbins & Xu 1997; Bian *et al.* 2007; Angell 2008; Du *et al.* 2000; Huang & McKenna 2001]. However, it remains an open question whether the connection exists. We investigate this question by studying the dynamic and thermodynamic behaviors of three different glassy systems: soda-lime borate (Na_2O-CaO-B_2O_3), soda-lime aluminosilicates (Na_2O-CaO-Al_2O_3-SiO_2), and sodium boroaluminosilicate (Na_2O-B_2O_3-Al_2O_3-SiO_2) glasses.

3.1 High-temperature Limit of Viscosity

Shear viscosity is a measure of the resistance of a liquid to shear deformation [Shelby 2005]. It is perhaps the single most important property of glass-forming liquids, since adequate control of flow behavior is essential for all steps of industrial glass production. The strain, annealing, softening, working, and melting points are crucial in the glass industry [Varshneya 2006]. For example, during glass formation, if a melt possesses high viscosity at its liquidus temperature (temperature at which the last crystals melt upon heating), crystallization is impeded since the high viscosity creates a large kinetic barrier toward atomic rearrangements. Therefore, such melts can normally easily be turned into glasses instead of crystals due to the slow dynamics. Moreover, the temperature dependence of viscosity also determines the maximum use temperature, at which a glass product can be processed or applied before its shape or properties change.

The shape of the viscosity vs. temperature curve varies greatly among different glass-forming liquids. If the shear viscosity at infinitively high temperature (η_∞) takes a composition independent value, it would simplify the process for modeling the composition dependence of liquid viscosity and it is an indication of the universal dynamics of silicate liquids at the high-temperature limit.

3.1.1 Viscosity Measurements

The viscosity of a glass-forming liquid decreases as the temperature increases. This is illustrated in Fig. 3.1 for a soda-lime borate composition. The viscosity data for glass-forming liquids are typically measured in two regimes: at temperatures slightly above the glass transition temperature and at temperature above the liquidus temperature. Below the glass transition temperature, the equilibrium viscosities cannot be obtained due to the slow dynamics of the system. The viscosity values in between the glass transition and liquidus temperatures can normally also not be measured due to the crystallization problem.

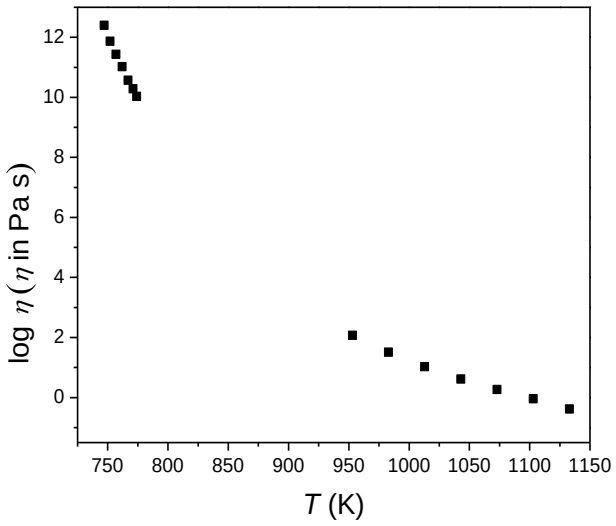

Figure 3.1 The logarithmic shear viscosity (log η) as a function of temperature for the glass-forming liquid with the composition (in mol%): $25Na_2O$-$10CaO$-$64B_2O_3$-$1Fe_2O_3$.

In Fig. 3.1, the low viscosities (approximately 10^0–10^3 Pa s) are measured using a concentric cylinder viscometer. In the high viscosity range (approximately 10^{10}–10^{13} Pa s), the viscosities are measured using micro-penetration viscometer with a vertical dilatometer. There is no one instrument or method can be used over the entire viscosity range. For the high viscosity range, there are several other methods that can be used, such as fiber elongation (~10^5-10^{13} Pa s), parallel plate (~10^5-10^9 Pa s), and beam bending (~10^7-10^{13} Pa s) viscometers.

3.1.2 Models of Liquid Viscosity

It follows from the above that there is a range of temperatures, for which it is difficult (or even impossible) to obtain viscosity values. Therefore, it is important to have an accurate model to describe the temperature dependence of viscosity. Furthermore, it is desirable if the model has as few fitting parameters as possible and that the parameters have a physical meaning. Among the three-parameter viscosity models, the Vogel-Fulcher-Tammann (VFT) equation [Scherer 1984] is the most frequently applied model:

$$\log_{10}\eta(T) = \log_{10}\eta_\infty + \frac{A}{T - T_0}\ . \tag{3.1}$$

where T is temperature, x is composition, and η_∞, A, and T_0 are the three fitting parameters. VFT works well for a variety of liquids, mostly oxide liquids with low fragility, but performs worse for the higher fragility liquids [Angell *et al.* 2000]. However, the main drawback of VFT

is that it appears to break down at low temperatures due to dynamic divergence at $T = T_0$ and consequently assumes vanishing configurational entropy at a finite temperature [Stickel *et al.* 1995]. Therefore, VFT often overpredicts viscosity values at low temperatures [Mauro *et al.* 2009b].

Avramov-Milchev (AM) equation of viscosity is an alternative three-parameter model. It describes the kinetics of the molecular motion in supercooled liquids using an atomic hopping approach [Avramov & Milchev 1988]. The AM equation is given by

$$\log_{10}\eta(T) = \log_{10}\eta_\infty + \left(\frac{\tau}{T}\right)^\alpha . \tag{3.2}$$

where η_∞, τ, and α are the AM fitting parameters. The AM equation predicts divergent configurational entropy in the limit of high temperature, which is physically unrealistic [Avramov 2005; Mauro *et al.* 2009b].

Recently, Mauro *et al.* presented a new three-parameter model named the Mauro–Yue–Ellison–Gupta–Allan (MYEGA) equation [Mauro *et al.* 2009b]. The MYEGA equation is derived from the Adam-Gibbs equation [Adam & Gibbs, 1965], which relates viscosity to the configurational entropy of the liquid, $S_c(T,x)$. The Adam-Gibbs equation has proved to be successful in describing the viscous flow behavior of a wide variety of systems [Scherer 1984] :

$$\log_{10}\eta(T) = \log_{10}\eta_\infty + \frac{B}{TS_c(T)} . \tag{3.3}$$

The configurational entropy is a complex quantity for glassy systems, but it can be modeled by using constraint theory (constraint theory will be explained in details in Chapter 4). In detail, the configurational entropy can be related to the topological degrees of freedom per atom ($f(T,x)$) [Phillips 1979; Phillips & Thorpe 1985], by employing the energy landscape analysis of Naumis [Naumis 2006] and the temperature-dependent constraint model of Gupta and Mauro [Gupta & Mauro 2009]. As described in detail in Ref. [Mauro *et al.* 2009b], a simple two-state system is applied to obtain the model for $f(T,x)$. In the model, the network constraints are either intact or broken, with an energy difference given by $H(x)$. Based on energy landscape analysis and the temperature-dependent constraint model for configurational entropy [Adam & Gibbs 1965; Gupta & Mauro 2009; Phillips & Thorpe 1985], the following three-parameter model is obtained [Mauro *et al.* 2009b]:

$$\log_{10}\eta(T) = \log_{10}\eta_\infty + \frac{K}{T}\exp\left(\frac{C}{T}\right). \tag{3.4}$$

where η_∞, K, and C are the fitting parameters. This model provides a physically realistic and accurate description of liquid dynamics [Mauro *et al.* 2009b]. This equation can be transformed into the following expression:

$$\log_{10}\eta(T) = \log_{10}\eta_\infty + \left(\log_{10}\eta_{Tg} - \log_{10}\eta_\infty\right)\frac{T_g}{T}\exp\left[\left(\frac{m}{\log_{10}\eta_{Tg} - \log_{10}\eta_\infty} - 1\right)\left(\frac{T_g}{T} - 1\right)\right] \tag{3.5}$$

where η_{Tg} is the viscosity at T_g. Among the three viscosity models, MYEGA is the only approach that performs a realistic extrapolation of configurational entropy in both the high and low temperature limits. With more accurate description of the low temperature scaling of viscosity and the absence of divergence at a finite temperature, MYEGA shows strong evidence against the existence of dynamic divergence in glass-forming liquids [Mauro *et al.* 2009b], which has also been demonstrated in the recent work of Hecksher *et al.* [Hecksher *et al.* 2008].

3.1.3 High-Temperature Viscosity Limit

The above-mentioned viscosity models all have a common parameter: the high-temperature limit of viscosity (η_∞). It is impossible to directly measure the high temperature limit of viscosity. Therefore, the value is a fitting parameter in the viscosity models and it is obtained by extrapolating the low temperature viscosity data to infinitely high temperature. The fitting of viscosity data would be significantly improved if the value of η_∞ is universal and composition independent, i.e., the fitting could be done with two instead of three fitting parameters. In previous studies, researchers have tried to fit viscosity data with different viscosity models to get η_∞ [Barrer 1943; Russell *et al.* 2003; Giordano *et al.* 2008]. However, these previously obtained values were obtained using a rather limited range of compositions. Hence, it was impossible to conclude whether η_∞ a universal constant is or not. Moreover, the viscosity models used in these previous studies (e.g., VFT and AM) all have the drawbacks that they do not give reasonable extrapolations at low and high temperatures, as discussed above.

As described in Paper II, we have investigated the universality of the high temperature limit of liquid viscosity by analyzing measured viscosity curves for 946 silicate liquids from Corning Incorporated, in addition to 6 borate [Smedskjaer *et al.* 2010a], 11 metallic [Zhang *et al.* 2010], 4 molecular [Mauro *et al.* 2009b], and 9 ionic liquids [Okoturo & VanderNoot 2004], and also water [Guevara-Carrion *et al.* 2011]. The 946 Corning liquids cover a wide composition space, from simple calcium aluminosilicate ternaries through complex boroaluminosilicates with up to eleven unique oxide components [Ellison & Cornejo 2010].

We then fit the three viscosity models (VFT, AM, and MYEGA) to the measured viscosity data for 946 different silicate liquids and for each model we obtain the high temperature limit of viscosity. In [Mauro *et al.* 2009b], by comparing the three viscosity models regarding the fitting quality, the MYEGA model has been found to be the best among them. For the 946 silicate liquids, based on the root-mean-square (RMS) error of the viscosity fits, the MYEGA model shows the best fit to the experimental data for the whole range of compositions, as compared to VFT and AM [Paper II].

Figure 3.2 shows the $\log_{10} \eta_\infty$ values obtained by fitting the three viscosity models to the 946 Corning liquids. The straight lines represent the average $\log_{10} \eta_\infty$ values. The average $\log_{10} \eta_\infty$ value predicted by MYEGA is -2.93, while AM produces an unrealistically high value (-1.74) [Kobeko 1952], and VFT gives a comparably low value (-3.87). The average $\log_{10} \eta_\infty$ value predicted by MYEGA is in line with previous estimates [Kobeko 1952; Russell *et al.* 2003]. Due to the unphysical divergence of configurational entropy in the high temperature limit of AM and unphysical divergence of viscosity at low temperatures of VFT, both these models give unrealistic predictions of $\log_{10} \eta_\infty$. MYEGA also gives the lowest standard deviation of $\log_{10} \eta_\infty$ for all the compositions, as shown in Fig. 3.2. According to [Mauro *et al.* 2009b], it has been proved that MYEGA is the most physically realistic viscosity model in both the

high and low temperature limits [Mauro *et al.* 2009b], therefore it is expected to yield the most accurate value of η_∞. In [Mauro *et al.* 2009b], the MYEGA model has been found to give the narrowest distribution of $\log_{10} \eta_\infty$ values around -3. Here we use more statistical data to confirm this.

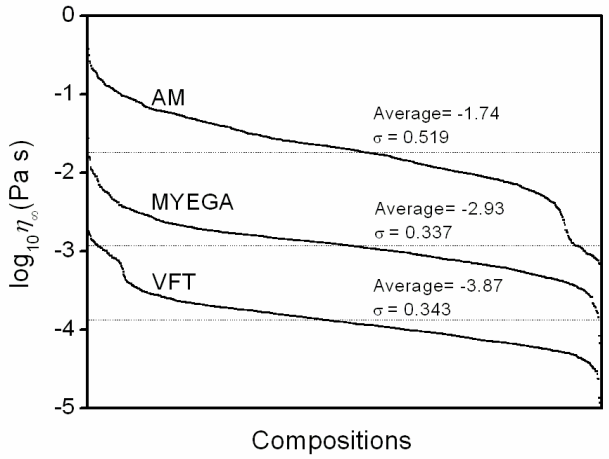

Figure 3.2 $\text{Log}_{10}\ \eta_\infty$ values obtained by fitting three viscosity models to 946 silicate liquids from Corning Incorporated. The straight lines represent the average $\log_{10}\ \eta_\infty$ values and σ is the standard deviation. Reproduced from Paper II.

Figure 3.2 shows that there is significant scatter in the $\log_{10}\ \eta_\infty$ values obtained by the three models. In order to investigate whether this scatter is due to experiment errors or actual dependence of $\log_{10}\ \eta_\infty$ on composition, we have plot the value of $\log_{10}\ \eta_\infty$ for different alkaline earth boroaluminosilicate compositions as a function of different composition variables. As shown in Fig. 3.3, there is no trend of $\log_{10}\ \eta_\infty$ with any of the composition variables, i.e., η_∞ exhibits a random variation around $10^{-2.93}$ Pa·s for the MYEGA model. This indicates that there is no composition dependence of $\log_{10}\ \eta_\infty$, i.e., the scatter around the average values is due to the experimental uncertainties and differences in the range of temperatures over which viscosity is measured.

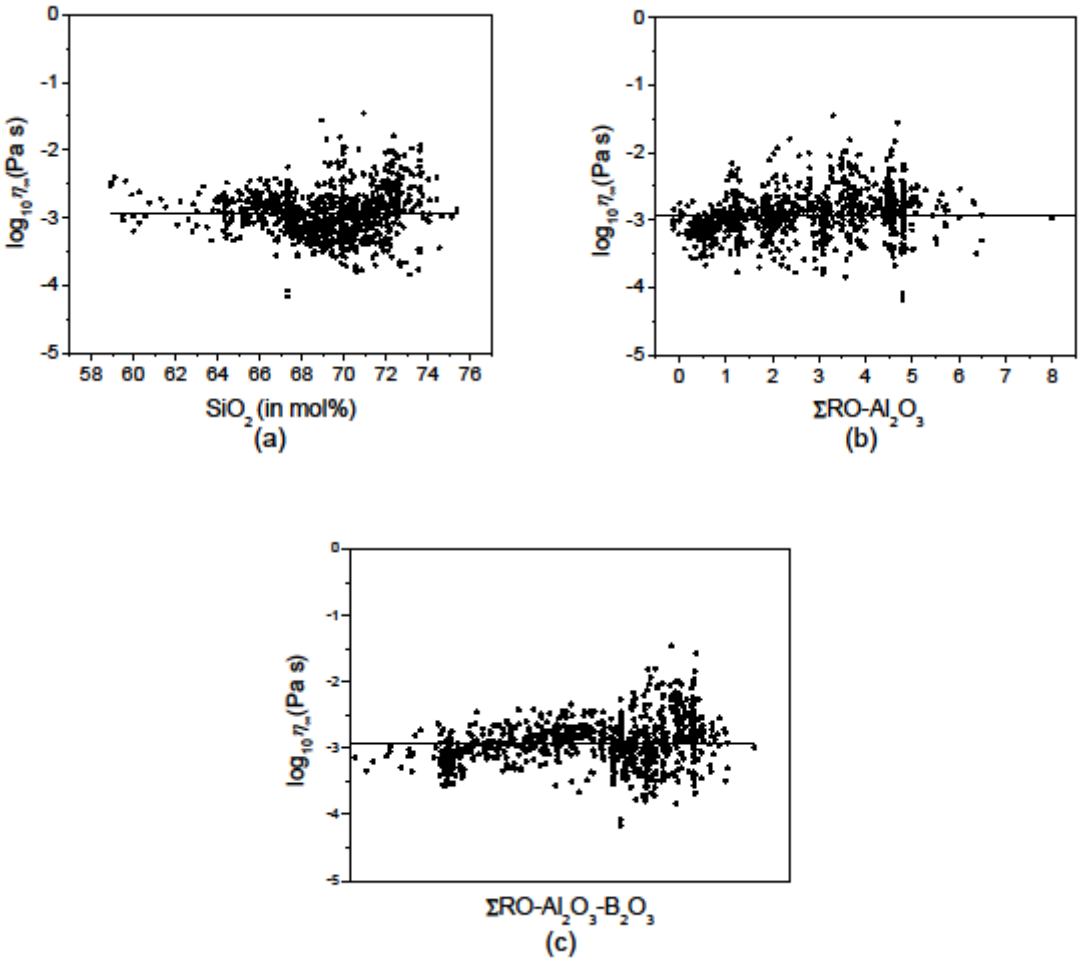

Figure 3.3 $Log_{10}\ \eta_\infty$ values obtained by fitting the MYEGA to the viscosity-temperature dataset of 946 Corning compositions, as a function (a) SiO_2, (b) $\sum RO - Al_2O_3$, and (c) $\sum RO - Al_2O_3–B_2O_3$ content. $\sum RO$ represents the total concentration of alkaline earth oxides. The oxide contents were measured by x-ray fluorescence. The straight lines represent the average values.

In addition to silicate liquids, we have also investigated a range of non-silicate liquids such as borate [Smedskjaer *et al.* 2010a], metallic [Zhang *et al.* 2010], molecular [Mauro *et al.* 2009b], and ionic liquids [Okoturo & VanderNoot 2004], and also water [Guevara-Carrion *et al.* 2011]. For these non-silicate liquids, we do not have as many data as for the silicate liquids and the statistically certainty of the result is therefore lower. However, the fitted values of η_∞ using the MYEGA model for these systems are indeed close to the average value of ~10^{-3} Pa·s (Fig. 3.4). Nevertheless, in future work, it is necessary to collect more systematic data for the non-silicate liquids in order to get test whether 10^{-3} Pa·s is truly a universal value of η_∞ for all glass-forming liquids.

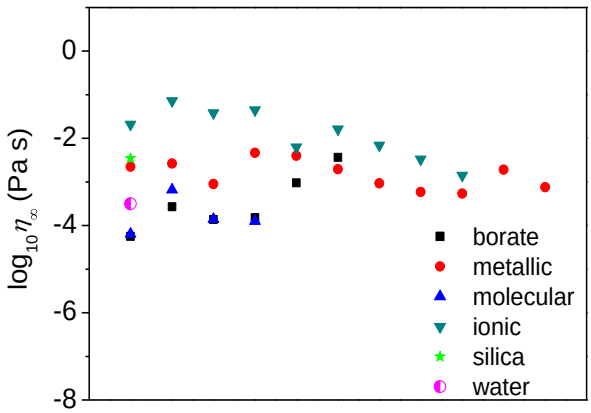

Figure 3.4 $\text{Log}_{10}\ \eta_\infty$ values obtained by fitting MYEGA to several borate [Smedskjaer *et al.* 2010a], metallic [Zhang *et al.* 2010], molecular [Mauro *et al.* 2009b], and ionic liquids [Okoturo & VanderNoot 2004], and water [Guevara-Carrion *et al.* 2011]. The abscissa represents an arbitrary composition space. Reproduced from Paper II.

The data reported here suggest that η_∞ is a universal, composition independent value. Then the question arises: why are dynamics of all liquids at infinitively high temperature universal? In order to answer this question, we first consider the Maxwell's relation, which has previously been used to predict the high-temperature viscosity limit [Russell *et al.* 2003; Giordano *et al.* 2008]. It is written as $\eta_\infty = G_\infty \tau_\infty$, where G_∞ is the shear modulus at infinite frequency and τ_∞ is the structural relaxation time at infinite temperature, which is equal to the liquid quasilattice vibration time ($\tau_\infty \approx 10^{-14}$ s) [Angell 1985]. G_∞ of oxide liquids is equal to ~29 GPa [Bornhöft & Brückner 1999] with only slight variation with composition and temperature above T_g. With these values of G_∞ and τ_∞, η_∞ is calculated to be around $10^{-3.5}$ Pa s. However, in our view, any explanation of a universal value of η_∞ based on vibrations is not correct. This is because at infinite temperature, the system is essentially not vibrating. Therefore, we need a more physically realistic explanation of the universality of η_∞.

In the following, we apply topological constraint theory to explain the physical meaning of the high-temperature viscosity limit. This theory will be explained in more details in Chapter 4, where it is also used to account for the composition dependence of macroscopic glass properties. According to the Phillips and Thorpe constraint theory [Phillips 1979; Thorpe 1983], the atomic structure of a glass or glass-forming liquid may be treated as a network of bond constraints. The network can be floppy (underconstrained), isostatic (optimally constrained), or stressed-rigid (overconstrained), depending on the average number of constraints per atom (n) compared to the network dimensionality (d). Each atom in the network has three translational degrees of freedom in the three-dimensional space. If the number of constraints is less than the degrees of freedom, the network is floppy. If the number of constraints is greater than the degrees of freedom, the network is considered to be stressed-rigid.

While the original Phillips-Thorpe theory is formulated for zero temperature conditions, Gupta and Mauro [Gupta & Mauro 2009] presented a topological modeling approach

incorporating a temperature dependence of constraints that become rigid as a liquid is cooled. At infinitely high temperature, all three degrees of freedom are floppy for each atom, so each atom has three continuous modes of deformation, independent of atom type. Therefore, all silicate liquids exhibit the same flow behavior in the limit of high temperature. In other words, a convergence of η_∞ values at $10^{-2.93}$ Pa·s for silicate liquids is physically meaningful in terms of constraint theory.

By defining the high temperature viscosity limit, the fitting parameters of the MYEGA model are reduced to only two, namely, the glass transition temperature and fragility index. This result simplifies the modeling process of the compositional dependence of viscosity.

3.2 Liquid Fragility

As mentioned above, understanding the temperature and composition dependence of the dynamics of glass-forming liquids is a longstanding problem in the condensed matter physics [Debenedetti & Stillinger 2001; Ediger *et al.* 1996; Angell *et al.* 2000; Mauro & Loucks 2007]. At the heart of this problem lies the glass transition, i.e., the process by which an equilibrium, ergodic liquid is gradually frozen into a nonequilibrium, nonergodic glassy state [Gupta & Mauro 2007; Mauro 2011b]. The most fascinating feature of a supercooled glass-forming liquid is arguably its dramatic rise in viscosity as it is cooled toward the glass transition (see Fig. 3.1). For most liquids, the temperature dependence of η is super-Arrhenius, which is captured by the viscosity models introduced in Section 3.1.2. Hence, η increases more dramatically upon cooling than expected from an Arrhenius law. In other words, the free energy activation energy barrier to viscous flow is not a constant, but rather dependent on temperature [Richert & Angell 1998; Dyre 2007; Ojovan *et al.* 2007].

Fragility is a common measure of the slowing down of liquid dynamics upon cooling through the glass transition. Liquids can be classified as either "strong" or "fragile" depending on whether they exhibit an Arrhenius or super-Arrhenius scaling of viscosity with temperature, respectively. The degree of non-Arrhenius scaling varies greatly among different glass-forming liquids and reflects the second derivative of the viscosity curve with respect to inverse temperature. In the well-known Angell plot [Angell 1988; Angell *et al.* 2000], the logarithm of viscosity, $\log_{10} \eta$, is plotted as a function of the T_g-scaled inverse temperature, T_g/T (Fig. 3.5). Here, T_g is the glass transition temperature, defined as the temperature at which the liquid viscosity equals 10^{12} Pa·s, and T is absolute temperature. The slope of the Angell curve at T_g defines the fragility index m,

$$m \equiv \left. \frac{\partial \log_{10} \eta}{\partial \left(T_g / T \right)} \right|_{T=T_g} . \tag{3.6}$$

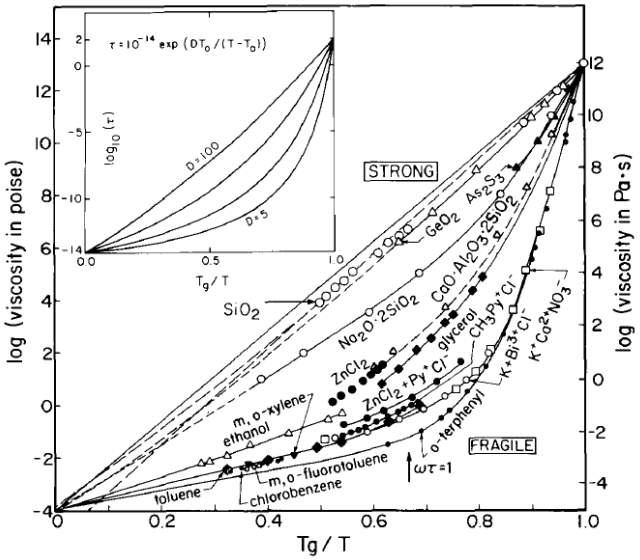

Figure 3.5 Angell fragility plot showing the logarithmic viscosity (log η) as a function of the T_g scaled inverse temperature (T_g/T) for various organic and inorganic glass-forming liquids. Reproduced from [Angell 1988].

Angell has proposed that the non-Arrhenius character is directly connected to fragility with the assumption of a universal high temperature limit of viscosity [Angell *et al.* 2000]. However, the assumption of η_∞ has not yet been validated by a systematic analysis of experimental data. With our work presented in Section 3.1.3, we have confirmed that silicate liquids have a universal value of η_∞ at around 10^{-3} Pa·s. Therefore, the non-Arrhenius scaling of liquid viscosity can be quantified through the fragility index *m* of the liquid.

The viscosity models introduced in Section 3.1.2 have different sets of adjustable fitting parameters. However, all of them can be rewritten in terms of the glass transition temperature, T_g, fragility index *m*, and high-temperature viscosity limit η_∞. Since the high-temperature viscosity limit is equal to approximately 10^{-3} Pa·s [Paper II] and the viscosity at T_g (η_{Tg}) is equal to 10^{12} Pa s for oxide glasses [Yue 2008], we have the relation log η_{Tg} – log η_∞=12-(-3)=15. Thus, Eq. (3.5) can be written as [Paper II],

$$\log_{10}\eta(T) = -3 + 15\frac{T_{g,vis}}{T}\exp\left[\left(\frac{m}{15}-1\right)\left(\frac{T_{g,vis}}{T}-1\right)\right]. \tag{3.7}$$

By defining the high temperature viscosity limit as a fixed value (i.e., log η_∞ =-3), the MYEGA model therefore only contains two fitting parameters (T_g and *m*). This result simplifies the modeling process of the compositional dependence of viscosity and indicates a common underlying physics of silicate liquids at the high temperature limit, as discussed above.

Based on Angell's [Angell *et al.* 2000] thought that strong liquids have stable structures with a high degree of short range order, strong liquids are expected to exhibit small property changes when going from the liquid state to the glassy state. On the other hand, fragile liquids are generally characterized by less well defined short range order, and they thus display dramatic changes in properties in the glass transition range [Huang & McKenna 2001; Shelby 2005]. Due to this structural difference in temperature dependence, fragile liquids are

expected to have large configurational heat capacities (i.e., large change in heat capacity during glass transition), resulting from dramatic temperature dependence of configurational entropy [Huang & McKenna 2001]. Hence, it is interesting to investigate the correlation between the fragility index *m* and thermodynamic property changes, such as heat capacity.

The fragility index determined from viscosity measurements is defined as the kinetic fragility. Some of the thermodynamic property changes during the glass transition can be determined from differential scanning calorimetry (DSC) measurements. Hence, DSC parameters associated with thermodynamic fragility can be calculated, such as the jump in isobaric heat capacity (ΔC_p) in the glass transition region [Angell 1995] and the glass transition width (ΔT_g) [Mauro & Loucks 2008].

There have been several attempts to connect the kinetic fragility index *m* determined from viscosity measurements with measures of thermodynamic fragility [Stebbins & Xu 1997; Bian *et al.* 2007; Angell 2008; Du *et al.* 2000; Huang & McKenna 2001]. Whether there is a parallel relation between the kinetic and the thermodynamic fragilities is still an unanswered question. In the following, we investigate the connection between kinetic and thermodynamic measures of liquid fragility for three glass-forming systems: soda-lime borate, soda-lime aluminosilicates, and sodium boroaluminosilicate compositions. We do so by comparing the experimental DSC and viscosity data with a previously proposed model for the correlation between *m* and ΔC_p.

3.2.1 Procedure for Analyzing DSC Data

In order to quantify the thermodynamic measures of liquid fragility, we have determined several DSC parameters: C_{pl} - C_{pg}, $C_{p.peak}$ - $C_{pg,}$ ΔT_g, and $(dC_p/dT)_{inflect}$. The procedure for determining these parameters is illustrated in Fig. 3.6. The jump in C_p during the glass transition is calculated as C_{pl} - C_{pg} = ΔC_p, where C_{pg} and C_{pl} are the isobaric heat capacities of the glass at T_g and the liquid, respectively. C_{pl} is determined as the offset value of the C_p overshoot above the glass transition range. Another characteristic value is the overshoot value of the glass transition peak, $C_{p.peak}$. The glass transition width ΔT_g is determined as $T_{g,offset} - T_g$, where $T_{g,offset}$ is the temperature at the offset of the C_p overshoot. We have also calculated the slope value of the sharp rising C_p curve at the inflection point, $(dC_p/dT)_{inflect}$.

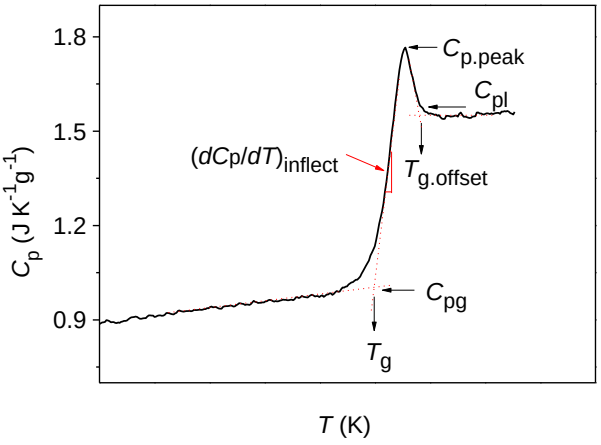

Figure 3.6 Illustration of the procedure for determining the characteristic temperatures (T_g and $T_{g,offset}$) and heat capacities (C_{pg}, C_{pl}, $C_{p.peak}$ and $(dC_p/dT)_{inflect}$) using DSC.

3.2.2 Configurational Heat Capacity Model

In the following, we present the model of configuration heat capacity ($C_{p,conf}$) introduced by Smedskjaer *et al.* [Smedskjaer *et al.* 2011a]. The model is derived based on a combined topological and thermodynamic approach that gives a correlation between ΔC_p and m, i.e., between thermodynamic and kinetic measures of fragility, respectively.

The model assumes that $C_{p,conf} \approx \Delta C_p$, since the glassy state contains primarily vibrational degrees of freedom, whereas the liquid state contains both vibrational and configurational degrees of freedom [Mauro *et al.* 2010; Potuzak *et al.* 2010]. However, this assumption may not be completely valid for all fragile systems [Martinez & Angell 2001]. First, $C_{p,conf}$ is written in terms of configurational enthalpy (H_{conf}) and entropy (S_{conf}) [Smedskjaer *et al.* 2011a]:

$$\Delta C_p = \left(\frac{\partial H_{conf}}{\partial T}\right)_p = \left(\frac{\partial H_{conf}}{\partial \ln S_{conf}}\right)_p \left(\frac{\partial \ln S_{conf}}{\partial T}\right)_p = \frac{1}{T}\left(\frac{\partial H_{conf}}{\partial \ln S_{conf}}\right)\left(\frac{\partial \ln S_{conf}}{\partial \ln T}\right)_p . \quad (3.8)$$

By combining the Adam-Gibbs model of liquid viscosity (Eq. 3.3) with the definition of fragility m (Eq. (5)), the following expression is obtained [Smedskjaer *et al.* 2011a]:

$$m = m_0\left(1 + \left.\frac{\partial \ln S_{conf}(T)}{\partial \ln T}\right|_{T=T_g}\right), \quad (3.9)$$

where $m_0 \approx 15$ is the fragility of a strong liquid. Insertion of Eq. 3.9 into Eq. 3.8 gives [Smedskjaer *et al.* 2011a]

$$\Delta C_p = \frac{S_{conf}}{T_g}\left(\frac{\partial H_{conf}}{\partial S_{conf}}\right)_{p,T=T_g}\left(\frac{m}{m_0} - 1\right). \quad (3.10)$$

S_{conf} at T_g is inversely proportional to T_g [Gupta & Mauro 2009]. $\partial H_{conf} / \partial S_{conf}$ is by definition equal to the configurational temperature (T_{conf}) at constant pressure [Araujo & Mauro 2010], which for a standard cooling rate is equal to T_g. Therefore, Eq. 3.10 can be rewritten as [Smedskjaer *et al.* 2011a]

$$\Delta C_p = \frac{A}{T_g}\left(\frac{m}{m_0} - 1\right), \quad (3.11)$$

where A is the proportionally constant connecting $S_{conf}(T_g)$ with T_g.

Using the measured values of ΔC_p, T_g, and m and A as the sole fitting parameter, Eq. 3.11 can be used to test the possible correlation between ΔC_p and m. As shown in Fig. 3.7a, the model works well for a series soda-lime borosilicate glasses, where the ratio of the network formers (SiO_2 and B_2O_3) change but the modifiers are constant [Smedskjaer *et al.* 2011a]. Here, we have also tested the model for a series of sodium silicate glasses containing different alkaline earth ions (Mg, Ca, Sr, and Ba) [Smedskjaer *et al.* 2009]. The model also works well for these glasses (Fig. 3.7b).

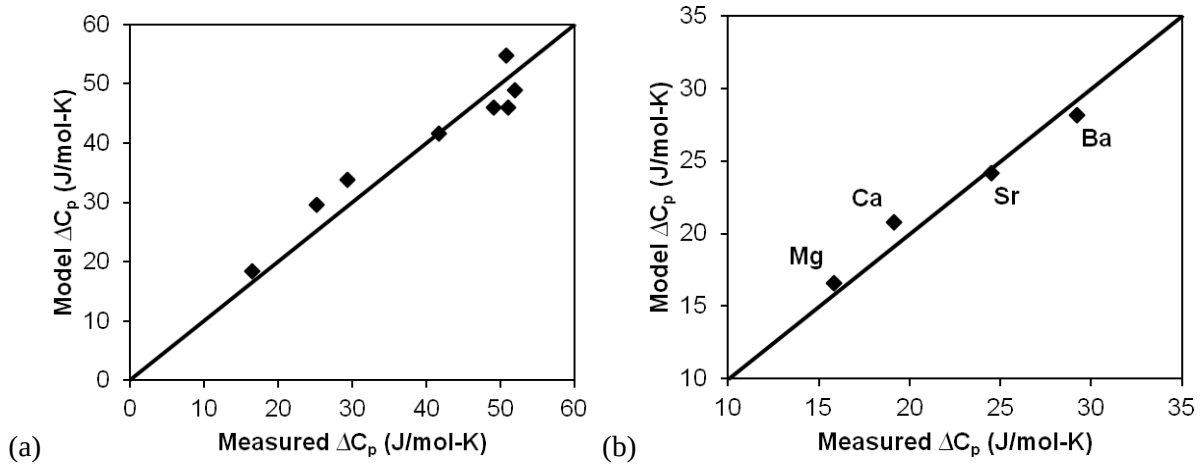

Figure 3.7 Measured versus predicted values of ΔC_p using Eq. 3.11 for (a) soda-lime borosilicate glasses [Smedskjaer *et al.* 2011a] and (b) sodium silicate glasses with different alkaline earth oxides [Smedskjaer *et al.* 2009].

3.2.3 Data for Oxide Systems

Soda-Lime Borate Liquids

The viscosity of the series of soda-lime borate liquids ($x$$Na_2O$-10CaO-(89-$x$)$B_2O_3-1Fe_2O_3$ with x = 5, 10, 15, 20, 25, 30 and 35) was measured by both micro-penetration and concentric cylinder viscometry. The viscosity data are fit to the MYEGA model, and the kinetic fragility index is derived from the best-fit of MYEGA [Paper IV]. m increases with increasing Na_2O content, but after reaching the maximum value at x = 25, m decreases with further addition of Na_2O. The structural origin of this composition dependence of m will be discussed in Chapter 4.

In order to quantify the thermodynamic measures of fragility, we have determined C_{pl}-C_{pg}, $C_{p.peak}$-C_{pg}, and ΔT_g. It has been found that C_{pl}-C_{pg} increases with the increase of m for many glass-forming systems, but not all systems follow this trend [Wang *et al.* 2006]. There is no apparent trend in C_{pl}-C_{pg} with composition for these soda-lime borate glasses (Fig. 3.8a), yet there is a trend in $C_{p.peak}$-C_{pg} and glass transition width with composition (Fig. 3.8b). The kinetic fragility shows a positive correlation with the values of $C_{p.peak}$-C_{pg} and the glass transition width since fragility is fundamentally a kinetic property, and the glass transition width is a reflection of kinetics (i.e., a steeper viscosity curves gives a more sudden breakdown of ergodicity [Huang & McKenna 2001; Mauro & Loucks 2008] at T_g). But C_{pl} - C_{pg} is a purely thermodynamic quantity, and the connection to kinetic fragility is apparently lost for these borate glasses.

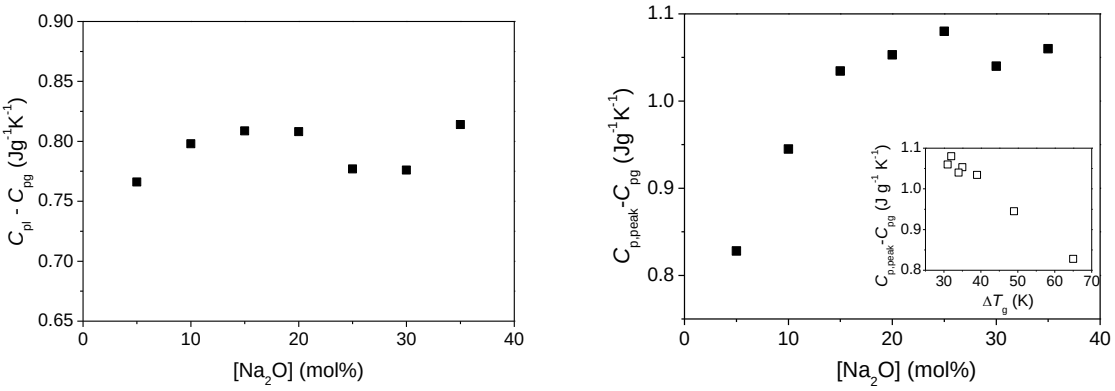

(a) (b)

Figure 3.8 (a) The step change in the heat capacity (C_{pl}-C_{pg}) and (b) $C_{p.peak}$-C_{pg} at the glass transition as a function of Na_2O content (x) for the seven glasses (xNa$_2$O-10CaO-(89-x)B$_2$O$_3$-1Fe$_2$O$_3$). Inset: $C_{p.peak}$-C_{pg} as a function of the glass transition width (ΔT_g) during heating. Reproduced from Paper IV.

We have applied the configurational heat capacity model (Eq. (10)) to these soda-lime borate glasses. The results are shown in Fig. 3.9. The model completely fails for this series of glasses, since the measured values of ΔC_p are fairly constant whereas the model predicts a change by a factor of nearly two. These borate liquids are relatively fragile (m around 50 to 75) and the assumption about $C_{p,conf} \approx \Delta C_p$ may thus not be valid for these systems.

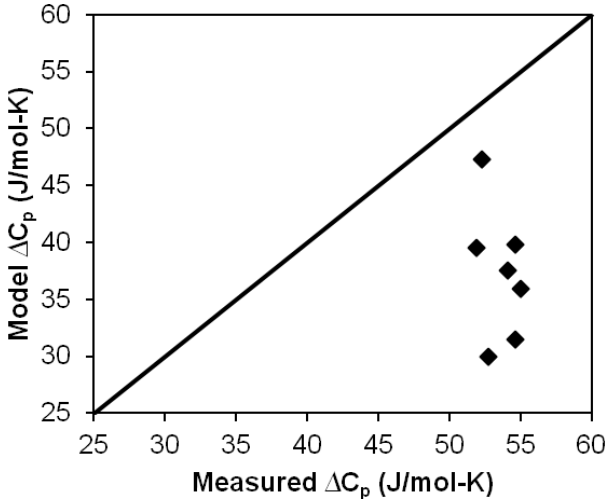

Figure 3.9 Measured versus predicted values of ΔC_p using Eq. 3.11 for soda-lime borate glasses with varying [Na_2O]/[B_2O_3] ratio [Paper IV].

Soda-Lime Aluminosilicate Liquids

We have explored the dynamic properties of the soda lime aluminosilicate glasses with compositions (in mol%) of (76-x)SiO_2−xAl_2O_3−16Na_2O−8CaO with x = 0, 2.7, 5.3, 8, 10.7, 13.3, 16, 18.7, 21.3, and 24. The glass transition temperature (T_g) and fragility index (m) of the glasses are determined by fitting measured viscosity data to the MYEGA model. The composition dependence of T_g and m is explained in terms of temperature-dependent constraint theory in Chapter 4.

In terms of the thermodynamic measures of fragility, Kjeldsen *et al*. have determined C_{pl}-C_{pg}, $C_{p.peak}$-C_{pg}, ΔT_g and $(dC_p/dT)_{inflect}$ [Kjeldsen *et al*. 2012]. As seen in Fig. 3.10a, C_{pl}-C_{pg} does not show obvious trend with composition, however, $C_{p.peak}$-C_{pg} displays approximately parallel relation with fragility (Fig. 4.6). The trends exhibit here is consistent with the discussion in the soda lime borate glasses. ΔT_g and $(dC_p/dT)_{inflect}$ are inversely correlated for the soda lime aluminosilicate glasses (Fig. 3.10b), i.e., the larger the value of ΔT_g, the smaller the value of $(dC_p/dT)_{inflect}$. These values are also expected to be correlated with the kinetic fragility index *m*. Although the relation is not so apparent for this glass system, the general trends can still be observed. We compare the C_{pl}-C_{pg} data obtained by DSC and predicted by the configurational heat capacity model. As shown in Fig.11, only the heat capacity change of some compositions follows this model.

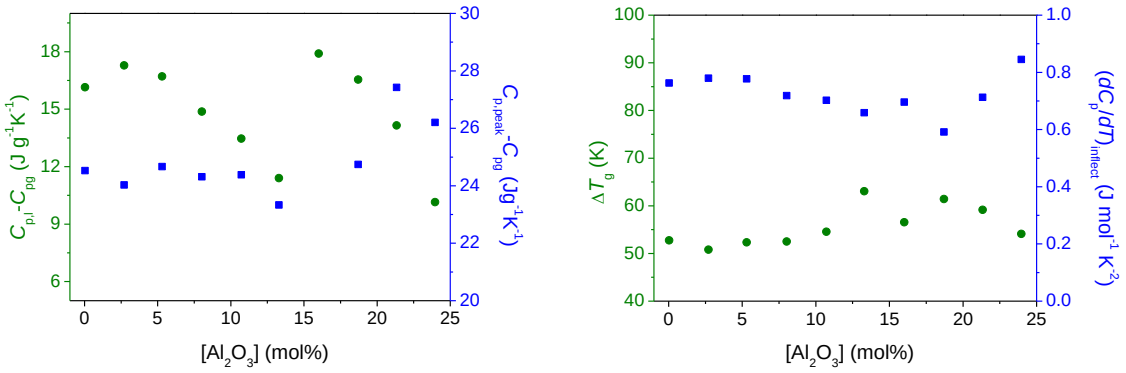

(a) (b)

Figure 3.10 (a) The step change in the heat capacity (C_{pl}-C_{pg}) vs. $C_{p.peak}$-C_{pg} at the glass transition (b) glass transition width (ΔT_g) vs. the slope of the rising heat capacity curve at the inflection point during glass transition ($(dC_p/dT)_{inflect}$) from DSC measurements as a function of Al_2O_3 content for the soda lime aluminosilicate glasses.

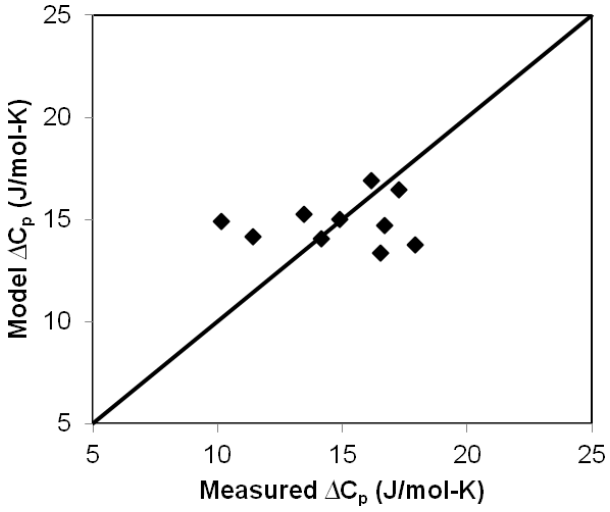

Figure 3.11 Measured versus predicted values of ΔC_p using Eq. 3.11 for soda lime aluminosilicate glasses.

Sodium Boroaluminosilicate Liquids

We have also investigated twenty sodium boroaluminosilicate systems of varying $[SiO_2]/[Al_2O_3]$ ratio with or without 1 mol% Fe_2O_3 [Paper III]. The glass transition temperature has been determined using both viscosity ($T_{g,vis}$) and DSC measurements ($T_{g,DSC}$). As shown in Paper III, there is an approximate one-to-one correspondence between $T_{g,vis}$ and $T_{g,DSC}$. Hence, the onset of the calorimetric glass transition corresponds approximately to the temperature at which the equilibrium liquid viscosity is 10^{12} Pa s. This is in agreement with the findings of Yue [Yue 2008; Yue 2009].

This glass system displays an approximately parallel relation between C_{pl}-C_{pg} and m [Paper III]. The configurational heat capacity model (Eq. 3.11) is thus to some extent able to capture the composition dependence of ΔC_p for these boroaluminosilicate glasses (Fig. 3.12).

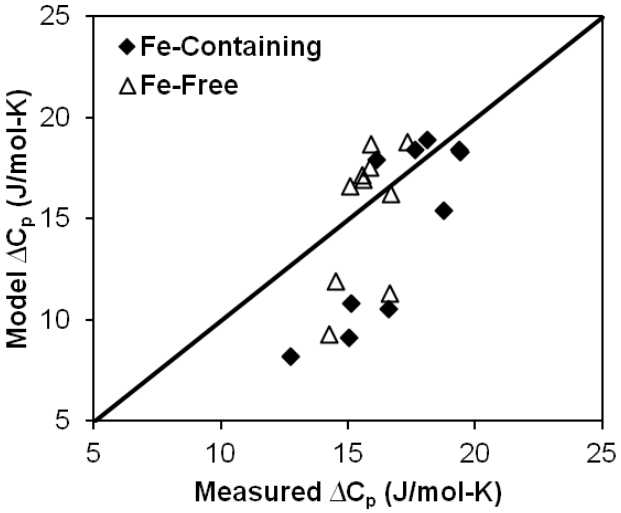

Figure 3.12 Measured versus predicted values of ΔC_p using Eq. 3.11 for sodium boroaluminosilicate glasses with or without iron and with varying $[SiO_2]/[Al_2O_3]$ ratio [Paper III].

ΔT_g and $(dC_p/dT)_{inflect}$ are also inversely correlated for the boroaluminosilicate glasses. Similar to the soda lime aluminosilicate glasse, our experimental findings here reveal that ΔT_g is inversely correlated with m and $(dC_p/dT)_{inflect}$ is positively correlated with m (Fig. 3.13). This is because a higher value of m leads to a sharper departure from supercooled liquid path during cooling and a more sudden and well-defined glass transition.

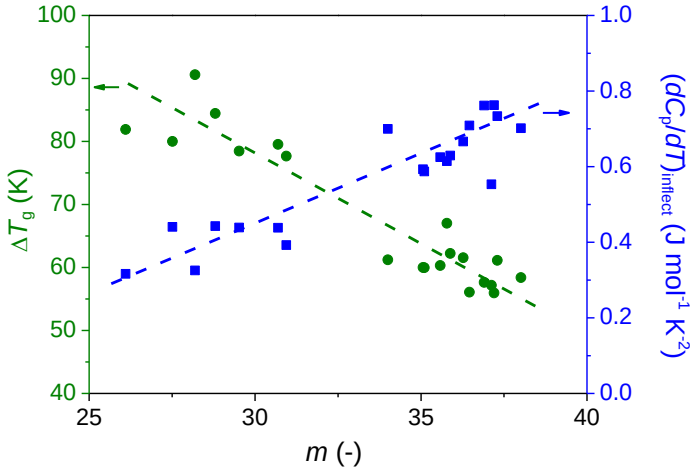

Figure 3.13 Glass transition width (ΔT_g) and slope of the rising heat capacity curve at the inflection point during glass transition ($(dC_p/dT)_{inflect}$) from DSC measurements as a function of *m* from viscosity measurements for both iron-containing and iron-free glasses. Reproduced from Paper III.

However, the results shown in Fig. 3.13 are only for a fairly limited range of composition and values of *m*. Hence, a detailed trend for the changes of both ΔT_g and $(dC_p/dT)_{inflect}$ with *m* still needs to be revealed by expanding the data sets and extending the fragility range. This has been done in Fig. 3.14, in which $(dC_p/dT)_{inflect}$ is plotted as a function of *m*. Here, we have included data for the soda-lime borate glasses [Paper IV], soda lime aluminosilicate glasses [Paper V], but also diopside [Yue 2012], calcium phosphate [Yue 2012], and silica [Yue 2012] glasses from literature. The positive correlation between $(dC_p/dT)_{inflect}$ and *m* is confirmed in this broader range of fragilities. $m = 15$ corresponds to the strongest possible system (Arrhenius viscosity curve). *m* of SiO_2 is around 17 and $(dC_p/dT)_{inflect}$ is correspondingly close to zero for this glass. It has been shown that the maximum fragility of any glass-forming liquid is around 175 [Wang & Mauro 2011]. This suggests that there should also exist an inherent upper limit to the value of $(dC_p/dT)_{inflect}$. More work is required to understand whether such upper limit exists and whether the trend of $(dC_p/dT)_{inflect}$ with *m* is linear or not. This could be investigated by including data for more fragile glass-formers (such as organic liquids).

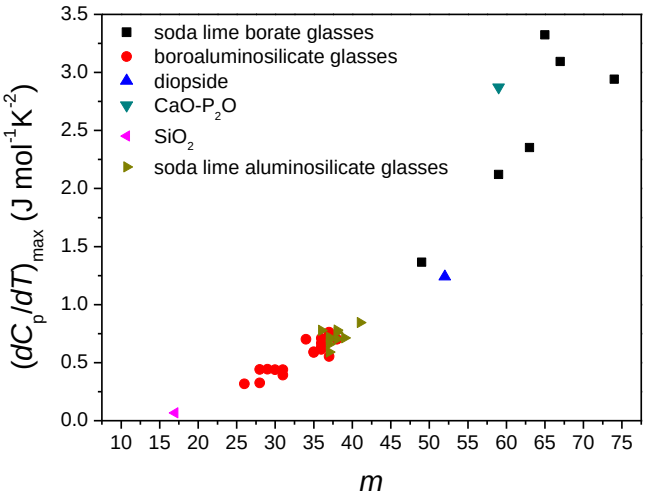

Figure 3.14 The slope of the rising heat capacity curve at the inflection point during glass transition ($(dC_p/dT)_{inflect}$) plotted as a function of m from viscosity measurements for a range of different glass-forming systems.

3.3 Summary

The temperature and composition dependence of viscous flow behavior is of critical importance for both fundamental understanding and industrial glass production. By analyzing 946 silicate liquids and 31 additional non-silicate liquids, we have found that there is a narrow spread of the high temperature limit of viscosity around 10^{-3} Pa·s for silicate liquids. There is no systematic dependence of the high temperature viscosity limit on chemical composition for the studied liquids. Having established this value, there are only two independent parameters governing the viscosity-temperature relation, namely, the glass transition temperature and fragility index. We have also shown that correlations between the dynamic and thermodynamic glass transition and fragility for different borate, aluminosilicate, and boroaluminosilicate systems. For the soda-lime borate glasses, the kinetic fragility shows a positive correlation with the values of $C_{p.peak}$-C_{pg} and the glass transition width, but there is no connection between the heat capacity jump and the kinetic fragility index. Similar to soda-lime borate glasses, the values of $C_{p.peak}$-C_{pg}, ΔT_g and $(dC_p/dT)_{inflect}$ are all positively related to the kinetic fragility, however, there is no apparent trend of C_{pl}-C_{pg} with kinetic fragility. For the sodium boroaluminosilicate system, an approximately parallel relation between C_{pl}-C_{pg} and m is displayed and a previously established model of configurational heat capacity is able to capture most of this trend. Moreover, ΔT_g is inversely correlated with m and $(dC_p/dT)_{inflect}$ is positively correlated with m. We have also demonstrated that this connection between kinetic fragility index and thermodynamic fragility exists for a wider range of compositions and fragilities.

4. Structure-Physical Property Correlations

Due to the complicated non-crystalline structure of glass and the non-equilibrium nature of the glassy state, the quantitative design of glasses with tailored properties is a longstanding problem in the glass community [Martin *et al.* 2002; Salmon 2002]. The strong relationships between glass structure and properties have been documented in numerous studies [Metwalli & Brown 2001; Zielniok *et al*. 2007; Saini *et al*. 2009]. However, accurate prediction of glass properties from first principles calculations is often impossible due to the long time scales involved with glass transition and relaxation phenomena. Therefore, despite many previous attempts in predicting glass properties based on structural information, it still remains a difficult task.

Here, we investigate the composition-structure-property correlations of the same model systems described in Chapter 2. The main focus will be on the industrially important boroaluminosilicate glasses. To better understand the composition dependence of their glass properties, we first consider the temperature-dependent constraint theory [Mauro 2011a]. This approach can be used to predict property trends and provide insight into the structural origins.

4.1 Temperature-Dependent Constraint Theory

In Chapter 3, topological constraint theory was introduced to explain the physical meaning of the high temperature viscosity limit. It is also a powerful tool to predict the temperature and composition dependence of glass properties such as shear viscosity and hardness. The Phillips-Thorpe constraint theory was originally considered for non-oxide covalent systems (i.e., chalcogenide glasses) [Phillips 1979; Phillips & Thorpe 1985]. According to their theory, the degrees of freedom of the glass network are removed by the presence of two-body (radial bond) and three-body (angular bond) constraints. As shown in Fig. 4.1, the two-body constraints correspond to the rigid bond lengths between pairs of atoms, and the three-body constraints correspond to rigid bond angles [Mauro 2011a; Smedskjaer *et al.* 2011a]. When the number of constraints exactly equals the number of degrees of freedom, the glass composition is considered to be optimum and the glass forming ability is maximized. In the floppy region, the atoms may easily arrange themselves into the crystalline state, whereas in the overconstrained regime, rigid structures easily percolate throughout the system, resulting in crystallization.

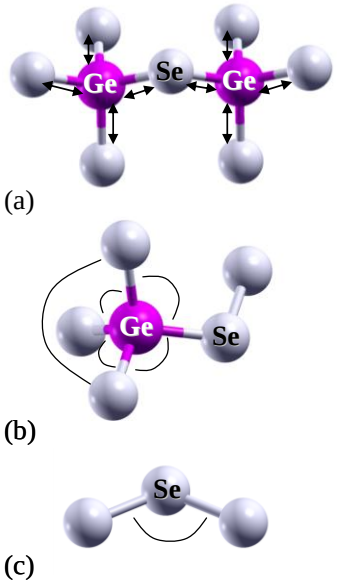

Figure 4.1 Basic structural building blocks in covalent Ge-Se glasses and their associated constraints. (a) Each pairwise bond constitutes a single two-body constraint. (b) There are five independent bond angle constraints (i.e., three-body constraints) for a rigid tetrahedron. (c) A two-coordinated atom such as selenium has one rigid bond angle. Reproduced from [Mauro 2011a].

Gupta and Mauro have extended the Phillips-Thorpe constraint theory by incorporating the effect of temperature. As illustrated in Fig. 4.2 [Mauro 2011a; Smedskjaer *et al.* 2011a], each type of bond α is assigned a constraint onset temperature, T_α, $q_\alpha(T)$ is the temperature dependence of the rigidity of the bond constraint α with the onset temperature T_α. In the limit of low temperature ($T < T_\alpha$), all constraints are rigid since there is insufficient thermal energy to break any type of bond, i.e. the constraint is rigid, i.e., $q_\alpha(T) \rightarrow 1$. In the high temperature limit ($T > T_\alpha$), all bonds can easily break due to the available thermal energy, i.e., all constraints are floppy, i.e., $q_\alpha(T) \rightarrow 0$ [Mauro 2011a]. According to Gupta and Mauro [Gupta & Mauro 2009], the temperature dependence of constraints can be written in either continuous or discrete forms. We use the discrete form for deriving analytical formulas for calculating glass transition temperature and hardness. Whereas the continuous form are useful for obtaining numerical solutions for liquid fragility [Mauro *et al*. 2009a]. The temperature-dependent constraint theory has proved to be useful for predicting the composition dependence of macroscopic properties such as glass transition temperature [Gupta & Mauro 2009; Mauro *et al*. 2009a] and fragility [Smedskjaer *et al*. 2010a]. In the following sections, we will refer to the temperature-dependent constraint theory in order to understand the origins of glass properties for several glass systems.

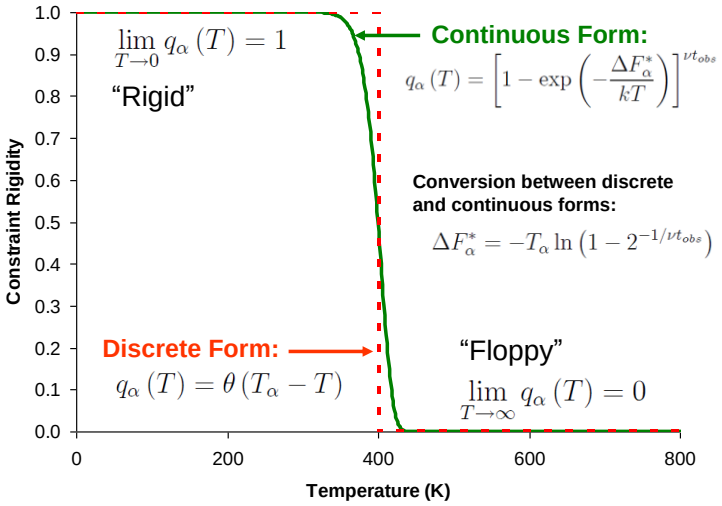

Figure 4.2 Temperature dependence of the rigidity ($q_\alpha(T)$) of the bond constraint α with the onset temperature T_α. $q_\alpha(T)$ can be written in either continuous or discrete forms [Gupta & Mauro 2009]. In the limits of low and high temperature the two forms converge, since all constraints are rigid and broken, respectively. Here, ΔF_α^* is the free energy to break constraint α, k is Boltzmann's constant, and νt_{obs} is the product of vibrational frequency and observation time. Reproduced from [Mauro 2011a].

4.2 Soda-Lime Borate Glasses

Smedskjaer *et al.* has applied the temperature-dependent constraint theory to predict the glass transition temperature (T_g) and fragility (m) of a series of soda-lime borate glasses. This is the same series described in Chapter 2 [Smedskjaer *et al.* 2010a]. Borate glasses are particularly challenging to investigate using molecular dynamics simulations. This is because it is difficult to account for the conversion of boron from three-fold to four-fold coordination as a function of composition and temperature using classical interatomic potentials [Kieu *et al.* 2011].

Application of temperature-dependent constraint theory involves identifying and counting the number of distinct network-forming species and the number of constrains associated with each species as a function of composition. Then, the constraints need to be ranked according to their relative bond strengths (i.e., constraint onset temperatures). Finally, different equations are applied to calculate various properties. The property calculations are done by connecting the change in the number of constraints per atom with a change in the specific property of interest. Gupta and Mauro derived expressions for calculating T_g and m based on Adam-Gibbs theory [Adam & Gibbs 1965] and the energy landscape analysis of Naumis [Naumis 2006]. $T_g(x)$ can be calculated as

$$\frac{T_g(x)}{T_g(x_R)} = \frac{f[T_g(x_R), x_R]}{f[T_g(x), x]} = \frac{d - n[T_g(x_R), x_R]}{d - n[T_g(x), x]}, \tag{4.1}$$

where x_R is some reference composition, $d = 3$ for a three-dimensional glass network, and $f(T,x)$ is the number of low-frequency floppy modes (atomic degrees of freedom) for composition x at temperature T. $n(T,,x)$ is the average number of constraints per atom. The

constraints per network node can be calculated by averaging over all network-forming species and each type of constraint. Following is the equation to calculate m:

$$m(x) = m_0 \left(1 + \left. \frac{\partial \ln f(T,x)}{\partial \ln T} \right|_{T=T_g(x)} \right), \tag{4.2}$$

where $m_0 \approx 17$ is the fragility of a strong liquid. The fragility index m is calculated from the temperature derivative of $f(T,x)$ [Gupta & Mauro 2009].

As shown in Fig. 4.3a, the calculated compositional trends of m using the temperature-dependent constraint model are in quantitative agreement with the experimental measurements [Smedskjaer *et al.* 2010a]. Hence, fragility first increases with increasing $[Na_2O]/[B_2O_3]$ ratio and then decreases for $[Na_2O] > 25$ mol%. The fraction of tetrahedral to total boron also achieves its maximum value at $[Na_2O] \approx 25$ mol%.

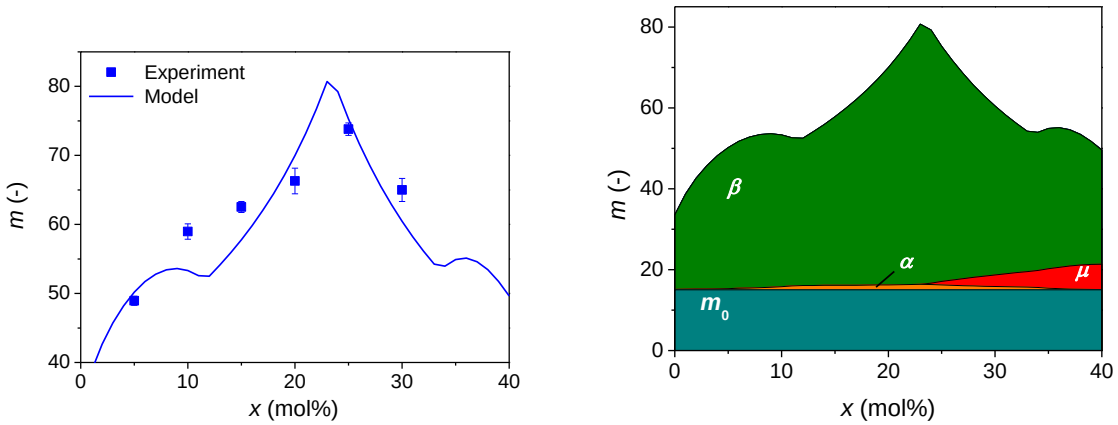

(a) (b)

Figure 4.3 (a) Dependence of fragility (m) on the Na_2O content (x) for the glasses ($x$$Na_2O$–10CaO–(89-x)$B_2O_3$–1$Fe_2O_3$). The solid line shows the predicted composition dependence of m using a topological model [Smedskjaer *et al.* 2010a]. (b) Contribution of each type of topological constraint to the calculated fragility. m_0 is defined as the fragility index of the theoretically strongest liquid, and found to be 15. Reproduced from Paper IV.

In order to further reveal the topological origins of the composition dependence fragility, we investigate the extent to which each type of constraint contributes to fragility. This is described in detail in Paper IV. Four types of network constraints are considered in the model: α) B-O and M^{NB}-O (M^{NB} is the network modifiers (Na and Ca) that create nonbridging oxygens) linear constraints; β) O-B-O angular constraints; γ) B-O-B angular constraints; and μ) additional modifier rigidity due to clustering effects. The contribution of each type of constraint to the calculated fragility is calculated and shown in Fig. 4.3b. Fragility is a first-derivative property and the constraint onset temperature of β constraints is close to T_g. The O–B–O angular constraints (β constraints) therefore provide the largest contribution to fragility. There are different numbers of β constraints on boron species, viz., five β constraints per four-fold coordinated boron and three β constraints per three-fold coordinated boron [Smedskjaer *et al.* 2010a]. Hence, the boron speciation substantially affects fragility.

The success of applying the temperature constraint theory on predicting glass transition temperature and fragility indicates that other thermal, mechanical, and dynamic properties may also be predicted. Indeed, Smedskjaer *et al.* have extended the temperature-dependent constraint approach to predict the composition dependence of glass hardness for the soda-lime borate glasses [Smedskjaer *et al*. 2010b]. It is shown that hardness is governed by the number of network constraints at room temperature and that a critical number of constraints is required for a material to display mechanical resistance. The predicted values of hardness by constraint theory are in excellent agreement with the experimental measurements as shown in Fig. 4.4 [Smedskjaer *et al.* 2010b]. Hence, constraint theory provides a quantitatively accurate solution to this previously unsolved problem in condensed matter physics [Mauro 2011a].

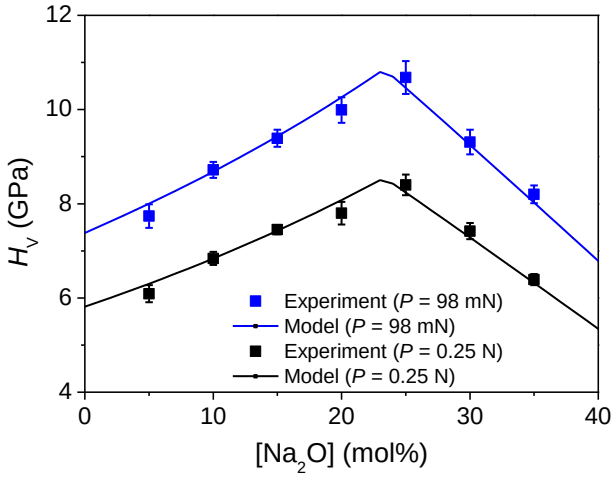

Figure 4.4 Measured Vickers hardness (H_V) at loads (P) of 98 mN and 0.25 N as functions of the concentration of Na_2O in the soda lime borate glasses. The solid lines represent the predicted hardness by temperature-dependent constraint approach [Smedskjaer *et al*. 2010b].

4.3 Soda-Lime Aluminosilicates Glasses

The dynamic properties of the soda lime aluminosilicate glasses are also studied. By fitting the viscosity data to the MYEGA model, the glass transition temperature (T_g) and fragility index (m) of the glasses are determined. The glass transition temperature obtained from equilibrium viscosity measurements systematically increases with increasing [Al_2O_3]/[SiO_2] ratio, which agrees well with the composition trend of T_g obtained from DSC measurements (Fig. 4.5). The number of non-bridging oxygen per tetrahedron (NBO/T) decreases as the sodium and calcium ions are used for charge-compensating tetrahedral aluminum instead of forming non-bridging oxygens (Fig. 2.3) which indicates that the network connectivity increases with the increase of [Al_2O_3]. T_g increases with increasing Al_2O_3 content due to an increase in the network connectivity.

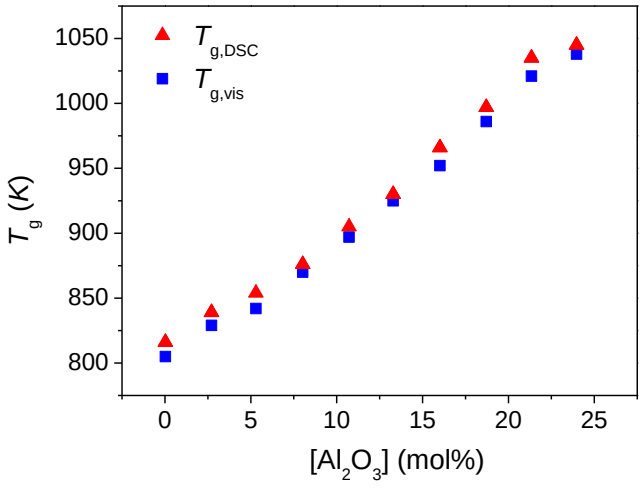

Figure 4.5 Composition dependence of the glass transition temperature obtained from DSC ($T_{g,DSC}$) and equilibrium viscosity ($T_{g,vis}$) measurements. Reproduced from Paper V.

The composition dependence of *m* is illustrated in Fig. 4.6. For low concentrations of Al_2O_3, *m* is approximately constant with increasing [Al_2O_3]. However, for [Al_2O_3] > 18.7 mol%, *m* starts to increase with increasing [Al_2O_3]. According to temperature-dependent constraint theory, *m* can be calculated from the temperature derivative of the number of atomic constraints [Gupta & Mauro 2009; Mauro *et al*. 2009a]. Based on equation 4.2, the increasing number of bond angle constraints will increase fragility [Smedskjaer *et al*. 2010a; Smedskjaer *et al*. 2011a]. Therefore, in the peraluminous regime, the increase of five-coordination Al (Al^V) leads to a greater number of bond angular constraints, which causes the increase of fragility.

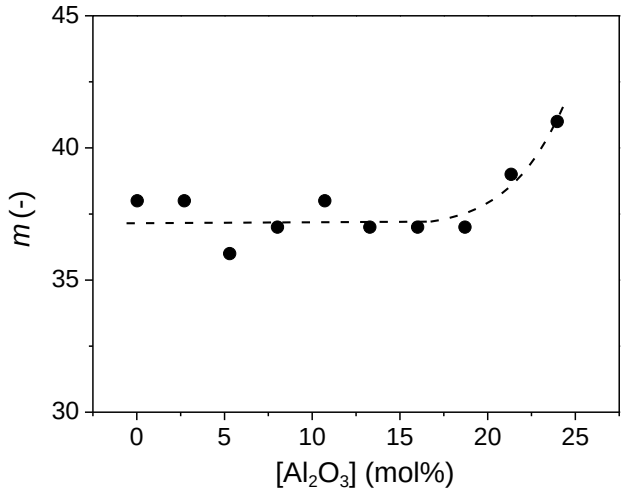

Figure 4.6 Composition dependence of the liquid fragility index *m* obtained from fitting the MYEGA equation [Mauro *et al*. 2009b] to the viscosity data. The dashed line is the guide for eyes. Reproduced from Paper V.

4.4 Sodium Boroaluminosilicate Glasses

As described in Chapter 2, the structure of sodium boroaluminosilicate glasses is complex due to the mixing of the various network-formers and the different structural roles of sodium. To understand structure-property correlations in these glasses, we again study the series of sodium boroaluminosilicate glasses with systematic variation of the $[Al_2O_3]/[SiO_2]$ ratio to access all of the different regimes of sodium behavior. We have also add 1 mol% of Fe_2O_3 to the glasses to study the effect of iron on glass properties, since iron is a common impurity in the raw materials. The glass compositions are listed in Table 4.1.

Table 4.1. Chemical composition, homogenization temperature (T_h), iron redox ratio ($[Fe^{3+}]/[Fe]_{tot}$), and fraction of tetrahedral to total boron (N_4) of the investigated iron-free and iron-containing glasses. Iron redox ratio was determined by ^{57}Fe Mössbauer spectroscopy with uncertainty of ±5% [Smedskjaer *et al*. 2011b]. N_4 was determined by ^{11}B MAS NMR spectroscopy with uncertainties of ±0.2% [Paper III].

Glass	Composition (mol%)					T_h	$[Fe^{3+}]/[Fe]_{tot}$	N_4
ID	SiO_2	Al_2O_3	B_2O_3	Na_2O	Fe_2O_3	(°C)	(at%)	(at%)
Al0*	79.35	0.29	4.88	14.57	0.91	1450	n/a	n/a
Al1*	78.92	0.69	4.95	14.52	0.93	1450	n/a	n/a
Al2.5*	77.40	2.20	4.90	14.60	0.90	1450	95	n/a
Al5*	74.70	4.70	5.00	14.60	1.00	1500	93	n/a
Al7.5*	71.80	7.60	4.90	14.70	1.00	1550	91	n/a
Al10*	68.90	10.30	5.00	14.80	1.00	1600	87	n/a
Al12.5*	67.10	12.60	5.00	14.30	1.00	1650	83	n/a
Al15*	64.10	15.60	5.00	14.30	1.00	1650	78	n/a
Al17.5*	62.31	17.94	5.07	13.75	0.94	1650	n/a	n/a
Al20*	61.13	19.38	4.98	13.63	0.88	1650	n/a	n/a
Al0	80.08	0.16	4.84	14.77	0.15	1450	n/a	94.9
Al1	79.38	1.16	4.85	14.60	0.14	1450	n/a	93.2
Al2.5	78.80	2.00	4.70	14.40	0.08	1450	n/a	94.6
Al5	78.10	4.00	4.20	13.60	0.07	1500	n/a	91.6
Al7.5	76.90	5.70	4.30	13.00	0.06	1550	n/a	83.1
Al10	75.90	7.50	4.30	12.30	0.07	1600	n/a	74.4
Al12.5	72.00	10.40	4.40	13.10	0.07	1650	n/a	43.6
Al15	69.20	12.70	4.60	13.50	0.07	1650	n/a	19.9
Al17.5	62.97	17.18	4.99	14.73	0.13	1650	n/a	1.0
Al20	60.52	19.61	5.00	14.73	0.14	1650	n/a	0.8

In Paper III, we have investigated and analyzed the composition dependence of the dynamic and selected physical properties (density, elastic moduli, and hardness) of these glass compositions. The importance of viscosity has been addressed in Chapter 3. The mechanical properties are also of crucial importance in glass products, e.g., for touch screen displays requiring high hardness and scratch resistance [Varshneya 2010]. In the following sections, we summarize the results from Paper III.

4.4.1 Dynamic Properties

We have determined T_g and m of the sodium boroaluminosilicate glasses by fitting measured viscosity data to the MYEGA equation. $T_{g,vis}$ is the glass transition temperature, defined as the temperature at which the equilibrium viscosity equals 10^{12} Pa·s, and T is the absolute temperature. We find that $T_{g,vis}$ increases with increasing value of $[Al_2O_3]$-$[Na_2O]$ for both

iron-free and iron-containing glasses (Fig. 4.5). There is a change in the slope of $T_{g,vis}$ vs. $[Al_2O_3]$-$[Na_2O]$ around $[Al_2O_3]$-$[Na_2O]$=0 and $T_{g,vis}$ increases faster in the peraluminous than in the peralkaline regime. Moreover, the glass transition temperature of the iron-containing glasses is generally lower than that of the iron-free glasses. We use the concept of topological constraints to explain the composition dependence of T_g. It is done by counting the number of constraints associated with the network forming species as a function of composition and temperature [Mauro 2011a; Bauchy & Micoulaut 2011], since T_g increases with the average number of network constraints per atom [Gupta& Mauro 2009; Mauro *et al.* 2009a]. In the peralkaline regime, the number of constraints increases with increasing $[Al_2O_3]$ due to the decrease concentration of NBOs, therefore T_g incrases. In the peraluminous regime, both boron speciation and the sodium environment are unchanged with composition. The increase of T_g is because we introduce five-fold coordinated aluminum species (i.e., Al^V) in the network, The higher coordination of aluminum contributes a greater number of constraints than four-fold coordinated silicon [Phillips 1979].

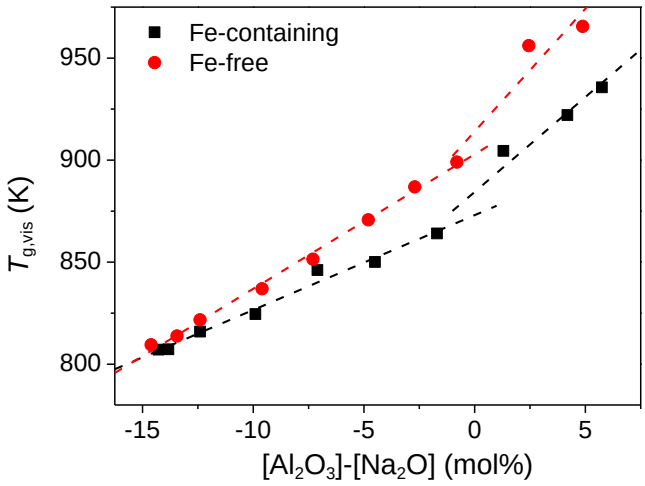

Figure 4.5 Composition dependence of the glass transition temperature ($T_{g,vis}$) obtained by fitting the measured viscosity data to MYEGA for both iron-free and iron-containing glasses. The dashed lines are linear fits to the data for $[Al_2O_3]$-$[Na_2O]$<0 and $[Al_2O_3]$-$[Na_2O]$>0, respectively. The uncertainty of $T_{g,vis}$ is approximately ±5 K. Reproduced from Paper III.

The liquid fragility index also exhibits a dramatic variation in the composition region around $[Al_2O_3]$-$[Na_2O]$=0 for both iron-free and iron-containing glasses (Fig. 4.6). The scaling of the liquid fragility index *m* with composition is also explained in terms of temperature-dependent constraint theory. As described in detail in 4.2, the O–B–O angular constraints (β constraints) provide the largest contribution to fragility. Since B^{IV} has more β constraints than B^{III}, the increase of N_4 will cause the increase of fragility. In the peralkaline regime, N_4 is relatively constant at low $[Al_2O_3]$ and then decreases nearly to 0% around $[Al_2O_3]$-$[Na_2O]$=0, in agreement with the composition variation of *m*. In the peraluminous regime, the boron speciation does not change, thus the increase of fragility could be attribute to the greater number of angular constraints with increasing concentration of Al^V.

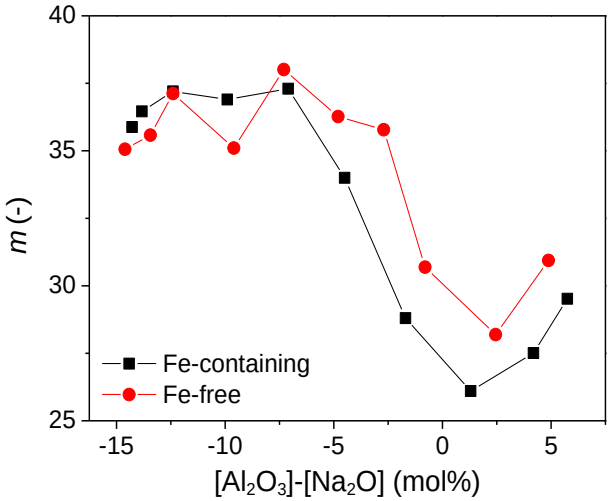

Figure 4.6 Composition dependence of the liquid fragility index (*m*) obtained by fitting the measured viscosity data to MYEGA for both iron-free and iron-containing glasses. The error range of *m* is approximately ±1. Reproduced from Paper III.

Both the glass transition temperature and the liquid fragility show sensitive change in the composition region around $[Al_2O_3]$-$[Na_2O]$=0. This is crucial for optimizing the industrial processes, since the glass workability and hence the processing parameters strongly depend on the liquid fragility and the glass transition temperature. The finding is thus instructive for designing glass compositions in the frame of boroaluminosilicate related products.

4.4.2 Elastic Moduli

Young's modulus (*E*) describes the resistance of a material to deformation along an axis when opposing forces are applied along that axis, while the shear modulus (*G*) describes the resistance to shear when acted upon by opposing forces. As shown in Fig. 4.7, the iron-containing and iron-free glasses show similar composition dependences for both *E* and *G*. In detail, we observe that there is a minimum of both Young's and shear moduli around $[Al_2O_3]$-$[Na_2O]$=0.

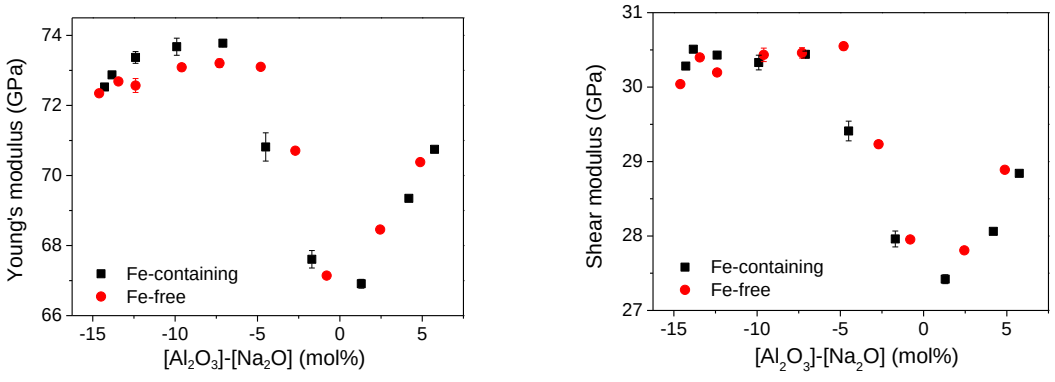

(a) (b)

Figure 4.7 Composition dependence of (a) Young's modulus *E* and (b) shear modulus *G* of both iron-containing and iron-free glasses. Reproduced from Paper III.

In the following, we discuss the composition dependence of E and G in three compositional regions. In the regime of -15<[Al_2O_3]-[Na_2O]<-5, the moduli increase slightly with increasing [Al_2O_3]. In this regime, the network connectivity increases since the concentration of NBOs decreases, and this increases the ability of the glasses to resist elastic deformation [DeGuire & Brown 1984]. In the regime of -5<[Al_2O_3]-[Na_2O]<0, there is a significant decrease in moduli with increasing [Al_2O_3]. The moduli are strongly lowered by an increase of the concentration of B^{III}, since B^{III} species make the structure less densely. Boron speciation plays an important role in governing the elastic response of the sodium boroaluminosilicate glasses. In the regime of [Al_2O_3]-[Na_2O]>0, the elastic moduli increase with increasing [Al_2O_3]. Although there is no change in boron speciation in this region, the concentration of Al^V increases which contributes more constraints than four-fold coordinated silicon atoms. Thus, the increased network connectivity may cause the incresase of the elastic moduli. This explains the existence of the minimum moduli around [Al_2O_3]-[Na_2O]=0.

4.4.3 Hardness

We have also investigated the composition dependence of Vickers hardness (H_V) using microindentation. H_V is defined as the resistance of the glass to permanent deformation under the pressure applied by the Vickers diamond pyramid indenter. As shown in Fig. 4.8, there also exists a minimum in H_V value around [Al_2O_3]-[Na_2O]=0. The composition dependence of hardness of the iron-containing and iron-free glasses is similar. However, the iron-free glasses are harder than the iron-containing glasses in the peraluminous regime.

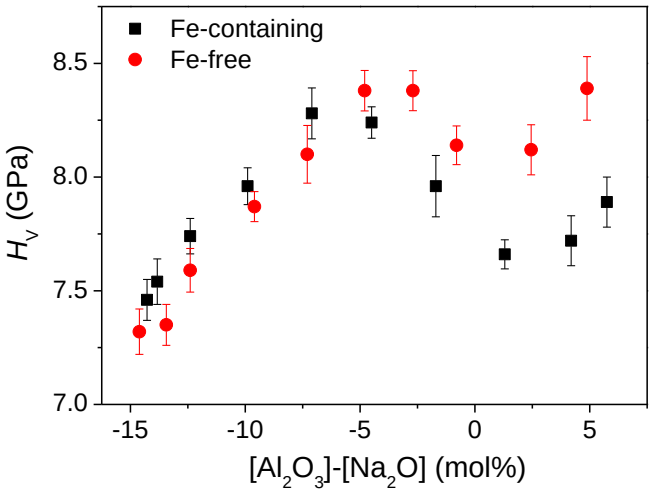

Figure 4.8 Composition dependence of Vickers microhardness (H_V) of both iron-containing and iron-free glasses. Reproduced from Paper III.

Again, we discuss the detailed responses of H_V to the compositional change in terms of three compositional regimes. In the regime of -15<[Al_2O_3]-[Na_2O]<-5, H_V increases with increasing [Al_2O_3] and reaches its maximum value around [Al_2O_3]-[Na_2O]=-5. Similar to elastic moduli, the number of constraints increases due to the decreased concentration of NBOs, which is the origin of the increase of hardness. In the regime of -5<[Al_2O_3]-[Na_2O]<0, H_V decreases with increasing [Al_2O_3]. Boron speciation also plays a dominant role for controlling hardness. H_V decreases as the concentration of B^{IV} decreases, since four-fold coordinated boron species contribute more constraints than three-fold coordinated boron [Phillips 1979]. In the regime of [Al_2O_3]-[Na_2O]>0, H_V increases again with increasing

$[Al_2O_3]$ right after reaching its minimum value around $[Al_2O_3]$-$[Na_2O]$=0. As shown in Fig. 2.6, boron speciation does not change in this region, indicating that the increase in hardness is related to the increase of the concentration of Al^V.

In summary, the plastic deformation we studied here all show sensitive variation in the composition region around $[Al_2O_3]$-$[Na_2O]$=0. The findings are important to optimize composition that possesses both high mechanical resistance and the economically favorable processing conditions.

4.4.3 Impact of Iron on Properties

As shown in Figs. 4.5 to 4.8, the properties of the iron-containing glasses are different from those of the iron-free glasses. In other words, the substitution of 1 mol% Fe_2O_3 for SiO_2 has an impact on the investigated glass properties. Iron normally exists as mixture of both Fe^{2+} and Fe^{3+} in oxide glasses. The $[Fe^{3+}]/[Fe^{2+}]$ ratio depends on the base glass composition, melting temperature and time, furnace atmosphere, and crucible material [Dyar 1985]. By using ^{57}Fe Mössbauer spectroscopy, we have found that the $[Fe^{3+}]/[Fe^{2+}]$ ratio decreases with increasing concentration of Al_2O_3 (Table 2.3).

Fe^{2+} and Fe^{3+} possess different structural roles in silicate glasses. It has been shown that Fe^{2+} can charge compensate Al^{IV}, similar to the role of Na^+ [Dickenson & Hess 1986; Rossano *et al*. 2008]. On the other hand, Fe^{3+} ions play a more network-forming role in the network, similar to that of Al^{3+} [Mysen & Richet, 2005]. The substitution of Fe_2O_3 for SiO_2 generally leads to a decrease in the glass transition temperature, elastic moduli, and Vickers hardness. The introduction of Fe_2O_3 increases the total modifier content in the glasses and thus decreases the overall network connectivity. The concentration of Fe^{2+} increases with the increase of $[Al_2O_3]$, i.e., there is a greater decrease of network connectivity at higher levels of Al_2O_3. Therefore, the difference between the properties of iron-containing and iron-free glasses increases with increasing $[Al_2O_3]$.

4.5 Summary

Temperature-dependent constraint theory is proved to be useful for predicting the composition dependence of macroscopic properties, e.g., glass transition temperature and fragility. The approach can also provide valuable insights into the underlying structural origins of glass properties for several glass systems. For the series of soda-lime borate liquids, we have calculated the contribution of each type of constraint to the calculated fragility, i.e., which reveals the topological origin of fragility. For the series of soda-lime aluminosilicate liquids, T_g increases with increasing Al_2O_3 content due to an increase in the network connectivity. In the peraluminous regime, the increase of Al^V leads to a greater number of bond angular constraints, which cause the increase of fragility. For the series of sodium boroaluminosilicate glasses, we have investigated several glass properties including dynamic properties, elastic moduli, and hardness. It is found that all the property display sensitive changes at around $[Al_2O_3]$-$[Na_2O]$=0 for both iron-free and iron-containing glasses. We explain the structure-property relationships of the glasses in terms of topological constraint theory. The existence of the minimum and the three compositional response regions are related to boron speciation. The results presented here are instructive for optimizing the industrial processes, since the glass workability and hence the processing parameters strongly depend on the liquid fragility. Finally, we have shown that the substitution of 1 mol% Fe_2O_3 for SiO_2 in the glasses results in lower values of glass transition temperature, hardness, and elastic moduli.

5. Glass-Forming Ability

There are many ways to prepare glass, e.g., chemical vapor deposition and sol–gel methods [Angell 1995; Varshneya 2006]. However, the predominant method is still the melt-quenching technique. In order to optimize the glass production process, it is important to know the glass-forming ability (GFA) of the melt. GFA is a measure of how easily a melt is vitrified and can be quantified by critical cooling rate q_c [Shelby 2005]. The critical cooling rate is the minimum cooling rate required to vitrify a melt, i.e., to obtain a glass with a crystallized volume fraction below a certain limit (such as 0.1%) [Uhlmann 1972]. The higher the critical cooling rate, the more difficult it is to obtain a glass, or the lower is the GFA of that composition.

However, it is difficult and time-consuming to determine the critical cooling rate precisely. It is tedious to continuously vary the cooling rate and it is hard to monitor any change in their vitrification behavior. Moreover, the quantitative characterization of the crystallized volume fraction is also challenging [Ferreira *et al.* 2011]. Some theories which relate GFA to crystallization rates have been proposed. The critical cooling rate to avoid a certain minimal crystallized fraction can be estimated by temperature–time–transformation (*TTT*) curves. *TTT* curves are temperature versus time graphs showing curves that correspond to specified fractions of transformed phase [Ferreira *et al.* 2011; Nascimento *et al.* 2005]. However, *TTT* curves are only available for a very few simple systems. For compositions with many components, *TTT* curves are very complex to obtain [Ferreira *et al.* 2011].

Therefore, alternative methods for quantifying GFA have been developed. GFA is the easiness for a liquid to be vitrified upon cooling, while glass stability (GS) is the glass resistance against devitrification on heating. It is a question that whether there is any direct relationship between these two parameters [Cabral Jr. *et al.* 1997; Nascimento *et al.* 2005]. Zanotto *et al*. [Ferreira *et al.* 2011; Nascimento *et al*. 2005] have tested several GS parameters by comparing them with the critical cooling rates of oxide liquids. All these GS parameters are calculated from three characteristic temperatures T_g, T_c and T_m, where T_g is the onset glass transition temperature, and T_c and T_m are the onset temperatures of the crystallization peak and the melting peak during heating. Figure 5.1 illustrates how these characteristic temperatures are determined experimentally using differential scanning calorimetry (DSC). Their results show that most of the GS parameters that consist of three characteristic DSC temperatures show better correlation with GFA than parameters that use only two characteristic temperatures. In particular, three of these parameters (K_W, K_H, and K_{LL}, see Table 5.1) show excellent correlation with GFA.

Among these GS parameters [Ferreira *et al.* 2011; Nascimento *et al*. 2005; Avramov *et al.* 2003; Lu & Liu 2003], the Hrubÿ parameter (K_H) shows a better correlation with GFA compared with other parameters and is commonly employed as a reliable and precise glass-forming criterion [Hrubÿ 1972; Kozmidis-Petrovic and Šesták 2011]. Therefore, we use K_H as a measure of GFA in this work. A high value of K_H indicates high glass stability. K_H is calculated as following:

$$K_H = \frac{T_c - T_g}{T_m - T_c}. \tag{5.1}$$

Table 5.1 Glass stability parameters (temperatures in K). Reproduced from [Ferreira *et al.* 2011].

	Reference	Equation number
$K_{\mathrm{LL}} = \frac{T_{\mathrm{x}}}{T_{\mathrm{g}} + T_{\mathrm{m}}}$	[Lu & Liu 2002; Lu & Liu 2003]	(1)
$K_{\mathrm{H}} = \frac{T_{\mathrm{x}} - T_{\mathrm{g}}}{T_{\mathrm{m}} - T_{\mathrm{x}}}$	Hrubÿ 1972]	(2)
$K_{\mathrm{W}} = \frac{T_{\mathrm{x}} - T_{\mathrm{g}}}{T_{\mathrm{m}}}$	[Weinberg 1994]	(3)
$K_{\mathrm{T}} = \frac{T_{\mathrm{g}}}{T_{\mathrm{m}}}$	[Turnbull 1969]	(4)
$K_{\mathrm{SP}} = \frac{(T_{\mathrm{x}} - T_{\mathrm{g}})(T_{\mathrm{c}} - T_{\mathrm{x}})}{T_{\mathrm{g}}}$	[Saad & Poulain 1987]	(5)
$K_1 = T_{\mathrm{m}} - T_{\mathrm{g}}$	[Nascimento *et al.*2005]	(6)
$K_2 = T_{\mathrm{x}} - T_{\mathrm{g}}$	[Nascimento *et al.*2005]	(7)
$K_3 = \frac{T_{\mathrm{x}}}{T_{\mathrm{m}}}$	[Nascimento *et al.*2005]	(8)
$K_4 = \frac{(T_{\mathrm{x}} - T_{\mathrm{g}})(T_{\mathrm{c}} - T_{\mathrm{x}})}{T_{\mathrm{m}}}$	[Nascimento *et al.*2005]	(9)

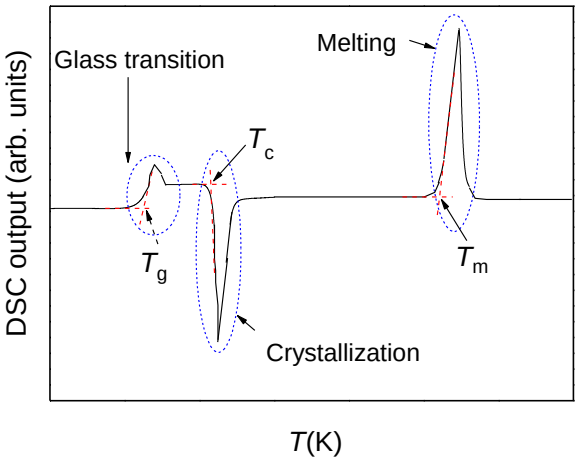

Figure 5.1 Typical DSC curve of a glass that easily crystallizes during heating. The procedure for determining the three characteristic temperatures T_g ,T_c and T_m is illustrated. Reproduced from Paper IV.

The liquidus (T_l) is the ultimate temperature of thermodynamic equilibrium between the solid and liquid phases of any material, above which crystals are unstable [Ferreira *et al.* 2010]. Besides GS parameters, it has been revealed that the viscosity at the liquidus temperature (or melting temperature), η (T_l) shows strong correlation with GFA [Lu *et al.* 2003]. In Chapter 3, we have mentioned that if a melt exhibits high liquidus viscosity, crystallization is impeded since the high viscosity creates a large kinetic barrier against atomic rearrangements. Thus,

such melts possess high GFA due to the slow dynamics. Nevertheless, in this thesis, we only focus on the GS parameters.

As discussed in chapter 3, shear viscosity is an important property of glass-forming liquids. It is also related to GFA, since the flow behavior determines the kinetic activation barriers for both nucleation and crystal growth [Avramov *et al.* 2003]. An inverse correlation between fragility index and GS has been found for various metallic glass-forming liquids in addition to some silicate liquids [Busch *et al.* 1998; Moesgaard and Yue 2009]. This is because "strong" melts have less change in rigidity with respect to changes in temperature, which could create steric hindrance towards crystallization during cooling. However, whether the fragility of borate and aluminosilicate glasses are correlated with their GS is still unclear. Here, we will investigate the GS of the soda-lime borate and soda-lime aluminosilicate glasses, and clarify the relation between *m* and GS in these glasses.

5.1 Soda-Lime Borate Liquids

Borate glasses have recently received significant attention due to their bioactive features, which may have some practical medical applications. Therefore, it has become important to investigate the GFA of the borate system. The GFA of binary alkali or alkali earth borate glasses have been widely studied [Ferreira *et al.* 2011; Ferreira *et al.* 2010]. However, the GFA of soda-lime borate has not been reported yet. Moreover, the "boron anomaly" makes the structure and properties of these glasses more interesting.

DSC upscans are performed on the soda lime borate glass series (Table 2.1) at a heating rate of 20 K/min to determine the glass stability upon heating (Fig. 5.2). For the four glasses with x = 20, 25, 30, and 35, K_H is calculated from T_g, T_c, and T_m and stated in Table 5.2. K_H decreases as the content of Na_2O increases. However, no crystallization peak is observed for the three glasses with x = 5, 10, and 15, which implies that these compositions have higher glass stability than the other compositions [Moesgaard & Yue 2009]. In general, the GS decreases with increasing substitution of Na_2O for B_2O_3 (Fig. 5.3a).

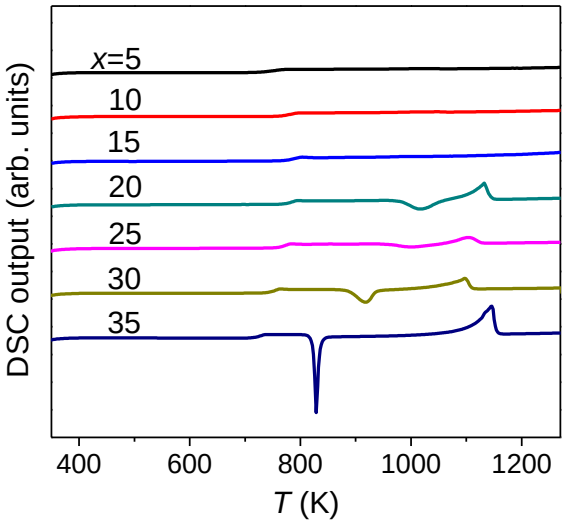

Figure 5.2 DSC output (arbitrary units) versus temperature (T) during heating at 20 K/min for the glasses with compositions of xNa$_2$O-10CaO-(89-x)B$_2$O$_3$-1Fe$_2$O$_3$. Reproduced from Paper IV.

Table 5.2 Characteristic temperatures, K_H, N_4 [Smedskjaer *et al.* 2010a], NBO/B, and m of the seven glasses ($x$$Na_2O$-10CaO-(89-$x$)$B_2O_3-1Fe_2O_3$). The errors in the characteristic temperatures are approximately ±2-3 K and uncertainties in N_4 are on the order of ±0.2 at%. Reproduced from Paper IV.

Sample (x=)	T_g (K)	T_c (K)	T_m (K)	K_H	N_4 [at%]	NBO/B	m
5	728	n/a	n/a	n/a	16	0.197	49±1
10	764	n/a	n/a	n/a	24	0.266	59±1
15	774	n/a	n/a	n/a	36	0.316	63±1
20	772	979	1062	2.49	40	0.47	67±2
25	760	954	1055	1.92	46	0.634	74±1
30	742	887	978	1.59	43	0.926	65±2
35	715	824	1118	0.37	42	1.247	n/a

The fractions of tetrahedral boron to total (N_4) and NBO/B are determined and listed in Table 5.2, where NBO/B is the average number of non-bridging oxygen per boron tetrahedron or triangle. As shown in Fig. 5.3a and b, K_H decreases as NBO/B increases. The results indicate that the GS is closely related to the degree of network connectivity [Phillips 1979]. Boron speciation also has a direct influence on the connectivity. However, N_4 does not show a direct relation with K_H. There is apparently an influence of both NBO/B and N_4 on GS, since both of these parameters affect the degree of network connectivity.

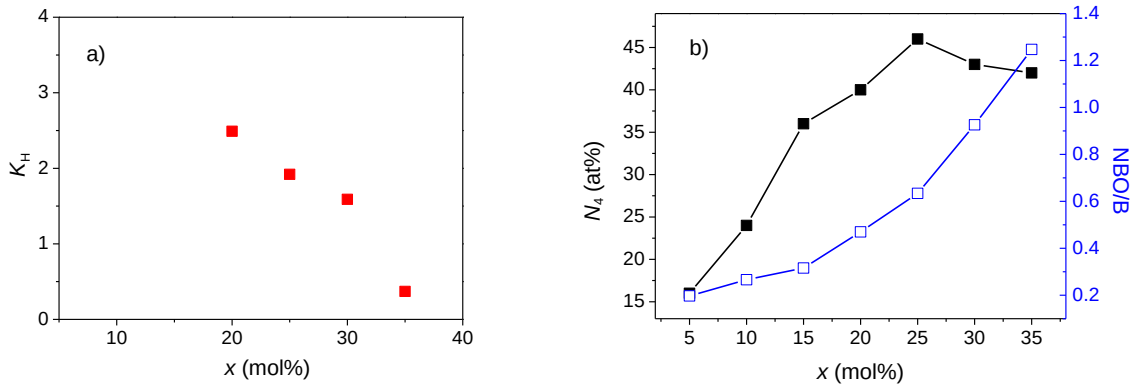

(a) (b)

Figure 5.3 (a) Hrubÿ parameter (K_H) as a function of the Na_2O content (x) for the four glasses with x = 20, 25, 30, and 35. (b) N_4 and NBO/B as a function of x. The uncertainties in N_4 are on the order of ±0.2 % and the errors in K_H are around ±0.03. Reproduced from Paper IV.

It should be noted that characteristic temperatures are dependent on the heating rate employed during the DSC measurements. For good glass formers, K_H cannot be determined using the accessible heating rates of a DSC since no crystallization peak is observed. The inherent limitations of the Hrubÿ parameter represent a universal drawback for any GS parameter, which includes characteristic temperatures.

As mentioned in chapter 4, the composition dependence of fragility is explained in terms of the temperature constraint theory. Comparing Fig. 4.2a with Fig. 5.3a, we find that fragility and GS do not exhibit a linearly inverse relation. Within different amounts of network

former, NBO/B plays a determining role in controlling GS, while the boron speciation plays a less important role for GS. However, when we calculate the fragility with topological constraint theory, the boron speciation is counted, which plays a less important role for GSin different compositions. Moreover, GS is related to many other properties, e.g., the degree of network connectivity [Moesgaard & Yue 2009], liquidus temperature [Ota *et al.* 1995; Angell 2008], but it is not necessarily related to only fragility [Bian *et al.* 2007]. Thus, the inverse relation between GS and fragility may not be applicable to every glass system.

Interestingly, two of the glasses under study (with x = 20 and 25) do not exhibit any crystallization exotherms during the second DSC upscan at 20 K/min to 1273 K when they have been subjected to a prior upscan to 1273 K at 20 K/min and a subsequent downscan at the same rate (Fig. 5.4). This means that the stability of these two glasses against crystallization is dramatically enhanced after they undergo a slow cooling process. The enhancement of the glass stability can also be observed in glasses containing higher Na_2O content. We explain the enhancement of GS in terms of the temperature dependence of the boron speciation.

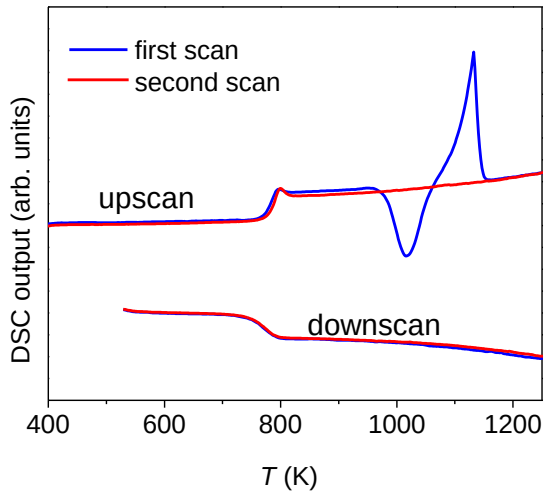

Figure 5.4 DSC scans for the glass with x=20 using 20 K/min heating and cooling. Reproduced from Paper IV.

According to Ref. [Majérus *et al.* 2003], the fraction of BO_4 tetrahedra decreases with increasing temperature above T_g, indicating that the BO_4 tetrahedra in the glass are converted to BO_3 triangles in the melt. The glass containing more BO_3 has a less rigid network structure and is facilitated to crystallization. Moreover, an increase of N_4 after the first upscan will result in a decrease of NBO, which is expected to cause an increase of GS. Therefore, this combination of two effects should lead to a substantially enhanced GS. The concentrations of BO_3 and BO_4 in a borate glass depend on the cooling rate that the borate melt experienced during production [Cormier *et al.* 2006; Wu *et al.* 2011]. The higher the cooling rate, the higher fraction of BO_3 is frozen-in. Upon re-heating, the rapidly cooled glass should crystallize more easily than the slowly cooled glass due to the factors mentioned above. Therefore, the GS is ultimately determined during this cooling process. Our ^{11}B MAS NMR measurements provide evidence for the possible link between the boron speciation and the enhanced GS [Paper IV].

5.2 Soda-Lime Aluminosilicate Liquids

Aluminosilicate glasses have found widespread applications in cutting edge technologies. However, the vitrification ability of the liquid becomes the obstacle of developing new aluminosilicate glass, which is particularly critical for glasses with high concentration of Al_2O_3. Hence, it is important to understand the correlation between the atomic structure of glass and its GFA.

We investigate the influence of the Al_2O_3 content on the GS for the series of soda lime aluminosilicate glasses with compositions (in mol%) of $(76\text{-}x)SiO_2{-}xAl_2O_3{-}16Na_2O{-}8CaO$ with x = 0, 2.7, 5.3, 8, 10.7, 13.3, 16, 18.7, 21.3, and 24. The DSC curves of the ten aluminosilicate glasses during heating (Fig. 5.5) show that the glasses with low Al_2O_3 content do not exhibit any crystallization exotherms. This indicates that these glasses possess high stability. The slight decrease in the DSC signal at high temperatures in these DSC curves is mainly due to experimental error. Interestingly, there is a loss of glass stability at Al_2O_3 content between 18.7 and 21.3 mol% since crystallization exotherms and subsequent melting endotherms are observed in the DSC spectra of these two glasses.

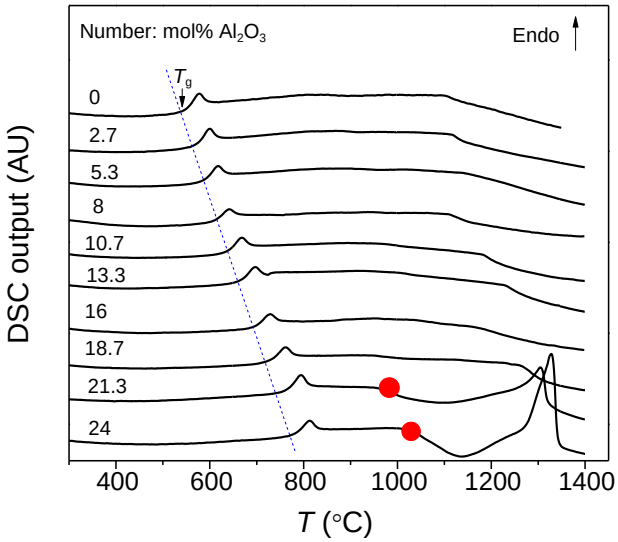

Figure 5.5 Calorimetric response to heating at 20 K/min in argon for the $(76\text{-}x)SiO_2{-}xAl_2O_3{-}16Na_2O{-}8CaO$ glasses with x = 0, 2.7, 5.3, 8, 10.7, 13.3, 16, 18.7, 21.3, and 24. The dashed blue line indicates the change in glass transition temperature (T_g) with composition. The red circles indicate the onset of crystallization in the glasses with 21.3 and 24 mol% Al_2O_3. Reproduced from Paper V.

We also investigate whether the inverse correlation between fragility and GS is applicable to this glass system. As shown in Fig. 4.6, m is approximately constant in the low $[Al_2O_3]$, it starts to increase with increasing $[Al_2O_3]$ from $[Al_2O_3]$ > 18.7 mol%. The inflection point of m is coincident with the loss of glass stability. This indicates that the GS and fragility is inversely correlated for these glasses.

To understand the structural origin of this loss of glass stability, we turn to the ^{27}Al MAS NMR results for these glasses [Smedskjaer *et al.* 2012]. These data (Fig. 2.2) show that when $[Na_2O]>[Al_2O_3]$, Al exists mainly in 4-fold coordination. For the glasses with $[Al_2O_3]\geqslant$

[Na_2O], Al in 5-fold coordination starts to appear [Risbud *et al.* 1987]. The fraction of Al^V increases with increasing Al_2O_3 content. This indicates that the structural change reflected in the aluminum speciation plays a dominant role in the loss of glass stability. For glasses with [Al_2O_3] = 10.7 and 13.3 mol%, the primary devitrification phase is anorthite ($CaAl_2Si_2O_8$). As [Al_2O_3] increases, nepheline ($NaAlSiO_4$) starts to form from the glass with [Al_2O_3] = 16 mol%. The GS starts to diminish in the region around [Al_2O_3] = 18.7 mol%. Aluminum exists in four-fold coordination in both the anorthite and nepheline crystals [Foit & Peacor 1973; Dollase & Thomas 1978], i.e., the presence of Al^V in the high-Al_2O_3 glasses could make the local structure less energetically stable. The Al^V domains could readily become nucleation sites that will grow when the glass is subjected to dynamic heating due to the high thermodynamic driving force for crystallization. Therefore, GS will decrease if sufficient Al^V-containing domains form by increasing Al_2O_3 content up to a critical level. It should be mentioned that a critical concentration of Al^V is an approximate value. In reality, there is a critical range of Al_2O_3 content above which GS will decrease sharply.

5.3 Summary

We have investigated the glass stability (GS) of a series of soda lime borate liquids. It is found that GS decreases when Na_2O is substituted for B_2O_3, implying that the network connectivity greatly controls GS of the studied systems. The inverse correlation between liquid fragility and GS, which has been found for some glass-forming liquid series, is not observed for these systems. We found that the glass stability becomes enhanced for some of the glasses after the first DSC up- and down-scans. This enhancement of GS can be attributed to the structural conversion of BO_3 units into BO_4 units during this slow cooling process. A loss of glass stability of the soda lime aluminosilicate glasses above a critical Al_2O_3 content is observed. The increase amount of five-fold coordinated aluminum in the high-Al_2O_3 glasses causes the structure to be less stable and is apparently responsible for the loss of glass stability. This finding suggests that five-fold coordinated aluminum species should be avoided when developing glasses with high GS.

6. General Discussion and Perspectives

The properties of glasses are determined by their atomic structure, therefore, understanding the glass properties based on the local atomic arrangements and topologies is of great industrial application. However, the atomic structure of glass lacks of periodicity and glass is not in thermal equilibrium state. Therefore, it is challenge to establish a unique structural model for any glass system as in crystalline compounds. The temperature-dependent constraint theory is applied to explain the composition-structure-property correlations in different glass systems. The properties we focus on in this thesis include dynamic properties, glass-forming ability (GFA) and mechanical properties. We have clarified the structure origins of these properties based on the temperature-dependent constraint theory. The findings are instructive in designing glass composition with high GFA and mechanical properties. In addition, the results can also be used to optimize the industrial process conditions.

In terms of dynamic properties, we have investigated the high temperature limit of liquid viscosity by analyzing measured viscosity curves for 946 silicate liquids and 31 other liquids including metallic, molecular, and ionic systems. We find that there is a narrow spread of high temperature limit of viscosity around 10^{-3} Pa·s for silicate liquids. This indicates a common underlying physics of silicate liquids at the high temperature limit. However, for non-silicate glass-forming liquids, we have less data available compared to the silicate liquids. Therefore, it is essential to extend the composition ranges for these systems. According to temperature dependent constraints theory, in the infinite temperature limit all three degrees of freedom are floppy for each atom, so each atom has three continuous modes of deformation, independent of atom type. Thus, the viscous flow behavior of any glass-forming liquids should be same in the high-temperature limit. Therefore, even though we have not collected enough large amounts of viscosity data of non-silicate liquids, we believe that they also have the same universal η_∞ value as silicate liquids. After analyzing more viscosity data of non-silicate liquids, we could experimentally judge whether a universal η_∞ value exists for all the glass-forming liquids.

We have also investigated the connection between kinetic and thermodynamic measures of liquid fragility for the three glass-forming systems. We compare kinetic fragility get from viscosity data with several thermodynamic fragility parameters obtain from DSC, including C_{pl} -C_{pg}, $C_{p.peak}$-C_{pg}, ΔT_g, and $(dC_p/dT)_{inflect}$. The kinetic fragility shows a positive correlation with the values of $C_{p.peak}$-C_{pg}, ΔT_g, and $(dC_p/dT)_{inflect}$. However, the parallel relation between C_{pl} -C_{pg} and kinetic fragility does not apply to all glass systems. The reason could be C_{pl} - C_{pg} is a purely thermodynamic quantity, whereas other thermodynamic fragility parameters are also kinetic property. Moreover, there could exist the maximum fragility of any glass-forming liquid, the question that whether there should also exist an inherent upper limit to the value of thermodynamic fragility parameters arises. To answer whether there is a parallel relation between the kinetic and the thermodynamic fragilities and whether there exist an inherent upper limit of thermodynamic fragilities, we still need to expand the data sets and the fragility range, in particular, we could include more data for fragile liquids, such as organic liquids.

We have attempted to understand the possible correlation between fragility and GS for soda lime borate liquids and soda lime aluminosilicate liquids. In some metallic glasses and silicate glasses, fragility could be used as a quantitative measure of GS for those systems, since an inverse correlation between fragility and GS has been found [Moesgaard & Yue

2009; Bian *et al.* 2007]. However, fragility and GS do not exhibit a linearly inverse relation for soda lime borate liquids. The results suggest that the positive correlation between GS and fragility is not so evident. The weakness of the correlation may indicate that GS is not primarily affected by fragility, it is also affected by other controlling factors, e.g., liquidus viscosity. In other works, fragility and GS are not physically independent with each other. The degree of short-range bond ordering is indeed one of the key physical factors controlling GS, in addition to other thermodynamic factors [Tanaka 2005]. Therefore, we can conclude that GS is related to many other properties rather than fragility [Bian *et al.* 2007], i.e., GS and fragility might not necessarily have a linear inverse correlation.

We have characterized GFA by measuring the glass stability (GS) against crystallization. GS is of importance during processes involving re-forming of an existing glass [Shelby 2005]. For example, when you prepare optical fibers by drawing glass from a preform, high GS is favored since crystalline is prohibited in this process. We have reported a striking thermal history dependence of the glass stability against crystallization for the soda-lime borate glasses. The GS of some of the glasses gets enhanced after being subjected to a relatively slow cooling cycle, e.g., a 10~20 K/min cooling rate. This indicates that the glass stability of these compositions can be enhanced by slowly cooling their melts to the glassy state, before any reheating. Our finding here is instructive for producing borate glasses with high GS against crystallization. Moreover, we could adjust the GS of borate glass by varying the previous cooling rate before reheating. Therefore, the borate glass might have wider applications in various industrial fields which require glasses with high GS.

We have used the Hrubÿ parameter to quantify the GS of various glass systems. For glasses with low GS, Hrubÿ parameter can be calculated easily since the characteristic temperatures can be obtained at the applied rates (10 and 20 K/min). For glasses with high stability, Hrubÿ parameter could not be determined since no crystallization was observed during heating at the applied rates (10 and 20 K/min). That is because the characteristic temperatures are dependent on the heating rate employed during the measurements. The crystallization and melting processes are bypassed when using a sufficiently high heating rate. This indicates the applicability limitation of the Hrubÿ parameter for the current DSC techniques. Similar to Hrubÿ parameter, there are also many other GS parameters which all use the same characteristic temperatures, i.e., T_g, T_c, and T_m. However, the inherent limitations of the Hrubÿ parameter represent a universal drawback for any GS parameter, which includes characteristic temperatures. Therefore, a more universal GFA parameter which can be applied to any glass-forming liquid needs to be established.

In order to quantify the GFA of good glass-formers by GS parameters, previous isothermal heat-treatments could be applied to induce crystallization before doing the DSC measurements. For instance, we could do isothermal heat-treatments on glass for different durations and subsequently cool the glass at 10 K/min in a furnace. The crystallization behavior of the glass can be characterized by SEM, optical microscopy, and XRD. The glasses that have been heat-treatments can be rescanned with DSC and the T_g, T_c, and T_m could be determined. These characteristic temperatures should vary with different heat-treatment conditions, which could provide additional GFA information. Besides GS, there are also other approaches to quantify GFA. Liquidus viscosity, $\eta(T_l)$, shows strong correlation with GFA. If a melt exhibits high liquidus viscosity, crystallization is impeded since the high viscosity creates a large kinetic barrier toward atomic rearrangements. Thus, such melts possess high GFA due to the slow dynamics. In order to quantify $\eta(T_l)$, we need both

viscosity and liquidus temperature data. For good glass-formers, it is challenging to obtain the liquidus temperature by DSC up-scans. Ferreira *et al.* proposed a DSC method to estimate T_l of good glass-formers [Ferreira *et al.* 2010]. Similarly, crystallization is induced by heat treatment of glass, and the liquidus temperature is then obtained by DSC. The best estimate for the liquidus temperature is obtained by extrapolating the melting temperature measured at different rates to 0 °C/min. By applying this technique, the η (T_l) of any glass system can be calculated and compared.

Moreover, the GFA is also related to the short-range order and/or medium-range order of the glass structure. For instance, as discussed in Chapter 5, a loss of the GS of the soda lime aluminosilicate glasses above a critical Al_2O_3 content is observed. The presence of Al^V in the high-Al_2O_3 glasses causes the structure to be less stable and is apparently responsible for the loss of glass stability. This indicates that the structure units, which could make the local structure less energetically stable, are prone to become nucleation sites and thus decrease the GS. In addition to the factors mentioned above, GFA could also be related to the crystallization driving force and so on. The development of a new universal GFA parameter for both poor and good glass forming systems, which incorporates all the related factors, still requires further detailed exploration.

Bioactive glasses have found their practical medical application for tissue engineering in bone repair [Hench 1991; Hench 1998; Bosetti *et al*. 2003; Silver *et al*. 2001]. The bone bonding properties of bioactive glasses were reported in 1971 by Hench *et al*. [Hench *et al*. 1971]. Most of the primary bioactive system is silicate-based materials, e.g. Bioglass®. Recently, researchers at the University of Missouri-Rolla have shown that some borate glasses are also bioactive [Conzone *et al*. 2002]. It has been discovered that borate glass nanofibers can promote the healing of flesh wounds [Wray 2011]. The bioactive feature of the glass is promising in clinical applications. Therefore, it is important to study the GFA of more complex borate liquids. The chemical durability of the borate glass is related to soft-tissue regeneration and the antimicrobial effect. Moreover, it would be useful to develop new borate glass compositions which possess optimized bioactivity for wound healing.

In order to explain the composition dependence of various mechanical properties, we apply the temperature-dependent constraint theory. This theory is the most powerful tool available today to predict the composition dependence of macroscopic properties. The advantage of this theory is that it is only involves straightforward pen-and-paper calculations based on a counting of network constraints [Mauro 2011a]. The implicit assumption of constraint theory of is that the network-forming structural units and their associated constraints can be identified. Such structure information can be obtained by structure characterization, such as NMR. Smedskjaer *et al.* have successfully applied the constraint theory to predict the glass transition temperature, fragility and some mechanical properties for soda-lime borate and borosilicate glasses. For our sodium boroaluminosilicate glasses, we only apply the temperature-dependent constraint theory to quantitatively explain the composition dependence of various physical properties. It would be interesting to directly use the constraint theory to predict the composition dependence of macroscopic properties. However, we had difficulty to accurately quantify the non-bridging oxygen on silicate due both to Al NNN complications and relatively poor signal to noise ratio. Actually, if the direct experimental structure information is not available, we could turn to molecular dynamics (MD) simulation, which can provide important structure information and the energies associated with various types of constraints [Mauro 2011a]. In the future, it is worthy to

incorporate MD data to temperature constraint theory when predicting glass properties for complicated glass systems. It should be mentioned that the constraint theory can be applied to predict glass properties based on the assumption that the glasses/liquids are compositionally homogeneous. If the glasses/liquids are heterogeneous, e.g phase separation takes place, the number of constraints cannot correctly be counted, therefore the constraint theory cannot be applied.

Due to the non-crystalline nature of glass, it is still challenging to develop a universal model to predict glass properties for any glass system based on the structure information. The temperature-dependent constraint theory provides some insights into the relation between glass structure and properties. However, more work is required to apply this model to glass systems with complicated structure. This thesis is useful for a general understanding the structure-property relation in oxide glasses and for developing oxide glasses with improved properties.

7. Conclusions

We have investigated the structure of three different glass systems: soda lime borate, soda lime aluminosilicate, and sodium boroaluminosilicate glasses. The boron speciation is affected by the content of modifiers, and the boron anomaly also exists in the soda lime borate glass. For soda lime aluminosilicate glasses, the fraction of Al^{V} increases with increasing Al_2O_3 content, which causes dramatic changes of some properties, e.g., glass stability against crystallization. When $[Na_2O]<[Al_2O_3]$, almost all sodium is used to charge compensate Al^{IV}. When $[Na_2O]>[Al_2O_3]$, sodium first charge compensates Al^{IV}, after charge compensating Al^{IV}, not all of the excess Na^{+} ions are used for converting B^{III} to B^{IV}, and some are used to create NBOs on both Si and B.

We have answered the question of whether there exist universal dynamics of silicate liquids at the high-temperature limit. Silicate liquids have a universal value of high temperature viscosity limit, i.e., $\log \eta_\infty = -3$. In other words, there is no systematic dependence of the high temperature viscosity limit on chemical composition for the silicate liquids. This result is based on systematic analysis of experimental data, including 946 silicate liquids and 31 other liquids including metallic, molecular, and ionic systems. After establishing this value, the non-Arrhenius scaling of liquid viscosity can be quantified through the fragility index *m* of the liquid. Moreover, there are only two independent parameters governing the viscosity-temperature relation, namely, the glass transition temperature and fragility index. This result also indicates a common underlying physics of silicate liquids at the high temperature limit.

We have discussed the link between the kinetic fragility index *m* determined from viscosity measurements and various thermodynamic fragility indices for the three glass-forming systems studies in this work. The thermodynamic fragility parameters include C_{pl} -C_{pg}, $C_{p.peak}$-C_{pg}, ΔT_g, and $(dC_p/dT)_{inflect}$, which are all obtained from DSC. The kinetic fragility shows a positive correlation with the values of $C_{p.peak}$-C_{pg}, ΔT_g, and $(dC_p/dT)_{inflect}$. However, the parallel relation between C_{pl} -C_{pg} and kinetic fragility does not apply to all glass systems. A previously established model of configurational heat capacity is able to capture the relation between C_{pl}-C_{pg} and *m* mostly for the sodium boroaluminosilicate system.

We apply the temperature dependent constraint theory to explain the composition dependence of several properties, e.g., dynamic, mechanical properties. For the series of soda-lime borate liquids, we have revealed the topological origin of fragility by calculating the contribution of each type of constraint to the fragility. For the series of soda-lime aluminosilicate liquids, the increase of Al^{V} leads to a greater number of bond angular constraints, which cause the increase of fragility. For the series of sodium boroaluminosilicate glasses, we have investigated several glass properties including dynamic properties, elastic moduli, and hardness. There is a pronounced change of the measured properties at around $[Al_2O_3]$-$[Na_2O]=0$ for both iron-free and iron-containing glasses. There are three compositional response regions for Young's and shear moduli and hardness. T_g is determined by the network connectivity and thus increases with increasing $[Al_2O_3]$-$[Na_2O]$. The liquid fragility shows a strong correlation with the fraction of tetrahedral boron in the glasses. The existence of the minimum and the three compositional response regions are related to boron speciation. Substitution of a small amount of Fe_2O_3 for SiO_2 in the glasses results in lower values of glass transition temperature, hardness, and elastic moduli. The findings are instructive for optimizing the composition and industrial process in the frame of boroaluminosilicate related products.

We have investigated the glass forming ability of the soda lime borate and soda lime aluminosilicate melts. We have characterized GFA by measuring the glass stability against crystallization using a differential scanning calorimeter (DSC). For the soda lime borate liquids, GS decreases when Na_2O is substituted for B_2O_3, implying that the network connectivity greatly controls GS of the studied systems. We also discuss the applicability limitation of the Hrubÿ parameter as a metric for quantifying GFA. The glass stability (GS) of some of the glasses get is enhanced after the first DSC up- and downscans. This indicates that the GS of these compositions can be enhanced by slowly cooling their melts to the glassy state, before any reheating. The enhancement of GS is related to the thermal history dependence of boron speciation. The inverse correlation between liquid fragility and GS is not observed for this glass system. In soda lime aluminosilicates, a loss of glass stability above a critical Al_2O_3 content is observed. 5-fold coordinated aluminum are formed for $[Al_2O_3] \geq [Na_2O]$, which plays a determining role in the loss of glass stability. The finding provides additional insight into the microscopic structural origins of GFA and will be a useful guidance for the development of new glass compositions.

8. Bibliography

G. Adam and J. H. Gibbs, *J. Chem. Phys.* **43** (1965) 139.

C. A. Angell, *J. Non-Cryst. Solids* **73** (1985) 1.

C. A. Angell, *J. Non-Cryst. Solids* **102** (1988) 205.

C. A. Angell, *Science* **267** (1995) 1924.

C.A. Angell, *J. Non-Cryst. Solids* **354** (2008) 4703.

C. A. Angell, K. L. Ngai, G. B. McKenna, P. F. McMillan, and S. W. Martin, *J. Appl. Phys.* **88**, (2000) 3113.

R. J. Araujo, *J. Non-Cryst. Solids* **42** (1980) 109.

R. J. Araujo, *J. Non-Cryst. Solids* **58** (1983) 201.

R. J. Araujo, *J. Non-Cryst. Solids* **81** (1986) 251.

R. J. Araujo and J. C. Mauro, *J. Am. Ceram. Soc.* **93** (2010) 1026.

I. Avramov, *J. Non-Cryst. Solids* **351** (2005) 3163.

I. Avramov and A. Milchev, *J. Non-Cryst. Solids* **104** (1988) 253.

I. Avramov, E. D. Zanotto, and M. O. Prado, *J. Non-Cryst. Solids* **320** (2003) 9.

R. M. Barrer, *Trans. Faraday Soc.* **39** (1943) 48.

M. Bauchy and M. Micoulaut, *J. Non-Cryst. Solids* **357** (2011) 2530.

X. F. Bian, J. Guo, X. Q. Lv, X. B. Qin, and C. D. Wang, *Appl. Phys. Lett.* **91** (2007) 221910.

H. Bornhöft and R. Brückner, *Glass Sci. Technol.* **72** (1999) 315.

M. Bosetti, L. Zanardi, L. L. Hench, M. Cannas, and J. Biomed. *Mater. Res.* **64A** (2003) 189.

Y. Bottinga and D. F. Weill, *Am. J. Sci.* **272** (1972) 438.

P. J. Bray and J. G. O'Keefe, *Phys. Chem. Glasses* **4** (1963) 37.

B. C. Bunker, R. J. Kirkpatrick, R. K. Brow, G. L. Turner, and C. Nelson, *J. Am. Ceram. Soc.* **74** (1991) 1430.

R. Busch, E. Bakke, and W. L. Johnson, *Acta Mater.* **46** (1998) 4725.

A. A. Cabral Jr., C. Fredericci, and E. D. Zanotto, *J. Non-Cryst. Solids* **219** (1997) 182.

J. C. C. Chan, M. Bertmer, and H. Eckert, *J. Am. Chem. Soc.* **121** (1999) 5238.

S. D. Conzone, R. F. Brown, D. E. Day, G. J. Ehrhardt, and J. Biomed. *Mater. Res.* **60** (2002) 260.

A. N. Cormack and Y. Cao, *Mol. Eng.* **6** (1996) 183.

L. Cormier, O. Majérus, D. R. Neuville, and G. Calas, *J. Am. Ceram. Soc.* **89** (2006) 13.

P. G. Debenedetti and F. H. Stillinger, *Nature* **410** (2001) 259.

M. R. DeGuire and S. D. Brown, *J. Am. Ceram. Soc.* **67** (1984) 270.

W. J. Dell, P. J. Bray, and S. Z. Xiao, *J. Non-Cryst. Solids* **58** (1983) 1.

M. P. Dickenson and P. C. Hess, *Contrib. Mineral. Petrol.* **92** (1986) 207.

W. A. Dollase and W. M. Thomas, Contrib. Mineral. Petrol. **66** (1978) 311.

W. F. Du, K. Kuraoka, T. Akai, and T. Yazawa, *J. Mater. Sci.* **35** (2000) 4865.

L. S. Du and J. F. Stebbins, *J. Non-Cryst. Solids* **351** (2005) 3508.

M. D. Dyar, *Am. Mineral.* **70** (1985) 304.

J. C. Dyre, *J. Phys.: Cond. Matter* **19** (2007) 205105.

M. D. Ediger, C. A. Angell, and S. R. Nagel, *J. Phys. Chem.* **100** (1996) 13200.

A. Ellison and I. A. Cornejo, *Int. J. Appl. Glass Sci.* **1** (2010) 87.

J. F. Emerson, P.E. Stallworth, and P.J. Bray, *J. Non-Cryst. Solids* **113** (1989) 253.

E. B. Ferreira, M. L. Lima, and E. D. Zanotto, *J. Am. Ceram. Soc.* **93** (2010) 3757.

E. B. Ferreira, E. D. Zanotto, S. Feller, G. Lodden, J. Banerjee, T. Edwards, and M. Affatigato, *J. Am. Ceram. Soc.* **94** (2011) 3833.

F. F. Foit and D. R. Peacor, Am. Mineral**. 58**(1973) 665.

D. Giordano, J. K. Russell, and D. B. Dingwell, *Earth and Planetary Sci Lett* **271** (2008)123.

G. N. Greaves and S. Sen, *Adv. in Phys.* **56** (2007) 1.

G. Guevara-Carrion, J. Vrabec, and H. Hasse, *J. Chem. Phys.* **134** (2011) 074508.

P. K. Gupta, In: Proceedings of the International Congress on Glass, p. 1-10, New Delhi, unpublished (1986).

P. K. Gupta and J. C. Mauro, *J. Chem. Phys.* **126** (2007) 224504.

P. K. Gupta and J. C. Mauro, *J. Chem. Phys.* **130** (2009) 094503.

T. Hecksher, A. I. Nielsen, N. B. Olsen, and J. C. Dyre, *Nature Physics* **4** (2008) 737.

L. L. Hench, *J. Am. Ceram. Soc.* **74** (1991) 1487.

L. L. Hench, *J. Am. Ceram. Soc.* **81** (1998) 1705.

L. L. Hench, R. J. Splinter, W. C. Allen, T. J. Greenlee Jr., and J. Biomed. *Mater. Res.* **2** (1971) 117.

A. Hrubÿ , *Czech. J. Phys.* **22** (1972) 1187.

P. Y. Huang, S. Kurasch, A. Srivastava, V. Skakalova, J. Kotakoski, A. V. Krasheninnikov, R. Hovden, Q. Y. Mao, J. C. Meyer, J. Smet, D. A. Muller, and U. Kaiser, *Nano Lett.* **12** (2012) 1081.

D. H. Huang and G. B. McKenna, *J. Chem. Phys.* **114** (2001) 5621.

M. D. Ingram, *Phys. Chem. Glasses* **28** (1987) 215.

C. M. Jantzen, K. G. Brown, and J. B. Pickett, *Int. J. Appl. Glass Sci.* **1** (2010) 38.

L. H. Kieu, J. M. Delaye, L. Cormier, and C. Stolz, *J. Non-Cryst. Solids* **357** (2011) 3313.

J. H. Kjeldsen, M. M. Smedskjaer, J. C. Mauro, and Y. Z. Yue (unpublished data), 2012.

P. P. Kobeko, *Amorfniye veshchestva* (Izd. AN SSSR, Moskva-Leningrad, 1952).

A. Kozmidis-Petrovic and J. Šesták, *J. Therm. Anal. Calorim.* DOI 10.1007/s10973-011-1926-6.

S. K. Lee, G. D. Cody, Y. W. Fei, and B. O. Mysen, *Chem. Geol.* **229** (2006) 162.

Z. P. Lu and C. T. Liu, *Acta Mater.* **50** (2002) 3501.

Z. P. Lu and C. T. Liu, *Phys. Rev. Lett.* **91** (2003) 115505.

Z. P. Lu, Y. Li, and C. T. Liu, *J. Appl. Phys.* **93** (2003) 286.

O. Majérus, L. Cormier, G. Calas, and B. Beuneu, *Phys. Rev. B* **67** (2003) 024210.

J. D. Martin, S. J. Goettler, N. Fosse, and L. Iton, *Nature* **419** (2002) 381.

L. M. Martinez and C. A. Angell, *Nature* **410** (2001) 663.

D. Massiot, F. Fayon, M. Capron, I. King, S. Le Calvé, B. Alonso, J. Durand, B. Bujoli, Z. Gan, and G. Hoatson, *Magn. Reson. Chem.* **40** (2002) 70.

J. C. Mauro, *Am. Ceram. Soc. Bull.* **90** (2011a) 31.

J. C. Mauro, *Int. J. Appl. Glass Sci.* **2** (2011b) 245.

J. C. Mauro, P. K. Gupta, and R. J. Loucks, *J. Chem. Phys.* **130** (2009a) 234503.

J. C. Mauro and R. J. Loucks, *Phys. Rev. B* **76** (2007) 174202.

J. C. Mauro and R. J. Loucks, *Phys. Rev. E* **78** (2008) 021502.

J. C. Mauro, R. J. Loucks, and S. J. Sen, *Chem. Phys* **133** (2010) 164503.

J. C. Mauro, Y. Z. Yue, A. J. Ellison, P. K. Gupta, and D. C. Allan, *Proc. Natl. Acad. Sci. U.S.A.* **106** (2009b) 19780.

E. Metwalli and R. K. Brown, *J. Non-Cryst. Solids* **289** (2001) 113.

M. Moesgaard and Y. Z. Yue, *J. Non-Cryst. Solids* **355** (2009) 867.

B. O. Mysen, P. Richet, Silicate Glasses and Melts – Properties and Structure, Elsevier, Amsterdam, 2005.

M. L. F. Nascimento, L. A. Souza, E. B. Ferreira, and E. D. Zanotto, *J. Non-Cryst. Solids* **351** (2005) 3296.

G. G. Naumis, *J Non-Cryst Solids* **352** (2006) 4865.

D. R. Neuville, L. Cormier, V. Montouillout, P. Florian, F. Millot, J.-C. Rifflet, and D. Massiot, *Am. Mineral.* **93** (2008) 1721.

M. I. Ojovan, K. P. Travis, and R. J. Hand, *J. Phys.: Cond. Matter* **19** (2007) 415107.

O. O. Okoturo and T. J. VanderNoot, *J. Electroanal. Chem.* **568** (2004) 167.

R. Ota, T. Wakasugi, W. Kawamura, B. Tuchiya, and J. Fukunaga, *J. Non-Cryst. Solids* **188** (1995) 136.

J. C. Phillips, *J. Non-Cryst. Solids* **34** (1979) 153.

J. C. Phillips and M. F. Thorpe, *Sol. State Commun.* **53** (1985) 699.

M. Potuzak, J. C. Mauro, T. J. Kiczenski, A. J. Ellison, and D. C. Allan, *J. Chem. Phys.* **133** (2010) 091102.

R. Richert and C. A. Angell, *J. Chem. Phys.* **108** (1998) 9016.

S. H. Risbud, R. J. Kirkpatrick, A. P. Taglialavore, and B. Montez, *J. Am. Ceram. Soc.* **70** (1987) C-10.

S. Rossano, H. Behrens, and M. Wilke, *Phys. Chem. Miner.* **35** (2008) 77.

J. K. Russell, D. Giordano, and D. B. Dingwell, *Am. Mineral.* **8** (2003) 1390.

M. Saad and M. Poulain, *Mater. Sci. Forum* **19–20** (1987) 11.

A. Saini, A. Khanna, V. K. Michaelis, S. Kroeker, F. Gonzalez, and D. Hernandez, *J. Non-Cryst. Solids* **355** (2009) 2323.

P. S. Salmon, *Nat. Mater.* **1** (2002) 87.

S. Sen and R. E. Youngman, *J. Phys. Chem. B* **108** (2004) 7557.

G. W. Scherer, *J. Am. Ceram. Soc.* **67** (1984) 504.

M. Schuch, C. R. Müller, P. Maass, and S. W. Martin, *Phys. Rev. Lett.* **102** (2009) 145902.

J. E. Shelby, *Introduction to Glass Science and Technology*, The Royal Society of Chemistry, Cambridge (2005).

I. A. Silver, J. Deas, and M. Erecińska, *Biomaterials* **22** (2001) 175.

M. M. Smedskjaer, J. C. Mauro, S. Sen, and Y. Z. Yue, *Chem. Mater.* **22** (2010a) 5358.

M. M. Smedskjaer, J. C. Mauro, R. E. Youngman, C. L. Hogue, M. Potuzak, and Y. Z. Yue, *J. Phys. Chem. B* **115** (2011a) 12930.

M. M. Smedskjaer, J. C. Mauro, and Y. Z. Yue, *Phys. Rev. Lett.* **105** (2010b) 115503.

M. M. Smedskjaer, R. E. Youngman, and J. C. Mauro (unpublished data), 2012.

M. M. Smedskjaer, Y. Z. Yue, J. Deubener, and H. P. Gunnlaugsson, *J. Phys. Chem. B* **113** (2009) 11194.

M. M. Smedskjaer, Q. J. Zheng, J. C. Mauro, M. Potuzak, S. Mørup, and Y. Z. Yue, *J. Non-Cryst. Solids* **357** (2011b) 3744.

M. M. Smedskjaer, "Structural and Topological Basis of Glass Properties and Diffusion", Ph.D. thesis, Aalborg University, 2011.

J. E. Stanworth, *J. Am. Ceram. Soc.* **54** (1971) 61.

J. F. Stebbins and Z. Xu, *Nature* **390** (1997) 60.

J. F. Stebbins and S. E. Ellsworth, *J. Am. Ceram. Soc.* **79[9]** (1996) 2247.

F. Stickel, E. W. Fischer, and R. Richert, *J. Chem. Phys.* **102** (1995) 6251.

H. Tanaka, *J. Non-Cryst. Solids* **351** (2005) 678.

M. F. Thorpe, *J. Non-Cryst. Solids* **57** (1983) 355.

D. Turnbull, *Contem. Phys.* **10 [5]** (1969) 473.

D. R. Uhlmann, *J. Non-Cryst. Solids* **7** (1972) 337.

A. K. Varshneya, *Fundamentals of Inorganic Glasses*, 2nd edition, Society of Glass Technology, Sheffield (2006).

A. K. Varshneya, *Int. J. Appl. Glass Sci.* **1** (2010) 131.

A. K. Varshneya and J. C. Mauro, *Glass Technol.: Eur. J. Glass Sci. Technol. A*, **51** (2010) 28.

L. M. Wang, C. A. Angell, and R. J. Richert, *J. Chem. Phys.* **125** (2006) 074505.

L. M. Wang and J. C. Mauro, *J. Chem. Phys.* **134** (2011) 044522.

M. C. Weinberg, *Phys. Chem. Glasses* **35** (1994) 119.

P. Wray, *Am. Ceram. Soc. Bull.* **90 (4)** (2011) 25.

J. S. Wu, M. Potuzak, and J. F. Stebbins, *J. Non-Cryst. Solids* **357** (2011) 3944.

H. B. Yu, W. H. Wang, and H. Y. Bai, *Appl. Phys. Lett.* **96** (2010) 081902.

Y. Z. Yue, *J. Non-Cryst. Solids* **354** (2008) 1112.

Y. Z. Yue, *J. Non-Cryst. Solids* **355** (2009) 737.

Y. Z. Yue, personal communication (2012).

Y. H. Yun and P. J. Bray, *J. Non-Cryst. Solids* **27** (1978) 363.

W. H. Zachariasen, *J. Am. Chem. Soc.* **54 (10)** (1932) 3841.

C. Z. Zhang1, L. N. Hu, Y. Z. Yue, and J. C. Mauro, *J. Chem. Phys.* **133** (2010) 014508.

J. Zhong and P. J. Bray, *J. Non-Cryst. Solids* **111** (1989) 67.

D. Zielniok, C. Cramer, and H. Eckert, *Chem. Mater*. **19** (2007) 3162.

L. Züchner, J. C. C. Chan, W. Müller-Warmuth, and H. Eckert, *J. Phys. Chem. B* **102** (1998) 4495.

List of Publications

I. Qiuju Zheng, Randall E. Youngman, Carrie L. Hogue, John C. Mauro, Marcel Potuzak, Morten M. Smedskjaer, Adam J. Ellison, Yuanzheng Yue," Structure of Boroaluminosilicate Glasses: Impact of $[Al_2O_3]/[SiO_2]$ Ratio on the Structural Role of Sodium," *Physical Review B*, **86**, 054203 (2012).

II. Qiuju Zheng, John C. Mauro, Adam J. Ellison, Marcel Potuzak, and Yuanzheng. Yue, "Universality of the high-temperature viscosity limit of silicate liquids," *Physical Review B* **83**, 212202 (2011).

III. Qiuju Zheng, Marcel Potuzak, John C. Mauro, Morten M. Smedskjaer, Randall E. Youngman, Yuanzheng Yue, "Composition-Structure-Property Relationships in Boroaluminosilicate Glasses," *Journal of Non-Crystalline Solids* **358**, 993-1002 (2012).

IV. Qiuju Zheng, John C. Mauro, Morten M. Smedskjaer, Randall E. Youngman, Marcel Potuzak, and Yuanzheng Yue, "Glass-Forming Ability of Soda Lime Borate Liquids," *Journal of Non-Crystalline Solids* **358**, 658-665 (2012).

V. Qiuju Zheng, Morten M. Smedskjaer, Randall E. Youngman, Marcel Potuzak, John C. Mauro, Yuanzheng Yue, "Influence of Aluminum Speciation on the Stability of Aluminosilicate Glasses against Crystallization," *Applied Physics Letters*, **101**, 041906 (2012).

VI. Morten M. Smedskjaer, Qiuju Zheng, John C. Mauro, Marcel Potuzak, Steen Mørup, and Yuanzheng Yue, "Sodium Diffusion in Boroaluminosilicate Glasses," *Journal of Non-Crystalline Solids* **357**, 3744-3750 (2011).

VII. Xinwei Wu, Jeremy D. Moskowitz, John C. Mauro, Marcel Potuzak, Qiuju Zheng, and Rüdiger Dieckmann, "Sodium Tracer Diffusion in Sodium Boroaluminosilicate Glasses," *Journal of Non-Crystalline Solids*, **358,** 1430–1437 (2012).

VIII. Qiuju Zheng, John C. Mauro, Morten M. Smedskjaer, Marcel Potuzak, Ralf Keding, and Yuanzheng Yue, "Glass Forming Ability of Soda Lime Borate Liquids," Abstract: *3rd International Congress on Ceramics*, Osaka, Japan (2010).

IX. Xinwei Wu, Qiuju Zheng, John Mauro, Marcel Potuzak, Adam J. Ellison, and Rüdiger Dieckmann, "Diffusion of Sodium in Sodium Boroaluminosilicate Glasses: Impact of Mixed Network Formers and the Influence of Water," Oral presentation: *2011 Glass & Optical Materials Division Meeting*, Savannah, USA (2011).

X. Qiuju Zheng, John C. Mauro, Morten M. Smedskjaer, Marcel Potuzak, Ralf Keding, and Yuanzheng Yue, "Glass-Forming Ability of Soda Lime Borate Liquids," Abstract: *2011 Glass & Optical Materials Division Meeting*, Savannah, USA (2011).

XI. Qiuju Zheng, Randall E. Youngman, Carrie L. Hogue, John C. Mauro, Marcel Potuzak, Adam J. Ellison, Morten M. Smedskjaer, and Yuanzheng Yue, "Structure and Topology of Na_2O-B_2O_3-Al_2O_3-SiO_2 Mixed Network Glasses," Oral presentation: *2011 Glass & Optical Materials Division Meeting*, Savannah, USA (2011).

XII. Qiuju Zheng, John C. Mauro, Adam J. Ellison, Marcel Potuzak, and Yuanzheng Yue, "Universality of the High Temperature Viscosity Limit of Glass-Forming Liquids," Oral presentation: *2011 Glass & Optical Materials Division Meeting*, Savannah, USA (2011).

XIII. Qiuju Zheng, Randall E. Youngman, Carrie L. Hogue, John C. Mauro, Marcel Potuzak, Adam J. Ellison, Morten M. Smedskjaer, and Yuanzheng Yue, "Impact of $[Al_2O_3]/[SiO_2]$ on the Structure of Boroaluminosilicate Glasses," Oral presentation: *Materials Science & Technology 2011 Conference and Exhibition*, Columbus, USA (2011).

XIV. Qiuju Zheng, Marcel Potuzak, John C. Mauro, Morten M. Smedskjaer, Adam J. Ellison, Randall E. Youngman, Yuanzheng Yue, "Structure-Property Relationships and the Mixed Network Former Effect in Boroaluminosilicate Glasses, " Oral presentation: *11^{th} ESG Conference*, Maastricht, The Netherlands (2012).

Paper I

Structure of boroaluminosilicate glasses: Impact of $[Al_2O_3]/[SiO_2]$ ratio on the structural role of sodium

Q. J. Zheng,[1,2] R. E. Youngman,[2,*] C. L. Hogue,[2] J. C. Mauro,[2] M. Potuzak,[2] M. M. Smedskjaer,[2] and Y. Z. Yue[1,3]

[1]*Section of Chemistry, Aalborg University, DK-9000 Aalborg, Denmark*

[2]*Science & Technology Division, Corning Incorporated, Corning, New York 14831, USA*

[3]*Shandong Key Laboratory of Glass and Ceramics, Shandong Polytechnic University, 250353 Jinan, China*

(Received 28 March 2012; published 22 August 2012)

In order to explore the structural roles of sodium in boroaluminosilicate glasses, we have designed ten Na_2O-B_2O_3-Al_2O_3-SiO_2 glasses with varied $[Al_2O_3]/[SiO_2]$ ratio to access different regimes of sodium behavior. Multinuclear nuclear magnetic resonance (NMR) experiments on ^{11}B, ^{27}Al, ^{29}Si, and ^{23}Na were performed to determine the complicated network former speciation and modifier environments as a function of glass composition. The different roles of sodium in relation with the network-forming cations (Si, B, and Al) have been clarified and quantified. When $[Na_2O] < [Al_2O_3]$, all available sodium is used to charge compensate fourfold coordinated aluminum (Al^{IV}), and deficiency in sodium concentration leads to fivefold coordinated aluminum (Al^{V}) groups. When $[Na_2O] > [Al_2O_3]$, sodium first charge compensates Al^{IV}, and thus all aluminum is fourfold coordinated and unaffected by other compositional changes. Hence, the preference in the formation of Al^{IV} over that of fourfold coordinated boron (B^{IV}) is confirmed. Excess sodium can be used to convert threefold coordinated boron (B^{III}) to B^{IV} or to create nonbridging oxygen (NBO) on Si and B, with a thermodynamic competition among these mechanisms. The NBOs on Si are quantified using ^{29}Si wide-line and magic angle spinning NMR. The fraction of silicon atoms associated with NBOs is calculated using a random model and compared with the NMR results. Finally, we have found that our previously proposed two-state statistical mechanical model of boron speciation accurately predicts the fraction of tetrahedrally coordinated boron atoms (N_4) in these mixed network former glasses.

DOI: 10.1103/PhysRevB.86.054203 PACS number(s): 61.43.Fs, 82.56.Hg, 81.05.Kf

I. INTRODUCTION

The macroscopic properties of a glass are the direct result of its microscopic structure,[1–7] as determined to a large extent by its chemical composition. In order to develop an enhanced understanding of structure-property relationships in glasses, it is thus critical to quantify the composition dependence of structural motifs within the glass network. This task is made especially difficult due to the lack of long-range structural order in glasses, which prevents the application of conventional structural characterization techniques such as x-ray diffraction. Alternative techniques, such as nuclear magnetic resonance (NMR) spectroscopy, have been particularly useful for elucidating many important aspects of both the short- and intermediate-range structural order in glass, especially in compositionally simple systems.[8,9] However, commercial glasses of industrial interest are typically multicomponent, and many unsolved structural puzzles still remain. Boroaluminosilicate glasses constitute a particularly important class of industrial material,[10–12] having found widespread applications in fields such as liquid crystal display substrates, optical components, fiberglass, radioactive waste containment, and photochromic glass. Understanding structure-property correlations in these glasses is especially challenging due to the mixed network former effect, which makes the structural speciation significantly more complicated.[13–15] In this paper, we present a detailed NMR study of network structure in this commercially important boroaluminosilicate glass system and evaluate several models for predicting network former speciation.

The role of network modifier cations in borate-containing glasses has been systematically investigated in prior studies.[16–20] In binary alkali borate glasses, the addition of a network modifier (such as Na_2O) to pure B_2O_3 initially converts threefold coordinated boron (B^{III}) to a fourfold coordination state (B^{IV}), with the network modifier cations acting as charge compensators for B^{IV}. The fraction of tetrahedral to total boron (N_4) reaches a maximum value with further modifier addition, when formation of nonbridging oxygen (NBO) becomes prevalent. In sodium borosilicate glasses, the empirical Dell–Bray model[21–23] is frequently invoked to predict N_4 and NBO concentrations as a function of glass composition. In this study, we consider quaternary sodium boroaluminosilicate glasses, the structure of which is more complicated due to the ability of sodium ions to interact not only with boron and silicon, but also with aluminum. Yamashita *et al.*[24,25] found that, in alkali boroaluminosilicate systems, when the three network formers coexist, the alkali oxides react preferably with Al_2O_3, and the value of N_4 can be estimated as $r/(1-r)$, where $r = ([Na_2O] - (Al_2O_3])/([Na_2O] - [Al_2O_3] + [B_2O_3])$. Stebbins *et al.*[13–15,26,27] have conducted a significant amount of work on understanding the structure of boroaluminosilicate glasses, e.g., they developed a modified Dell–Bray model[21–23] to account for their experimentally determined N_4 values. Smedskjaer *et al.* have recently introduced a new statistical mechanical model of boron speciation for accurate prediction of both the composition and thermal history dependence of boron speciation in borosilicate glasses.[28] In this model, the addition of network modifiers leads to a thermodynamic competition between the formation of NBO and the conversion of boron from trigonal to tetrahedral configuration. The model offers improved prediction of boron speciation and provides a natural

explanation for the observed thermal history dependence of N_4.

Nevertheless, cation speciation in complex oxide glasses is not yet fully understood, especially with the inherent competition between network modifiers and at least three different glass-forming oxide constituents. A new model that can better predict N_4 needs to be developed for such materials, since boron speciation is a very important parameter controlling several glass properties.[7] The network former speciation and modifier environments are determined by different structural roles (e.g., charge compensation) of sodium in sodium boroaluminosilicate glasses. In order to gain more knowledge of this system, we have studied ten Na_2O-B_2O_3-Al_2O_3-SiO_2 glasses with systematic variation of the $[Al_2O_3]/[SiO_2]$ ratio to access different regimes of sodium behavior: (1) Na^+ to stabilize aluminum in a tetrahedral configuration, (2) Na^+ to convert boron from trigonal to tetrahedral coordination, and (3) Na^+ to form NBO on silicon or boron. We obtain thorough structure details, e.g. network speciation and modifier cation environment, from a multinuclear NMR study of all cations (^{11}B, ^{27}Al, ^{29}Si, and ^{23}Na) using both magic angle spinning (MAS) and triple quantum (3Q) MAS NMR spectroscopy. Based on the resulting structural information, the different roles of Na_2O as a modifier are discussed in detail. We also extend the two-state statistical mechanical model of boron speciation, originally developed for borosilicate glasses, to these sodium boroaluminosilicate glasses, showing excellent agreement between predicted and measured N_4 values. This comprehensive study of alkali boroaluminosilicate glasses provides additional insight into glass structure and will serve as an important contribution to understanding and developing more complex multicomponent oxide glasses.

II. EXPERIMENTAL

A. Sample preparation

The batched compositions of the glasses were $x$$Al_2O_3-5B_2O_3$-(80-$x$)$SiO_2-15Na_2O$ with x = 0, 1, 2.5, 5, 7.5, 10, 12.5, 15, 17.5, and 20 (mol%). The analyzed compositions were slightly different from the batched compositions, but we retain the original naming convention based on $x$$Al_2O_3$, as listed in Table I. Figure 1 shows the ternary B_2O_3-Al_2O_3-SiO_2 composition diagram (mol%) plus 15% Na_2O and fining agent. We keep the Na_2O content constant in order to calculate the concentrations of B_2O_3, Al_2O_3, and SiO_2 in this diagram. All glasses were prepared by conventional melt quenching methods. The batch materials used in glass melting were SiO_2, Al_2O_3, H_3BO_3, and Na_2CO_3. Here, 0.1 mol% As_2O_3 or SnO_2 was added as a fining agent. The batch materials were mixed and then melted in a covered silica crucible at different homogenization temperatures T_h (see Table I) for 6 h in air. The melts were quenched in water, and the resulting glass shards were crushed and remelted for another 6 h at their respective melting temperatures to ensure chemical homogeneity. Finally, the melts were poured onto a stainless steel plate to obtain glasses. The glasses were annealed for 2 h at different temperatures (between 450 and 560 °C) depending on chemical composition. The chemical compositions of the

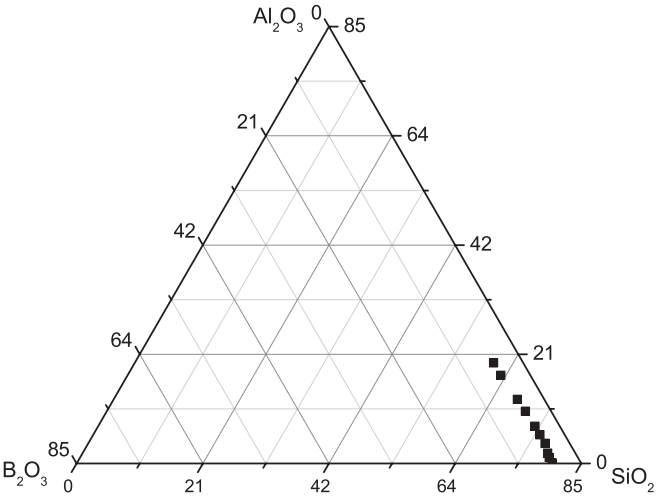

FIG. 1. The designed glass compositions indicated in the B_2O_3-Al_2O_3-SiO_2 diagram (85 mol% in total). 15 mol% Na_2O is not included in the composition diagram.

TABLE I. Analyzed chemical compositions, homogenization temperature (T_h), glass transition temperature (T_g), and fraction of tetrahedral to total boron (N_4) of the boroaluminosilicate glasses.

	Compositions (mol%)							
Glass ID	SiO_2	Al_2O_3	B_2O_3	Na_2O	Fining agent	T_h(°C)	T_g[a](K)	N_4(at%)
Al0	80.08	0.16	4.84	14.77	0.15	1450	809	94.9
Al1	79.38	1.16	4.85	14.60	0.14	1450	814	93.2
Al2.5	78.80	2.00	4.70	14.40	0.08	1450	822	94.6
Al5	78.10	4.00	4.20	13.60	0.07	1500	837	91.6
Al7.5	76.90	5.70	4.30	13.00	0.06	1550	851	83.1
Al10	75.90	7.50	4.30	12.30	0.07	1600	871	74.4
Al12.5	72.00	10.40	4.40	13.10	0.07	1650	887	43.6
Al15	69.20	12.70	4.60	13.50	0.07	1650	899	19.9
Al17.5	62.97	17.18	4.99	14.73	0.13	1650	956	1.0
Al20	60.52	19.61	5.00	14.73	0.14	1650	966	0.8

[a]T_g was obtained by fitting viscosity data with MYEGA equation (Ref. 29) and determined as the temperature at which equilibrium viscosity is 10^{12} Pa s.[7] The uncertainty of T_g is approximately ± 5 K. Al0, Al1, Al17.5 and Al20 used SnO_2 as fining agent while the rest of these glasses used As_2O_3 as a fining agent.

glasses, as reported in Table I, were determined by traditional wet chemistry methods.

B. Nuclear magnetic resonance

The annealed glass samples were ground for NMR experiments using an agate mortar and pestle. All NMR experiments were performed on commercial NMR spectrometers (Chemagnetics Infinity, Agilent VNMRS). ^{27}Al NMR experiments were conducted using an 11.7 T wide-bore superconducting magnet (Oxford). The resonance frequency of ^{27}Al at this magnetic field was 130.22 MHz. The ground glass samples were packed into 2.5 mm zirconia rotors having low Al background. Nuclear magnetic resonance spectra were collected using a 2.5 mm double-resonance MAS NMR probe, with spinning speeds of 22 kHz. ^{27}Al MAS NMR spectra were acquired with short radio-frequency pulses of 0.6 μs ($\pi/12$ tip angle) and signal averaging of nominally 1000 scans using a recycle delay of 1 s. ^{27}Al 3QMAS NMR spectra were collected using a hypercomplex 3QMAS pulse sequence with a Z filter.[30] The solid $\pi/2$ and $3\pi/2$ pulse widths were optimized to 0.7 and 2.0 μs, respectively. A lower power $\pi/2$ pulse width of 15.0 μs was used as the soft reading pulse of the Z filter. ^{27}Al 3QMAS NMR data were typically collected using 512 to 1024 acquisitions at each of 48 to 60 t_1 points, with a recycle delay of 0.2 to 0.5 s. The ^{27}Al NMR data were processed with commercial software using minimal line broadening (zero whenever possible) and referenced to aqueous aluminum nitrate at 0.0 ppm.

^{11}B NMR experiments were also conducted using an 11.7 T wide-bore superconducting magnet (Oxford). The resonance frequency of ^{11}B at this magnetic field was 160.34 MHz. The ground glass samples were packed into 3.2 mm zirconia rotors, and the NMR spectra were collected using a 3.2 mm double-resonance MAS NMR probe, with spinning speeds of 20 kHz. Short radio-frequency pulses ($\pi/12$ tip angle) were used for quantitative excitation of MAS NMR spectra. ^{11}B 3QMAS NMR spectra were collected using the same pulse sequence as for ^{27}Al, with solid $\pi/2$ and $3\pi/2$ pulse widths of 1.1 and 2.5 μs, respectively. The soft reading pulse of the Z filter was calibrated to 20.0 μs. ^{11}B 3QMAS NMR data were typically collected using 1024 acquisitions at each of 160 to 256 t_1 points, with a recycle delay of 1 s. The ^{11}B NMR data were processed with commercial software, without apodization and were referenced to aqueous boric acid at 19.6 ppm (relative to the standard BF_3-Et_2O).

^{23}Na NMR experiments were also conducted at 11.7 T (132.19 MHz resonance frequency). The ground glass samples were packed into 3.2 mm zirconia rotors, and the NMR spectra were collected using a 3.2 mm double-resonance MAS NMR probe, with spinning speeds of 20 kHz. Short radio-frequency pulses ($\pi/12$ tip angle) were used for excitation of MAS NMR spectra. 3QMAS NMR of ^{23}Na was also conducted using the Z-filtered hypercomplex pulse sequence described above, with solid $\pi/2$ and $3\pi/2$ pulse widths of 1.2 and 2.8 μs, respectively. The Z filter reading pulse was set to 15.0 μs. ^{23}Na 3QMAS NMR data were collected with signal averaging of 1000 scans at each of 36 t_1 points, all with a recycle delay of 1 s. The ^{23}Na NMR data were processed with minimal line broadening (zero if possible) and referenced to aqueous NaCl at 0.0 ppm.

^{29}Si wide-line (static) and MAS NMR experiments were conducted using a 4.7 T superconducting magnet (39.7 MHz resonance frequency). All experiments made use of a 7.5 mm MAS NMR probe, although samples were held static for the wide-line NMR experiments. The samples were packed into ZrO_2 rotors and MAS NMR data were collected at a spinning rate of 4 KHz, using a short radio-frequency pulse ($\pi/6$) with a long recycle delay (180 s). Signal averaging of $\sim$1000 acquisitions was necessary to obtain ^{29}Si MAS spectra of sufficient quality. All NMR spectra were processed with modest line broadening (50 Hz) and were externally referenced to TMS (0 ppm).

III. RESULTS

A. ^{27}Al NMR

The ^{27}Al MAS NMR spectra of the ten mixed network-former glasses are shown in Fig. 2. These data confirm the strong association between Na^+ and tetrahedral aluminum groups (Al^{IV}). When $[Na_2O] \geqslant [Al_2O_3]$, the spectra all consist of a narrow peak centered at around +50 ppm, consistent with Al^{IV}.[31] The spectra for glasses with $[Na_2O] \geqslant [Al_2O_3]$ are thus all very similar to one another, both in position and shape of the ^{27}Al resonance, which indicates that there is no significant difference in the Al^{IV} environment as a function of glass composition. For the two peraluminous glasses (Al17.5 and Al20), the ^{27}Al MAS NMR spectra are significantly and asymmetrically broader, mainly on the more shielded side (lower shift), which indicates the presence of higher Al coordination.[31] As shown by the overlay in Fig. 3, these two spectra contain different Al species, which can either be

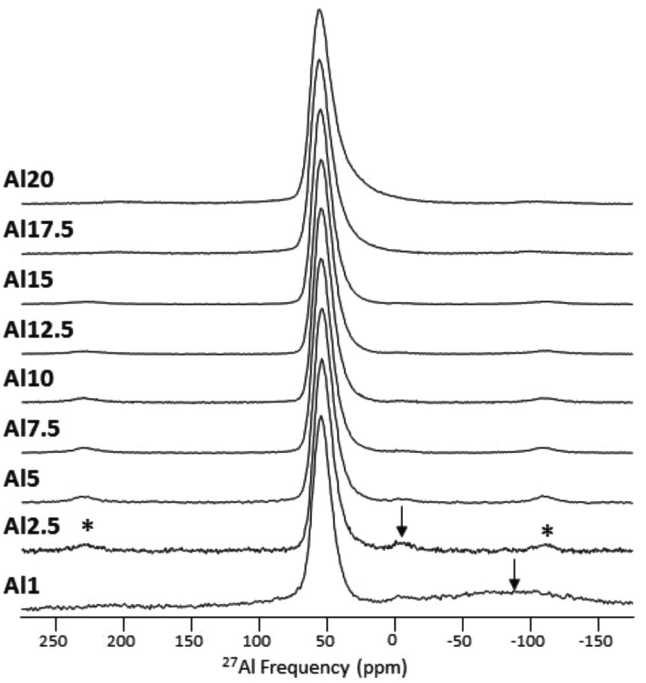

FIG. 2. ^{27}Al MAS NMR spectra of the boroaluminosilicate glasses as described and labeled in Table I. The asterisks mark spinning sidebands, and arrows denote background signal from rotor components, which is only seen at the lowest $[Al_2O_3]$.

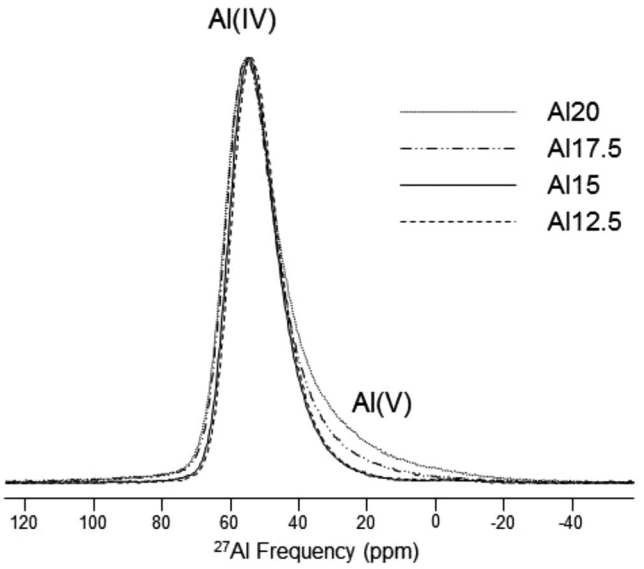

FIG. 3. Overlay of the ^{27}Al MAS NMR spectra from the four glasses containing the highest $[Al_2O_3]$.

spectrally subtracted from one another, or more precisely, simulated to reproduce MAS NMR line shapes for both the Al^{IV} and a second resonance around $+30$ ppm. The latter is consistent with Al^{V} groups.[31]

Two-dimensional ^{27}Al 3QMAS NMR spectra of representative glasses containing low (Al2.5) and high (Al17.5) $[Al_2O_3]$ are shown in Fig. 4. 3QMAS NMR spectroscopy provides higher resolution for quadrupolar nuclei such as ^{27}Al, enabling better resolution of different coordination environments in the isotropic dimension. In the case of the Al2.5 glass, the ^{27}Al 3QMAS NMR spectrum contains only a single set of contours, consistent with the MAS NMR spectra in Figs. 2 and 3, and the presence of only Al^{IV} polyhedra. In contrast, the ^{27}Al 3QMAS NMR spectrum of the Al17.5 glass contains a similar set of contours from a large quantity of Al^{IV} groups, as well as a barely detectable second signal attributed to a small fraction of Al^{V} groups. This is also consistent with the ^{27}Al MAS NMR data where, for $[Al_2O_3] > [Na_2O]$, the glasses appear to contain at least two different Al resonances.

B. ^{11}B NMR

^{11}B MAS NMR spectra of the ten glasses are shown in Fig. 5. These spectra are characterized by a broad peak centered at $+10$ ppm, corresponding to B^{III} sites, and a relatively narrow peak centered around -2 ppm, corresponding to B^{IV} sites. The relative peak intensities vary with composition, as evident in Fig. 5, which reflects changes in the relative proportions of B^{III} and B^{IV}. When $[Al_2O_3] \leqslant [Na_2O]$ (i.e., Al0 through Al15), these MAS NMR spectra show the presence of both B^{III} and B^{IV}. When $[Al_2O_3] > [Na_2O]$, most of the boron atoms exist in trigonal groups, with little evidence for the B^{IV} resonance. The fraction of B^{IV} (N_4) was determined by fitting the ^{11}B MAS NMR spectra in Fig. 5 and is reported in Table I for the entire series of glasses. We find that N_4 decreases with increasing $[Al_2O_3]$.

In addition to the boron coordination changes, the ^{11}B MAS NMR spectra in Fig. 5 reveal changes in the B^{III} NMR line

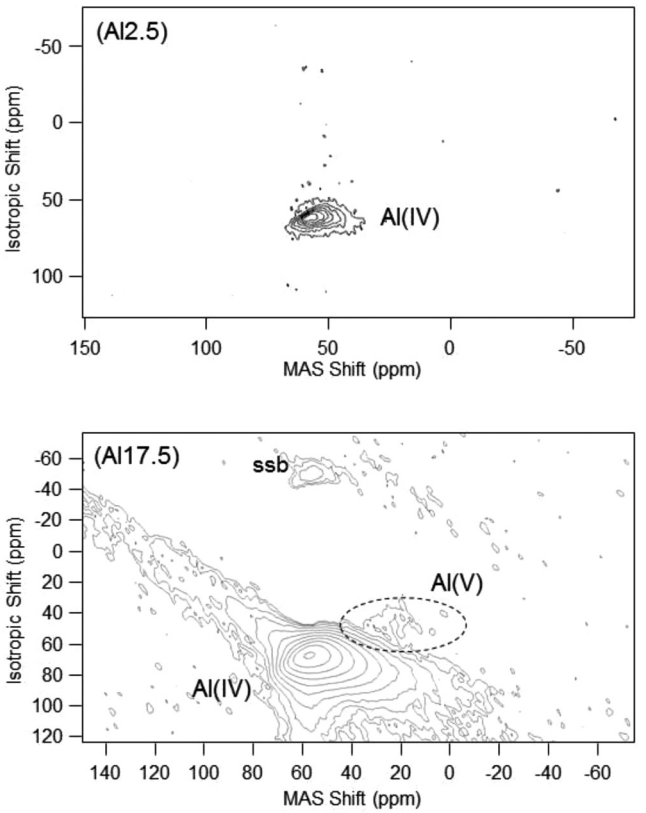

FIG. 4. ^{27}Al 3QMAS NMR spectra of two representative glasses containing low (Al2.5) and high (Al17.5) $[Al_2O_3]$. Contours from different Al coordination environments, as well as spinning sidebands (ssb), are denoted.

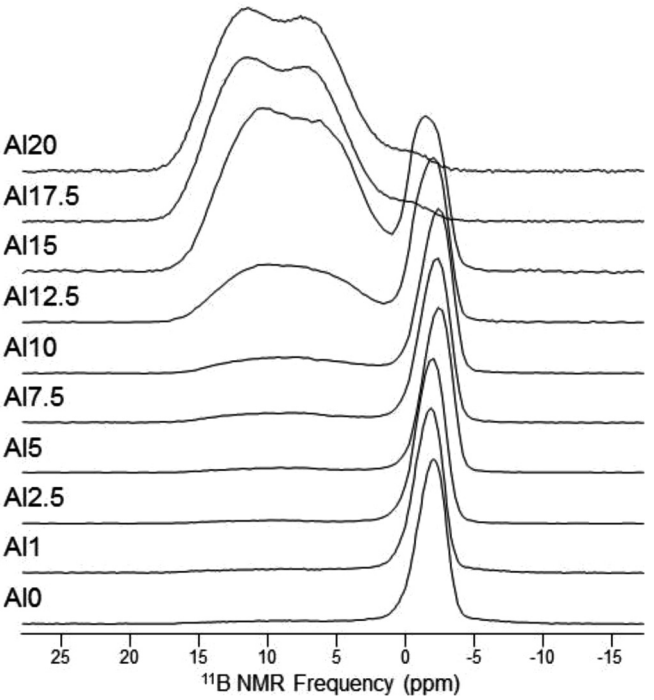

FIG. 5. ^{11}B MAS NMR spectra of the boroaluminosilicate glasses as described and labeled in Table I.

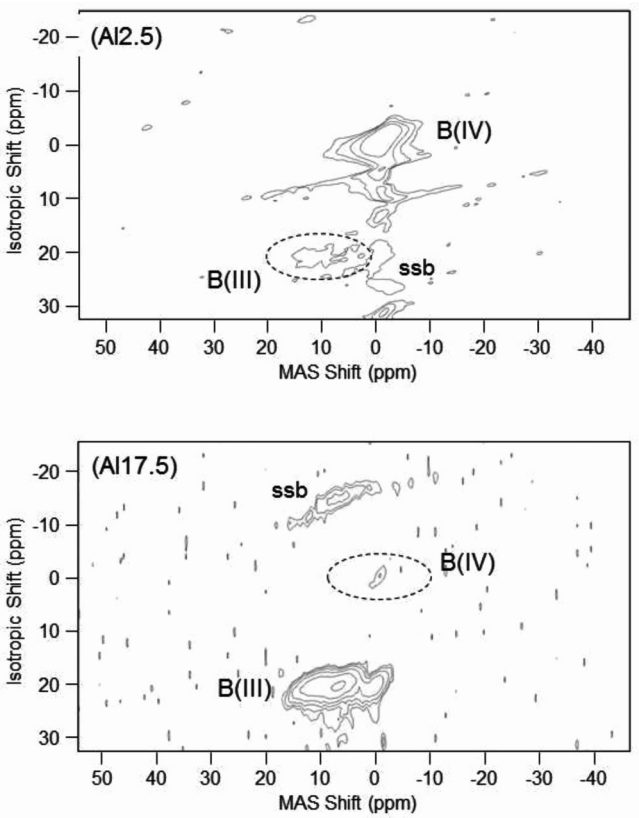

FIG. 6. ^{11}B 3QMAS NMR spectra of two representative glasses containing low (Al2.5) and high (Al17.5) [Al_2O_3]. The two different boron resonances are denoted, along with any spinning sidebands (ssb).

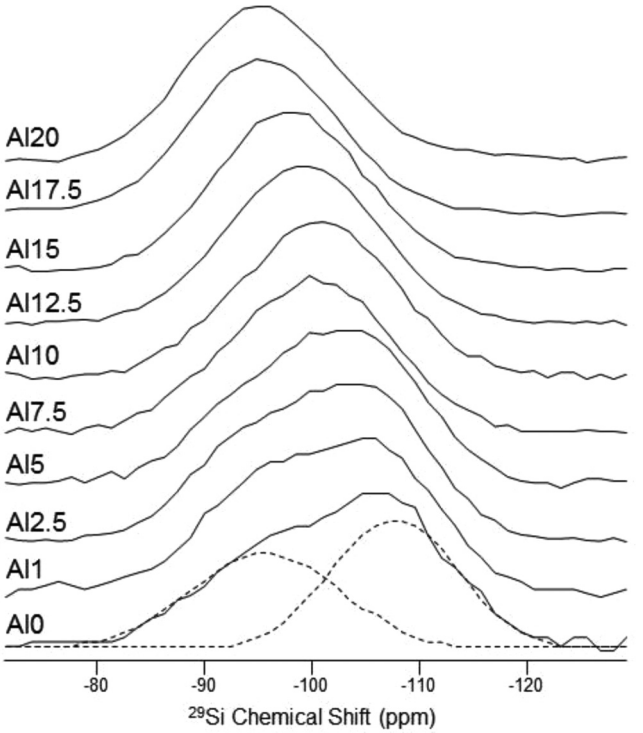

FIG. 7. ^{29}Si MAS NMR spectra of the boroaluminosilicate glasses. The spectra are labeled as in Table I. The spectrum of Al0 includes a Gaussian deconvolution into two distinct resonances (dashed lines).

shape, indicating some impact of glass composition on the short-range structure around trigonal boron. The frequency and line width of the B^{IV} resonances also change with composition, but such changes are not necessarily systematic with glass composition. This could indicate multiple types of B^{IV} sites or changes in local environment due to differing next nearest neighbors or intermediate-range order.

^{11}B 3QMAS NMR spectra of representative glasses containing low (Al2.5) and high (Al17.5) [Al_2O_3] are shown in Fig. 6. These spectra confirm the presence of multiple boron sites (i.e., both B^{III} and B^{IV} sites). More importantly, the data for the high [Al_2O_3] glass contain a small quantity of B^{IV} units, which is not immediately obvious in the ^{11}B MAS NMR spectra in Fig. 5 due to overlapping MAS NMR line shapes.

C. ^{29}Si NMR

^{29}Si MAS NMR spectra of the ten boroaluminosilicate glasses are shown in Fig. 7. There are clear changes in these spectra as a function of glass composition, with a systematic deshielding (to higher chemical shift) of the signal as [Al_2O_3] increases. In addition to this shift, the spectra, particularly at lower values of [Al_2O_3], also appear to be comprised of at least two separate resonances, which can be fit to a sum of Gaussian line shapes, as shown for the Al0 MAS NMR spectrum.

Further details of the silicon speciation, especially with respect to numbers of bridging and nonbridging oxygen, can be obtained by analysis of ^{29}Si wide-line (static) NMR spectral line shapes. This is because symmetry around the silicon atom controls the static NMR powder patterns. Figure 8 shows a stack plot of the ^{29}Si wide-line NMR spectra for the ten glasses, indicating that the overall line shape does change with composition. The spectra for low [Al_2O_3] glasses are highly asymmetric, with a pronounced feature on the deshielded side of the main peak near -100 ppm. As [Al_2O_3] increases, the ^{29}Si wide-line spectrum becomes broader and less asymmetric, reflecting changes in the Si speciation of these glasses, consistent with the ^{29}Si MAS NMR data.

D. ^{23}Na NMR

Figure 9(a) shows the ^{23}Na MAS NMR spectra of the ten glasses. These MAS NMR data show what appears to be a single, asymmetric resonance for all of the glasses. However, the line shape is sensitive to glass composition, with a significant narrowing of the resonance with increasing [Al_2O_3] [Fig. 9(b)]. The ^{23}Na MAS NMR spectra of the high [Al_2O_3] glasses also appear to be considerably less asymmetric than spectra for glasses containing low [Al_2O_3].

Two-dimensional ^{23}Na 3QMAS NMR spectra of representative glasses containing low (Al2.5) and high (Al17.5) [Al_2O_3] are shown in Fig. 10. Both sets of contour plots contain a single sodium resonance, which was also found for the entire series of compositions (data not shown). These data were further analyzed to determine average values of isotropic chemical shift (δ_{CS}) and quadrupolar coupling product (P_Q) for ^{23}Na in all glass samples (Table II).

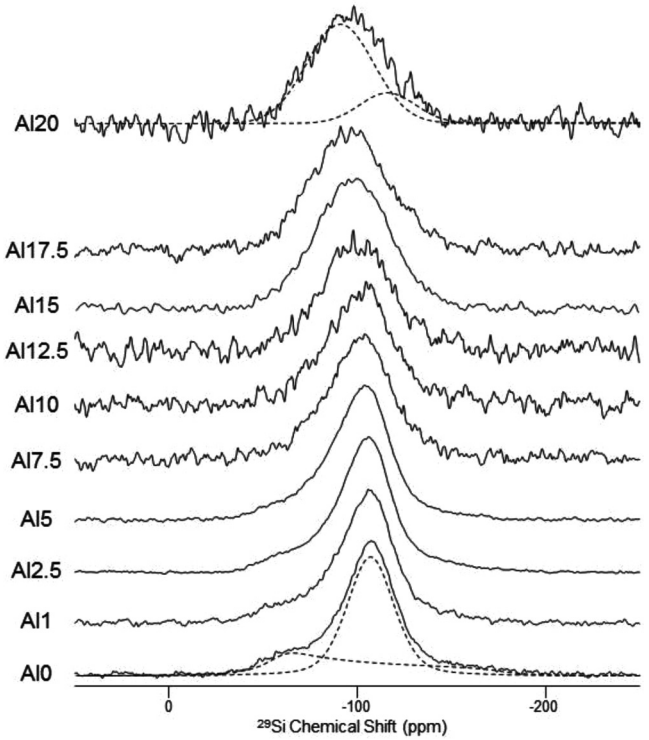

FIG. 8. Wideline ^{29}Si NMR spectra of the boroaluminosilicate glasses. The spectra are labeled using the naming convention in Table I. Dashed lines denote line shape simulations as described in the text.

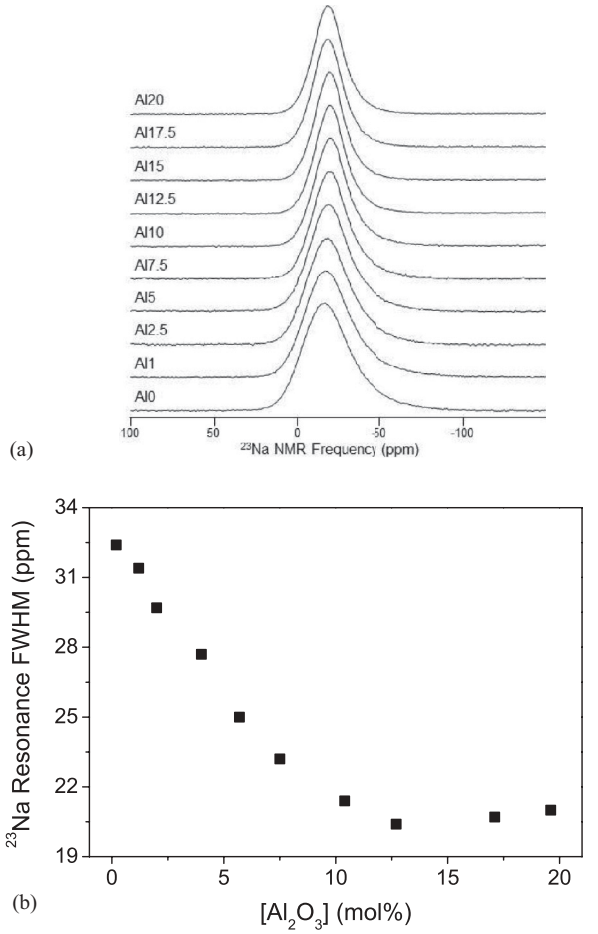

FIG. 9. (a) ^{23}Na MAS NMR spectra of the boroaluminosilicate glasses. The spectra are labeled using the naming convention in Table I. (b) Full width at half maximum (FWHM) of the ^{23}Na resonance as a function of $[Al_2O_3]$.

IV. DISCUSSION

A. Aluminum speciation

The ^{27}Al MAS and 3QMAS NMR results reported here clearly indicate that the aluminum-to-sodium ratio controls Al speciation. For the peralkaline compositions, there is sufficient Na^+ to stabilize all aluminum in fourfold coordination, and thus only a single Al resonance is detected in the ^{27}Al NMR spectra. These Al^{IV} environments are mostly unchanged when altering the amount of Al_2O_3 in the glasses. There are thus only minor changes in NMR parameters, particularly for P_Q, as shown in Table II, which are likely within the error of measurement or potentially a consequence of structural disorder. There is no obvious systematic change in either δ_{CS} or P_Q as a function of composition, which would be consistent with cation ordering around the Al^{IV} tetrahedra as the glass-former ratios are changed (e.g., decreasing Si next nearest neighbor (NNN) with increasing $[Al_2O_3]$).

For the peraluminous compositions, a small fraction of Al^V is detected in both the ^{27}Al MAS and 3QMAS NMR data. This asymmetric broadening of the MAS NMR spectra in Figs. 2 and 3 occurs in the region around $[Na_2O] = [Al_2O_3]$, where the onset of Al^V formation would be expected.[31] Furthermore, a distinct second resonance, which can be assigned to Al^V groups, is detected in the 3QMAS NMR spectra of the two peraluminous glasses (Fig. 4). Based on analysis of the ^{27}Al MAS NMR line shapes for the Al17.5 and Al20 glasses (Fig. 3), we are able to quantify the relative proportions of Al^{IV} and Al^V. We roughly estimate ($\pm$3%) that there exists 10% of the total Al as Al^V in the Al20 glass and 4% of the total Al as Al^V in the Al17.5 glass, both consistent with peraluminous compositions requiring Al^V polyhedra for proper charge balancing.[32] As indicated by the weak peak intensities, the population of Al^V is less obvious in the 3QMAS NMR spectra, similar to other reported data for aluminosilicate glasses.[33] By significantly expanding the vertical scales of these data (Fig. 4) and looking in the noise, we confirm the presence of Al^V and are therefore confident that the changing ^{27}Al MAS NMR line shapes are a result of increasing Al^V concentration when $[Al_2O_3] > [Na_2O]$.

This fivefold coordination environment around Al is expected for such compositions, where the amount of charge-balancing modifier cations (Na^+) is insufficient to stabilize all Al in fourfold coordination. As a consequence, some higher coordination Al species are formed and believed to provide an additional source of charge compensation in these networks.[31,32] Binary SiO_2-Al_2O_3 glasses with $[Al_2O_3] > 1$ wt% contain a mixture of Al^{IV}, Al^V, and Al^{VI} species.[31,32] The relative proportions of these species depend strongly on composition, and the high-coordinated Al species serve as charge compensators of tetrahedral Al^{IV} species. However, the addition of alkalis to these binary glasses results in the rapid disappearance of Al^V and Al^{VI} and stabilization of

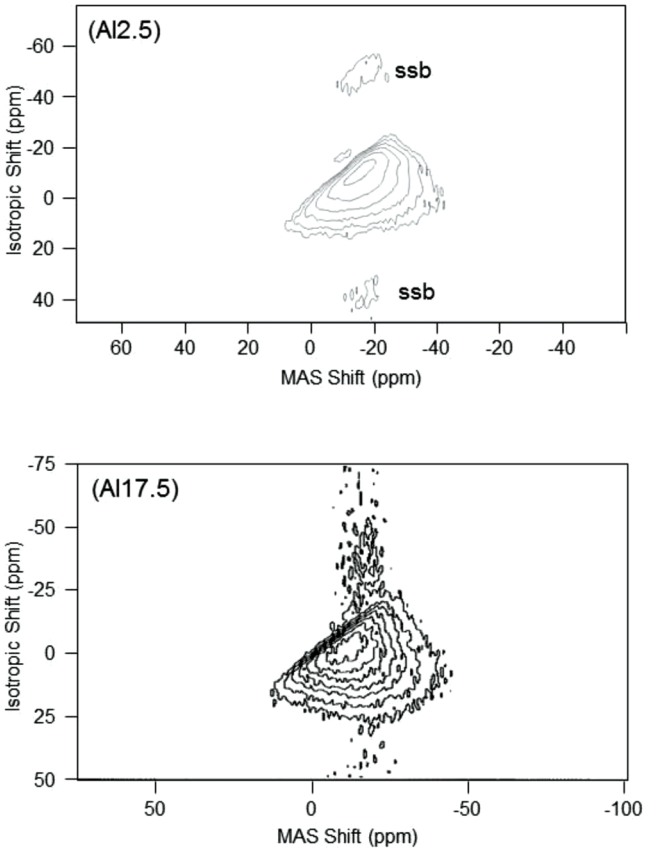

FIG. 10. ^{23}Na 3QMAS NMR spectra of two representative glasses containing low (Al2.5) and high (Al17.5) [Al_2O_3].

Al^{IV}.[32] A careful analysis of the high [Al_2O_3] glasses in the present study (Al17.5 and Al20) using both ^{27}Al MAS and 3QMAS NMR spectroscopy shows that only Al^{IV} and Al^{V} polyhedra are present, indicating that the amount of excess Al_2O_3 (i.e., [Al_2O_3] − [Na_2O]) is small and does not lead to the formation of Al^{VI} groups. These results confirm that we can confidently use the difference ([Na_2O] − [Al_2O_3]) to calculate an effective modifier concentration in a pseudoternary sodium borosilicate glass. The Al speciation is completely controlled by the sodium-to-aluminum ratio, viz., for [Al_2O_3] < [Na_2O], we can simply subtract [Al_2O_3] from [Na_2O] to get the amount of modifier left to act in other roles, including stabilization of B^{IV} and creation of NBOs, as discussed later. Similarly, the two glasses for which [Al_2O_3] > [Na_2O] appear to consume all Na^+ in charge-balancing Al tetrahedra, with a small fraction of Al^{V} to account for the insufficient amount of sodium, and more importantly, no modifier available for acting in other charge-balancing roles.

B. Boron speciation

Evidence for the above-mentioned behavior is also found in the ^{11}B MAS NMR spectra (Fig. 5), which show a large variation of boron speciation as a function of composition. At low [Al_2O_3], where there is a substantial excess of Na^+, the boron atoms are found to be predominantly in fourfold coordination, as evidenced by the very intense and narrow ^{11}B NMR resonance near −2 ppm in Fig. 5. With increasing [Al_2O_3], this peak remains the most intense spectral feature for most of the glasses, until the Al12.5 composition, where the intensity of the broad, asymmetric resonance centered around 10 ppm increases substantially. The latter feature is indicative of B^{III}, the relative population of which is sensitive to [Al_2O_3]. In the ^{11}B MAS NMR spectra, it reflects second-order quadrupolar line broadening due to lower symmetry around the B^{III} triangles than is found for the nearly symmetric B^{IV} units. The significant line shape differences for B^{III} triangles and B^{IV} tetrahedra are consistent with previous studies of boron coordination in simple modified borate glasses.[17,34] Such differences in line shape, especially when measured at sufficiently high magnetic fields to obtain separation of the two peaks, allow accurate quantification of the boron coordination and ultimately the fraction of B^{IV} (N_4). Here, N_4 was determined for all of the glasses by fitting the ^{11}B MAS NMR spectra to a series of three- and fourfold coordinated line shapes, the results of which are given in Table I. These data clearly show that N_4 is controlled by the excess modifier content of the glasses. Hence, for low [Al_2O_3], there is a significant amount of sodium available to convert boron from B^{III} to B^{IV}. As [Al_2O_3] increases and the effective modifier content decreases, N_4 decreases.

In the two glasses with the highest [Al_2O_3], where ^{27}Al NMR indicated all Na^+ is used for charge-balancing Al^{IV} groups, a very small fraction of B^{IV} is detected ($\leqslant$1%). These nonzero values of N_4 are determined from fitting the overlapping resonances in the ^{11}B MAS NMR spectra, which likely has some associated uncertainty. However, we have directly detected B^{IV} groups in the ^{11}B 3QMAS NMR spectra, where a weak but clearly present peak is found for B^{IV} groups in the Al17.5 glass (Fig. 6). Similar evidence for a small fraction of B^{IV} units in the Al20 glass was also obtained (data not shown), indicating that even for peraluminous compositions, a minor degree of network modification beyond Al^{IV} group stabilization occurs. This implies that, in the peraluminous regime, there is a competition for Na^+ between charge compensating Al^{IV} and B^{IV}. However, the formation of Al^{IV} is strongly favored over that of B^{IV}, since only minor concentrations of B^{IV} exist. In the peralkaline regime, Na^+ will first charge compensate all Al as Al^{IV}, and there is no competition for Na^+ between charge compensating Al^{IV} and B^{IV}, as confirmed by only Al^{IV} groups in the ^{27}Al NMR data.

In sodium borosilicates, the Dell and Bray model[21–23] is a frequently used empirical model to predict the composition dependence of N_4. It should be mentioned that [Al_2O_3] is not involved in the Dell and Bray model. In order to apply this model to the boroaluminosilicate glasses, we have taken [Na_2O] − [Al_2O_3] as the effective modifier concentration and have not considered the effect of aluminum speciation on the network connectivity. According to the Yun and Bray invocation of this model,[22] $N_4 = ([Na_2O] - [Al_2O_3])/[B_2O_3]$ when [Na_2O] − [Al_2O_3] < [B_2O_3] and $N_4 = 1$ when [Na_2O] − [Al_2O_3] > [B_2O_3] for our glasses ($SiO_2/B_2O_3 \geqslant 8$). The composition dependence of the N_4 values predicted from this model is plotted in Fig. 11. We note that these N_4 values are excessively high compared to the experimental values from the present study.

According to Du and Stebbins,[13] the experimental deviation of N_4 from the Dell and Bray model could be due to the energy

TABLE II. Isotropic chemical shift (δ_{CS}) and quadrupolar coupling parameters for ^{27}Al, ^{11}B and ^{23}Na using MAS and 3QMAS NMR data. The quadrupolar coupling product ($P_Q = C_Q(1 + \eta^2/3)^{1/2}$) was determined from 3QMAS NMR spectra of ^{27}Al and ^{23}Na as described in the text. Missing values for the Al0 glass are due to lack of ^{27}Al 3QMAS NMR data for this glass. Fitting of ^{11}B MAS NMR spectra (Ref. 45) provided further delineation between C_Q (quadrupolar coupling constant) and η (asymmetry parameter).

			^{11}B MAS NMR					
	^{27}Al 3QMAS NMR[a]		δ_{CS} (ppm)				^{23}Na 3QMAS NMR	
Glass ID	δ_{CS} (ppm)	P_Q (MHz)	[BO_3]	[BO_4]	C_Q (MHz)[b]	η[b]	δ_{CS} (ppm)	P_Q (MHz)
Al0			16.8	−1.1 −2.1	2.55	0.52	−3	3.5
Al1	61	4.2	16.9	−0.8 −1.9	2.55	0.53	−3	3.6
Al2.5	59	3.7	16.4	−1.1 −2.2	2.44	0.57	−5	2.4
Al5	59	4.1	16.7	−0.8 −1.9	2.52	0.57	−7	2.5
Al7.5	60	3.9	16.7	−0.5 −1.8	2.58	0.49	−9	2.3
Al10	60	3.9	16.4	−0.4 −2	2.62	0.48	−10	2.2
Al12.5	60	3.7	16.4	−0.4 −1.7	2.67	0.42	−12	2.1
Al15	61	4.0	16.2	−0.3 −1.8	2.67	0.38	−11	2.1
Al17.5	62	4.2	16 18.4	−0.5	2.63 2.75	0.22 0.22	−11	2.5
Al20	63	4.2	14 17	−0.5	2.59 2.67	0.25 0.31	−11	2.3

[a]NMR parameters were determined for only Al^{IV} groups using ^{27}Al 3QMAS NMR data.
[b]Quadrupolar coupling parameters for ^{11}B were only determined for the B^{III} sites, as C_Q and η for the tetrahedral B^{IV} units are small and therefore not included in the MAS NMR line shape simulations.

penalty from the mixing of B^{IV} and Al^{IV} groups, i.e., with the presence of negatively charged Al^{IV} groups, the formation of B^{IV} units is energetically unfavorable. For boroaluminosilicate glasses, Du and Stebbins[13] have developed a modified Dell–Bray model. This model groups Al and B as a single type of cation based on the consideration that the mixing behavior for Al^{IV} is similar to that of B^{IV} and the variation of N_4 is related to avoidance among B^{IV} and Al^{IV} species. Predicted values of N_4 for our glasses using this model are also plotted in Fig. 11. We find a certain degree of discrepancy between the Du–Stebbins model and our experimental results. The discrepancy could be attributed to the assumption that the mixing behavior for Al^{IV} is similar to that of B^{IV}. However, according to Du and Stebbins,[13] their model is not expected to accurately predict the N_4 of the glass system with the composition range of Al ≫ B. This is exactly the range where the discrepancy between the predicted and experimental N_4 values appears (Fig. 11). In spite of this apparent discrepancy, the Du–Stebbins model provides a good prediction of the N_4 variation with composition for the glasses studied in the present work.

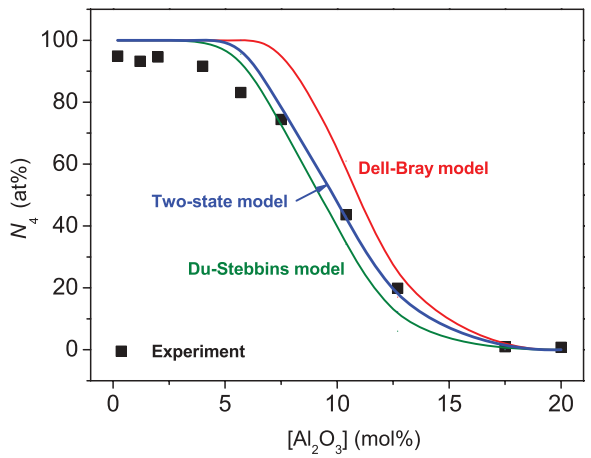

FIG. 11. (Color online) Comparison of the N_4 data obtained from NMR and three different models. The errors of the experimental N_4 values (±0.2%) are smaller than the size of the symbols.

C. Nonbridging oxygen formation

For both the Dell–Bray and Du–Stebbins models, N_4 values are overpredicted at low [Al_2O_3]. This suggests that, after charge compensating Al^{IV}, not all of the excess Na^+ ions are used in converting B^{III} to B^{IV}. Instead, some of the excess modifier is available for other types of network modification, in particular, formation of NBOs. It is well known that excess modifier can lead to formation of NBO on both boron and silicon.[35,36] In alkali borosilicates, this is apparent in the maximum value of N_4 for various compositions, at which point additional modifier is used to create NBO rather than

B^{IV}. Hence, the maximum value of N_4 is not 100%, similar to what we have observed for the low-Al_2O_3 glasses in this study.

The ^{11}B NMR spectra in Fig. 5 contain some evidence for NBO formation on B^{III}. However, due to the low fraction of B^{III} for glasses with alumina content smaller than that of Al10, such effects are difficult to identify. Vertical expansion of these spectra (not shown) indicates that the B^{III} line shape is changing with glass composition. For example, comparing the data for Al12.5 and Al20 reveals that the B^{III} line shape is noticeably different for different [Al_2O_3]. Simulations of the ^{11}B MAS NMR spectra, especially the resonances from B^{III}, confirm the presence of multiple environments, which differ in terms of the quadrupolar asymmetry parameter η. This parameter is shown in Table II for all B^{III} sites in these glasses. We find that it systematically changes with [Al_2O_3]. At high [Al_2O_3], where most of the sodium is used for stabilizing Al^{IV}, the value of η is relatively low (0.2 to 0.4). As the amount of excess modifier increases, the B^{III} asymmetry parameter also increases, reaching values as high as 0.57 for some of the low [Al_2O_3] compositions. Such values of η are typical of B^{III} having an asymmetric distribution of bridging and NBO, as would be the case for B^{III} units with one or two NBO.[23] Essentially, the ^{11}B MAS NMR line shape for B^{III} is changing from one comprised of all symmetric B^{III} units to one with at least some fraction of B^{III} with NBO. Thus, for glasses where the effective modifier concentration is nonzero and likely greater than ∼2 mol%, we detect formation of NBO on B^{III} atoms.

The ^{11}B 3QMAS NMR spectra appear to contain only a single B^{III} resonance, with the exception of the Al17.5 and Al20 glasses. This likely reflects a distribution of environments with average values of η higher than those in glasses having only symmetric B^{III} units, as discussed above for spectral simulation of the ^{11}B MAS NMR spectra. The inability to resolve distinct symmetric and asymmetric B^{III} line shapes in the 3QMAS NMR spectra (Fig. 6), makes accurate quantification of NBO on boron difficult, but nonetheless the presence of such units confirms the activity of excess effective modifier in peralkaline glasses. There are two glasses in which multiple B^{III} resonances were distinctly resolved in the ^{11}B 3QMAS NMR spectra: Al17.5 and Al20. These glasses are both peraluminous and already shown to contain almost exclusively B^{III}, and they appear to contain two symmetric (low η) B^{III} sites, reminiscent of ring and nonring B^{III} units in v-B_2O_3 and slightly modified borate glasses.[37,38] The isotropic chemical shifts for these resonances (Table II) are also consistent with symmetric B^{III} units in different superstructural or intermediate-range order environments.

In addition to changes in boron speciation, including both N_4 and NBO formation, the excess modifier in the peralkaline compositions can also impact the speciation of silicon. Nonbridging oxygen formation on Si, resulting in $Q^{n\neq4}$ [n is the number of bridging oxygens (BOs) per tetrahedral silicon], e.g., Q^3, Q^2 and other Si tetrahedra, is well known in alkali silicates and aluminosilicates.[39,40] One might expect similar behavior in the glasses studied here, in particular for those having the highest excess modifier concentrations. Therefore, ^{29}Si NMR data were collected to ascertain the Si speciation as a function of glass composition. ^{29}Si MAS NMR spectra show evolution of the signal with increasing [Al_2O_3] (Fig. 7). The nominally Al-free glass (Al0) contains two fairly well-resolved ^{29}Si resonances centered at approximately −96 and −108 ppm. In Al-free glasses, these peaks correspond well to Q^3 and Q^4 sites, respectively,[41,42] suggesting that the Al0 glass contains a moderate quantity of NBO on Si (e.g., Q^3 sites). The other glasses in this study contain nonnegligible concentrations of Al, and the presence of Al polyhedra as NNN to Si tetrahedra substantially complicates the interpretation and quantification of ^{29}Si MAS NMR spectra.[43,44] It is thus mostly due to increasing [Al_2O_3] that the peaks in the MAS NMR spectra in Fig. 7 move to less negative chemical shifts, since increasing Al NNN has this direct impact on Q^n chemical shifts. Notwithstanding this limitation, it does appear evident from the evolution in the ^{29}Si MAS NMR data that the spectra are simplified with increasing [Al_2O_3]. For glasses at the highest [Al_2O_3], the ^{29}Si line shape is much more symmetric and likely reflects fewer distinct Si species. This of course is expected based on the availability of modifier in these glasses, i.e., higher [Al_2O_3] reduces the amount of effective modifier available for NBO formation on Si, eventually eliminating any possibility for non-Q^4 groups.

D. Structural modeling

To further identify and estimate the NBO concentration on Si tetrahedra, static or wide-line ^{29}Si NMR measurements were conducted. As shown in Fig. 8, there is again a gradual change in the ^{29}Si spectra with glass composition, signifying some type of evolution in Si speciation. We first fit the Al1 spectrum using parameters which gave a reasonable fit and then froze those parameters (mainly line broadening and chemical shift anisotropy terms) in all subsequent fits. These wide-line ^{29}Si NMR spectra were fit with DMFit[45] and provided quantitative estimates for the relative amounts of Q^3 and Q^4 along the entire series of glasses (Table III). As with the ^{29}Si MAS NMR data, the Q^3 concentration drops steadily with increasing [Al_2O_3]. For [Al_2O_3] $\geqslant$ ∼12 mol%, the Q^3 fraction and thus the NBO on Si content goes to zero. For [Al_2O_3] above this level, the glasses apparently have insufficient modifier to stabilize Al^{IV} and B^{IV} groups, as well as formation of NBO on Si. In spite of the complications in accurately determining Q^3 populations in these glasses, due both to Al NNN complications and poor signal to noise, the ^{29}Si NMR data do show conclusively the presence and compositional dependence of NBO on Si tetrahedra, further demonstrating the many different modifier roles of Na in these glasses. The various NMR data indicate that after charge compensating Al^{IV}, not all of the excess Na_2O is used for converting B^{III} to B^{IV}. Instead some of the Na^+ ions are used to create NBO on both Si and B. There is a competition between converting B^{III} to B^{IV} and creating NBO. In order to quantify this effect, we next consider the two-state statistical mechanical model of boron speciation, which originally was developed for borosilicate glasses.[28]

According to the two-state model, the free energy associated with NBO formation on Si^{IV} takes an intermediate value compared to those of the B^{III} to B^{IV} conversion and NBO-on-B^{III} formation,[28,46–48] and this value appears close to the energy associated with B^{III} to B^{IV} conversion. We define

TABLE III. Q^n units calculated by the random model and measured by NMR for the boroaluminosilicate glasses as described and labeled in Table I. $Q^{3\prime}$ is estimated for comparison to the NMR results by assuming $Q^2 = 2Q^3$ and ignoring the minor contributions from Q^1 in the random model.

	Random model						
Glass ID	Q^4 (%)	Q^3 (%)	Q^2 (%)	Q^1 (%)	Q^0 (%)	$Q^{3\prime}$ (%)	NMR Q^3 (%)
Al0	77.28	20.57	2.05	0.09	0.00	24.68	33
Al1	79.41	18.85	1.68	0.07	0.00	22.20	24
Al2.5	81.33	17.25	1.37	0.05	0.00	19.99	18
Al5	86.11	13.12	0.75	0.02	0.00	14.62	12
Al7.5	90.72	8.95	0.33	0.01	0.00	9.61	5
Al10	95.89	4.04	0.06	0.00	0.00	4.17	2
Al12.5	97.90	2.08	0.02	0.00	0.00	2.12	0
Al15	100	0	0	0	0	0	0
Al17.5	100	0	0	0	0	0	0
Al20	100	0	0	0	0	0	0

ΔH as the enthalpy difference between NBO formation and B^{III} to B^{IV} conversion. Whether the modifiers are used for B^{III} to B^{IV} conversion or NBO-on-Si^{IV} formation is determined by the enthalpy difference between the two states (ΔH) and the number of available boron vs silicon sites (i.e., an entropic effect governed by the fictive temperature T_f and $[SiO_2]$ vs $[B_2O_3]$).

Since we have confirmed that all aluminum is in fourfold coordination when $[Na_2O] > [Al_2O_3]$, we can safely use $[Na_2O] - [Al_2O_3]$ to calculate the effective modifier concentration. When $[Na_2O] < [Al_2O_3]$, we state that $N_4 = 0$, which is close to the values determined from ^{11}B NMR. When $[Na_2O] > [Al_2O_3]$, N_4 can be calculated as

$$N_4 = \frac{[Na_2O] - [Al_2O_3]}{[B_2O_3] + [SiO_2]\exp[-\Delta H/kT_f]}, \quad (1)$$

where k is Boltzmann's constant. The fictive temperature T_f is taken as equal to the glass transition temperature (cooled at 10 K/s), i.e., $T_f = T_g$.[49] If ΔH is large, the modifiers are more likely to be used for charge-balancing B^{IV}, so N_4 will be large. With higher fictive temperatures and high SiO_2 concentrations, N_4 attains a lower value due to the effect of entropy. Using the experimentally determined values of $T_g = T_f$ listed in Table I, we obtain good agreement between the two-state model and the NMR results (Fig. 11) taking $\Delta H = 0.28$ eV as the sole fitting parameter. During the fit of ΔH, N_4 is constrained to be in the range of $0 \sim 1$. The uncertainty of ΔH is ± 0.01 eV. As shown in Fig. 11, the Dell–Bray model overpredicts N_4 and the Du–Stebbins model underpredicts N_4. The two-state model gives the best agreement with NMR data among these models. It should be noted that the two-state model has its limitations. First, the fictive temperature effect on N_4 applies only to silicate and boroaluminosilicate glasses, and this is seen from Eq. (1). For borate glasses, the effect of fictive temperature on N_4 also exists, but it is not considered in this model. Second, N_4 is predicted to increase monotonically with Na_2O content. Despite these limitations, the two-state model gives a relatively accurate description of the boron speciation for the glass compositions studied in the present work.

The random model, which is used to describe the distribution of Q^n units in silicate glasses, assumes a statistical distribution of Q^n units for discrete values of n between 0 and 4. Here, we apply this model to the boroaluminosilicate glasses. Following this model,[50–52] we first calculate the probability (p) that a randomly chosen Si-O bond includes a NBO. It is equal to the ratio between the number of NBOs and the total number of bonds [NBO] + [BO], where BO is a bridging oxygen. For silicate glasses, $p = \mathrm{NBO}/(Z[Si^{IV}])$, where Z is the coordination number of the network former. For our aluminoborosilicate glasses, $p = \mathrm{NBO}/(4[Si^{IV}] + 3[B^{III}])$, since NBOs exist both on Si^{IV} and B^{III}, i.e., the existence of B^{III} lowers the probability for a NBO to be associated with Si. Since addition of sodium to boroaluminosilicate glasses results in the formation of Al^{IV}, B^{IV}, and/or NBO, the concentration of NBOs can be calculated as $2([Na_2O] - [Al^{IV}] - [B^{IV}])$. By using

$$Q^n = \frac{4!}{n!(4-n)!}(1-p)^n p^{4-n}, \quad (2)$$

the Q^n values are calculated and listed in Table III. In order to compare the calculated values of Q^n to the Q^3 and Q^4 values obtained from NMR, one Q^2 unit was counted as two Q^3 units and Q^1 and Q^0 units were ignored, since their concentrations are predicted to be less than 1%. Figure 12 shows that Q^3 calculated by the random model agrees well with that measured by NMR, viz., Q^3 decreases as $[Al_2O_3]$ increases. The discrepancy at Al0, which is the data point having the most accuracy, indicates that the random model does not work well for all glasses in this series. Without Al_2O_3 in the glass, all of the Na^+ is being consumed by B^{IV} and NBO, the latter of which is essentially all on Si as determined by both ^{11}B and ^{29}Si NMR. This situation, which is perhaps unique to this particular glass composition, is reflected in the higher Q^3 population of Fig. 12.

E. Structural role of sodium

The local Na^+ environment is significantly impacted by $[Al_2O_3]$. The broad ^{23}Na MAS line shapes at low $[Al_2O_3]$ suggest multiple or at least a large distribution of sodium environments (Fig. 9). They are likely from Na^+ as a charge-balancing cation for B^{IV}, NBO on boron and/or silicon, as well as a small fraction of Al^{IV}. The ^{23}Na MAS line shapes

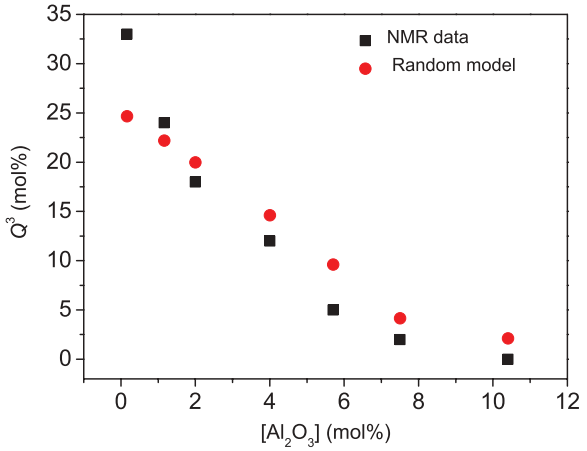

FIG. 12. (Color online) Comparison of Q^3 data calculated by the random model and measured by NMR of the boroaluminosilicate glasses as described and labeled in Table I. The error range of the NMR data is $\pm 5\%$.

narrow considerably at higher $[Al_2O_3]$, suggesting a more uniform environment (and role) of Na^+ ions, i.e., they are mostly used to charge balance Al^{IV} at the higher $[Al_2O_3]$. The ^{23}Na 3QMAS NMR spectra confirm changes in the ^{23}Na resonance with increasing $[Al_2O_3]$, as well as the fact that only one distinct sodium environment is resolved for all of the glasses. Both δ_{CS} and P_Q of ^{23}Na vary for these glasses as a function of composition, with an initial decrease in δ_{CS} with increasing $[Al_2O_3]$, until at $[Al_2O_3] \sim 10$ mol%, where the ^{23}Na chemical shift levels at a value of -10 to -12 ppm. The initial decrease in chemical shift correlates very well with the increasing amount of Al^{IV} groups that require Na cations for charge compensation. These Al^{IV} groups, as well as B^{IV} groups, are negatively charged polyhedra which do not possess NBO atoms.

It has been reported that, in glasses where Na is the only non-network forming cation, δ_{CS} for ^{23}Na increases systematically with increasing $[Na_2O]$, in part because of increasing fraction of NBO in the average Na coordination shells and the accompanying shortening of mean Na-O distances.[14,26,53] In our glass systems, δ_{CS} decreases with an increase in $[Al_2O_3]$, indicating that the NBO content is decreasing as well. This agrees well with our direct determination of NBO content, where both ^{11}B and ^{29}Si NMR spectra show a decrease in the NBO content with increasing $[Al_2O_3]$. As $[Al_2O_3]$ increases, more Na^+ ions are required for stabilizing Al^{IV} groups until this is essentially the only environment for Na, i.e., an environment without any NBO in the local coordination environment. Similarly, we find a marked decrease in P_Q with increasing $[Al_2O_3]$, consistent with a more uniform coordination environment as well as an increase in the average coordination number of Na.[14,26,53] Both observations reflect changes from multiple Na sites (i.e., structural roles) to a relatively uniform distribution of Na^+ in Al^{IV} charge-balancing positions, and the increase in Na coordination number simply reflects fewer NBO in its coordination sphere as these species diminish with increasing $[Al_2O_3]$. Finally, it should be mentioned that the change in the Na environment with composition is a continuous variation in the types and numbers of different kinds of oxygen, e.g., NBO vs various BO (connected to Si or B or Al) in the average Na coordination shell. This aspect will be closely studied in our future work.

V. SUMMARY

We have studied the structure of ten Na_2O-B_2O_3-Al_2O_3-SiO_2 glasses with varying $[Al_2O_3]/[SiO_2]$ ratio to access different regimes of sodium behavior. The network speciation and modifier cation environments have been characterized as a function of composition using multinuclear NMR spectroscopy. Based on these NMR results, the different roles of sodium with respect to the network-forming cations (Si, B, and Al) have been clarified and quantified. We confirm that when $[Na_2O] < [Al_2O_3]$, almost all sodium is used to charge compensate Al^{IV}; however, there are also Al^V species which act as charge compensators due to insufficient sodium. When $[Na_2O] > [Al_2O_3]$, sodium first charge compensates Al^{IV}, i.e., all aluminum is fourfold coordinated, and there is no compositional dependence of the aluminum speciation. After charge compensating Al^{IV}, not all of the excess Na^+ ions are used for converting B^{III} to B^{IV}, since some are used to create NBOs on both Si and B. This indicates a competition in the boroaluminosilicate glasses between B^{III} to B^{IV} conversion and NBO formation. Consequently, we have found that the Dell–Bray and Du–Stebbins models do not fully predict values of N_4 determined experimentally, since both models do not account for such competition. To account for this competition, we have extended our two-state statistical mechanical model of boron speciation developed for borosilicate glasses to boroaluminosilicate glasses. By doing so, we have obtained better agreement between the predicted and measured values of N_4. Furthermore, the composition dependence of Q^3 has been described by using a random model that agrees well with the experimental values obtained from ^{29}Si wide-line NMR spectroscopy.

ACKNOWLEDGMENTS

The authors would like to thank Adam Ellison (Corning Incorporated) for valuable discussion on glass composition and characterization approaches.

*Corresponding author: youngmanre@corning.com

[1] S. K. Lee, G. D. Cody, Y. W. Fei, and B. O. Mysen, Chem. Geol. **229**, 162 (2006).
[2] G. Yang, B. Bureau, T. Rouxel, Y. Gueguen, O. Gulbiten, C. Roiland, E. Soignard, J. L. Yarger, J. Troles, J. C. Sangleboeuf, and P. Lucas, Phys. Rev. B **82**, 195206 (2010).
[3] G. N. Greaves, J. Non-Cryst. Solids **71**, 203 (1985).
[4] M. Hanaya and R. K. Harris, J. Phys. Chem. A **101**, 6903 (1997).
[5] J. F. Stebbins and Z. Xu, Nature **390**, 60 (1997).
[6] M. Bauchy, M. Micoulaut, M. Celino, S. Le Roux, M. Boero, and C. Massobrio, Phys. Rev. B **84**, 054201 (2011).

[7]Q. J. Zheng, M. Potuzak, J. C. Mauro, M. M. Smedskjaer, R. E. Youngman, and Y. Z. Yue, J. Non-Cryst. Solids **358**, 993 (2012).
[8]F. Angeli, O. Villain, S. Schuller, T. Charpentier, D. de Ligny, L. Bressel, and L. Wondraczek, Phys. Rev. B **85**, 054110 (2012).
[9]S. Sen, T. Topping, P. Yu, and R. E. Youngman, Phys. Rev. B **75**, 094203 (2007).
[10]N. Ollier, T. Charpentier, B. Boizot, and G. Petite, J. Phys.: Condens. Matter **16**, 7625 (2004).
[11]F. Angeli, T. Charpentier, S. Gin, and J. C. Petit, Chem. Phys. Lett. **341**, 23 (2001).
[12]J. M. Egan and K. T. Mueller, J. Phys. Chem. B **104**, 9580 (2000).
[13]L. S. Du and J. F. Stebbins, J. Non-Cryst. Solids **351**, 3508 (2005).
[14]J. S. Wu and J. F. Stebbins, J. Non-Cryst. Solids **355**, 556 (2009).
[15]J. S. Wu and J. F. Stebbins, J. Non-Cryst. Solids **356**, 2097 (2010).
[16]L. S. Du and J. F. Stebbins, J. Non-Cryst. Solids **315**, 239 (2003).
[17]R. E. Youngman and J. W. Zwanziger, J. Phys. Chem. **100**, 16720 (1996).
[18]F. Angeli, T. Charpentier, D. D. Ligny, and C. Cailleteau, J. Am. Ceram. Soc. **93**, 2693 (2010).
[19]M. M. Smedskjaer, J. C. Mauro, S. Sen, and Y. Z. Yue, Chem. Mater. **22**, 5358 (2010).
[20]A. Vegiri, C. P. E. Varsamis, and E. I. Kamitsos, Phys. Rev. B **80**, 184202 (2009).
[21]W. J. Dell, P. J. Bray, and S. Z. Xiao, J. Non-Cryst. Solids **58**, 1 (1983).
[22]Y. H. Yun and P. J. Bray, J. Non-Cryst. Solids **27**, 363 (1978).
[23]J. H. Zhong and P. J. Bray, J. Non-Cryst. Solids **111**, 67 (1989).
[24]H. Yamashita, H. Yoshino, K. Nagata, H. Inoue, T. Nakajin, and T. Maekawa, J. Non-Cryst. Solids **270**, 48 (2000).
[25]H. Yamashita, K. Inoue, T. Nakajin, H. Inoue, and T. Maekawa, J. Non-Cryst. Solids **331**, 128 (2003).
[26]J. F. Stebbins, Solid State Ionics **112**, 137 (1998).
[27]S. K. Lee and J. F. Stebbins, Geochim. Cosmochim. Acta **67**, 1699 (2003).
[28]M. M. Smedskjaer, J. C. Mauro, R. E. Youngman, C. L. Hogue, M. Potuzak, and Y. Z. Yue, J. Phys. Chem. B **115**, 12930 (2011).
[29]J. C. Mauro, Y. Z. Yue, A. J. Ellison, P. K. Gupta, and D. C. Allan, Proc. Natl. Acad. Sci. USA **106**, 19780 (2009).
[30]J. P. Amoureux, C. Fernandez, and S. Steuernagel, J. Magn. Reson. A **123**, 116 (1996).
[31]S. H. Risbud, R. J. Kirkpatrick, A. P. Taglialavore, and B. Montez, J. Am. Ceram. Soc. **70**, C-10 (1987).
[32]S. Sen and R. E. Youngman, J. Phys. Chem. B **108**, 7557 (2004).
[33]D. R. Neuville, L. Cormier, and D. Massiot, Geochim. et Cosmochim. Acta **68**, 5071 (2004).
[34]R. E. Youngman and J. W. Zwanziger, J. Am. Chem. Soc. **117**, 1397 (1995).
[35]D. Manara, A. Grandjean, and D. R. Neuville, Am. Mineral. **94**, 777 (2009).
[36]A. C. Wright, Phys. Chem. Glasses: Eur. J. Glass Sci. Technol. B **51**, 1 (2010).
[37]R. E. Youngman and J. W. Zwanziger, J. Non-Cryst. Solids **168**, 293 (1994).
[38]S. Sen, Z. Xu, and J. F. Stebbins, J. Non-Cryst. Solids **226**, 29 (1998).
[39]E. Schneider, J. F. Stebbins, and A. Pines, J. Non-Cryst. Solids **89**, 371 (1987).
[40]J. F. Stebbins, J. Non-Cryst. Solids **106**, 359 (1988).
[41]E. Lippmaa, M. Mägi, A. Samoson, G. Engelhardt, and A. R. Grimmer, J. Am. Chem. Soc. **102**, 4889 (1980).
[42]M. Mägi, E. Lippmaa, G. Engelhardt, and A. R. Grimmer, J. Phys. Chem. **88**, 1518 (1984).
[43]S. K. Lee and J. F. Stebbins, J. Phys. Chem. B **104**, 4091 (2000).
[44]S. K. Lee and J. F. Stebbins, J. Non-Cryst. Solids **270**, 260 (2000).
[45]D. Massiot, F. Fayon, M. Capron, I. King, S. Le Calvé, B. Alonso, J. Durand, B. Bujoli, Z. Gan, and G. Hoatson, Magn. Reson. Chem. **40**, 70 (2002).
[46]R. J. Araujo, J. Non-Cryst. Solids **42**, 109 (1980).
[47]R. J. Araujo, J. Non-Cryst. Solids **58**, 201 (1983).
[48]R. J. Araujo, J. Non-Cryst. Solids **81**, 251 (1986).
[49]Y. Z. Yue, J. Non-Cryst. Solids **354**, 1112 (2008).
[50]M. Moesgaard, R. Keding, J. Skibsted, and Y. Z. Yue, Chem. Mater. **22**, 4471 (2010).
[51]J. F. Stebbins, J. Non-Cryst. Solids **106**, 359 (1988).
[52]I. Avramov, C. Rüssel, and R. Keding, J. Non-Cryst. Solids **324**, 29 (2003).
[53]L. M. Peng and J. F. Stebbins, J. Non-Cryst. Solids **353**, 4732 (2007).

Paper II

Universality of the high-temperature viscosity limit of silicate liquids

Qiuju Zheng,[1,2] John C. Mauro,[2,*] Adam J. Ellison,[2] Marcel Potuzak,[2] and Yuanzheng Yue[1,3,*]
[1]*Section of Chemistry, Aalborg University, DK-9000 Aalborg, Denmark*
[2]*Science and Technology Division, Corning Incorporated, Corning, New York, 14831 USA*
[3]*Key Laboratory for Glass & Ceramics, Shandong Polytechnic University, Jinan, China*
(Received 17 February 2011; published 29 June 2011)

We investigate the high-temperature limit of liquid viscosity by analyzing measured viscosity curves for 946 silicate liquids and 31 other liquids including metallic, molecular, and ionic systems. Our results show no systematic dependence of the high-temperature viscosity limit on chemical composition for the studied liquids. Based on the Mauro-Yue-Ellison-Gupta-Allan (MYEGA) model of liquid viscosity, the high-temperature viscosity limit of silicate liquids is $10^{-2.93}$ Pa·s. Having established this value, there are only two independent parameters governing the viscosity-temperature relation, namely, the glass transition temperature and fragility index.

DOI: 10.1103/PhysRevB.83.212202 PACS number(s): 66.20.Ej, 66.20.Cy, 83.80.Ab

Shear viscosity is perhaps the single most important property of glass-forming liquids, since adequate control of flow behavior is essential for all steps of industrial glass production. It is also critical for understanding the relaxation characteristics of liquids, as in the well-known Angell plot[1] where the logarithm of viscosity, $\log_{10}\eta$, is plotted as a function of the T_g-scaled inverse temperature, T_g/T. Here, T_g is the glass transition temperature, defined as the temperature at which the liquid viscosity equals 10^{12} Pa·s, and T is absolute temperature. The slope of the Angell curve at T_g defines the fragility index m,

$$m \equiv \left.\frac{\partial \log_{10}\eta}{\partial(T_g/T)}\right|_{T=T_g}. \quad (1)$$

Fragility is a common measure of the slowing down of liquid dynamics upon cooling through the glass transition.

According to Angell,[1] liquids can be classified as either "strong" or "fragile" depending on whether they exhibit an Arrhenius or super-Arrhenius scaling of viscosity with temperature, respectively. The degree of non-Arrhenius scaling varies greatly among different glass-forming liquids and reflects the second derivative of the viscosity curve with respect to inverse temperature. With the assumption of a universal high-temperature limit of viscosity, η_∞, Angell proposed that this non-Arrhenius character is directly connected to the fragility index, m, a first-derivative property of the viscosity curve at T_g.[2] However, the assumption of a universal high-temperature limit of viscosity, which enables this direct connection between first- and second-derivative properties, has not yet been validated by a systematic analysis of experimental data.

In this Brief Report, we analyze viscosity-temperature curves of 946 silicate liquids and 31 other liquids, including water and silica, as well as borate, metallic, molecular, and ionic liquids. Our results show that there is no systematic dependence of η_∞ on composition and point to a narrow spread around $\eta_\infty = 10^{-2.93}$ Pa·s for silicate liquids. This result implies the existence of a universal high-temperature limit of viscosity, indicating that the fragility index m does have a direct relationship to the non-Arrhenius scaling of liquid viscosity (a measure of curvature), at least for silicate liquids. Our results indicate that there are only two independent parameters governing the viscosity of silicate liquids: T_g and m. This simplifies the process for modeling the composition dependence of liquid viscosity and is an indication of the universal dynamics of silicate liquids at the high-temperature limit.

To evaluate η_∞, we analyze experimental viscosity data using three of the most popular three-parameter equations for liquid viscosity. First, we consider the Vogel-Fulcher-Tammann (VFT) equation, which is historically the most frequently applied model,

$$\log_{10}\eta = \log_{10}\eta_\infty + \frac{A}{T - T_0}. \quad (2)$$

Here, η_∞, A, and T_0 are fitting parameters. VFT works well for most classical oxide liquids with low fragility, but it does not apply well for higher fragility liquids.[2] A major drawback of VFT is that it breaks down at low temperatures due to divergence at $T = T_0$.[3–6] Hence, it often overpredicts viscosity values at low temperatures.

Avramov and Milchev (AM) proposed an alternative three-parameter equation that describes the kinetics of the molecular motion in undercooled melts using an atomic hopping approach.[7] The AM equation is

$$\log_{10}\eta = \log_{10}\eta_\infty + \left(\frac{\theta}{T}\right)^\alpha, \quad (3)$$

where η_∞, θ, and α are treated as fitting parameters. The AM equation does not suffer from the problem of dynamic divergence at finite temperature; however, this equation gives a divergence of configurational entropy in the high-temperature limit.[8,9]

Finally, based on energy landscape analysis and the temperature-dependent constraint model for configurational entropy,[10–12] the recent Mauro-Yue-Ellison-Gupta-Allan (MYEGA) equation[9] was derived as

$$\log_{10}\eta = \log_{10}\eta_\infty + \frac{K}{T}\exp\left(\frac{C}{T}\right). \quad (4)$$

This model provides a physically realistic and accurate description of liquid dynamics[9,13–15] since it is the only approach that accounts for a reasonable extrapolation of configurational entropy in both the high- and low-temperature limits. It should be mentioned that in the high-temperature limit, VFT can

be derived as a simple approximation to MYEGA through a Taylor series expansion.[13] This implies that VFT is a reasonable approximation at high temperatures but becomes less accurate as temperature is decreased.

All of the aforementioned models have the high-temperature limit of viscosity, η_∞, as a common parameter. However, direct measurement of η_∞ is not possible, so the value of η_∞ must be obtained either through extrapolation of measured viscosity data or through a separate model designed specifically for η_∞. According to the viscous flow theories of Frenkel[16] and Eyring,[17] the high-temperature viscosity limit is $\eta_\infty = 10^{3.5\pm1}$ Pa·s. However, this is a rough estimate since they describe the temperature dependence of viscosity using an Arrhenius equation, which does not account for liquid fragility. The η_∞ values of some glass-forming liquids were also determined by Barrer,[18] where the viscosity data are also simply fitted by the Arrhenius equation. The obtained η_∞ values are scattered over several orders of magnitude and are nonphysically described as a function of temperature. Kobeko[19] showed a value equal to $\eta_\infty = 10^{-3\pm1.5}$ Pa·s for all liquids. Russell *et al.*[20] fitted the viscosity data of 333 silicate melts using the VFT and Adam-Gibbs (AG) models and obtained a high-temperature limit as $\eta_\infty = 10^{-4.3\pm0.74}$ and $10^{-3.2\pm0.66}$ Pa·s, respectively. Recently, Giordano *et al.*[21] obtained a common high-temperature viscosity limit for silicate melts of $\eta_\infty = 10^{-4.6}$ Pa·s based on the VFT equation. However, these previously obtained values of η_∞ were obtained using a fairly limited range of compositions.

We begin our investigation by fitting the three viscosity models (VFT, AM, and MYEGA) to measured viscosity data for 946 different silicate liquids from Corning Incorporated, in addition to 6 borate,[22] 11 metallic,[23] 4 molecular,[9] and 9 ionic liquids.[24] The fitting was done using a constrained Monte Carlo algorithm to avoid becoming trapped in local minima. The 946 Corning liquids cover a wide range of composition space, from simple calcium aluminosilicate ternaries through complex borosilicates with up to eleven unique oxide components.[25] Overall, the compositions cover a range of fragility values from 25.9 to 73.8. Each composition is represented by 6–13 data points in the range of 10 to 10^6 Pa·s, obtained via a rotating spindle method. Most are also represented by data points at $10^{6.6}$ Pa·s (the softening point, obtained via parallel plate viscometry) and 10^{11} Pa·s (obtained via beam bending viscometry). The measured isokom (i.e., constant viscosity) temperatures are accurate to within ±1 K. Figure 1 shows the root mean square (RMS) error of the viscosity fit to 946 Corning compositions as a function of each composition, plotted from highest to lowest error. MYEGA provides the best fit with the lowest root mean square (RMS) error for the whole range of compositions, as compared to VFT and AM, although the difference between MYEGA and VFT models is subtle. The superior fitting quality of MYEGA is due to its derivation from physically realistic considerations in both the high- and low-temperature limits; hence, it is expected to yield the most accurate value of η_∞.[9] In Fig. 1, we also consider a recent viscosity model by Elmatad, Chandler, and Garrahan (ECG), in which the viscosity curves are considered to be parabolic in inverse temperature space.[26] However, this model provides a significantly worse fitting quality compared

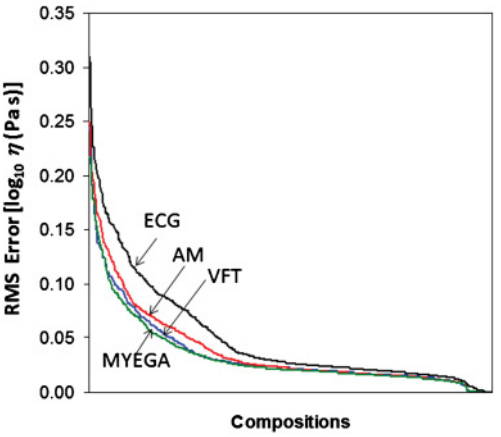

FIG. 1. (Color online) Root mean square error of the viscosity models when fitting measured data of 946 Corning compositions.

to the other three models, and due to its parabolic form, the extrapolation of η_∞ is not physically meaningful. Therefore, we consider only the VFT, AM, and MYEGA models in the remainder of our analysis.

Figure 2 shows the fitted values of $\log_{10}\ \eta_\infty$ for the Corning liquids. The straight lines in the figure represent the average values of η_∞ obtained from the three models. The average value of $\log_{10}\ \eta_\infty$ predicted by MYEGA is −2.93, which is in line with previous estimates.[19,20] AM produces an unrealistically high value of η_∞[9] due to an unphysical divergence of configurational entropy in the high-temperature limit. In contrast, VFT produces comparatively low values of η_∞ as a by-product of its unphysical divergence of viscosity at low temperatures. Our results show that the lowest standard deviation of $\log_{10}\ \eta_\infty$ for all the compositions occurs using the MYEGA model ($\sigma = 0.337$, compared to 0.343 and 0.519 for VFT and AM, respectively). The difference among these models reflects the fact that $\log_{10}\ \eta_\infty$ is an extrapolated quantity well beyond the range of measurements.[20,27] Since MYEGA produces the most accurate fits and is physically derived, the value yielded by this equation is expected to be reasonable.[9]

The next question is whether the scatter in Fig. 2 is due to stochastic measurement error or if it is the result of an actual

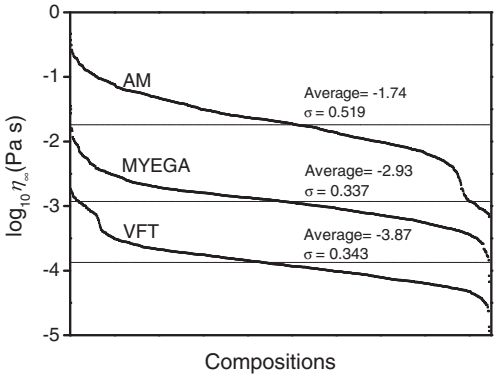

FIG. 2. $\text{Log}_{10}\ \eta_\infty$ values obtained by fitting three viscosity models to 946 Corning compositions. The straight lines represent the average $\log_{10}\ \eta_\infty$ values, and σ is the standard deviation.

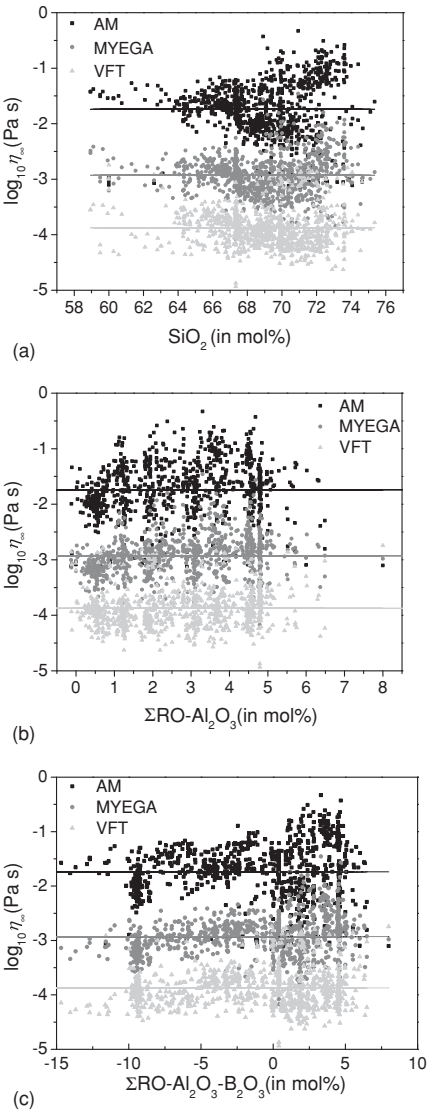

FIG. 3. $\mathrm{Log}_{10}\ \eta_\infty$ values of 946 Corning compositions plotted as a function (a) SiO_2, (b) $\sum RO–Al_2O_3$, and (c) $\sum RO–Al_2O_3–B_2O_3$ content. $\sum RO$ represents the total concentration of alkaline earth oxide as measured through x-ray fluorescence. The straight lines are the average values.

dependence of $\log_{10}\eta_\infty$ on composition. In order to answer this question, we analyze the fitted values of $\log_{10}\eta_\infty$ as a function of every composition variable. For example, Fig. 3 shows the $\log_{10}\eta_\infty$ values for different alkaline earth boroaluminosilicate compositions as a function of alkaline earth concentration. Within the error range of the data, there is no trend of η_∞ with composition, and η_∞ has a fairly narrow spread around $10^{-2.93}$ Pa·s. Similar results are obtained when plotting $\log_{10}\eta_\infty$ versus any composition variable. These results suggest that the value of η_∞ is independent of composition and that the scattering of the data is due to the experimental noise and differences in the range of temperatures over which viscosity is measured.

The range of liquid fragility values (m) of the 946 glass compositions investigated is between 25.9 and 73.8. In order to find out whether relatively strong liquids (i.e., with $m < 25$) show similar η_∞ values to $10^{-2.93}$ Pa·s, we also

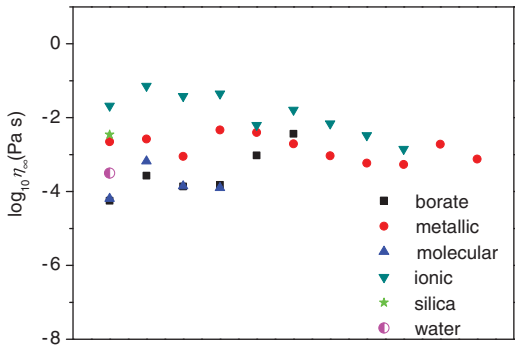

FIG. 4. (Color online) $\mathrm{Log}_{10}\ \eta_\infty$ values obtained by fitting MYEGA to several borate,[22] metallic,[23] molecular,[9] and ionic[24] liquids, and water.[28] The abscissa represents an arbitrary composition space.

analyze the viscosity data of silica, an archetypical strong glass-former. Here, we obtain a value of $\eta_\infty = 10^{-2.46}$ Pa·s for Corning code 8655 high-purity fused silica (HPFS). In addition, we obtain the η_∞ values of several fragile liquids with $m > 75$, e.g., o-terphenyl ($m = 99$) and $4Ca(NO_3)_2$-$6KNO_3$ ($m = 115$), by fitting their viscosity data to the MYEGA equation. We plot the η_∞ values of the two liquids in Fig. 4, along with those of other nonsilicate liquids, such as borate,[22] metallic,[23] molecular,[9] and ionic liquids[24] and water.[28] Although there are significantly less statistics here compared to the silicate compositions, we find that the values of η_∞ do indeed fall near 10^{-3} Pa·s for all of these liquids. However, the viscosity data of more nonsilicate liquids need to be analyzed to judge whether a universal η_∞ value exists for all the glass-forming liquids.

The narrow spread of η_∞ points to a common underlying physics of silicate liquids at the high-temperature limit. It should be noted that the high-temperature limit refers to the viscosity of a *liquid* at high temperature. In other words, it does not involve the gaseous state, but rather a superheated liquid state. In his early work, Angell suggests that the value of η_∞ is determined by the liquid quasi-lattice vibration time ($\tau_\infty \approx 10^{-14}$ s), which is the time between successive assaults on the energy barrier for atomic rearrangements.[1] Maxwell's relation ($\eta_\infty = G_\infty\tau_\infty$, where G_∞ is the shear modulus at infinite frequency at temperature above T_g, and τ_∞ is the structural relaxation time at infinite temperature) was used to calculate the high-temperature viscosity limit from $\tau_\infty \approx 10^{-14}$ s[20,21] For oxide liquids, G_∞ varies only slightly with temperature and was measured over a large range of temperatures above T_g to be around 29 GPa.[29] However, for some organic liquids, both G_∞ and τ_∞ vary with composition and temperature.[30–32] In our view, any explanation of η_∞ based on vibrations is not correct, since at infinite temperature, the system is not really vibrating. Rather, it is exploring the upper region of the energy landscape dominated by high entropy and low activation barriers.[33] Moreover, the atoms have an infinite amount of thermal energy to overcome any barrier, so they do not even see the activation barriers at all and hence cannot be vibrating. Therefore, a more physically realistic explanation of η_∞ is needed.

For this explanation, we turn to the topological constraint approach of Phillips and Thorpe,[11,12] which states that the

atomic structure of a glass-forming liquid may be treated as a network of bond constraints. By comparing the average number of constraints per atom (n) to the network dimensionality (d), the network can be floppy (underconstrained), isostatic (optimally constrained), or stressed-rigid (overconstrained). When $n < d$, the network is underconstrained and contains low-frequency deformation modes (so-called "floppy modes"). The network is optimally rigid when $n = d$, and it is stressed-rigid when $n > d$. Based on this original work of Phillips and Thorpe, Gupta and Mauro[10] presented a topological modeling approach incorporating a temperature dependence of constraints. At infinitely high temperature, any constraint is easily broken and hence does not contribute to the rigidity of the network. In a three-dimensional space, the atomic degrees of freedom, $f = d - n$, i.e., the number of low-frequency "floppy modes," is equal to $d = 3$ for any system. In other words, in the infinite temperature limit, all three degrees of freedom are floppy for each atom, so each atom has three continuous modes of deformation, independent of atom type, and the configurational entropy has achieved its maximal value. Hence, all silicate liquids will exhibit the same flow behavior in the high-temperature limit. We are in a three-dimensional space; however, if we were operating in a different dimensional space (i.e., $d = 2$ or $d = 4$), there would exist different values of η_∞. We thus argue that our result of a convergence of η_∞ values at $10^{-2.93}$ Pa·s for silicate liquids is physically meaningful in terms of constraint theory. The narrow spread of the high-temperature viscosity limit is an implication of the universal dynamics of silicate liquids at the high-temperature limit.

In summary, by analyzing 946 silicate liquids and 31 nonsilicate liquids, we find that there is a narrow spread of high-temperature limit of viscosity around 10^{-3} Pa·s for silicate liquids. This implies that silicate liquids have a universal value of η_∞. Thus, in accordance with the work of Angell, the non-Arrhenius scaling of liquid viscosity can be quantified through the fragility index m of the liquid. Moreover, by defining the high-temperature viscosity limit as a fixed value, i.e., $\log_{10} \eta_\infty = -3$, the MYEGA model contains only two fitting parameters. This result simplifies the modeling process of the compositional dependence of viscosity and indicates a common underlying physics of silicate liquids at the high-temperature limit.

We express our sincere thanks to the Advanced Materials Processing Laboratory at Corning Incorporated for their tireless work in sample preparation and to the Characterization Sciences and Services Directorate at Corning for their care in obtaining reliable viscosity data.

*Corresponding authors: mauroj@corning.com, yy@bio.aau.dk

[1] C. A. Angell, J. Non-Cryst. Solids **73**, 1 (1985).
[2] C. A. Angell, K. L. Ngai, G. B. McKenna, P. F. McMillan, and S. W. Martin, J. Appl. Phys. **88**, 3113 (2000).
[3] G. W. Scherer, J. Am. Ceram. Soc. **67**, 504 (1984).
[4] H. Tanaka, Phys. Rev. Lett. **90**, 055701 (2003).
[5] F. Sciortino, W. Kob, and P. Tartaglia, Phys. Rev. Lett. **83**, 3214 (1999).
[6] F. Stickel, E. W. Fischer, and R. Richert, J. Chem. Phys. **102**, 6251 (1995).
[7] I. Avramov and A. Milchev, J. Non-Cryst. Solids **104**, 253 (1988).
[8] I. Avramov, J. Non-Cryst. Solids **351**, 3163 (2005).
[9] J. C. Mauro, Y. Z. Yue, A. J. Ellison, P. F. Gupta, and D. C. Allan, Proc. Natl. Acad. Sci. USA **106**, 19780 (2009).
[10] P. K. Gupta and J. C. Mauro, J. Chem. Phys. **130**, 094503 (2009).
[11] J. C. Phillips, J. Non-Cryst. Solids **34**, 153 (1979).
[12] J. C. Phillips and M. F. Thorpe, Solid State Commun. **53**, 699 (1985).
[13] M. M. Smedskjaer, J. C. Mauro, and Y. Z. Yue, J. Chem. Phys. **131**, 244514 (2009).
[14] P. Lunkenheimer, S. Kastner, M. Köhler, and A. Loidl, Phys. Rev. E **81**, 051504 (2010).
[15] Th. Bauer, M. Köhler, P. Lunkenheimer, A. Loidl, and C. A. Angell, J. Chem. Phys. **133**, 144509 (2010).
[16] Ya. I. Frenkel, *Kineticheskaya teorija zhidkostey* (Izd. AN SSSR, Moskva-Leningrad, 1945).
[17] S. N. Glasstone, K. Laidler, and H. Eyring, *The Theory of Rate Processes* (McGraw-Hill, New York, 1941).
[18] R. M. Barrer, Trans. Faraday Soc. **39**, 48 (1943).
[19] P. P. Kobeko, *Amorfniye veshchestva* (Izd. AN SSSR, Moskva-Leningrad, 1952).
[20] J. K. Russell, D. Giordano, and D. B. Dingwell, Am. Mineral. **8**, 1390 (2003).
[21] D. Giordano, J. K. Russell, and D. B. Dingwell, Earth Planet. Sci. Lett. **271**, 123 (2008).
[22] M. M. Smedskjaer, J. C. Mauro, S. Sen, and Y. Z. Yue, Chem. Mater. **22**, 5358 (2010).
[23] C. Z. Zhang, L. N. Hu, Y. Z. Yue, and J. C. Mauro, J. Chem. Phys. **133**, 014508 (2010).
[24] O. O. Okoturo and T. J. VanderNoot, J. Electroanal. Chem. **568**, 167 (2004).
[25] A. Ellison, and I. A. Cornejo, Int. J. Appl. Glass Sci. **1**(1), 87 (2010).
[26] Y. S. Elmatad, D. Chandler, and J. P. Garrahan, J. Phys. Chem. B **113**, 5563 (2009).
[27] Y. Bottinga, P. Richet, and A. Sipp, Am. Mineral. **80**, 305 (1995).
[28] G. Guevara-Carrion, J. Vrabec, and H. Hasse, J. Chem. Phys. **134**, 074508 (2011).
[29] H. Bornhöft, and R. Brückner, Glass Sci. Technol. **72**, 315 (1999).
[30] N. Menon, S. R. Nagel, and D. C. Venerus, Phys. Rev. Lett. **73**, 963 (1994).
[31] P. K. Dixon, L. Wu, and S. R. Nagel, Phys. Rev. Lett. **65**, 1108 (1990).
[32] N. B. Olsen, J. C. Dyre, and T. Christensen, Phys. Rev. Lett. **81**, 1031 (1998).
[33] J. C. Mauro, R. J. Loucks, A. K. Varshneya, and P. K. Gupta, Sci. Model. Simul. **15**, 241 (2008).

Paper III

Journal of Non-Crystalline Solids 358 (2012) 993–1002

Contents lists available at SciVerse ScienceDirect

Journal of Non-Crystalline Solids

journal homepage: www.elsevier.com/ locate/ jnoncrysol

Composition–structure–property relationships in boroaluminosilicate glasses

Qiuju Zheng [a,b], Marcel Potuzak [b], John C. Mauro [b,*], Morten M. Smedskjaer [b], Randall E. Youngman [b], Yuanzheng Yue [a,**]

[a] Section of Chemistry, Aalborg University, DK-9000 Aalborg, Denmark
[b] Science and Technology Division, Corning Incorporated, Corning, NY, USA

ARTICLE INFO

Article history:
Received 10 December 2011
Received in revised form 11 January 2012
Available online 11 February 2012

Keywords:
Boroaluminosilicate;
Boron speciation;
Network connectivity;
Liquid fragility;
Mechanical properties

ABSTRACT

The complicated structural speciation in boroaluminosilicate glasses leads to a mixed network former effect yielding nonlinear variation in many macroscopic properties as a function of chemical composition. Here we study the composition–structure–property relationships in a series of sodium boroaluminosilicate glasses from peralkaline to peraluminous compositions by substituting Al_2O_3 for SiO_2. Our results reveal a pronounced change in all the measured physical properties (density, elastic moduli, hardness, glass transition temperature, and liquid fragility) around $[Al_2O_3]–[Na_2O] = 0$. The structural origin of this change is elucidated through nuclear magnetic resonance analyses and topological considerations. Furthermore, we find that addition of 1 mol% Fe_2O_3 exerts a complicated impact on the measured properties.

1. Introduction

Boroaluminosilicate glasses have a wide variety of applications, including liquid crystal display substrates [1], glass fibers for reinforcement [2], thermal shock-resistant glass containers [2], and radioactive waste glasses [3]. Controlling the properties of this glass family is thus of the utmost importance. The properties of such mixed network glasses are a result of their complicated structural speciation [4–8], which leads to a mixed network former effect yielding nonlinear variation in many macroscopic properties [9–11]. The structure of boroaluminosilicate glasses is rather complicated due to the uncertainty of the extent and nature of mixing of the network-forming cations (Si, B, and Al). Structure–property correlations for boroaluminosilicate glasses and their relation with glass composition are thus still unclear.

The short range structure of boroaluminosilicate glasses has been studied to a large extent, particularly by ^{11}B NMR spectroscopy [12–19]. This technique has successfully captured the composition dependence of the fraction of tetrahedral and trigonal boron species (B^{IV} and B^{III}). In borate-containing glasses, it is now well known that the initial addition of modifier oxides (such as Na_2O or CaO) to pure B_2O_3 results in the conversion of B^{III} to B^{IV}. With increasing modifier content, the fraction of tetrahedral to total boron (N_4) reaches a maximum and then decreases due to formation of non-bridging oxygens (NBOs) on B^{III} [13,19]. In borosilicate glasses, the maximum value of N_4 depends on the $[SiO_2]/[B_2O_3]$ ratio. The empirical model of Dell and Bray [15,17] has traditionally been applied to predict the composition dependence of N_4. Smedskjaer et al. have recently introduced a new statistical mechanical model of boron speciation for accurate prediction of both the composition and thermal history dependence of boron speciation [20]. In this model, the addition of network modifiers leads to a thermodynamic competition between the formation of NBO and the conversion of boron from trigonal to tetrahedral configuration. The model offers improved predictions of boron speciation and provides a natural explanation for the observed thermal history dependence of N_4.

The addition of Al_2O_3 to borosilicate glasses involves several structural complications. Like boron, aluminum requires network modifiers for charge compensation for stabilization in a tetrahedral configuration (Al^{IV}) and thus acts as an effective network former [21–23]. However, it has been found that there is a preference in the formation of Al^{IV} over than of B^{IV}, since the addition of Al_2O_3 in these glasses results in an observed decrease in N_4 [22]. ^{27}Al NMR studies have shown that five- and six-fold coordinated aluminum species (Al^{V} and Al^{VI}) generally start to form when the molar ratio of modifier cation to Al is smaller than one [22–24]. It has also been reported that the mixing behavior in these glasses is driven by the mutual avoidance of B^{IV} and Al^{IV} [25–27], i.e., direct linkages between tetrahedral trivalent cations are not energetically favorable due to the difficulty in charge balancing the high net charge on the bridging oxygens.

The network modifier cations in boroaluminosilicate glasses can thus possess various structural roles depending on the chemical composition. To understand structure–property correlations in these glasses, it is important to access all of those regimes. In this work, we have therefore designed a series of sodium boroaluminosilicate glasses with systematic variation of the $[Al_2O_3]/[SiO_2]$ ratio to access

* Corresponding author. Tel.: +1 607 974 2185; fax: +1 607 974 2410.
** Corresponding author. Tel.: +45 99408522; fax: +45 9635 0558.
E-mail addresses: mauroj@corning.com (J.C. Mauro), yy@bio.aau.dk (Y.Z. Yue).

0022-3093/$ – see front matter © 2012 Elsevier B.V. All rights reserved.
doi:10.1016/j.jnoncrysol.2012.01.030

different regimes of sodium behavior: 1) Na^+ to stabilize aluminum in a tetrahedral configuration; 2) Na^+ to convert boron from trigonal to tetrahedral coordination; 3) Na^+ to form nonbridging oxygens on silicon or trigonal boron. Thorough structural information has been gained by magic angle spinning (MAS) NMR and triple quantum (3Q) MAS NMR in our parallel study [28]. We will refer to those findings when we discuss the results obtained here.

In this paper, we will investigate and analyze the composition dependence of the rheological and selected physical properties (density, elastic moduli, and hardness) of these glass compositions. In industrial glass melting processes, adequate control of the temperature and composition dependence of viscous flow behavior is essential and therefore shear viscosity is a very important property [2]. The mechanical properties are also crucial for glass application. For instance, touch screen displays require high hardness and scratch resistance [29]. We also explore the effect of iron on the measured properties, since iron is a common impurity in the utilized raw materials. Hence, it is important to know how it will affect the properties of real industrial glasses. In order to study the effect of iron on the properties, we have added 1 mol% Fe_2O_3 to the glasses, even though this concentration is much higher than that of most industrial glasses, where it usually occurs only as a trace-level contaminant.

2. Experiments

2.1. Sample preparation

We prepared two sets of sodium boroaluminosilicate glasses with and without iron (see sample IDs and compositions in Table 1). 0.1 mol% As_2O_3 or SnO_2 was added as fining agent in the iron-free compositions. First, the batch materials (SiO_2, Al_2O_3, H_3BO_3, Na_2CO_3, Fe_2O_3, As_2O_3, and SnO_2) were thoroughly mixed for 60 min using a ball mill. The mixed batch materials were then melted in covered Pt crucibles at different homogenization temperatures T_h (see Table 1) for 6 h in air. In order to improve the chemical homogeneity, the melts were first quenched in water and the resulting glass shards were crushed and remelted for another 6 h at their respective T_h. Finally, these melts were poured onto a stainless steel plate in air and then annealed for 2 h at different temperatures depending on chemical composition.

We analyzed the chemical compositions of the glasses using wet chemistry methods. The analyzed compositions are reported in Table 1. The iron redox state in the iron-containing glasses was determined by ^{57}Fe Mössbauer spectroscopy with uncertainty of ±5% [30]. The densities were determined using Archimedes principle. The errors of the reported density values do not exceed ±1%.

Table 1
Chemical composition, homogenization temperature (T_h), iron redox ratio ($[Fe^{3+}]/[Fe]_{tot}$), and fraction of tetrahedral to total boron (N_4) of the investigated iron-free and iron-containing glasses. Iron redox ratio was determined by ^{57}Fe Mössbauer spectroscopy with uncertainty of ±5% [30]. N_4 was determined by ^{11}B MAS NMR spectroscopy with uncertainties of ±0.2% [28].

Glass	Composition (mol%)					T_h	$[Fe^{3+}]/[Fe]_{tot}$	N_4
ID	SiO_2	Al_2O_3	B_2O_3	Na_2O	Fe_2O_3	(°C)	(at%)	(at%)
Al0*	79.35	0.29	4.88	14.57	0.91	1450	n/a	n/a
Al1*	78.92	0.69	4.95	14.52	0.93	1450	n/a	n/a
Al2.5*	77.40	2.20	4.90	14.60	0.90	1450	95	n/a
Al5*	74.70	4.70	5.00	14.60	1.00	1500	93	n/a
Al7.5*	71.80	7.60	4.90	14.70	1.00	1550	91	n/a
Al10*	68.90	10.30	5.00	14.80	1.00	1600	87	n/a
Al12.5*	67.10	12.60	5.00	14.30	1.00	1650	83	n/a
Al15*	64.10	15.60	5.00	14.30	1.00	1650	78	n/a
Al17.5*	62.31	17.94	5.07	13.75	0.94	1650	n/a	n/a
Al20*	61.13	19.38	4.98	13.63	0.88	1650	n/a	n/a
Al0	80.08	0.16	4.84	14.77	0.15	1450	n/a	94.9
Al1	79.38	1.16	4.85	14.60	0.14	1450	n/a	93.2
Al2.5	78.80	2.00	4.70	14.40	0.08	1450	n/a	94.6
Al5	78.10	4.00	4.20	13.60	0.07	1500	n/a	91.6
Al7.5	76.90	5.70	4.30	13.00	0.06	1550	n/a	83.1
Al10	75.90	7.50	4.30	12.30	0.07	1600	n/a	74.4
Al12.5	72.00	10.40	4.40	13.10	0.07	1650	n/a	43.6
Al15	69.20	12.70	4.60	13.50	0.07	1650	n/a	19.9
Al17.5	62.97	17.18	4.99	14.73	0.13	1650	n/a	1.0
Al20	60.52	19.61	5.00	14.73	0.14	1650	n/a	0.8

2.2. Viscosity measurements

The temperature dependence of equilibrium viscosity of the glass-forming liquids was determined by beam bending and parallel plate compressing experiments for all of the compositions under study. For selected compositions, we also performed concentric cylinder rotating experiments to determine viscosities above the liquidus temperature. The compositions are thus represented by data points at $10^{6.6}$ Pa·s (the softening point, obtained via parallel plate viscometry), 10^{11} Pa·s (obtained via beam bending viscometry), and 6–13 data points in the range of 10 to 10^6 Pa·s (obtained via a concentric cylinder viscometry). For beam bending experiments, bars of 5.5 cm length and 2.5×2.5 mm^2 cross-section were cut from the bulk glasses. For parallel plate compressing experiments, cylinders of 6 mm diameter and 5 mm thickness were core-drilled and afterwards the flats were polished. For concentric cylinder rotating experiments, ~600 g of crushed glass was used. The errors associated with determining the 10^{11} Pa·s point by the beam bending method and the $10^{6.6}$ Pa·s point by the parallel plate method are ±2 and ±5 °C, respectively. The estimated error in viscosity for the high temperature measurements (by the concentric cylinder method) is $\Delta \log_{10} \eta = \pm 0.02$ (η in Pa·s) [31].

2.3. DSC measurements

The calorimetric measurements of the glasses were performed using a differential scanning calorimeter (DSC 404 C, Netzsch). The measurements were conducted under a flow of argon at 40 ml/min. The samples were heated at 10 K/min to 100 K above the glass transition temperature in order to relax the sample fully and then cooled at 10 K/min to 313 K. The sample was then subjected to another upscan at 10 K/min. The recorded heat flow of the first upscan reflects the enthalpy response of a sample with an unknown thermal history (i.e., an unknown cooling rate experienced by the sample during melt-quenching), whereas that of the second upscan reflects the enthalpy response of the sample with a well-defined thermal history (i.e., a known cooling rate). The isobaric heat capacity (C_p) curve for each measurement was calculated relative to the C_p curve of a sapphire reference material with the same mass (56 mg).

2.4. Mechanical testing

The elastic properties (Young's and shear moduli) were measured at room temperature using resonant ultrasound spectroscopy. Prisms of dimensions 10 mm × 8 mm × 6 mm^3 were used to gather resonance spectra from 100 to 300 kHz. For each sample, the first five resonant peaks as a function of frequency resulting from excited resonant eigenmodes were used to calculate the elastic properties.

The Vickers microhardness (H_V) of the glasses was measured using a Duramin 5 indenter (Struers A/S). The measurements were performed in air atmosphere at room temperature. We applied a load of 0.49 N for duration of 5 s and 30 indentations were performed on each sample. The Vickers hardness was calculated from the lengths of the indentation diagonals.

3. Results

3.1. Rheological properties

The temperature dependence of viscosity of a glass-forming melt is one of the most important properties for industrial glass formation [2]. Various models exist for fitting and describing the temperature dependence of viscosity. Recently Mauro et al. [32] proposed a new model for the viscosity–temperature relationship that is derived from fundamental physics and provides realistic extrapolations of configurational entropy at both the low and high temperature limits, as shown below:

$$\log_{10}\eta = \log_{10}\eta_\infty + \frac{K}{T}\exp\left(\frac{C}{T}\right), \tag{1}$$

where η_∞ is the high-temperature limit of the liquid viscosity, and K and C are constants. The viscosity data for four of the iron-containing compositions containing low and high $[Al_2O_3]$ are plotted in Fig. 1. The data are shown in the form of an Angell plot [33], where the logarithm of viscosity ($\log_{10}\eta$) is plotted as a function of the $T_{g,vis}$-scaled inverse temperature ($T_{g,vis}/T$). Here, $T_{g,vis}$ is the glass transition temperature, defined as the temperature at which the equilibrium viscosity equals 10^{12} Pa·s, and T is the absolute temperature. Glass-forming liquids are classified as either "strong" or "fragile" depending on whether they exhibit an Arrhenius or super-Arrhenius scaling of viscosity with temperature, respectively. This effect is quantified by the slope of the Angell curve at $T_{g,vis}$, which defines the liquid fragility index m:

$$m \equiv \left.\frac{\partial \log_{10}\eta}{\partial\left(T_g/T\right)}\right|_{T=T_{g,vis}} \tag{2}$$

Moreover, the high-temperature viscosity limit has recently been shown to be composition independent and equal to approximately 10^{-3} Pa·s [34]. With these definitions of glass transition temperature, high-temperature viscosity limit, and fragility, Eq. (2) can be rewritten as [32,34],

$$\log_{10}\eta(T) = -3 + 15\frac{T_{g,vis}}{T}\exp\left[\left(\frac{m}{15}-1\right)\left(\frac{T_{g,vis}}{T}-1\right)\right] \tag{3}$$

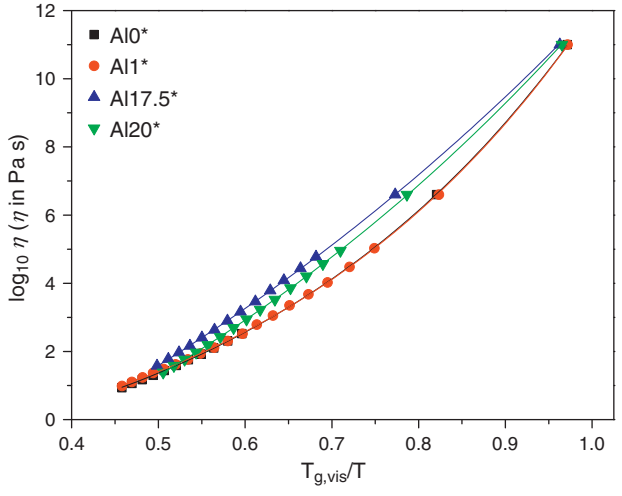

Fig. 1. Angell fragility plot showing the logarithmic viscosity ($\log_{10}\eta$) as a function of the $T_{g,vis}$ scaled inverse temperature ($T_{g,vis}/T$) for four representative iron-containing glasses with low and high $[Al_2O_3]$. The temperature errors of 10^{11} Pa·s (by the beam bending method) and $10^{6.6}$ Pa·s points (by the parallel plate method) are ±2 and ±5 °C, respectively. The estimated error in viscosity for the high temperature measurements (by the concentric cylinder method) is $\Delta\log_{10}\eta = \pm 0.02$ (η in Pa·s) [31].

We fit the experimental data to Eq. (3) using a Levenberg–Marquardt algorithm [35,36], as shown in Fig. 1 for four of the glass-forming liquids. The fitted values of $T_{g,vis}$ and m are listed in Table 2 and shown in Figs. 2 and 3, respectively. We plot these values and other properties against the value $[Al_2O_3]$–$[Na_2O]$, i.e., the excess concentration of Al^{3+} not being charge-balanced in tetrahedral configuration by Na^+.

We find that $T_{g,vis}$ increases with increasing value of $[Al_2O_3]$–$[Na_2O]$ for both iron-free and iron-containing glasses (Fig. 2). However, there exist two regimes for the composition dependence of $T_{g,vis}$, as illustrated in Fig. 2 by the dashed lines that are linear fits to the data for $[Al_2O_3]$–$[Na_2O] < 0$ and $[Al_2O_3]$–$[Na_2O] > 0$, respectively. In the peraluminous regime ($[Al_2O_3]$–$[Na_2O] > 0$), $T_{g,vis}$ increases more rapidly with increasing $[Al_2O_3]$ than in peralkaline regime ($[Al_2O_3]$–$[Na_2O] < 0$). In other words, there is a change in the slope of $T_{g,vis}$ vs. $[Al_2O_3]$–$[Na_2O]$ around $[Al_2O_3]$–$[Na_2O] = 0$ and $T_{g,vis}$ increases faster in the peraluminous regime than in the peralkaline regime. The data in Fig. 2 also show that the glass transition temperature of the iron-containing glasses is generally lower than that of the iron-free glasses.

Fig. 3 shows the composition dependence of fragility for both iron-containing and iron-free compositions. In the peralkaline compositions regime, the liquid fragility is relatively composition independent and equal to around 35–38 for $-15 < [Al_2O_3]$–$[Na_2O] < -5$. As $[Al_2O_3]$ increases for $[Al_2O_3]$–$[Na_2O] > -5$, the value of m decreases dramatically and attains its minimum value around $[Al_2O_3]$–$[Na_2O] = 2$. In the peraluminous regime, m increases with increasing $[Al_2O_3]$. We also note that the iron-free compositions are generally more fragile than the iron-containing compositions.

3.2. Glass transition

As shown in Figs. 4(a) and (b), the isobaric heat capacity (C_p) is plotted as a function of temperature for the iron-containing and iron-free glasses using DSC. The glass transitions of all the glasses are recorded at a heating rate of 10 K/min subsequent to a cooling rate of 10 K/min. From these heat capacity curves, we have determined two characteristic temperatures, $T_{g,DSC}$ and $T_{g,offset}$, which are the standard calorimetric glass transition temperature and the offset temperature of the C_p overshoot in the glass transition zone, respectively. $T_{g,DSC}$ is defined as the temperature at the intersection point between the extrapolated straight line of the glass C_p curve and the tangent line at the inflection point of the sharp rising C_p curve in the transition zone. This method has an uncertainty of approximately ±2 to 3 K. The procedure for determining these values is illustrated in Fig. 5 by using glass Al2.5* as an example. In the figure, C_{pg} and C_{pl} refer to the isobaric heat capacities for the glass at $T_{g,DSC}$ and the liquid state, respectively. The latter is determined as the offset value of the C_p overshoot above the glass transition range. We have also calculated the slope value of the sharp rising C_p curve at the inflection point, $(dC_p/dT)_{inflect}$. The jump in C_p during the glass transition is calculated as $C_{pl} - C_{pg}$. The glass transition width (ΔT_g) is determined as $T_{g,offset} - T_{g,DSC}$.

Fig. 6 shows the composition dependence of $T_{g,DSC}$, which is similar to that of $T_{g,vis}$ (Fig. 2), i.e., the glass transition temperature increases with increasing value of $[Al_2O_3]$–$[Na_2O]$. There also exist two regimes for the composition dependence of $T_{g,DSC}$, since it increases faster in the peraluminous regime compared to the peralkaline regime, as illustrated by the dashed lines in Fig. 6. Moreover, $T_{g,DSC}$ of the iron-containing glasses is generally lower than that of the iron-free glasses. The composition dependencies of the values of $C_{pl} - C_{pg}$, ΔT_g, and $(dC_p/dT)_{inflect}$ are shown in Figs. 7(a), (b), and (c), respectively. For iron-free glasses, the value of $C_{pl} - C_{pg}$ appears to be relatively independent of composition, whereas that of the iron-containing glasses exhibits similar composition dependence as m (Fig. 3). ΔT_g generally increases with increasing $[Al_2O_3]$, with only minor differences between glasses with and without iron. $(dC_p/dT)_{inflect}$ generally decreases with

Table 2
Glass transition temperature determined from viscosity ($T_{g,vis}$) and DSC measurements ($T_{g,DSC}$), liquid fragility index from viscosity (m), jump in isobaric heat capacity during glass transition (ΔC_p), slope of the heat capacity curve during glass transition ($(dC_p/dT)_{inflect}$), glass transition width (ΔT_g), density (ρ), molar volume (V_m), Young's modulus (E), and shear modulus (G) of the investigated glasses.

Glass ID	$T_{g,vis}$ (K)	$T_{g,DSC}$ (K)	m (−)	ΔC_p (J mol^{-1} K^{-1})	$(dC_p/dT)_{inflect}$ (J mol^{-1} K^{-2})	ΔT_g (K)	ρ (g cm^{-3})	V_m (cm^3 mol^{-1})	E (GPa)	G (GPa)
Al0*	807	810	35.9	16.0	0.63	62	2.443	25.3	72.5	30.3
Al1*	807	809	36.5	17.6	0.71	56	2.444	25.4	72.9	30.5
Al2.5*	816	815	37.2	18.1	0.76	56	2.448	25.6	73.4	30.5
Al5*	825	823	36.9	19.4	0.76	58	2.449	26.0	73.7	30.4
Al7.5*	846	839	37.3	19.5	0.73	61	2.449	26.5	73.8	30.5
Al10*	850	849	34.0	18.8	0.70	61	2.433	27.2	70.8	29.3
Al12.5*	864	856	28.8	15.2	0.44	84	2.419	27.7	67.6	27.8
Al15*	905	892	26.1	13.0	0.32	82	2.413	28.3	66.9	27.4
Al17.5*	922	917	27.5	15.1	0.44	80	2.425	28.6	69.4	28.1
Al20*	936	923	29.5	16.9	0.44	78	2.440	28.6	70.8	28.8
Al0	809	804	35.1	15.7	0.59	60	2.421	25.2	72.4	30.0
Al1	814	808	35.6	16.0	0.63	60	2.414	25.5	72.7	30.4
Al2.5	822	819	37.1	16.0	0.55	57	2.409	25.6	72.6	30.2
Al5	837	833	35.1	15.2	0.59	60	2.406	26.0	73.1	30.4
Al7.5	851	840	38.0	17.6	0.70	58	2.402	26.3	73.2	30.5
Al10	871	859	36.3	15.9	0.67	62	2.392	26.8	73.1	30.6
Al12.5	887	865	35.8	17.3	0.61	67	2.398	27.2	70.7	29.2
Al15	899	875	30.7	15.1	0.44	80	2.384	27.8	67.1	28.0
Al17.5	956	931	28.2	14.6	0.33	91	2.400	28.4	68.5	27.8
Al20	966	943	30.9	17.0	0.39	78	2.409	28.7	70.4	28.9

increasing $[Al_2O_3]$ for both iron-containing and iron-free glasses with the greatest change for $-5<[Al_2O_3]–[Na_2O]<0$.

3.3. Physical properties

Fig. 8(a) shows the composition dependence of the measured densities. For any given value of $[Al_2O_3]–[Na_2O]$, the iron-containing glasses are denser than the iron-free glasses. For both glass series, the density exhibits a minimum around the charge balanced composition $[Al_2O_3]–[Na_2O]=0$. The evolution of molar volume (V_m) of the glasses is shown in Fig. 8(b). V_m is calculated from dividing molar mass of the analyzed chemical compositions by measured densities. The molar volume of iron-containing and iron-free glasses exhibits the same trend, viz., V_m monotonically increases with increasing value of $[Al_2O_3]–[Na_2O]$.

Young's modulus (E) describes the resistance of a material to deformation along an axis when opposing forces are applied along that axis, while the shear modulus (G) describes the resistance to shear when acted upon by opposing forces. We have determined both of these moduli from resonant ultrasound spectroscopy measurements as shown in Figs. 9(a) and (b). First, we note that the iron-containing and iron-free glasses display similar composition dependences for both E and G. In the peralkaline regime, the elastic moduli decrease with increasing $[Al_2O_3]$ for $-5<[Al_2O_3]–[Na_2O]<0$. For $[Al_2O_3]–[Na_2O]<-5$, the elastic moduli are essentially constant. In the peraluminous regime, the elastic moduli increase with increasing $[Al_2O_3]$, i.e., there is a minimum of both Young's and shear modulus around $[Al_2O_3]–[Na_2O]=0$.

The Vickers hardness (H_V) was determined from microindentation experiments. Since hardness values of glasses depend on the loading conditions [37,38], all indentations were carried out using identical load and loading time. Furthermore, we note that there was no initiation of radial cracks from the indents at the applied load of 0.49 N. Fig. 10 shows the composition dependence of hardness of the iron-containing and iron-free glasses. In the peralkaline regime, hardness first increases with increasing $[Al_2O_3]$ until reaching its maximum value around $[Al_2O_3]–[Na_2O]=-5$, and then it starts to decrease with further increase of $[Al_2O_3]$. In the peraluminous regime,

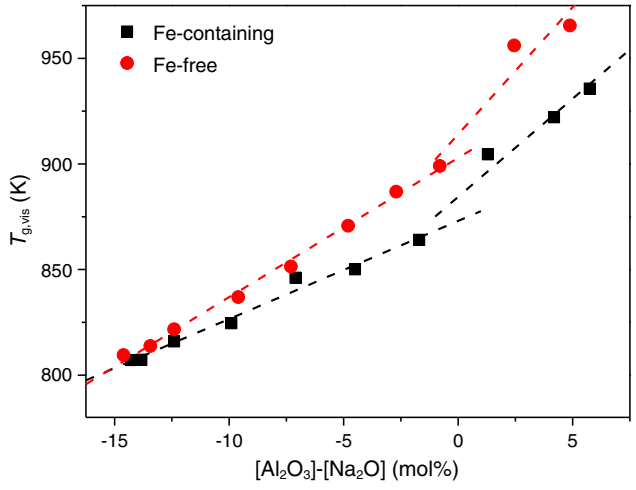

Fig. 2. Composition dependence of the glass transition temperature ($T_{g,vis}$) obtained by fitting the measured viscosity data to Eq. (3) for both iron-free and iron-containing glasses. The dashed lines are linear fits to the data for $[Al_2O_3]–[Na_2O]<0$ and $[Al_2O_3]–[Na_2O]>0$, respectively. The uncertainty of $T_{g,vis}$ is approximately ±5 K.

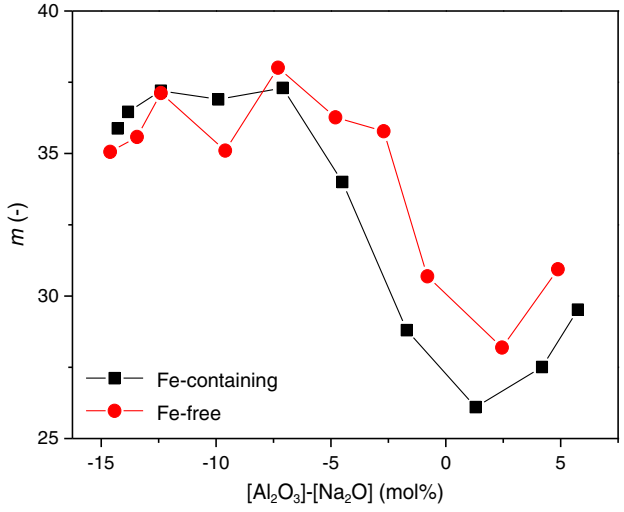

Fig. 3. Composition dependence of the liquid fragility index (m) obtained by fitting the measured viscosity data to Eq. (3) for both iron-free and iron-containing glasses. The error range of m is approximately ±1.

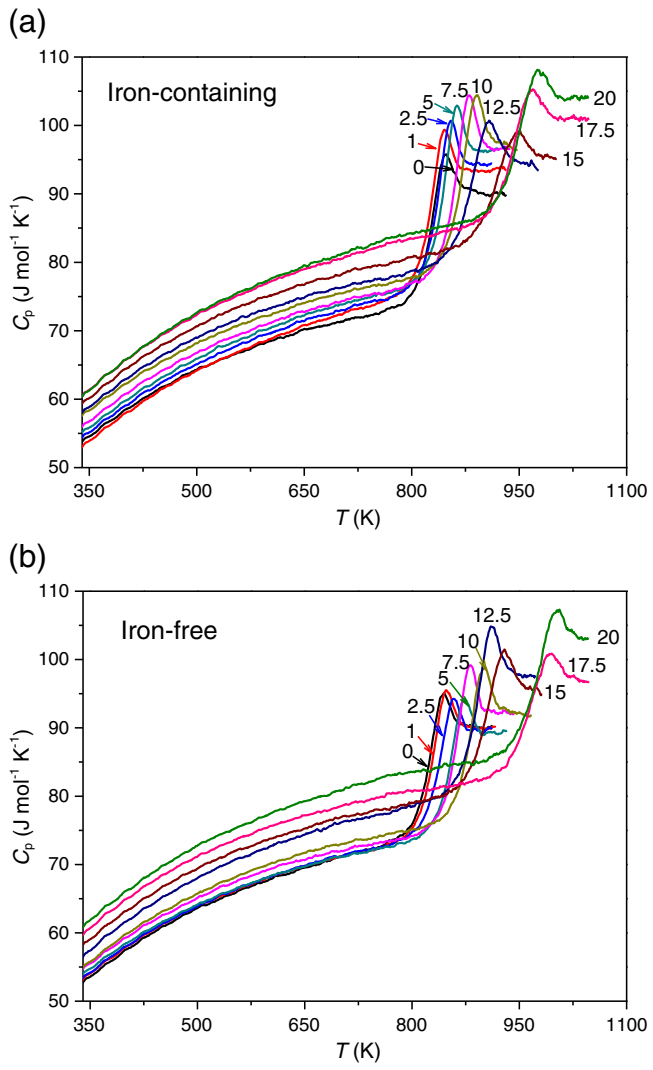

Fig. 4. Glass transitions of the (a) iron-containing and (b) iron-free glasses as determined by DSC at a heating rate of 10 K/min subsequent to a cooling rate of 10 K/min. Plots are shown as the isobaric heat capacity (C_p) against temperature (T). Numbers refer to the substituted amount of Al_2O_3 for SiO_2 (mol%) of the initially designed glass compositions.

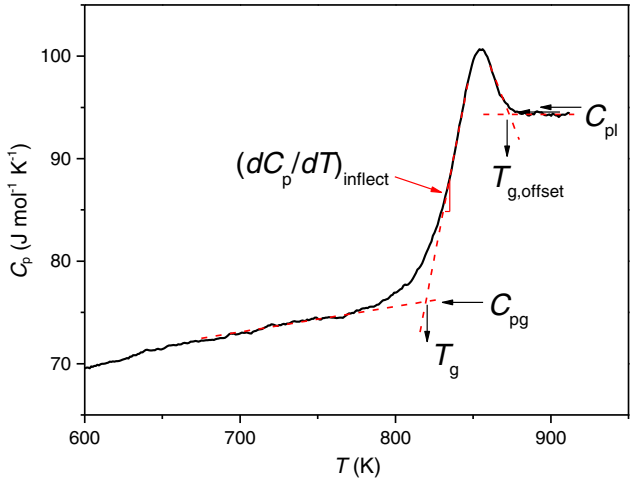

Fig. 5. Illustration of the procedure for determining the characteristic temperatures (T_g and $T_{g,offset}$) and heat capacities (C_{pg}, C_{pl}, and $(dC_p/dT)_{inflect}$) using DSC. The shown curve is for the Al2.5* glass scanned at a heating rate of 10 K/min subsequent to a cooling rate of 10 K/min.

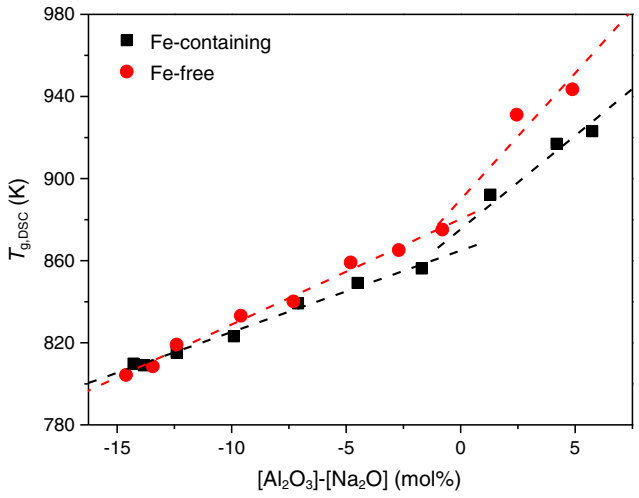

Fig. 6. Composition dependence of the glass transition temperature ($T_{g,DSC}$) as determined by DSC at a heating rate of 10 K/min subsequent to a cooling rate of 10 K/min for both iron-free and iron-containing glasses. The dashed lines are linear fits to the data in the $[Al_2O_3]$–$[Na_2O]<0$ and $[Al_2O_3]$–$[Na_2O]>0$ regimes. The uncertainty of $T_{g,DSC}$ is approximately ± 2–3 K.

H_V again increases with increasing $[Al_2O_3]$. There is thus a minimum value of hardness around $[Al_2O_3]$–$[Na_2O]=0$. In the peraluminous regime, the iron-free glasses are harder than the iron-containing glasses, whereas there are only minor differences in the peralkaline regime.

3.4. Iron redox state

Iron exists primarily in two redox states in glasses (Fe^{2+} and Fe^{3+}). We have determined the $[Fe^{3+}]/[Fe]_{tot}$ ratio, where $[Fe]_{tot}=[Fe^{3+}]+[Fe^{2+}]$, in the iron-containing glasses by ^{57}Fe Mössbauer spectroscopy. The uncertainty of this method is about ± 5%. Details including the experimental procedure can be found in Ref. [30]. As shown in Table 1, the $[Fe^{3+}]/[Fe]_{tot}$ ratio decreases with increasing $[Al_2O_3]$.

4. Discussion

4.1. Thermodynamic vs. kinetic fragilities

DSC measurements can be used to determine the glass transition temperature and obtain thermodynamic measures of liquid fragility. Here we compare the DSC data with the viscosity data with respect to both the glass transition temperatures and the liquid fragility. Fig. 11 shows an approximate equivalence between the $T_{g,DSC}$ and the $T_{g,vis}$ values for all glass samples, although the former is slightly lower than the latter in the range of high temperature. This agrees with the results of previous studies [39,40].

There have been several attempts to connect the kinetic fragility index m determined from viscosity measurements with thermodynamic property changes at the glass transition determined using DSC [20,33,41–44]. “Fragile” liquids have dramatic viscosity changes at the glass transition, and they are thus expected to have large configurational heat capacities, as a consequence of their configurational entropy changing rapidly with temperature [42]. The glassy state contains primarily vibrational degrees of freedom, whereas the liquid state contains both vibrational and configurational degrees of freedom [45]. Therefore, $C_{pl}-C_{pg}$ is approximately equal to the configurational heat capacity. Hence, for most systems, it has been found that $C_{pl}-C_{pg}$ increases with the increase of m, but not all glass-forming liquids follow this trend [33]. The sodium boroaluminosilicate system studied here displays

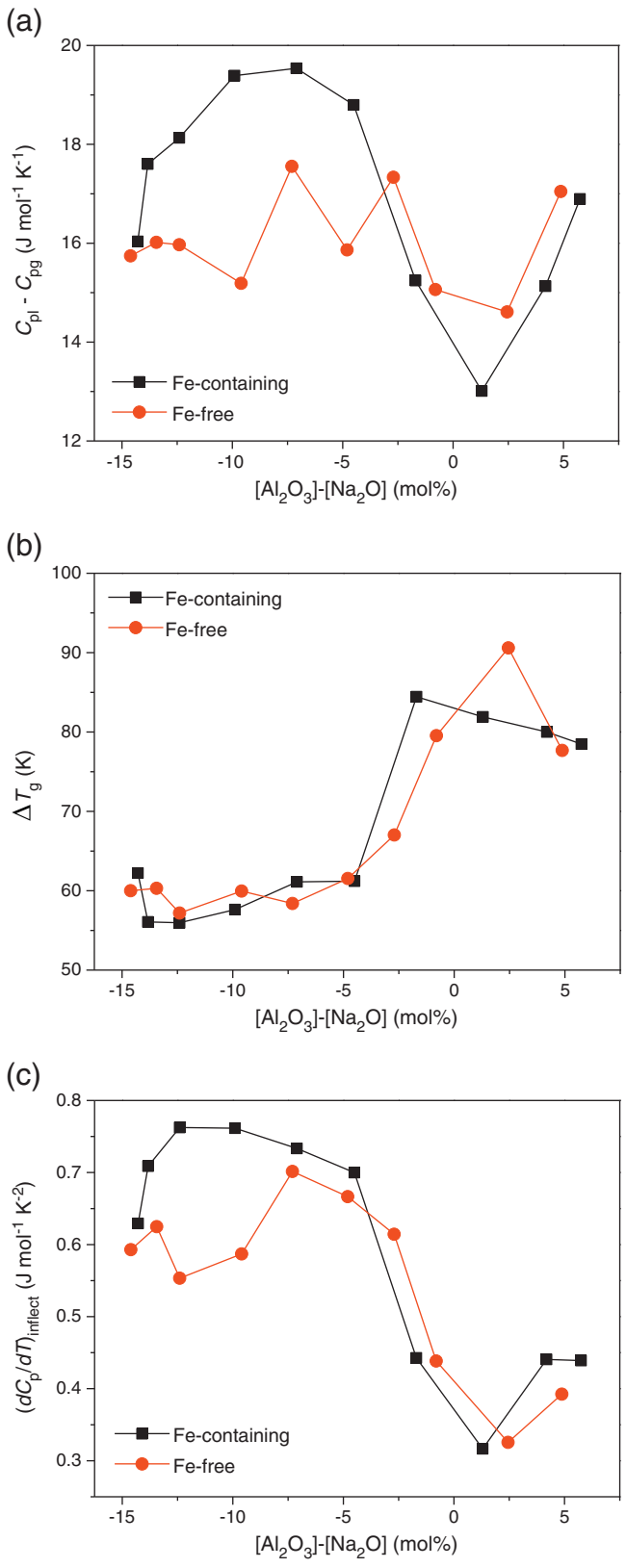

Fig. 7. Composition dependence of (a) jump in heat capacity during glass transition ($C_{pl} - C_{pg}$), (b) glass transition width (ΔT_g), and (c) slope of heat capacity curve during glass transition ($(dC_p/dT)_{inflect}$) for both iron-free and iron-containing glasses. The values were determined by using DSC at a heating rate of 10 K/min subsequent to a cooling rate of 10 K/min. The uncertainty of $C_{pl} - C_{pg}$ is on the order of ±2–3%. The errors in ΔT_g are approximately ±2–3 K. The uncertainty of $(dC_p/dT)_{inflect}$ is approximately ±10%.

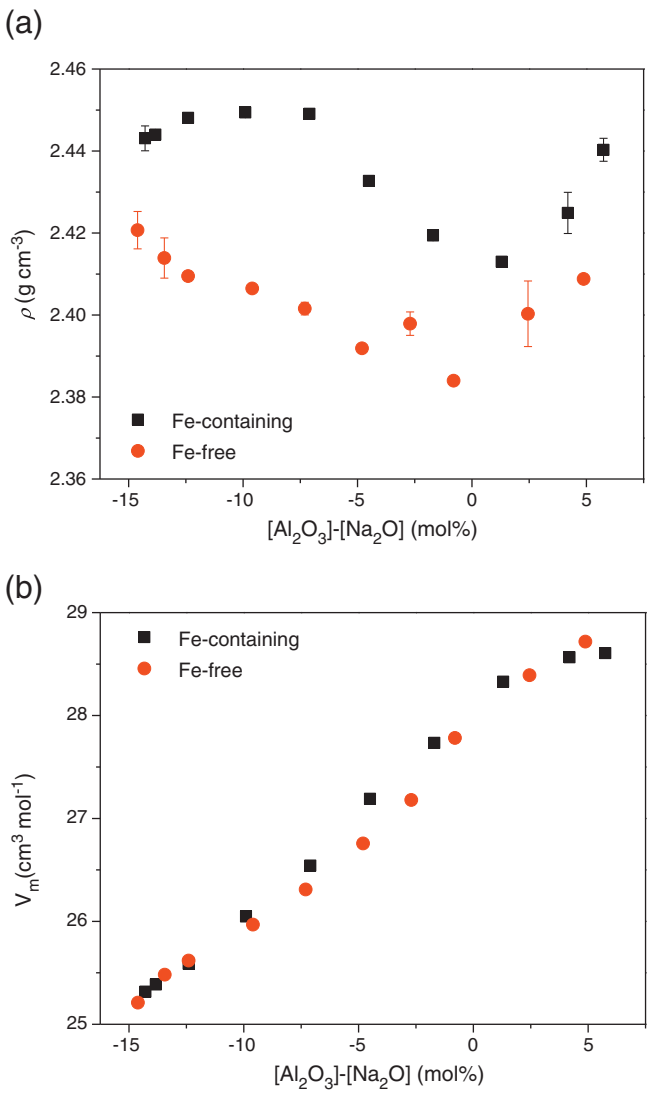

Fig. 8. Composition dependence of (a) density (ρ) and (b) molar volume (V_m) of both iron-free and iron-containing glasses. The errors of the reported density values do not exceed ±1%.

an approximately parallel relation between $C_{pl} - C_{pg}$ and m (Fig. 12(a)).

Furthermore, we have determined both the glass transition width ΔT_g and the slope at the inflection point of the C_p jumping curve in the glass transition regime, i.e., $(dC_p/dT)_{inflect}$, from DSC measurements (Fig. 5). These two values are inversely correlated, i.e., the larger the value of ΔT_g, the smaller the value of $(dC_p/dT)_{inflect}$. These values are also expected to be correlated with the kinetic fragility index m [46]. This is because an increase in the fragility of a system results in a more rapid increase of the free energy barriers to structural relaxation as the system is cooled [47]. Above the glass transition temperature, the free energy barriers are lower for the higher-fragility system due to entropic effects, i.e., it follows more closely the supercooled liquid path. Below the glass transition temperature, the free energy barriers are greater for the higher-fragility system due to enthalpic effects, i.e., there must be a sharper departure from the supercooled liquid path and a more sudden glass transition. In other words, a higher value of the fragility m leads to a sharper breakdown of ergodicity and a more well-defined glass transition [48]. We therefore expect ΔT_g to be inversely correlated with m and $(dC_p/dT)_{inflect}$ to be positively correlated with m, which exactly agrees with our experimental

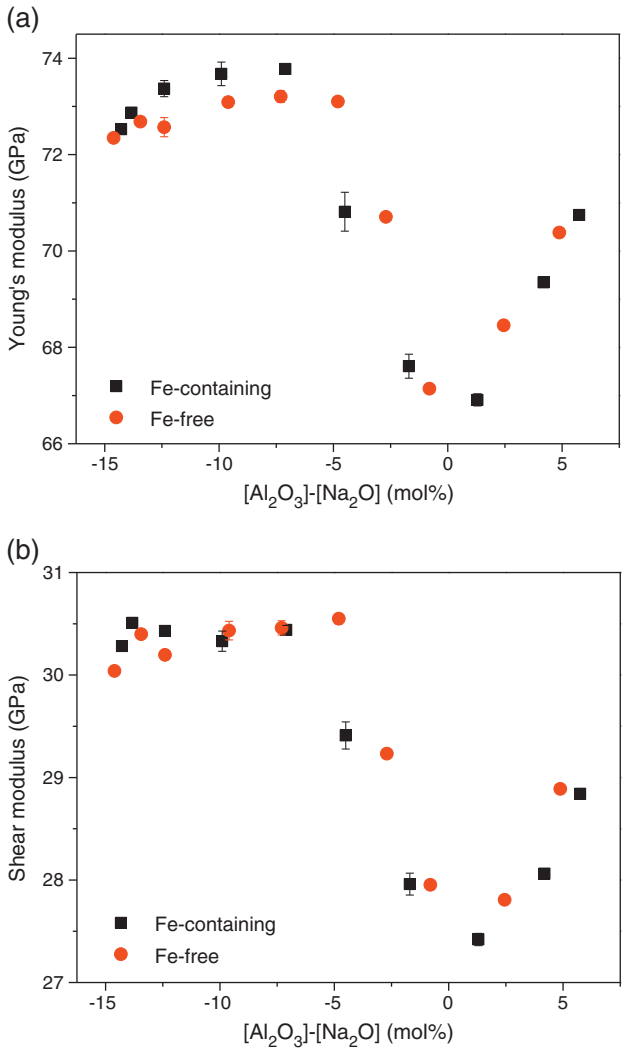

Fig. 9. Composition dependence of (a) Young's modulus E and (b) shear modulus G of both iron-containing and iron-free glasses.

findings (Fig. 12(b)). The dashed lines in Fig. 12(b) are just drawn as guides for the eye and show the inverse correlation for ΔT_g and $(dC_p/dT)_{inflect}$, but not necessarily a linear correlation. A detailed trend for the changes of both ΔT_g and $(dC_p/dT)_{inflect}$ with m still

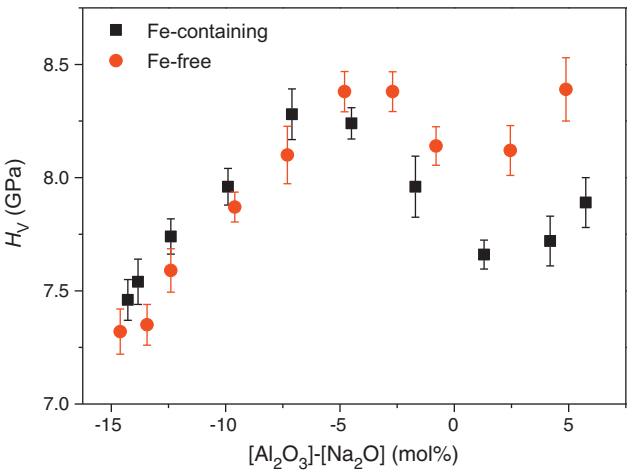

Fig. 10. Composition dependence of Vickers microhardness (H_V) of both iron-containing and iron-free glasses.

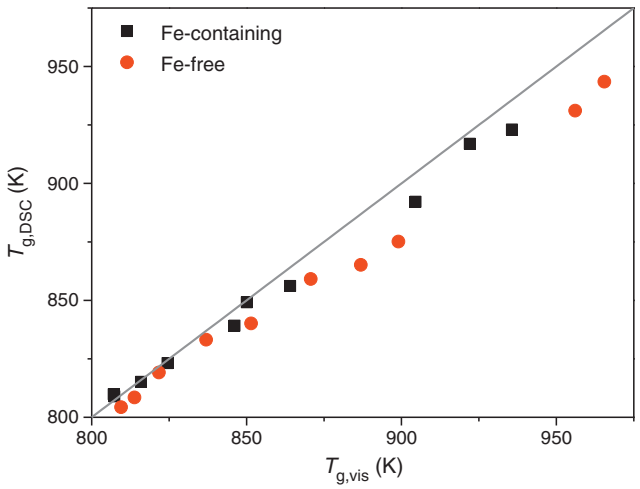

Fig. 11. Comparison of the glass transition temperatures obtained from viscosity measurements ($T_{g,vis}$) and those obtained DSC measurements ($T_{g,DSC}$). $T_{g,DSC}$ is the onset glass transition temperature determined at the upscan rate 10 K/min that is equal to the prior downscan rate, whereas $T_{g,vis}$ is determined as the temperature at which the viscosity is equal to 10^{12} Pa·s. The uncertainty of $T_{g,DSC}$ is approximately ±2–3 K. The uncertainty of $T_{g,vis}$ is approximately ±5 K.

needs to be revealed by expanding the data sets and extending the fragility range.

4.2. Structural and topological origins of glass properties

In order to understand the structural and topological origins of the observed composition–property correlations, we have clarified the structural roles of sodium and the network formers as a function of composition using multinuclear NMR spectroscopy in a parallel study [28]. According to this study, in the peralkaline regime ($[Al_2O_3]$–$[Na_2O]<0$), sodium is first used to charge compensate Al^{IV}, i.e., all aluminum is four-fold coordinated and unaffected by compositional changes in this regime. These results thereby confirm the preference in the formation of Al^{IV} over that of B^{IV} [22]. The excess sodium not used for charge compensating aluminum can be used to convert trigonal to tetrahedral boron or to create non-bridging oxygens (NBOs) on silicon and/or boron. There is a competition among these three structural roles of sodium and some of the species like Al^{IV}, Al^{V}, B^{IV}, B^{III}, Si^{IV}, and NBO coexist. With the increase of $[Al_2O_3]$, the concentration of Al^{IV} increases while the concentrations of NBOs and B^{IV} decrease as shown in Fig. 13(a). In the peraluminous regime ($[Al_2O_3]$-$[Na_2O]>0$), all sodium is used to charge compensate Al^{IV} and some of the aluminum is found in five-fold coordination due to the insufficient amount of sodium. Therefore, there are essentially no B^{IV} or NBOs on silicon or boron in this regime. The concentration of Al^{V} increases with increasing $[Al_2O_3]$, while the local sodium environment is unaffected by composition in the peraluminous regime. In the following sections, we discuss the structural and topological origins of the composition and structure dependence of various properties.

4.2.1. Glass transition temperature

The scaling of glass transition temperature (T_g) with composition can be accurately predicted using temperature-dependent constraint theory [20,49–52]. This is done by counting the number of two-body bond-stretching and three-body bond-bending constraints associated with the network forming species as a function of composition and temperature [52,53], since T_g increases with the average number of network constraints per atom [49,50]. In other words, T_g is governed by the network connectivity and introducing NBOs into a SiO_2 glass thus generally decreases T_g [2], whereas converting boron from three-fold to four-fold coordination in a B_2O_3 glass increases T_g [50].

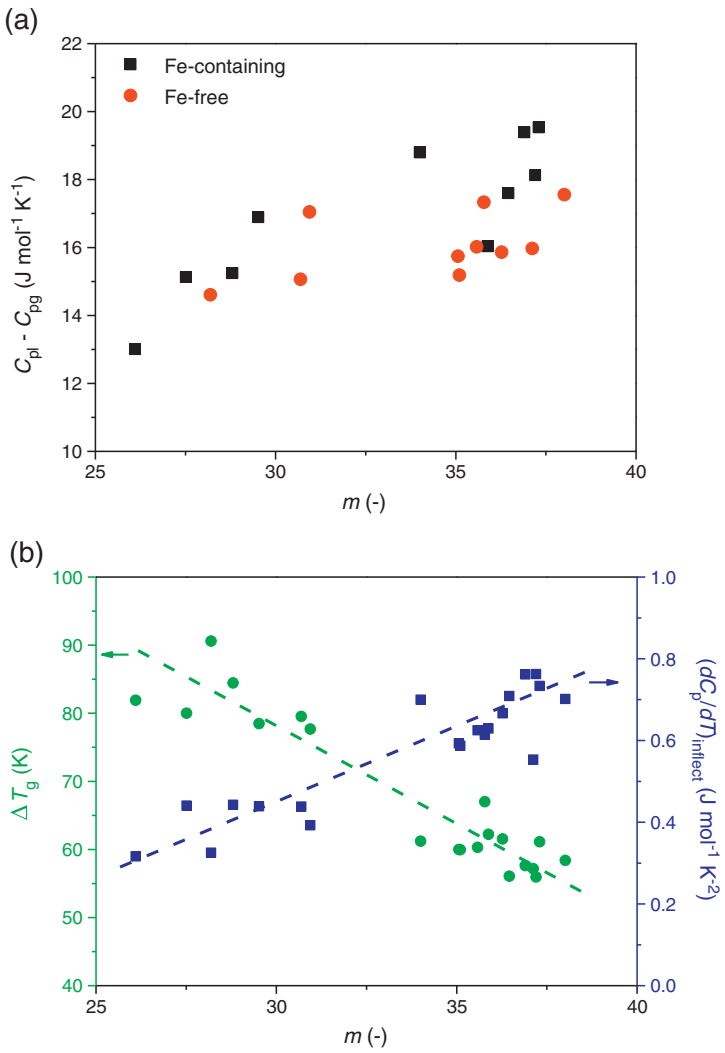

Fig. 12. (a) Jump in heat capacity during glass transition ($C_{pl} - C_{pg}$) from DSC measurements as a function of the liquid fragility index (m) from viscosity measurements. (b) Glass transition width (ΔT_g) and slope of the rising heat capacity curve at the inflection point during glass transition ($(dC_p/dT)_{inflect}$) from DSC measurements as a function of m from viscosity measurements for both iron-containing and iron-free glasses. The error range of m is approximately ± 1. The uncertainty of $C_{pl} - C_{pg}$ is on the order of ± 2–3%. The errors in ΔT_g are approximately ± 2-3 K. The uncertainty of $(dC_p/dT)_{inflect}$ is approximately ± 10%. The dashed lines are drawn as guides for the eyes.

In this study we use the concept of topological constraints to explain the composition dependence of T_g.

In Figs. 2 and 6 it is seen that T_g generally increases with increasing $[Al_2O_3]$. In the peralkaline regime, the number of constraints increases with increasing $[Al_2O_3]$, since the concentration of NBOs decreases as sodium is used for charge compensating Al^{IV}. However, the concentration of B^{IV} also decreases (Fig. 13(a)), but apparently this effect is relatively small compared to the effect of removing NBOs due to the low concentration of B_2O_3 (5 mol%). Around $[Al_2O_3]$-$[Na_2O] = 0$, the slope of T_g vs. $[Al_2O_3]$ changes, i.e., T_g changes more rapidly with increasing $[Al_2O_3]$ in the peraluminous regime. In this regime, both boron speciation and the sodium environment are essentially unaffected by composition. Therefore, the change of T_g in this regime must be due to the changes in the aluminum speciation. When we substitute Al_2O_3 for SiO_2 in this regime, we incorporate higher coordinated aluminum species (i.e., Al^V) in the network, while removing four-fold coordinated silicon species. The higher coordination of aluminum contributes a greater number of constraints than silicon [54], and hence T_g increases.

4.2.2. Liquid fragility index

The scaling of the liquid fragility index m with composition can also be predicted using temperature-dependent constraint theory. m is calculated from the temperature derivative of the number of atomic constraints, as described in detail elsewhere [49,50]. For borosilicate and borate glasses, boron speciation is the main contributor to increasing the fragility index [20,55]. This is because fragility is a first-derivative property and the constraint onset temperature (i.e., temperature at which the constraints become rigid upon cooling) of O–B–O angular constraints is close to T_g. Consequently, the derivative of the O–B–O constraints is large, and these constraints therefore have a large positive contribution to m.

There are five O–B–O constraints for every tetrahedral boron and only three for every trigonal boron. For our glasses, in the peralkaline regime, N_4 is relatively constant at low $[Al_2O_3]$ (Fig. 13(a)). As $[Al_2O_3]$ increases, N_4 decreases dramatically and reaches nearly 0% around $[Al_2O_3]$–$[Na_2O] = 0$, i.e., the total number of O–B–O constraints decreases, in agreement with the decrease of m in the same regime (Fig. 3). This indicates that the boron speciation plays a dominant role in controlling the fragility of these boroaluminosilicate liquids in the peralkaline regime. In the peraluminous regime, the boron speciation is unaffected by composition (Fig. 13(a)). Even though, fragility increases when substituting Al_2O_3 for SiO_2 (Fig. 3). This might be due to the greater number of angular constraints with increasing concentration of Al^V. To illustrate the dominant role of boron

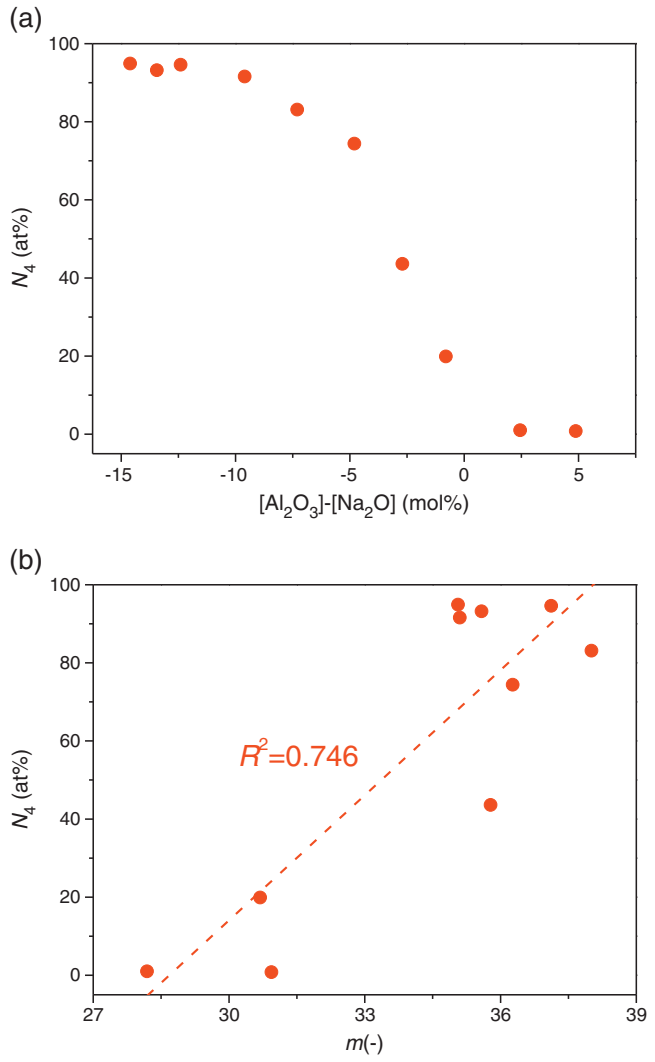

Fig. 13. (a) Composition dependence of the fraction of tetrahedral to total boron (N_4) for the iron-free glasses [28]. (b) N_4 as a function of liquid fragility index (m) for the iron-free glasses. The uncertainties in N_4 are on the order of ± 0.2%. The error range of m is approximately ± 1. The line is drawn as a guide for the eye.

speciation in controlling the fragility of these boroaluminosilicate liquids, particularly in the peralkaline regime, N_4 is plotted as a function of m in Fig. 13(b). We find that around 75% of the composition variation of m can be accounted for by the change in boron speciation.

In summary, both the liquid fragility and the glass transition temperature are sensitive to a variation in composition for the boroaluminosilicate system, in particular, in the composition region around $[Al_2O_3]$–$[Na_2O]=0$. This is crucial for optimizing the industrial processes since the glass workability and hence the processing parameters strongly depend on the liquid fragility and the glass transition temperature. The finding is also instructive in designing glass composition in the frame of boroaluminosilicate related products.

4.2.3. Elastic moduli

Young's and shear moduli follow the same trend in terms of their responses to composition change. In Fig. 9, a striking phenomenon can be observed, i.e., there is a minimum of both Young's and shear moduli around $[Al_2O_3]$–$[Na_2O]=0$. The responses of the two moduli to the compositional change are analyzed in terms of three compositional regions as follows.

In the regime of $-15<[Al_2O_3]$–$[Na_2O]<-5$, the moduli increase slightly with increasing $[Al_2O_3]$. This is the same composition regime where there is no change in boron speciation (Fig. 13(a)). In this regime, the concentration of NBOs decreases as Al_2O_3 is substituted for SiO_2, i.e., the network connectivity increases, and this increases the ability of the glasses to resist elastic deformation [56]. In the regime of $-5<[Al_2O_3]$–$[Na_2O]<0$, there is a significant decrease in moduli with increasing $[Al_2O_3]$. This is the same region where N_4 decreases to 0% with increasing $[Al_2O_3]$, suggesting that the moduli are strongly lowered by an increase of the concentration of B^{III}, since B^{III} species make the structure less densely packed, even in such low B_2O_3-containing glasses (5 mol%). In other words, B^{III} reduces the moduli in comparison to B^{IV}. This agrees with the early findings that E-glass fibers have smaller (10%) Young's modulus than E-glass bulk [57,58], because glass fibers have more B^{III} groups and also lower moduli than bulk glass [57]. The glass fibers have higher fictive temperatures (T_f) than bulk glass and B^{III} groups are more abundant in high T_f glasses [59]. Boron speciation thus plays an important role in governing the elastic response of the sodium boroaluminosilicate glasses studied here. In the regime of $[Al_2O_3]$–$[Na_2O]>0$, the elastic moduli increase with increasing $[Al_2O_3]$. This is the regime with no changes in boron speciation, but with an increase of Al^V and Al^V contributes more constraints than Al^{IV}. This increased network connectivity may cause the increase of the elastic moduli. This is why the minimum moduli exist around $[Al_2O_3]$-$[Na_2O]=0$, as shown in Figs. 9a and b.

The identification of these three compositional response regions for elastic moduli is helpful for tailoring other mechanical properties, e.g., the tensile strength and fracture behavior, of the boroaluminosilicate glass product since these properties are closely associated with the elastic moduli [60].

4.2.4. Vickers hardness

Vickers hardness (H_V) is another property that can be predicted using temperature dependent constraint theory [20,61,62]. Unlike T_g and m, H_V is determined by the number of room temperature constraints, i.e., at a temperature where we can assume all constraints to be rigid. In Fig. 10, a H_V minimum around $[Al_2O_3]$–$[Na_2O]=0$ is observed for both the iron-free and the iron-containing series of glasses. The detailed responses of H_V to the compositional change are again discussed in terms of three compositional regions as follows.

In the regime of $-15<[Al_2O_3]$–$[Na_2O]<-5$, H_V increases with increasing $[Al_2O_3]$ and reaches its maximum value around $[Al_2O_3]$–$[Na_2O]=-5$. As also discussed in Section 4.2.3, in this regime, the boron speciation is essentially independent of composition, but the concentration of NBOs decreases with increasing $[Al_2O_3]$. Hence, the increasing number of constraints could cause the increase of hardness. In the regime of $-5<[Al_2O_3]$–$[Na_2O]<0$, H_V decreases with increasing $[Al_2O_3]$, despite the fact that NBOs are gradually converted to bridging oxygens (BOs) in the network. Thus, it can be inferred that the boron speciation also plays a dominant role for controlling hardness in this regime. This could be related to the fact that four-coordinated boron species contributes more constraints than three-fold coordinated boron [54]. In the regime of $[Al_2O_3]$–$[Na_2O]>0$, H_V increases again with increasing $[Al_2O_3]$ right after reaching its minimum value around $[Al_2O_3]$–$[Na_2O]=0$. Boron speciation does not change with composition for $[Al_2O_3]$–$[Na_2O]>0$, implying that the increase of the concentration of five-fold coordinated aluminum could be responsible for the increase in hardness.

In summary, the plastic deformation behavior of these glasses is sensitive to composition variation, in particular, in the composition region around $[Al_2O_3]$–$[Na_2O]=0$. Such information, combined with other results reported in this work, is important for finding the optimum composition that possesses both high mechanical resistance and the economically favorable processing conditions.

4.3. Impact of iron on properties

The substitution of 1 mol% Fe_2O_3 for SiO_2 exhibits an impact on the investigated glass properties as shown in Figs. 2, 6, 9, and 10. To understand this impact, it is important to note that iron exists both as Fe^{2+} and Fe^{3+} in oxide glasses (Fe^0 may also form under reducing conditions). As shown in Table 1, the $[Fe^{3+}]/[Fe^{2+}]$ ratio decreases with increasing $[Al_2O_3]$. This may be due to the increase in the employed melt homogenization temperature with increasing $[Al_2O_3]$, considering that the redox reactions are shifted to the more reduced side with increasing temperature [2]. Knowledge of the iron redox state is important, since Fe^{2+} and Fe^{3+} have different structural roles in silicate glasses. It has been shown that Fe^{2+} can charge compensate Al^{IV}, similar to the role of Na^+ [63,64]. Thus, some Fe^{2+} ions can compete with Na^+ ions for charge compensating Al^{IV}, despite there being a preference for charge balancing by Na^+ [63,64]. Furthermore, Fe^{2+} ions can play a network-modifying role in the network and create NBOs. On the other hand, Fe^{3+} ions play a more network-forming role in the network, similar to that of Al^{3+} [65].

The substitution of iron oxide for SiO_2 generally leads to a decrease in the glass transition temperature (Figs. 2 and 6), elastic moduli (Fig. 9), and Vickers hardness (Fig. 10). This should be because the substitution of Fe_2O_3 increases the total modifier content in the glasses and thus decreases the overall network connectivity. The concentration of Fe^{2+} increases with increasing $[Al_2O_3]$, i.e., the effect of lowering the network connectivity by iron becomes more pronounced as $[Al_2O_3]$ is raised. This could be the reason why the difference between the properties of iron-containing and iron-free glasses becomes greater with increasing $[Al_2O_3]$.

5. Conclusions

We have studied the composition–structure–property relationships of a series of sodium boroaluminosilicate glasses from peralkaline to peraluminous compositions by substituting Al_2O_3 for SiO_2. Interestingly, we find a minimum of the measured property values including density, fragility, Young's and shear moduli, and hardness around $[Al_2O_3]$–$[Na_2O] = 0$ for both iron-free and iron-containing glasses. In detail, we find three compositional response regions for Young's and shear moduli and microhardness. For $-15 < [Al_2O_3]$–$[Na_2O] < -5$, formation of NBOs controls the composition dependence of the properties, whereas they are controlled by boron speciation for $-5 < [Al_2O_3]$-$[Na_2O] < 0$. For $[Al_2O_3]$–$[Na_2O] > 0$, the formation of higher coordinated aluminum species have a pronounced impact on the glass properties. Moreover, we find that T_g is determined by the network connectivity and thus increases with increasing $[Al_2O_3]$–$[Na_2O]$. However, the increase in T_g with $[Al_2O_3]$–$[Na_2O]$ has a greater slope above $[Al_2O_3]$–$[Na_2O] = 0$ than below it. The liquid fragility shows a strong correlation with the fraction of tetrahedral boron in the glasses, in agreement with previous findings for borate and borosilicate glasses. The existence of the minimum and the three compositional response regions are related to boron speciation, i.e., B^{III} and B^{IV}, which contributes a different number of constraints to the glassy networks. The liquid fragility index is thus particularly sensitive to composition variation around $[Al_2O_3]$–$[Na_2O] = 0$. This is crucial for optimizing the industrial processes since the glass workability and hence the processing parameters strongly depend on the liquid fragility. Substitution of a small amount of iron oxide for SiO_2 in the glasses results in lower values of glass transition temperature, hardness, and elastic moduli, since the substitution increases the total modifier content in the glasses and thus decreases the overall network connectivity.

Acknowledgments

We thank the Advanced Materials Processing Laboratory and Characterization Sciences and Services Directorate at Corning Incorporated for help with glass preparation and characterization, respectively. Moreover, we thank Carrie L. Hogue and Adam J. Ellison (Corning Incorporated) for valuable discussions.

References

[1] A. Ellison, I.A. Cornejo, Int. J. Appl. Glass Sci. 1 (2010) 87.
[2] A.K. Varshneya, Fundamentals of Inorganic Glasses, Society of Glass Technology, Sheffield, 2006.
[3] C.M. Jantzen, K.G. Brown, J.B. Pickett, Int. J. Appl. Glass Sci. 1 (2010) 38.
[4] B.O. Mysen, D. Virgo, F.A. Seifert, Am. Miner. 70 (1985) 88.
[5] E. Metwalli, R.K. Brown, J. Non-Cryst. Solids 289 (2001) 113.
[6] D. Zielniok, C. Cramer, H. Eckert, Chem. Mater. 19 (2007) 3162.
[7] A. Saini, A. Khanna, V.K. Michaelis, S. Kroeker, F. Gonzalez, D. Hernandez, J. Non-Cryst. Solids 355 (2009) 2323.
[8] S. Sen, R.E. Youngman, J. Phys. Chem. B 108 (2004) 7557.
[9] M.D. Ingram, Phys. Chem. Glasses 28 (1987) 215.
[10] S.W. Martin, J. Am. Ceram. Soc. 74 (1991) 1767.
[11] M. Schuch, C.R. Müller, P. Maass, S.W. Martin, Phys. Rev. Lett. 102 (2009) 145902.
[12] A.H. Silver, P.J. Bray, J. Chem. Phys. 29 (1958) 984.
[13] P.J. Bray, J.G. O'Keefe, Phys. Chem. Glasses 4 (1963) 37.
[14] S. Greenblatt, P.J. Bray, Phys. Chem. Glasses 8 (1967) 190.
[15] Y.H. Yun, P.J. Bray, J. Non-Cryst. Solids 27 (1978) 363.
[16] Y.H. Yun, S.A. Feller, P.J. Bray, J. Non-Cryst. Solids 33 (1979) 273.
[17] W.J. Dell, P.J. Bray, S.Z. Xiao, J. Non-Cryst. Solids 58 (1983) 1.
[18] J. Zhong, P.J. Bray, J. Non-Cryst. Solids 84 (1986) 17.
[19] J. Zhong, P.J. Bray, J. Non-Cryst. Solids 111 (1989) 67.
[20] M.M. Smedskjaer, J.C. Mauro, R.E. Youngman, C.L. Hogue, M. Potuzak, Y.Z. Yue, J. Phys. Chem. B 115 (2011) 12930.
[21] M. Bertmer, L. Züchner, J.C.C. Chan, H. Eckert, J. Phys. Chem. B 104 (2000) 6541.
[22] J.C.C. Chan, M. Bertmer, H. Eckert, J. Am. Chem. Soc. 121 (1999) 5238.
[23] L. Züchner, J.C.C. Chan, W. Müller-Warmuth, H. Eckert, J. Phys. Chem. B 102 (1998) 4495.
[24] B.C. Bunker, R.J. Kirkpatrick, R.K. Brow, G.L. Turner, C. Nelson, J. Am. Ceram. Soc. 74 (1991) 1430.
[25] W. Loewenstein, Am. Miner. 39 (1954) 92.
[26] L.-S. Du, J.F. Stebbins, J. Non-Cryst. Solids 315 (2003) 239.
[27] L.-S. Du, J.F. Stebbins, J. Phys. Chem. B 107 (2003) 10063.
[28] Q. J. Zheng, R. E. Youngman, C. L. Hogue, J. C. Mauro, M. Potuzak, A. J. Ellison, M. M. Smedskjaer, Y. Z. Yue, to be published.
[29] A.K. Varshneya, Int. J. Appl. Glass Sci. 1 (2010) 131.
[30] M.M. Smedskjaer, Q.J. Zheng, J.C. Mauro, M. Potuzak, S. Mørup, Y.Z. Yue, J. Non-Cryst. Solids 357 (2011) 3744.
[31] M. Solvang, Y.Z. Yue, S.L. Jensen, D.B. Dingwell, J. Non-Cryst. Solids 351 (2005) 499.
[32] J.C. Mauro, Y.Z. Yue, A.J. Ellison, P.K. Gupta, D.C. Allan, Proc. Natl. Acad. Sci. U.S.A. 106 (2009) 19780.
[33] C.A. Angell, Science 267 (1995) 1924.
[34] Q.J. Zheng, J.C. Mauro, A.J. Ellison, M. Potuzak, Y.Z. Yue, Phys. Rev. B 83 (2011) 212202.
[35] K. Levenberg, Quart. Appl. Math. 2 (1944) 164.
[36] D.W. Marquardt, J. Soc. Indust. Appl. Math. 11 (1963) 431.
[37] H. Li, R.C. Bradt, J. Non-Cryst. Solids 146 (1992) 197.
[38] R. Roesky, J.R. Varner, J. Am. Ceram. Soc. 74 (1991) 1129.
[39] Y.Z. Yue, J. Non-Cryst. Solids 354 (2008) 1112.
[40] Y.Z. Yue, J. Non-Cryst. Solids 355 (2009) 737.
[41] L.-M. Martinez, C.A. Angell, Nature 410 (2001) 663.
[42] D.H. Huang, G.B. McKenna, J. Chem. Phys. 114 (2001) 5621.
[43] C.M. Roland, P.G. Santangelo, C.G. Robertson, K.L. Ngai, J. Chem. Phys. 118 (2003) 10351.
[44] L.M. Wang, C.A. Angell, R. Richert, J. Chem. Phys. 125 (2006) 074505.
[45] M. Potuzak, J.C. Mauro, T.J. Kiczenski, A.J. Ellison, D.C. Allan, J. Chem. Phys. 133 (2010) 091102.
[46] C.A. Angell, Chem. Rev. 102 (2002) 2627.
[47] J.C. Mauro, R.J. Loucks, Phys. Rev. E 78 (2008) 021502.
[48] J.C. Mauro, D.C. Allan, M. Potuzak, Phys. Rev. B 80 (2009) 094204.
[49] P.K. Gupta, J.C. Mauro, J. Chem. Phys. 130 (2009) 094503.
[50] J.C. Mauro, P.K. Gupta, R.J. Loucks, J. Chem. Phys. 130 (2009) 234503.
[51] M.M. Smedskjaer, J.C. Mauro, S. Sen, Y.Z. Yue, Chem. Mater. 22 (2010) 5358.
[52] J.C. Mauro, Am. Ceram. Soc. Bull. 90 (4) (2011) 31.
[53] M. Bauchy, M. Micoulaut, J. Non-Cryst. Solids 357 (2011) 2530.
[54] J.C. Phillips, J. Non-Cryst. Solids 34 (1979) 153.
[55] Q.J. Zheng, J.C. Mauro, M.M. Smedskjaer, R.E. Youngman, M. Potuzak, Y.Z. Yue, J. Non-Cryst. Solids 358 (2012) 658.
[56] M.R. DeGuire, S.D. Brown, J. Am. Ceram. Soc. 67 (1984) 270.
[57] N. Lonnroth, C.L. Muhlstein, C. Pantano, Y.Z. Yue, J. Non-Cryst. Solids 354 (2008) 3887.
[58] W.H. Otto, J. Am. Ceram. Soc. 44 (1961) 68.
[59] T.J. Kiczenski, L.-S. Du, J. Stebbins, J. Non-Cryst. Solids 351 (2005) 3571.
[60] W.H. Wang, J. Appl. Phys. 99 (2006) 093506.
[61] M.M. Smedskjaer, J.C. Mauro, Y.Z. Yue, Phys. Rev. Lett. 105 (2010) 115503.
[62] M.M. Smedskjaer, J.C. Mauro, S. Sen, J. Deubener, Y.Z. Yue, J. Chem. Phys. 133 (2010) 154509.
[63] M.P. Dickenson, P.C. Hess, Contrib. Mineral. Petrol. 92 (1986) 207.
[64] S. Rossano, H. Behrens, M. Wilke, Phys. Chem. Miner. 35 (2008) 77.
[65] B.O. Mysen, P. Richet, Silicate Glasses and Melts – Properties and Structure, Elsevier, Amsterdam, 2005.

Paper IV

Journal of Non-Crystalline Solids 358 (2012) 658–665

Contents lists available at SciVerse ScienceDirect

Journal of Non-Crystalline Solids

journal homepage: www.elsevier.com/ locate/ jnoncrysol

Glass-forming ability of soda lime borate liquids

Qiuju Zheng [a,b], John C. Mauro [b,*], Morten M. Smedskjaer [b], Randall E. Youngman [b], Marcel Potuzak [b], Yuanzheng Yue [a,c,**]

[a] Section of Chemistry, Aalborg University, DK-9000 Aalborg, Denmark
[b] Science and Technology Division, Corning Incorporated, Corning, 14831 NY, USA
[c] Key Laboratory of Glass and Ceramics, Shandong Polytechnic University, Jinan 250353, China

ARTICLE INFO

Article history:
Received 22 September 2011
Received in revised form 3 November 2011
Available online 28 November 2011

Keywords:
Glass-forming ability;
Glass stability;
Soda lime borate glasses;
Fragility;
Boron speciation

ABSTRACT

We investigate the composition dependence of glass-forming ability (GFA) of a series of iron-containing soda lime borate liquids by substituting Na_2O for B_2O_3. We have characterized GFA by measuring the glass stability against crystallization using a differential scanning calorimeter (DSC). The results show that the GFA decreases when substituting Na_2O for B_2O_3. Moreover, we find that there is no direct link between the kinetic fragility and GFA for the soda lime borate series studied herein. We have also discovered and clarified a striking thermal history dependence of the glass stability against crystallization. In particular, the two glasses containing 20 and 25 Na_2O mol% do not exhibit crystallization exotherms during the second DSC upscan at 10 and 20 K/min following prior slow (10 and 20 K/min) downscans. This indicates that the glass stability of these compositions can be enhanced by cooling their melts to the glassy state slowly, before any reheating. We explain this phenomenon in terms of the thermal history dependence of boron speciation.

1. Introduction

Inorganic glasses are predominantly produced using the melt-quenching technique, where the batch materials are heated to a temperature above the liquidus temperature and then cooled sufficiently fast to avoid crystallization [1–3]. In order to optimize the glass production process, it is important to know the glass-forming ability (GFA) of the melt. The GFA has been systematically investigated for a range of silicate [4], aluminosilicate [5], borosilicate [6], alkali borate [7], and alkaline earth borate [6] liquids. Traditionally borate glasses have found only limited applications due to their poor chemical durability, but recently it has been found that borate glass nanofibers are bioactive and promote the healing of flesh wounds [8]. Hence, it has become increasingly important to understand the GFA of more complex borate liquids. To the best of our knowledge, the GFA of alkali alkaline earth borate liquids has not received much attention. Moreover, the so-called boron anomaly makes the structural foundation of borate glass and liquid properties especially interesting. In borate compositions, the initial addition of alkali or alkaline earth oxides affects properties differently compared to further additions of these same modifiers due to conversion of boron between three-fold (trigonal) coordination and four-fold (tetrahedral) coordination [9]. Hence, the effect could also cause an "anomalous" composition dependence of GFA, and it may thus be particularly interesting to explore this effect [7,9,10]. In this paper, we therefore attempt to quantify and understand the GFA of a series of soda lime borate compositions and connect these results back to general features of glass formation in inorganic liquids.

GFA is a measure of how easily a melt is vitrified and can be quantified by determining the critical cooling rate q_c [1], which is defined as the minimum cooling rate required to vitrify a melt, i.e., to obtain a glass with a crystal concentration lower than a certain standard value such as 1 ppm. However, it is difficult and time-consuming to determine q_c precisely, and therefore alternative methods for quantifying GFA have been developed. For example, various glass stability (GS) parameters have been proposed [6,11]. Generally speaking, these parameters all describe the ability of a glass to bypass crystallization upon heating. It has been found that GFA and GS parameters have a direct relationship [4,5], i.e., GS increases with increasing GFA. While there are several proposed metrics for GS, the Hruby parameter (K_H) shows a better correlation with GFA compared with other parameters [12]. Therefore, we use K_H as a measure of GFA in this work. K_H can be calculated from three characteristic temperatures:

$$K_H = \frac{T_c - T_g}{T_m - T_c}, \quad (1)$$

where T_g is the onset glass transition temperature, and T_c and T_m are the onset temperatures of the crystallization peak and the melting peak during heating. A high value of K_H indicates high glass stability. These characteristic temperatures can be determined experimentally using

* Corresponding author. Tel.: +1 607 974 2185; fax: +1 607 974 2410.
** Corresponding author. Tel.: +45 99408522; fax: +45 9635 0558.
E-mail addresses: mauroj@corning.com (J.C. Mauro), yy@bio.aau.dk (Y.Z. Yue).

0022-3093/$ – see front matter © 2011 Elsevier B.V. All rights reserved.
doi:10.1016/j.jnoncrysol.2011.11.004

differential scanning calorimetry (DSC). A typical DSC curve for a glass exhibiting high tendency for crystallization has three well-defined characteristic peaks upon heating: an endothermic glass transition peak, an exothermic crystallization peak, and an endothermic melting peak (Fig. 1). T_g, T_c, and T_m are the onset temperatures of these three peaks, which are determined as the intersection of tangents to the curve, traced on the baseline and on the peak side (Fig. 1). This method is called the "tangent method" [13] and it has its limitations due to the uncertainty in drawing tangents along the sides of the DSC peaks. The inherent drawbacks of using the GS parameters such as K_H are discussed later in this paper.

Shear viscosity of glass-forming liquids is an important temperature-dependent property governing glass formation [14]. It is also related to the GFA, since the flow behavior determines the kinetic activation barriers for both nucleation and crystal growth [6]. Several models have been proposed for describing the temperature dependence of the viscosity (η) of a melt, e.g., Vogel–Fulcher–Tammann (VFT) [15] and Avramov–Milchev (AM) [16]. However, these models exhibit systematic error when extrapolating to low temperatures as described elsewhere [17]. Recently, based on energy landscape analysis and the temperature-dependent constraint model for configurational entropy [18–20], Mauro et al. have derived a new three-parameter viscosity model [17]:

$$\log \eta = \log \eta_\infty + \frac{K}{T}\exp\left(\frac{C}{T}\right) \tag{2}$$

where η_∞ is the high-temperature viscosity limit and K and C are constants. This model has been shown to provide improved fitting quality of measured viscosity–temperature curves compared to the existing models. Furthermore, it provides a physically realistic description of liquid dynamics across the full range of temperatures [17,21]. Based on the analysis in [17,21], it has been concluded that η_∞ is a universal composition-independent constant equal to approximately 10^{-3} Pa s. Since the viscosity at T_g (η_{Tg}) is equal to 10^{12} Pa s for oxide glasses [22], $\log \eta_{Tg} - \log \eta_\infty = 12-(-3) = 15$. Eq. (2) can then be expressed in terms of the liquid fragility index m and T_g:

$$\log_{10}\eta(T) = -3 + 15\frac{T_g}{T}\exp\left[\left(\frac{m}{15}-1\right)\left(\frac{T_g}{T}-1\right)\right]. \tag{3}$$

The definition of the fragility m is due to Angell [3], who noted that liquids can be classified as either "strong" or "fragile" depending on whether they exhibit an Arrhenius or super-Arrhenius scaling of viscosity with temperature, respectively. The slope of the Angell curve ($\log \eta$ as a function of T_g scaled inverse temperature (T_g/T)) at

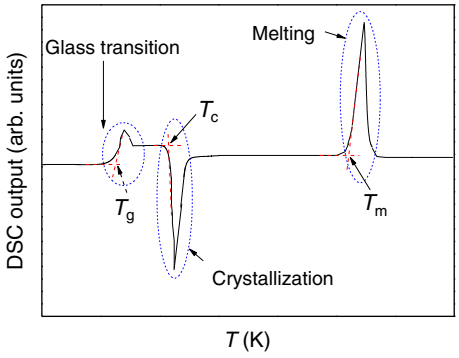

Fig. 1. Typical DSC curve of a glass that easily crystallizes during heating. The procedure for determining the three characteristic temperatures T_g ,T_c and T_m is illustrated.

T_g defines the fragility index,

$$m = \frac{\partial \log_{10}\eta}{\partial\left(T_g/T\right)}\Big|_{T=T_g}. \tag{4}$$

An inverse correlation between fragility index and GFA has been found for various metallic glass-forming liquids in addition to some silicate liquids [23,24]. "Strong" melts have a more consistently rigid structure upon temperature changes compared to "fragile" melts. This rigidity could create steric hindrance towards crystallization during cooling, and therefore strong melts are expected to have better GFA. However, it remains unknown if and how the fragility of borate liquids is correlated with their GFA. Clarifying this relation is one of the objectives of the current study, where we characterize the GFA of these systems by determining their crystallization tendency and viscous flow behavior. We also demonstrate a dramatic enhancement of the glass stability against crystallization for two of the high-Na_2O compositions under study after imposing a new thermal history on these glasses. Finally, we discuss the possible structural origin of the enhancement of glass stability.

2. Experiments

2.1. Sample preparation

Eight glass samples were synthesized using analytical reagent-grade H_3BO_3 (Sigma-Aldrich, ≥99.5%), Na_2CO_3 (Sigma-Aldrich, ≥99.5%), $CaCO_3$ (Fluka, ≥99%), and Fe_2O_3 (Aldrich, ≥99.9%) powders. Seven of them have the compositions (mol%) of $x$$Na_2O$-10CaO-(89-$x$)$B_2O_3-1Fe_2O_3$ with $x = 5$, 10, 15, 20, 25, 30, and 35. The eighth glass has a composition (mol%) of 25Na_2O-10CaO-65B_2O_3 (denoted B-Na25). The thoroughly mixed batches were melted in a covered $Pt_{90}Rh_{10}$ crucible at 1323–1423 K for ~15 min in an inductively heated furnace. Melting by using a covered crucible and the relatively low melting temperatures and short times were chosen to minimize boron evaporation, and homogeneity was ensured by the convection currents created in the melt due to the induction furnace. In order to obtain glasses, the melts were cast onto a brass plate and cooled in air to room temperature. Measurements of the weight loss due to melting indicate that the glasses are within 1–2 wt.% of the desired compositions [25].

Owing to the hygroscopic character of the borate glasses, all samples were kept in glass or plastic containers with desiccant. All of the glasses under study besides B-Na25 contain 1 mol% Fe_2O_3, since they have also been used in a parallel study that established the influence of boron speciation on ionic transport [26]. The transport properties were studied using an inward cationic diffusion approach, which requires the presence of a polyvalent element in the glass [27]. Moreover, the structure and topology of these glasses have been studied in [25].

2.2. DSC measurements

For the glass stability investigations, the three characteristic temperatures (T_g, T_c, and T_m) were determined using a calorimetric method as shown in Fig. 1. The differential scanning calorimetry (DSC) measurements were performed with a simultaneous thermal analyzer (STA 449 C Jupiter, Netzsch, Selb, Germany) at a rate of 20 K/min for both up- and downscanning in a purged argon atmosphere. The samples were heated to 1273 K to locate the glass transition, crystallization, and melting peaks. As mentioned earlier, the characteristic temperatures were determined using the "tangent method". This method has uncertainties of approximately ±2 to 3 K.

In order to obtain the heat capacity curves of the standard glass (cooling and heating at 10 K/min), the samples were subjected to two runs of DSC upscans and downscans. The rates of the upscans

and downscans were always equal to 10 K/min. The recorded heat flow of the first upscan reflects the enthalpy response of a sample with an unknown thermal history (i.e., an unknown cooling rate experienced by the sample during melt-quenching), whereas that of the second upscan reflects the enthalpy response of the sample with a well-defined thermal history (i.e., a known cooling rate). The standard T_g is determined from the second upscan curve as the onset temperature of the glass transition peak [28]. The isobaric heat capacity (C_p) curve for each measurement was calculated relative to the C_p curve of a sapphire reference material of comparable mass.

2.3. Viscosity measurements

In order to determine the liquid fragility index, viscosity measurements were performed. The low viscosities (approximately 10^0–10^3 Pa s) were measured using a concentric cylinder viscometer. The viscometer consisted of four parts: furnace, viscometer head, spindle, and sample crucible. The viscometer head (Physica Rheolab MC1, Paar Physica) was mounted on top of a high temperature furnace (HT 7, Scandiaovnen A/S). Spindle and crucible were made of $Pt_{80}Rh_{20}$. The viscometer was calibrated using the National Bureau of Standards (NBS) 710A standard glass. In the high viscosity range (approximately 10^{10}–10^{13} Pa s), the viscosity was measured using micro-penetration viscometry with a vertical dilatometer (Model VIS 405, Bähr-Termoanalyse, Hüllhorst, Germany). The precision of the equipment was tested using the Deutsche Glastechnische Gesellshaft (DGG) standard glass I and was found to be within ±1% of the standard linear viscosities stated in [29]. The viscosity of the $x=35$ composition could not be measured due to its high tendency for crystallization.

2.4. ^{11}B MAS NMR spectroscopy

Boron speciation in glasses depends on thermal history [30]. In order to investigate the thermal history dependence of boron speciation and how it affects GFA of the soda-lime borate liquids, we carried out ^{11}B magic angle spinning (MAS) NMR measurements on selected samples. The NMR spectra were collected at 11.7 T (160.34 MHz resonance frequency) using a 2.5 mm MAS NMR probe and sample spinning at 20 kHz. The data were acquired using a short (π/12) pulse width of 0.6 μs and 1 s recycle delays. 600 scans were collected; data were processed without line broadening and referenced to an external aqueous boric acid sample (19.6 ppm from BF_3-Et_2O).

^{11}B MAS NMR spectra were fit using DMFit [31], with two trigonal and two tetrahedral lineshapes for each spectrum. The trigonal sites were reproduced using second-order quadrupolar broadened lineshapes, and a mixture of Gaussian and Lorentzian lineshapes was sufficient to fit the 4-fold coordinated boron resonances. The experimental data required at least two distinct 3-fold coordinate boron peaks and one 4-fold coordinated boron resonance. A second 4-fold coordinated peak was added to the simulations to account for minor peak intensity to the higher-shielded side of the 4-fold coordinated boron resonance. Regardless of the exact number of distinct sites in these glasses, all data were fit using identical methods and thus uncertainties in the fraction of tetrahedral to total boron (N_4) are on the order of ±0.2%.

2.5. XRD measurements

The resulting crystalline phases after the first DSC scan were determined from X-ray diffraction (XRD) measurements. The quantitative XRD analyses were performed using a PANalytical CUBIX PRO instrument. XRD signals were recorded in the range $5°<2\theta<65°$ with a stepsize of 0.02 and a steptime of 120 sec/step. The X-rays were generated by a Cu Kα target operated at 40 kV and 45 mA. 10 wt.% TiO_2 was added as internal standard by mixing in a Herzog disk mill twice for 30 s each.

3. Results

DSC upscans are performed on the borate glass series at a heating rate of 20 K/min to determine the glass stability upon heating. Fig. 2 shows the temperature dependence of the DSC output (in arbitrary units) for the seven glasses. The first endothermic peak is attributed to the glass transition. For the four glasses with $x=20$, 25, 30, and 35, there is an exothermic peak well above T_g, which is attributed to crystallization of the glass. An endothermic crystal melting peak occurs following the crystallization peak [13]. No crystallization peak is observed for the three glasses with $x=5$, 10, and 15 during dynamic heating at 20 K/min and therefore K_H cannot be calculated for those glasses. This implies that these compositions have higher glass stability than the other compositions [24]. The determined values of T_g, T_c, and T_m and the Hruby parameter K_H [12] are stated in Table 1.

It has been found that GFA and kinetic fragility have an inverse correlation for some glass-forming systems [23,24]. Here the question is whether this inverse relation exists for the soda lime borate liquid series. Fragility is traditionally determined from viscosity measurements to obtain the kinetic fragility index m. Besides determining m, we also determine the thermodynamic values, which are associated with thermodynamic fragility for many glass systems, such as the jump in isobaric heat capacity (C_p) in the glass transition region [3,32–34] and glass transition width (ΔT_g) [35]. Therefore, another question is whether there is a parallel relation between the kinetic and the thermodynamic fragilities.

The temperature dependence of viscosity obtained from both micro-penetration and concentric cylinder viscometry is illustrated by the Angell plot in Fig. 3. The experimental data are fitted to Eq. (3) [17], and the kinetic fragility (m) is derived from the best-fit of Eq. (3) (see Table 1). We find that m increases with increasing concentration of Na_2O, but after reaching its maximum value at $x=25$, it starts to decrease. For the thermodynamic fragility, we determine the C_p jump as $C_{pl}-C_{pg}$, where C_{pg} and C_{pl} are the isobaric heat capacities for the glass at T_g and the liquid, respectively, as shown in Fig. 4. C_{pl} is determined as the offset value of the C_p overshoot above the glass transition range. Another characteristic value is the overshoot value of the glass transition peak, $C_{p.peak}$. It should be noted that this peak value is not the intrinsic heat capacity of the glass at the peak temperature; instead it is a reflection of the kinetic consequence of the glass transition during upscanning. The glass transition width (ΔT_g) is determined as $T_{g\cdot offset}-T_g$, where $T_{g\cdot offset}$ is the temperature at the offset

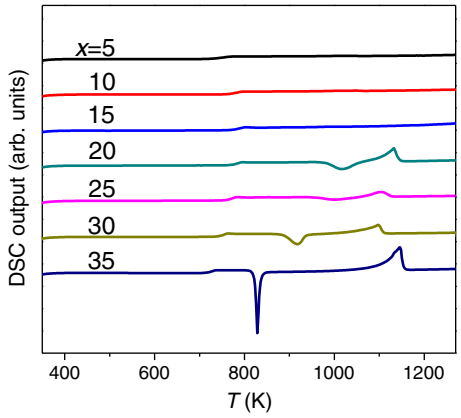

Fig. 2. DSC output (arbitrary units) versus temperature (T) during heating at 20 K/min for the glasses with compositions of xNa_2O–10CaO–(89-x)B_2O_3–1Fe_2O_3.

Table 1
Characteristic temperatures, K_H, N_4 [25], NBO/B, and m of the seven glasses ($x$$Na_2O$-10CaO-(89-$x$)$B_2O_3-1Fe_2O_3$). The errors in the characteristic temperatures are approximately ±2-3 K and uncertainties in N_4 are on the order of ±0.2%.

Sample (x=)	T_g (K)	T_c (K)	T_m (K)	K_H	N_4 [at%]	NBO/B	m
5	728	n/a	n/a	n/a	16	0.197	49 ± 1
10	764	n/a	n/a	n/a	24	0.266	59 ± 1
15	774	n/a	n/a	n/a	36	0.316	63 ± 1
20	772	979	1062	2.49	40	0.47	67 ± 2
25	760	954	1055	1.92	46	0.634	74 ± 1
30	742	887	978	1.59	43	0.926	65 ± 2
35	715	824	1118	0.37	42	1.247	n/a

of the C_p overshoot. The procedures for determining C_{pl}, C_{pg}, $C_{p.peak}$, and ΔT_g are illustrated in the inset of Fig. 4.

The composition dependencies of the values of C_{pl}–C_{pg}, $C_{p.peak}$–C_{pg}, and ΔT_g are shown in Figs. 5–7, respectively. It can be seen that there is no apparent trend in C_{pl}–C_{pg} with composition (Fig. 5), yet there is a trend in $C_{p.peak}$–C_{pg} and ΔT_g with composition (Fig. 6). The kinetic fragility (quantified by m) shows a positive correlation with the values of $C_{p.peak}$–C_{pg} and the glass transition width, which are in this work regarded as indirect measures of the thermodynamic fragility. This is expected because fragility is fundamentally a kinetic property, and the glass transition width is a reflection of kinetics (i.e., a steeper viscosity curves gives a more sudden breakdown of ergodicity [35,37] at T_g). But $C_{pl} - C_{pg}$ is a purely thermodynamic quantity, and the connection to kinetic fragility is apparently lost for these borate glasses. In Section 4.2, we will discuss whether there is a correlation between fragility and GFA.

Interestingly, two of the glasses under study (with $x = 20$ and 25) do not exhibit any crystallization exotherms during the second DSC upscan at 20 K/min to 1273 K when they have been subjected to a prior upscan to 1273 K at 20 K/min and a subsequent downscan at the same rate. The DSC curves for the glass with $x = 20$ are shown in Fig. 8(a). The same phenomenon is also observed when the second upscan rate is lowered to 10 K/min (Fig. 8(b)). This means that the stability of these two glasses against crystallization is dramatically enhanced after they undergo a slow cooling process. The enhancement of the glass stability can also be observed in glasses containing higher Na_2O content, e.g. glasses with $x = 30$ and 35 as shown in Fig. 9. The glass with $x = 30$ shows a crystallization peak during the first downscan at 20 K/min. This implies that the cooling rate is lower than the critical cooling rate, and hence the melt crystallizes during cooling. After cooling, the sample contains both glass and crystal phases. In the second upscan, there is no crystallization peak, indicating that the remaining glass phase does not crystallize during the second upscan. In other words, the GS of the remaining glass is enhanced after the first downscan. The glass with $x = 35$ shows similar behavior to that with $x = 30$.

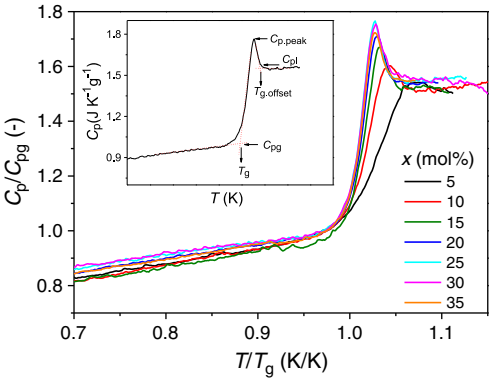

Fig. 4. Glass transition of the glasses ($x$$Na_2O$–10CaO–(89-$x$)$B_2O_3$–1$Fe_2O_3$) determined by DSC at a heating rate of 10 K/min subsequent to a cooling rate of 10 K/min. The plots are shown as the isobaric heat capacity (C_p) divided by C_p at T_g ($C_p/C_p(T_g)$) against T/T_g.

We have also determined the crystal phases of the sample with $x = 20$ resulting from the first DSC upscan. This was done by conducting X-ray diffraction (XRD) measurements on samples that were heated in a muffle furnace by using the same conditions as during the DSC scan. As shown in Fig. 10, the sample that has been heat treated contains both crystalline and glassy phases. Using the Rietveld refinement method with an internal standard, the amounts of crystalline and glassy phase are determined to be 56 and 44 wt.%, respectively. The main crystalline phase (97.7 wt.%) is calcium sodium pentaborate, which consists of complex metaborate sheets with a B_5O_9 building block. The B_5O_9 unit contains BO_4 and BO_3 groups in the ratio of 2:3 in two rings, and Na and Ca are partially ordered in sites in channels between the metaborate sheets [38]. There are also two other low concentration crystals: boron oxide (2.0 wt.%) and iron boride (0.3 wt.%).

4. Discussion

4.1. Glass stability

Fig. 11 (a) shows the Hruby parameter (K_H) as a function of Na_2O concentration (x) for the four glasses with $x = 20$, 25, 30, and 35. In general, the GFA decreases with increasing substitution of Na_2O for

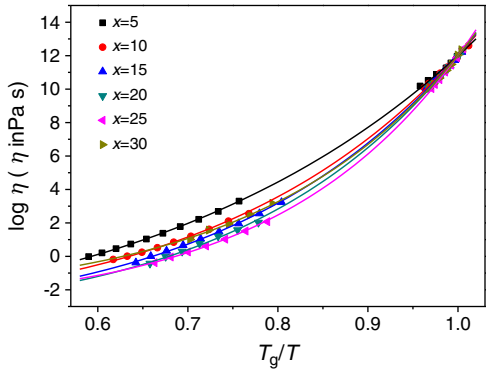

Fig. 3. Angell fragility plot showing the logarithmic viscosity ($\log \eta$) as a function of the T_g scaled inverse temperature (T_g/T) for the glasses with compositions of $x$$Na_2O$–10CaO–(89-$x$)$B_2O_3$–1$Fe_2O_3$.The error ranges for the high viscosity measurements (by the micro-penetration method) and for the low viscosity measurements (by the concentric cylinder method) were $\Delta \log \eta = \pm 0.06$ and ± 0.02 (η in Pa s), respectively [36].

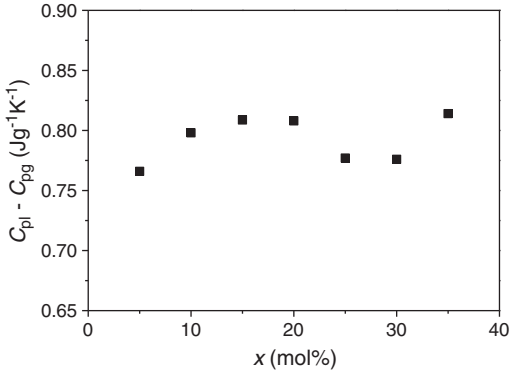

Fig. 5. The step change in the heat capacity (C_{pl}–C_{pg}) at the glass transition as a function of Na_2O content (x) for the seven glasses ($x$$Na_2O$–10CaO–(89-$x$)$B_2O_3$–1$Fe_2O_3$). The step change is determined as $C_{pl} - C_{pg}$, where C_{pg} is the isobaric heat capacity of the glass at T_g and C_{pl} is the isobaric heat capacity of the liquid, which is determined as the offset value of the C_p overshoot above the glass transition range. The uncertainties in $C_{pl} - C_{pg}$ are on the order of ±2–3%.

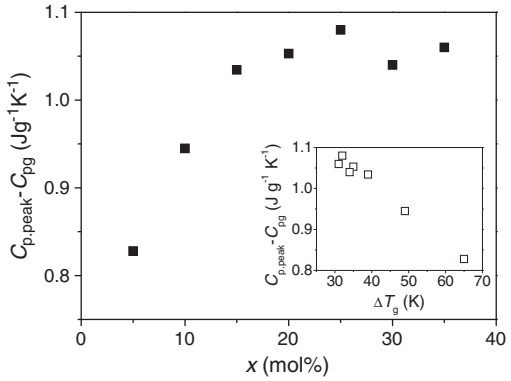

Fig. 6. $C_{p,peak}$–C_{pg} as a function of the Na_2O content (x) for the glasses ($x$$Na_2O$–10CaO–(89-$x$)$B_2O_3$–1$Fe_2O_3$), where $C_{p,peak}$ is the heat capacity value of the C_p overshoot peak. Inset: $C_{p,peak}$-C_{pg} as a function of the glass transition width (ΔT_g) during heating. The uncertainties in $C_{p,peak}$–C_{pg} are on the order of ±2-3%.

B_2O_3. To understand this trend, the fractions of tetrahedral boron to total (N_4) and NBO/B are determined and listed in Table 1, where NBO/B is the average number of non-bridging oxygens per boron tetrahedron or triangle. With the values of N_4, we are able to calculate the number of NBOs per boron. The boron itself can be tetrahedral or trigonal. As shown in Table 1, K_H decreases as the NBO/B increases for $x = 20$, 25, 30, and 35. The K_H values of glasses with $x = 5$, 10, and 15 are unknown higher values, but we suppose that the GFA increases as the value x decreases, i.e., NBO/B decreases. An increase of NBO/B lowers the connectivity of the network, which creates escape channels for the moving particles [39]. Consequently it is easy for the particles to rearrange, and hence there may be a greater tendency for crystallization. However, following Phillips–Thorpe constraint theory, we note that a sufficiently low value of NBO/B would also promote crystallization, since rigid structures would then easily percolate throughout the system resulting in crystallization [19,20].

Fig. 11(b) shows N_4 and NBO/B as a function of Na_2O concentration for all seven glasses. The results indicate that the GFA is closely related to the degree of network connectivity [19]. Boron speciation also has a direct influence on the connectivity. However, N_4 does not show a direct relation with K_H. There is apparently an influence of both NBO/B and N_4 on GFA, since both of these parameters affect the degree of network connectivity. This indicates that when comparing two glasses with different amounts of network former, NBO/B plays a determining role in controlling GFA, while the boron speciation plays a less important role. However, when comparing two glasses with the same amount of network former, the N_4 will play an important role, as will be discussed in Section 4.3.

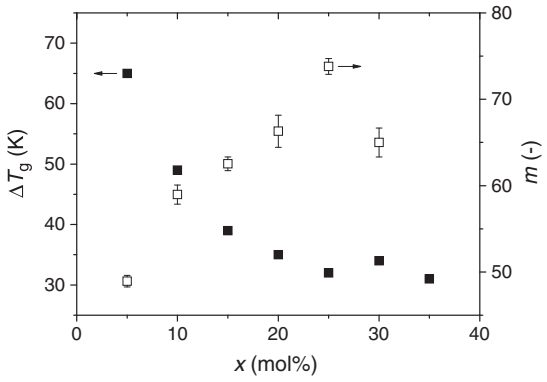

Fig. 7. Glass transition width (ΔT_g) and liquid fragility index (m) as a function of the Na_2O content (x) for the glasses ($x$$Na_2O$–10CaO–(89-$x$)$B_2O_3$–1$Fe_2O_3$). ΔT_g is determined as $T_{g\text{-}offset} - T_g$, where $T_{g\text{-}offset}$ is the temperature at the offset of the C_p overshoot. The errors in ΔT_g are approximately ±2-3 K.

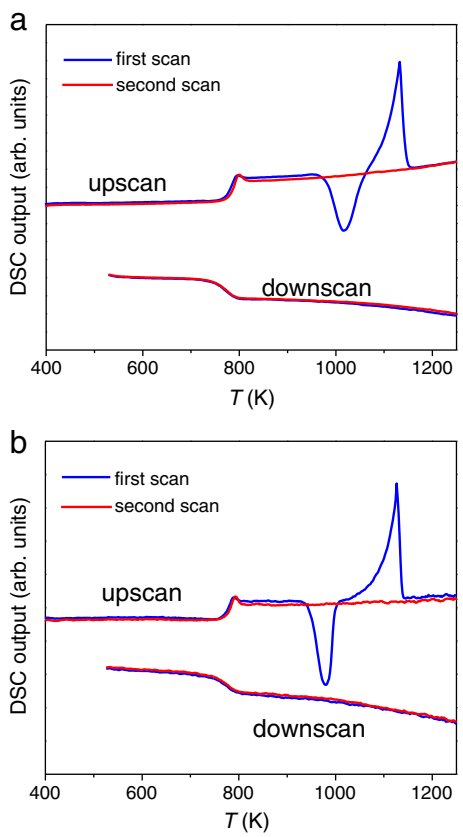

Fig. 8. DSC scans for the glass with $x = 20$ using (a) 20 K/min heating and cooling and (b) 10 K/min heating and cooling.

For three of the glasses under study, the Hruby parameter could not be determined, since no crystallization was observed during heating at the applied rates (10 and 20 K/min). It should be noted that the phase transitions observed during a DSC scan are dynamic, i.e., the characteristic temperatures are dependent on the heating rate employed during the measurements. Especially for glasses with high stability (e.g., $x = 5$, 10, 15), the crystallization and melting processes can be bypassed when using a sufficiently high heating rate. For good glass formers, K_H cannot be determined using the accessible heating rates of a DSC since no crystallization peak is observed. However, theoretically K_H must have a finite value that could be determined using a sufficiently low heating rate beyond the DSC heating rate window. This highlights the limitation of the Hruby parameter with the current DSC techniques. Actually there are several other GS parameters, e.g. K_T, K_W, K_{LL} [4,5], which all use the same characteristic

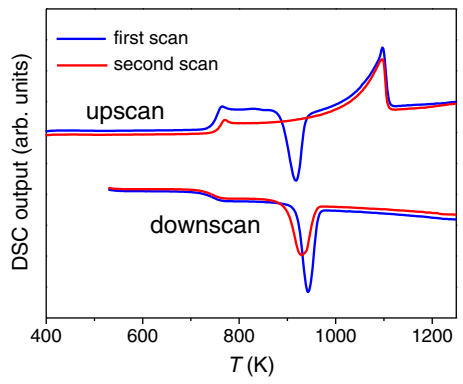

Fig. 9. DSC scans for the glass with $x = 30$ at 20 K/min heating and cooling.

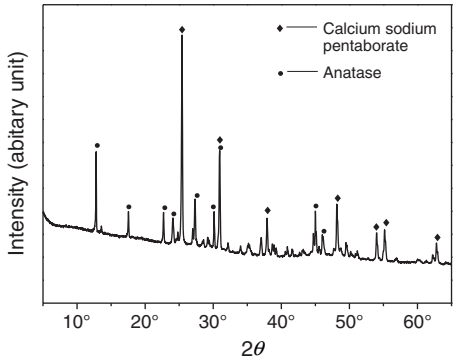

Fig. 10. X-ray diffraction (XRD) pattern of the glass with $x=20$ after crystallization resulting from the first DSC upscan. 10 wt.% of crystalline anatase has been added as an internal standard. The intensities of anatase signals were then used to quantify the amount of the other crystalline phases.

temperatures, i.e., T_g, T_c, and T_m. Here, we have only shown the results of the representative Hruby parameter, since the other parameters show similar trends. However, the inherent limitations of the Hruby parameter represent a universal drawback for any GS parameter, which includes characteristic temperatures. Therefore, a more universal GFA parameter which can be applied to any glass-forming liquid is needed.

4.2. Relationship between Fragility and GFA

In our attempt to understand the composition dependence of GFA for soda lime borate liquids, we will investigate the possible correlation between fragility and GFA. However, for this correlation to be insightful, it is important first to understand the composition

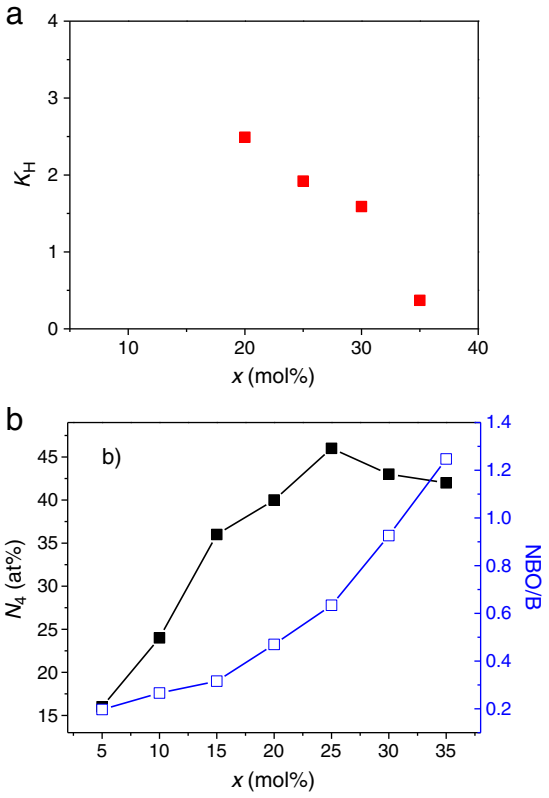

Fig. 11. (a) Hruby parameter (K_H) as a function of the Na_2O content (x) for the four glasses with $x=20$, 25, 30, and 35. (b) N_4 and NBO/B as a function of x. The uncertainties in N_4 are on the order of $\pm 0.2\%$ and the errors in K_H are around ± 0.03.

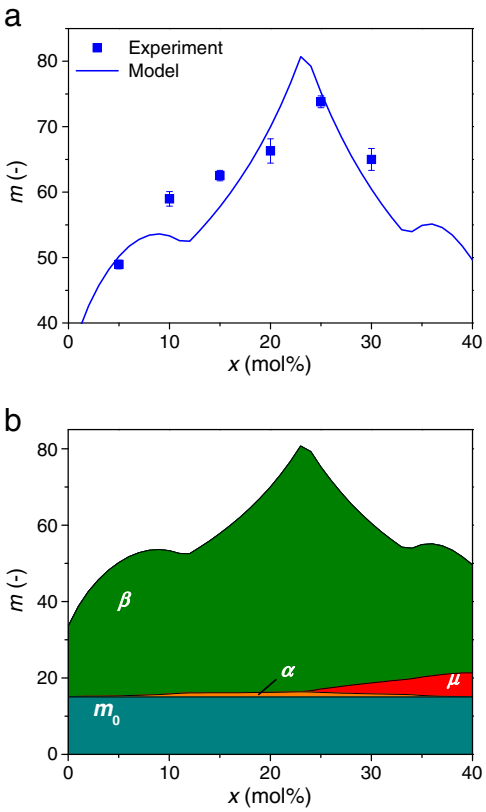

Fig. 12. (a) Dependence of fragility (m) on the Na_2O content (x) for the glasses (xNa_2O–10CaO–(89-x)B_2O_3–1Fe_2O_3). The solid line shows the predicted composition dependence of m using a topological model [25]. (b) Contribution of each type of topological constraint to the calculated fragility. m_0 is defined as the fragility index of the theoretically strongest liquid, and found to be 15 from Eq. (4).

dependence of fragility. We obtain this understanding from topological constraint theory [19,20], since Gupta and Mauro [9,18] have developed a new topological modeling approach that enables accurate prediction of the scaling of both glass transition temperature and fragility with composition. A key feature of the approach is the incorporation of temperature-dependent constraints that become rigid as a liquid is cooled. Recently, Smedskjaer et al. have extended the topological modeling approach to soda-lime borate systems [25]. The basic three steps to apply the topological modeling approach are: (1) identify and count the number of distinct network forming species (i.e., BO_4, BO_3, O, and M^{NB} (network modifiers (Na and Ca) that create NBOs); (2) identify and count the number of constraints associated with each species; and (3) calculate fragility in terms of atomic degrees of freedom. Fig. 12(a) shows both the measured and predicted values of m using the topological constraint model (solid line) [25]. The experimental values of m obtained from viscosity measurements are in good agreement with the modeled fragility values.

Four types of bonding constraints are considered in the model: α) B–O and M^{NB}–O linear constraints; β) O–B–O angular constraints; γ) B–O–B angular constraints; and μ) additional modifier rigidity due to clustering effects. We note that the borate glasses are intrinsically hygroscopic and thus contain hydroxyl groups that are expected to break linear and angular constraints. This effect is not included in the current model, but the good agreement between data and model predictions of m suggests that neglecting the hydroxyl effect is a good approximation. Fig. 12 (b) shows the contribution of each type of constraint to the calculated fragility, i.e., it reveals the topological origins of fragility. The β constraints provide the largest contribution to fragility, while α and μ constraints have little influence on the fragility value. There are five β constraints per four-fold coordinated

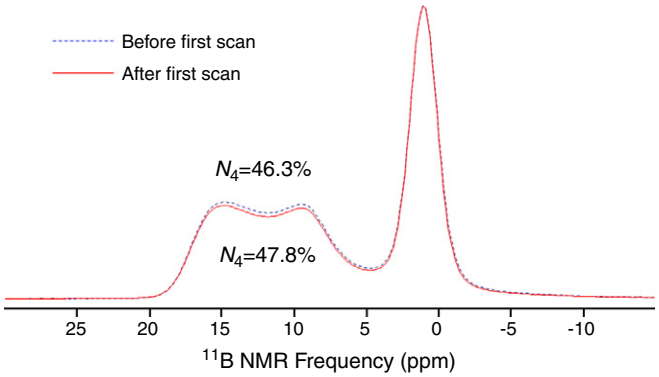

Fig. 13. ^{11}B MAS NMR spectrum of the glass with $x=25$ (Fe-free) before and after first dynamic DSC scan at 20 K/min. The uncertainties in N_4 are on the order of $\pm 0.2\%$.

boron to form a rigid BO_4 tetrahedron and three β constraints per three-fold coordinated boron to keep the BO_3 unit planar [25]. Most importantly, fragility is a first-derivative property and the constraint onset temperature of β constraints is close to T_g. Therefore, the derivative of β constraints is large, and these constraints therefore have a large contribution to fragility. Thus, the boron speciation substantially affects fragility.

The indirect measures of the thermodynamic fragility (i.e., $C_{p,peak}$–C_{pg} and glass transition width) both exhibit a positive correlation with kinetic fragility m. The $C_{p,peak}$–C_{pg} measurement is a reflection of both thermodynamics and kinetics, since higher fragility leads to a sharper and more well-defined glass transition [37] and the value of $C_{p,peak}$ is influenced by the kinetic glass transition process. Therefore, m has a positive relation with both $C_{p,peak}$–C_{pg} and the glass transition width.

An inverse correlation between fragility and GFA has been found for various metallic glasses [24,40], and hence fragility can be used as a quantitative measure of GFA for those systems. However, we find that this is not the case for these soda lime borate compositions. Comparing Fig. 12(a) with Fig. 11(a), we can see that fragility and GFA do not exhibit a linearly inverse relation. In addition, the thermodynamic fragility (shown in Figs. 6 and 7) and GFA also do not exhibit this relation. As mentioned above, both NBO/B and boron speciation affects the degree of network connectivity. Within different amounts of network former, NBO/B plays a determining role in controlling GFA, while the boron speciation plays a less important role for GFA. However, when we calculate the fragility with topological constraint theory, the boron speciation is counted, which plays a less important role for GFA in different compositions. In addition, GFA is related to many other properties, e.g., the degree of network connectivity [24], liquidus temperature [14,41], but it is not necessarily related to only fragility [40]. Therefore, GFA and m might not have a linear inverse correlation.

4.3. Enhancement of glass stability

Interestingly, the glass stability becomes enhanced for some of the glasses after the first DSC up- and downscans, as shown in Figs. 8 and 9. Now the question arises: what is the origin of the enhancement of the GS after slow cooling? To answer this question, we discuss several factors which could affect the crystallization behavior of these glasses.

For borate systems, liquid-liquid phase separation is often an issue to consider [42]. Phase separation could occur during the first DSC upscan, since phase separation is more favorable at higher temperatures due to the supplementation of thermal energy. Hence, the atoms more easily overcome the energy barriers to rearrange and favor phase separation [1]. If phase separation has occurred, there will be two glassy phases and during the second DSC upscan, the T_g and the C_p jump should have changed and a second glass transition peak should have been observed. However, we did not observe these changes and we therefore exclude this factor. Moreover, the enhancement of GS is likely not attributed to the evaporation of boron during the DSC scans. Boron vaporizes rapidly when the temperature is above 1473 K [43], but the sample was only scanned to 1273 K, and therefore the temperature was low enough to exclude significant boron evaporation. Another possible explanation could be that during the first upscan, the glass disk was inserted in the Pt crucible with relatively poor contact between glass and Pt crucible. However, during the second upscan, the sample stuck to the Pt-crucible due to the melting during the first upscan. The heat transfer was then more efficient during the second upscan, since there is minimal air gap between the sample and the bottom of the Pt crucible. In order to explore this possible explanation for a change in GS, we melted the glass inside the Pt-crucible in the induction furnace and then performed the DSC scan. We observed the same phenomenon, i.e., the enhancement of GS first occurs during the second upscan. Thus, we can also exclude any effects related to the surface contact between glass and crucible.

Instead, the enhancement of GS might be related to the temperature dependence of the boron speciation. Temperature-induced changes in boron speciation have been reported in alkali borate glasses and melts [44,45]. According to these previous studies, the fraction of BO_4 tetrahedra decreases with increasing temperature above T_g, indicating that the BO_4 tetrahedra in the glass are converted to BO_3 triangles in the melt [44]. The BO_4 to BO_3 conversion can lower the rigidity of the glasses, since the degree of cross-linking of the borate framework with covalent B–O bonds is lowered [44]. According to [25], there are five β constraints (O–B–O angular constraints) per B^4 to form a rigid BO_4 tetrahedron and three β constraints per B^3 to keep the BO_3 unit planar. Thus, the glass containing more BO_3 has a less rigid network structure. In other words, the degrees of freedom of the liquid at the crystallization temperature increase with increasing BO_3 concentration. This facilitates rearrangement of the structural units, and hence crystallization. Consequently, the glass stability is lowered. In Section 4.1 we mentioned that in glasses with different amount of network former, NBO/B plays a determining role in controlling GFA, while the boron speciation plays a less significant role. However, considering a constant concentration of network former, the boron speciation conversion will have a significant effect. An increase of N_4 after the first upscan will result in a decrease of NBO, which is expected to cause an increase of GS. Therefore, this combination of two effects should lead to a substantially enhanced GS.

The concentrations of BO_3 and BO_4 in a borate glass depend on the cooling rate that the borate melt experienced during production, i.e., its thermal history [46–49]. The GFA is ultimately determined during this cooling process. The as-produced glasses studied here have been subjected to a relatively fast cooling (approximately 1000 K/s [50]). After the first DSC upscan, the melt was cooled at a slower rate, i.e., 0.17 K/s. The higher the cooling rate, the higher fraction of BO_3 is frozen-in. Upon re-heating, the rapidly cooled glass should crystallize more easily than the slowly cooled glass due to the factors mentioned above. In order to test whether these inferences are reasonable, ^{11}B MAS NMR measurements have been conducted on the Fe-free glass (B-Na25) before and after the first upscan. We choose an iron-free analogous glass in order to avoid the effect of dipolar coupling between ^{11}B nuclear spin and unpaired spin of d-electrons in Fe during the NMR measurement. As shown in Fig. 13, the N_4 values for the glass before and after the first upscan are 46.3 and 47.8 at%, respectively. For relatively fast cooling (before first upscan), more BO_3 species are frozen-in and the N_4 value is low. For a slower cooling (after first upscan), less BO_3 species are frozen-in and N_4 attains a higher value. N_4 increases by 1.5 at% after the first up- and downscans. This provides evidence for the possible link between the boron speciation and the enhanced GS.

5. Conclusions

The glass forming ability (GFA) of a series of soda lime borate liquids has been determined using a calorimetric method. Specifically, we express GFA in terms of the Hruby parameter. It is found that GFA decreases when Na_2O is substituted for B_2O_3, implying that the network connectivity greatly controls GFA of the studied systems. We note that the applicability of the Hruby parameter is limited only to the poor glass formers. The inverse correlation between liquid fragility and GFA, which has been found for some glass-forming liquid series, is not observed for these systems. We also report a remarkable result concerning the stability of two glasses, containing 20 and 25 mol% Na_2O, against crystallization. Their GS during heating is enhanced when the glasses have previously been subjected to a relatively slow cooling cycle, e.g., a 10–20 K/min cooling rate. This enhancement of GFA can be attributed to the structural conversion of BO_3 units into BO_4 units during this slow cooling process. This conversion increases the network connectivity of the glass, and hence the GFA.

Acknowledgments

We thank Mette Moesgaard for performing the XRD measurements and Ralf Keding for valuable discussions.

References

[1] J.E. Shelby, Introduction to Glass Science and Technology, second Ed. The Royal Society of Chemistry, 2005.
[2] A.K. Varshneya, Fundamentals of Inorganic Glasses, Academic, 1994.
[3] C.A. Angell, Science 267 (1995) 1924.
[4] A.A. Cabral Jr., C. Fredericci, E.D. Zanotto, J. Non-Cryst. Solids 219 (1997) 182.
[5] M.L.F. Nascimento, L.A. Souza, E.B. Ferreira, E.D. Zanotto, J. Non-Cryst. Solids 351 (2005) 3296.
[6] I. Avramov, E.D. Zanotto, M.O. Prado, J. Non-Cryst. Solids 320 (2003) 9.
[7] A.A. Soliman, I. Kashif, Phys. B 405 (2010) 247.
[8] P. Wray, Am. Ceram. Soc. Bull. 90 (2011) 25.
[9] J.C. Mauro, P.K. Gupta, R.J. Loucks, J. Chem. Phys. 130 (2009) 234503.
[10] T. Wakasugi, R. Ota, J. Fukunaga, J. Am. Ceram. Soc. 75 (1992) 3129.
[11] Z.P. Lu, C.T. Liu, Phys. Rev. Lett. 91 (2003) 11505.
[12] A. Hruby, Czech. J. Phys. B 22 (1972) 1187.
[13] E.B. Ferreira, M.L. Lima, E.D. Zanotto, J. Am. Ceram. Soc. 93 (2010) 3757.
[14] R. Ota, T. Wakasugi, W. Kawamura, B. Tuchiya, J. Fukunaga, J. Non-Cryst. Solids 188 (1995) 136.
[15] F. Stickel, E.W. Fischer, R. Richert, J. Chem. Phys. 102 (1995) 6251.
[16] I. Avramov, A. Milchev, J. Non-Cryst. Solids 104 (1988) 253.
[17] J.C. Mauro, Y.Z. Yue, A.J. Ellison, P.K. Gupta, D.C. Allan, Proc. Natl. Acad. Sci. U. S. A. 106 (2009) 19780.
[18] P.K. Gupta, J.C. Mauro, J. Chem. Phys. 130 (2009) 094503.
[19] J.C. Phillips, J. Non-Cryst. Solids 34 (1979) 153.
[20] J.C. Phillips, M.F. Thorpe, Solid State Commun. 53 (1985) 699.
[21] Q.J. Zheng, J.C. Mauro, A.J. Ellison, M. Potuzak, Y.Z. Yue, Phys. Rev. B 83 (2011) 212202.
[22] Y.Z. Yue, J. Non-Cryst. Solids 354 (2008) 1112.
[23] R. Busch, E. Bakke, W.L. Johnson, Acta Mater. 46 (1998) 4725.
[24] M. Moesgaard, Y.Z. Yue, J. Non-Cryst. Solids 355 (2009) 867.
[25] M.M. Smedskjaer, J.C. Mauro, S. Sen, Y.Z. Yue, Chem. Mater. 22 (2010) 5358.
[26] M.M. Smedskjaer, J.C. Mauro, S. Sen, J. Deubener, Y.Z. Yue, J. Chem. Phys. 133 (2010) 154509.
[27] M.M. Smedskjaer, J. Deubener, Y.Z. Yue, Chem. Mater. 21 (2009) 1242.
[28] Y.Z. Yue, J. de C. Christiansen, S.L. Jensen, Chem. Phys. Lett. 357 (2002) 20.
[29] N. Böse, G. Klingenberg, G. Meerlender, Glass Sci. Technol. 74 (2001) 115.
[30] T.J. Kiczenski, L.S. Du, J. Stebbins, J. Non-Cryst. Solids 351 (2005) 3571.
[31] D. Massiot, F. Fayon, M. Capron, I. King, S.L. Calvé, B. Alonso, J. Durand, B. Bujoli, Z. H. Gan, G. Hoatson, Magn. Reson. Chem. 40 (2002) 70.
[32] K. Ito, C.T. Moynihan, C.A. Angell, Nature 398 (1999) 492.
[33] L.M. Wang, C.A. Angell, R.J. Richert, J. Chem. Phys. 125 (2006) 074505.
[34] D.H. Huang, G.B. McKenna, J. Chem. Phys. 114 (2001) 5621.
[35] J.C. Mauro, R.J. Loucks, Phys. Rev. E 78 (2008) 021502.
[36] M. Solvang, Y.Z. Yue, S.L. Jensen, D.B. Dingwell, J. Non-Cryst. Solids 351 (2005) 499.
[37] J.C. Mauro, D.C. Allan, M. Potuzak, Phys. Rev. B 80 (2009) 094204.
[38] J. Fayos, R.A. Howie, F.P. Glasser, Acta Crystallogr. C 41 (1985) 1394.
[39] J.F. Stebbins, Z. Xu, Nature 390 (1997) 60.
[40] X.F. Bian, J. Guo, X.Q. Lv, X.B. Qin, C.D. Wang, Appl. Phys. Lett. 91 (2007) 221910.
[41] C.A. Angell, J. Non-Cryst. Solids 354 (2008) 4703.
[42] W.F. Du, K. Kuraoka, T. Akai, T. Yazawa, J. Mater. Sci. 35 (2000) 4865.
[43] P.W. Angel, A.R. Cooper, J. Non-Cryst. Solids 221 (1997) 70.
[44] O. Majérus, L. Cormier, G. Calas, B. Beuneu, Phys. Rev. B 67 (2003) 024210.
[45] T. Yano, N. Kunimine, S. Shibata, M. Yamane, J. Non-Cryst. Solids 321 (2003) 147.
[46] S. Sen, J. Non-Cryst. Solids 253 (1999) 84.
[47] L. Cormier, O. Majérus, D.R. Neuville, G. Calas, J. Am. Ceram. Soc. 89 (2006) 13.
[48] J.F. Stebbins, S.E. Ellsworth, J. Am. Ceram. Soc. 79 (1996) 2247.
[49] J.S. Wu, M. Potuzak, J.F. Stebbins, J. Non-Cryst. Solids 357 (2011) 3944.
[50] Y.Z. Yue, R. von der Ohe, S.L. Jensen, J. Chem. Phys. 120 (2004) 8053; ibid. 121 (2004) 11508.

Paper V

Influence of aluminum speciation on the stability of aluminosilicate glasses against crystallization

Qiuju Zheng,[1] Morten M. Smedskjaer,[1] Randall E. Youngman,[2] Marcel Potuzak,[2] John C. Mauro,[2] and Yuanzheng Yue[1,3,a)]
[1]*Section of Chemistry, Aalborg University, DK-9000 Aalborg, Denmark*
[2]*Science and Technology Division, Corning Incorporated, Corning, New York 14831, USA*
[3]*Key Laboratory for Glass and Ceramics, Shandong Polytechnic University, Jinan 250353, China*

(Received 28 May 2012; accepted 10 July 2012; published online 24 July 2012)

In this letter, we investigate the correlation between glass microstructure and glass stability (GS) in soda lime aluminosilicates. We find a loss of GS (i.e., an onset of crystallization) in the glasses above a critical concentration of Al_2O_3 when heating at the standard rate of 20 K/min. This loss in GS may be attributed to formation of five-fold coordinated Al species when $[Al_2O_3]/[Na_2O] > 1$. The primary crystalline phase is identified as nepheline, in which Al exists in four-fold coordination. This implies that the five-fold coordinated Al is energetically less stable compared to Al in a tetrahedral environment. © *2012 American Institute of Physics*. [http://dx.doi.org/10.1063/1.4739005]

Aluminosilicate glasses are ubiquitous in nature and technology[1] and have found widespread use[2] in applications such as substrate glass for liquid crystal displays[3] and chemically strengthened cover glass for personal electronic devices.[4,5] However, the relationships among glass composition, structure, and glass-forming ability (GFA) in those glasses are not fully understood.[6–9] GFA is a measure of the critical cooling rate at which the glass-forming liquid must be cooled to yield a crystallized volume fraction below a certain limit (such as 0.1%).[10] The development of new aluminosilicate glass compositions is limited by the vitrification ability of the liquid, which is particularly important for glasses with high concentration of Al_2O_3. Hence, it is important to understand the correlation between the atomic structure of glass and its GFA. Due to the complexity of measuring the critical cooling rate, the resistance of a glass against crystallization upon reheating is often used as a measure of GFA.[11–13] This resistance is defined as the glass stability (GS).

Understanding the correlation between structure and GFA for aluminosilicate liquids is particularly challenging due to the dual structural role of aluminum, viz., it can act either as a network-former in four-fold coordination or in a charge compensating role in five- or six-fold coordination.[14] Al^{3+} is stabilized in tetrahedral coordination (Al^{IV}) when associated with charge balancing cations (such as Na^+ and Ca^{2+}).[15,16] It is generally a good approximation that only Al^{IV} exists in compositions with excess network modifiers. However, this simple structural model of aluminosilicate glasses and melts has been questioned, since higher coordinated aluminum (e.g., five-fold coordination, Al^V) species have been experimentally detected in peralkaline alkali and alkaline earth aluminosilicate glasses, where only Al^{IV} is expected due to the excess of modifier cations.[17–20] There exists a larger proportion of Al^V in glasses with modifier cations of relatively high field strength, such as divalent alkaline earth elements.[16,21,22]

In this letter, we investigate the influence of the Al_2O_3 content on the GS for a series of ten soda lime aluminosilicate (Na_2O-CaO-Al_2O_3-SiO_2) glasses. We correlate the changes in GS with the microstructural evolution of the glassy network quantified through ^{27}Al magic-angle spinning nuclear magnetic resonance (MAS NMR) measurements. We show that the GS is intimately linked with the medium range structure of the network, which has important consequences for the viscous flow behavior of the glass-forming liquids.

Glasses with compositions (in mol%) of (76-x) SiO_2–xAl_2O_3–16Na_2O–8CaO with $x = 0$, 2.7, 5.3, 8, 10.7, 13.3, 16, 18.7, 21.3, and 24 were prepared by melt quenching methods, as described in detail elsewhere.[23] The glasses were doped with ~0.15 mol% SnO_2 as a fining agent and the chemical compositions were determined by x-ray fluorescence and found to be within 0.5 mol% of the nominal ones. The GS was determined using differential scanning calorimetry (DSC). The annealed and polished samples (diameter: 6 mm; thickness: 1 mm) were heated in Al_2O_3 crucibles at a rate of 20 K/min in argon in a STA 449 C Jupiter (Netzsch) instrument. The primary devitrification phase at the liquidus temperature was determined using a temperature gradient furnace and x-ray diffraction analysis. The NMR experiments were performed on commercial NMR spectrometers (Chemagnetics Infinity, Agilent VNMRS) at 11.7 T. The ground glass samples were packed into 2.5 mm zirconia rotors and the NMR spectra were collected using a 2.5 mm double-resonance MAS NMR probe, with spinning speeds of 22 kHz and short radio-frequency pulses of 0.6 μs (~$\pi/12$ tip angle). The temperature dependence of equilibrium viscosity was measured by performing beam bending, parallel plate, and concentric cylinder experiments, as described elsewhere.[24,25]

Figure 1 shows the DSC curves of the ten aluminosilicate glasses during heating in argon. It is seen that the glasses with low Al_2O_3 content do not exhibit any crystallization exotherms during the DSC upscans at 20 K/min. This is indicative of the high stability of these glasses. The slight decrease in the DSC signal at high temperatures observed in

a)Author to whom correspondence should be addressed. Electronic mail: yy@bio.aau.dk.

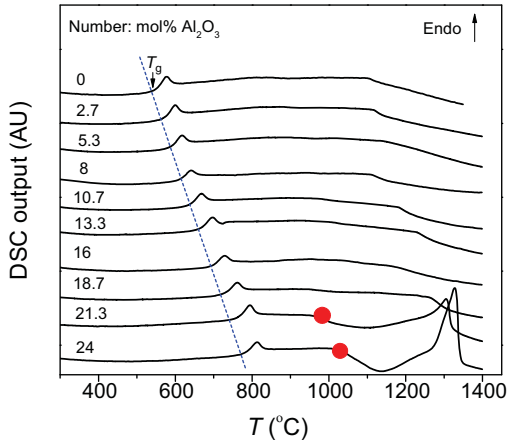

FIG. 1. Calorimetric response to heating at 20 K/min in argon for the $(76-x)SiO_2-xAl_2O_3-16Na_2O-8CaO$ glasses with $x=0$, 2.7, 5.3, 8, 10.7, 13.3, 16, 18.7, 21.3, and 24. The dashed blue line indicates the change in glass transition temperature (T_g) with composition. The red circles indicate the onset of crystallization in the glasses with 21.3 and 24 mol% Al_2O_3.

Fig. 1 is presumably due to the instrumental uncertainties at these temperatures. Interestingly, the two glasses with the highest Al_2O_3 contents exhibit crystallization exotherms and subsequent melting endotherms (Fig. 1). Hence, there is a loss of glass stability at Al_2O_3 content between 18.7 and 21.3 mol%.

As shown in Figs. 1 and 2(a), the glass transition temperature ($T_{g,DSC}$) systematically increases with increasing $[Al_2O_3]/[SiO_2]$ ratio. $T_{g,vis}$ is the glass transition temperature obtained from viscosity measurements, and it is defined as the temperature at which the equilibrium viscosity equals 10^{12} Pa s. $T_{g,vis}$ can be derived from the Mauro-Yue-Ellison-Gupta-Allan (MYEGA) model which describes the temperature dependence of viscosity.[24] The MYEGA model is written as follows:

$$\log_{10}\eta(T) = \log_{10}\eta_\infty + (12-\log_{10}\eta_\infty)\frac{T_g}{T} \times \exp\left[\left(\frac{m}{12-\log_{10}\eta_\infty}-1\right)\left(\frac{T_g}{T}-1\right)\right], \quad (1)$$

where η_∞ is the high-temperature viscosity limit and m is the liquid fragility index, which quantifies the departure from an Arrhenius temperature dependence of viscosity.[1] The temperature dependence of viscosity is illustrated by the Angell plot where the logarithmic viscosity ($\log\eta$) is plotted as a function of the T_g scaled inverse temperature (T_g/T) in Fig. 2(b). We fit the viscosity data to Eq. (1) using a Levenberg–Marquardt algorithm for all the glass-forming liquids.[26,27] The $T_{g,vis}$ and m values are shown in Figs. 2(a) and 3, respectively. As shown in Fig. 2(a), the increase of $T_{g,DSC}$ is in agreement with that of $T_{g,vis}$.

An inverse correlation between fragility and GFA has been reported for some metallic and silicate glass-forming liquids.[28–31] This is because "strong" melts have less change in rigidity with respect to changes in temperature, which could create steric hindrance towards crystallization during cooling. Fig. 3 shows that m is approximately constant with increasing Al_2O_3 content up to 18.7 mol%. However, when $[Al_2O_3]$ exceeds 18.7 mol%, m starts to increase with

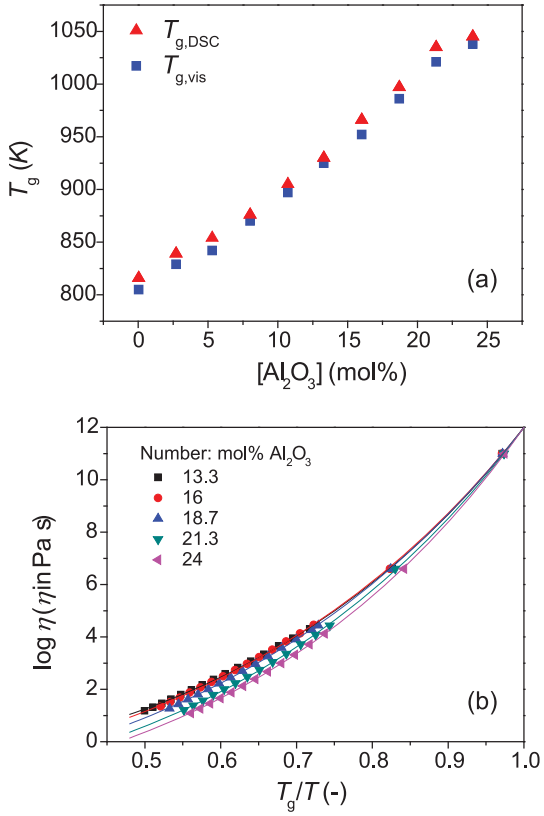

FIG. 2. (a) Composition dependence of the glass transition temperature obtained from DSC ($T_{g,DSC}$) and equilibrium viscosity ($T_{g,vis}$) measurements. (b) Angell fragility plot showing the logarithmic viscosity ($\log\eta$) as a function of the T_g scaled inverse temperature (T_g/T) for five selected liquids.

increasing alumina content, and this inflection point is coincident with the loss of glass stability. According to temperature-dependent constraint theory, m can be calculated from the temperature derivative of the number of atomic constraints.[32,33] The increase in the number of bond angle constraints plays a governing role in determining the fragility.[34,35] Hence, in the peraluminous regime, fragility increases as the higher coordination number of Al leads to a greater number of bond angular constraints that increase fragility.

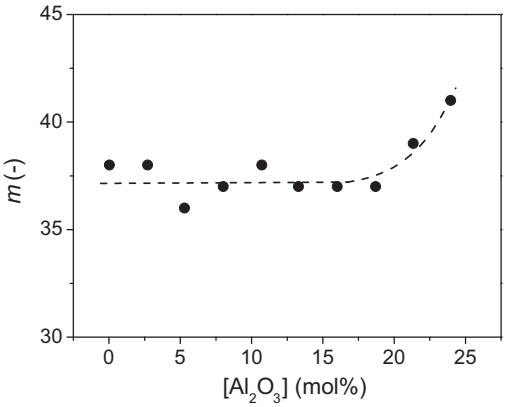

FIG. 3. Composition dependence of the liquid fragility index m obtained from fitting the MYEGA equation (see Ref. 24) to the viscosity data. The dashed line is the guide for eyes.

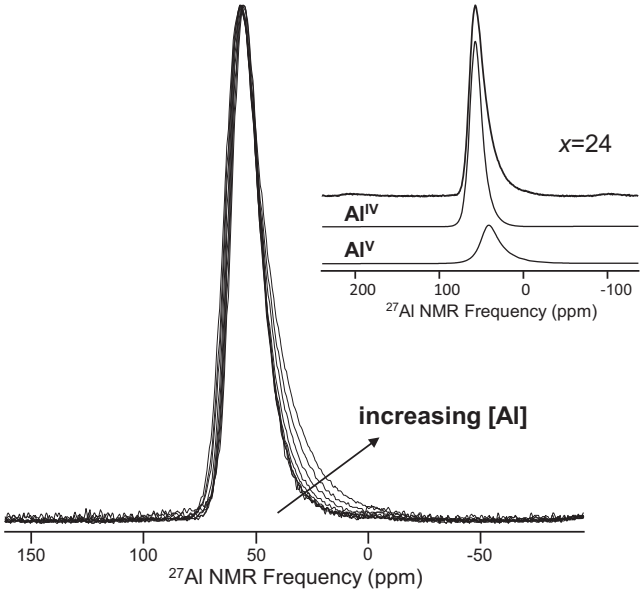

FIG. 4. ^{27}Al MAS NMR spectra of the aluminosilicate glasses (see Ref. 36). The spectra show unchanging lineshapes for glasses having $[Al_2O_3] < [Na_2O]$ and asymmetrical broadening for glasses with $[Al_2O_3] \geq [Na_2O]$. The inset shows simulation of the Al^{IV} and Al^{V} resonances for the $x = 24$ glass.

To reveal the structural origin of this loss of glass stability, we next consider the ^{27}Al MAS NMR results in Figure 4.[36] When the concentration of Na_2O is higher than that of Al_2O_3, the spectra primarily consist of a narrow peak centered at around +50 ppm, consistent with Al in 4-fold coordination.[37] At higher alumina concentrations, the MAS NMR lineshape broadens asymmetrically on the more shielded side (lower shift). This is due to the presence of Al in 5-fold coordination.[37] The two Al species can be simulated to reproduce MAS NMR lineshapes for both Al^{IV} around +50 ppm and Al^{V} around +30 ppm. The fraction of Al^{V} increases with increasing Al_2O_3 content. The presence of Al^{V} implies that Ca^{2+} is not as effective as Na^{+} in charge-balancing tetrahedral aluminum species. This statement can be understood in terms of the aluminum avoidance principle, according to which Al-O-Al linkages in the glass are energetically unfavorable and hence two AlO_4 tetrahedra avoid connecting with each other.[38] Thus, the probability for Ca^{2+} ions to stabilize Al cations in two not linked aluminum tetrahedra is relatively low since two adjacent Al ions are too distant to share one Ca^{2+} ion. Note that the aluminum avoidance can be avoided under certain circumstances.[39]

The Al-O-Al linkages could exist in peraluminous system, or even in the high-Al_2O_3 containing peralkaline systems (e.g., 18–21 mol% Al_2O_3 used in the present work). But in the latter case, the majority of Al is in 4-fold coordination and its tetrahedra are still connected with SiO_4 tetrahedra. Only the minority of Al is in 5-fold coordination, where Ca^{2+} charge-balances only one Al^{3+} and this is easier than balancing two Al^{3+} in the Al-O-Al linkages. Thus, Al^{V} will form in the glasses with $[Al_2O_3] > 18.7$ mol%. However, Al^{V} in glass state is less energetically favorable compared to the Al^{IV} in crystalline state. When an Al^{V} containing glass is heated up to a certain temperature well above T_g, Al^{V} is readily converted to Al^{IV} in the crystalline state. Therefore, the formation of Al^{V} is the possible origin of the loss of glass stability of the glass when $[Al_2O_3]$ reaches a critical concentration (e.g., >18.7 mol%).

It should be mentioned that the aluminum speciation is also temperature dependent,[40] similar to boron speciation.[41] It has been found that the content of Al^{V} increases with fictive temperature (T_f), which is confirmed by *in situ* high temperature ^{27}Al data on calcium aluminosilicate glasses.[42] However, the changes in aluminum speciation with temperature are rather small (~1%) and much smaller than the differences between the samples. Therefore, the differences in aluminum speciation measured at room-temperature are also present at the higher temperatures experienced by the samples during the DSC measurements. Based on the fraction of Al^{V}, we can calculate the number of non-bridging oxygen per tetrahedron (NBO/T), which is a measure of the connectivity of the glass network. The composition dependence of NBO/T is shown in Figure 5. NBO/T decreases as the sodium and calcium ions are used for charge-compensating tetrahedral aluminum instead of forming non-bridging oxygens. Normally, the decrease of NBO/T (i.e., the increase of the network connectivity) leads to an increase of GS.[43,44] However, our results show the opposite trend. This implies that the negative effect of an increase in the Al^{V} content on GS is more dominant than the positive impact of an increase in network connectivity for the glass series studied in this work.

Furthermore, structural heterogeneity is another important factor for enhancing nucleation in glasses. It has been reported that the medium-range quasi-heterogeneity exists in aluminosilicate glasses.[44] Specifically, there exists clustering of regions rich in highly polymerized AlO_4 and SiO_4 units and other regions rich in highly depolymerized SiO_4 units. The extent of the quasi-heterogeneity increases with increasing Al_2O_3 content, leading to declining glass stability against crystallization during reheating.[29,44] This observation is in agreement with the result obtained in the present work.

The findings reported above imply that the structural change reflected in the aluminum speciation plays a dominant role in the loss of glass stability. The primary crystalline phase of glasses with $[Al_2O_3] = 10.7$ and 13.3 mol% is found to be anorthite ($CaAl_2Si_2O_8$). As $[Al_2O_3]$ increases, nepheline ($NaAlSiO_4$) starts to form from the glass with

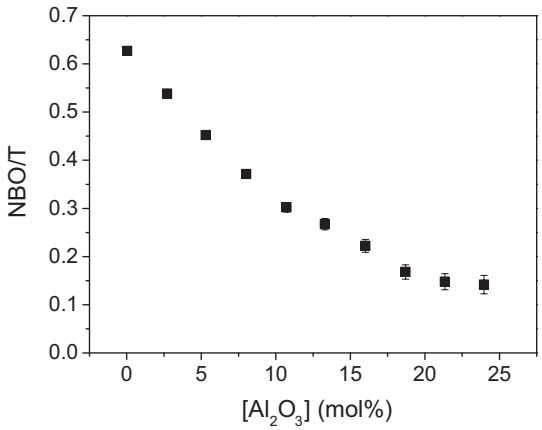

FIG. 5. Composition dependence of the number of NBO/T calculated based on the analyzed compositions and the fraction of tetrahedral aluminum from ^{27}Al MAS NMR.

$[Al_2O_3] = 16$ mol%. In the region around $[Al_2O_3] = 18.7$ mol%, the GS starts to diminish. According to Refs. 45 and 46, Al exists in four-fold coordination in both the anorthite and nepheline crystals. The presence of Al^V in the high-Al_2O_3 glasses could make the local structure less energetically stable, since the Al^V polyhedra in glass are less stable than both Al^{IV} in glass and Al^{IV} in both anorthite and nepheline (note that Al^{IV} in glass is less stable than in crystals). Owing to the high thermodynamic driving force for crystallization, the Al^V domains could readily become nucleation sites that will grow when the glass is subjected to dynamic heating. In other words, the thermodynamically unstable structural domains will be spontaneously transformed into the crystalline state with lower potential energy when the glass is heated up. Therefore, GS will decrease if sufficient Al^V-containing domains form by increasing Al_2O_3 content up to a critical level.

Finally, it should be mentioned that a minor concentration of crystals has presumably been formed already slightly below the critical Al_2O_3 content, but they are so few in number that the DSC has reached the limit of detection of crystals and hence no obvious exothermic peaks are detected (Fig. 1). This means that a critical concentration of Al^V is an approximate value. In reality, there is a critical range of Al_2O_3 content above which GS will decrease sharply.

In summary, a loss of glass stability of soda lime aluminosilicate glasses above a critical Al_2O_3 content is observed. The glass transition temperature increases with increasing Al_2O_3 content due to an increase in the network connectivity when sodium and calcium ions are used for charge-compensating tetrahedral aluminum species instead of creating non-bridging oxygens. However, calcium is not as effective as sodium in stabilizing Al tetrahedra. Consequently, five-fold coordinated aluminum species are formed for $[Al_2O_3] \geq [Na_2O]$, providing another means for charge-compensation. This causes the structure to be less stable and is apparently responsible for the loss of glass stability. This finding suggests that five-fold coordinated aluminum species should be avoided when developing glasses with high GS.

[1]C. A. Angell, Science **267**, 1924 (1995).
[2]A. K. Varshneya, *Fundamentals of Inorganic Glasses* (Society of Glass Technology, Sheffield, 2006).
[3]A. Ellison and I. A. Cornejo, Int. J. Appl. Glass Sci. **1**, 87 (2010).
[4]A. K. Varshneya, Int. J. Appl. Glass Sci. **1**, 131 (2010).
[5]A. Tandia, K. D. Vargheese, J. C. Mauro, and A. K. Varshneya, J. Non-Cryst. Solids **358**, 316 (2012).
[6]Y. Li, Q. Guo, J. A. Kalb, and C. V. Thompson, Science **322**, 1816 (2008).
[7]D. H. Xu, B. D. Wirth, J. Schroers, and W. L. Johnson, Appl. Phys. Lett. **97**, 024102 (2010).
[8]H. B. Yu, W. H. Wang, and H. Y. Bai, Appl. Phys. Lett. **96**, 081902 (2010).
[9]S. Kohara, J. Akola, H. Morita, K. Suzuya, J. K. R. Weber, M. C. Wilding, and C. J. Benmore, Proc. Natl. Acad. Sci. U.S.A. **108**, 14780 (2011).
[10]D. R. Uhlmann, J. Non-Cryst. Solids **7**, 337 (1972).
[11]M. L. F. Nascimento, L. A. Souza, E. B. Ferreira, and E. D. Zanotto, J. Non-Cryst. Solids **351**, 3296 (2005).
[12]E. B. Ferreira, E. D. Zanotto, S. Feller, G. Lodden, J. Banerjee, T. Edwards, and M. Affatigato, J. Am. Ceram. Soc. **94**, 3833 (2011).
[13]J. Sestak, A. Kozmidis-Petrovic, and Z. Zivkovic, J. Min. Metall. Sect. B-Metall. **47**, 229 (2011).
[14]Y. Bottinga and D. F. Weill, Am. J. Sci. **272**, 438 (1972).
[15]B. O. Mysen and P. Richet, *Silicate Glasses and Melts—Properties and Structure* (Elsevier, Amsterdam, 2005).
[16]J. C. C. Chan, M. Bertmer, and H. Eckert, J. Am. Chem. Soc. **121**, 5238 (1999).
[17]M. J. Toplis, S. C. Kohn, M. E. Smith, and I. J. F. Poplett, Am. Mineral. **85**, 1556 (2000).
[18]D. R. Neuville, L. Cormier, and D. Massiot, Chem. Geol. **229**, 173 (2006).
[19]J. F. Stebbins, S. Kroeker, S. K. Lee, and T. J. Kiczenski, J. Non-Cryst. Solids **275**, 1 (2000).
[20]D. R. Neuville, L. Cormier, V. Montouillout, P. Florian, F. Millot, J. C. Rifflet, and D. Massiot, Am. Mineral. **93**, 1721 (2008).
[21]L. S. Du and J. F. Stebbins, J. Non-Cryst. Solids **351**, 3508 (2005).
[22]P. Florian, N. Sadiki, D. Massiot, and J. P. Coutures, J. Phys. Chem. B **111**, 9747 (2007).
[23]M. M. Smedskjaer, S. A. Saxton, A. J. Ellison, and J. C. Mauro, Opt. Lett. **37**, 293 (2012).
[24]J. C. Mauro, Y. Z. Yue, A. J. Ellison, P. K. Gupta, and D. C. Allan, Proc. Natl. Acad. Sci. U.S.A. **106**, 19780 (2009).
[25]Q. J. Zheng, M. Potuzak, J. C. Mauro, M. M. Smedskjaer, R. E. Youngman, and Y. Z. Yue, J. Non-Cryst. Solids **358**, 993 (2012).
[26]K. Levenberg, Q. Appl. Math. **2**, 164 (1944).
[27]D. W. Marquardt, J. Soc. Ind. Appl. Math. **11**, 431 (1963).
[28]R. Busch, E. Bakke, and W. L. Johnson, Acta Mater. **46**, 4725 (1998).
[29]M. Moesgaard and Y. Z. Yue, J. Non-Cryst. Solids **355**, 867 (2009).
[30]L. M. Wang, Y. J. Tian, and R. P. Liu, Appl. Phys. Lett. **97**, 181901 (2010).
[31]J. H. Na, M. D. Demetriou, and W. L. Johnson, Appl. Phys. Lett. **99**, 161902 (2011).
[32]P. K. Gupta and J. C. Mauro, J. Chem. Phys. **130**, 094503 (2009).
[33]J. C. Mauro, P. K. Gupta, and R. J. Loucks, J. Chem. Phys. **130**, 234503 (2009).
[34]M. M. Smedskjaer, J. C. Mauro, S. Sen, and Y. Z. Yue, Chem. Mater. **22**, 5358 (2010).
[35]M. M. Smedskjaer, J. C. Mauro, R. E. Youngman, C. L. Hogue, M. Potuzak, and Y. Z. Yue, J. Phys. Chem. B **115**, 12930 (2011).
[36]M. M. Smedskjaer, R. E. Youngman, and J. C. Mauro, "Structure of MgO/CaO Sodium Aluminosilicate Glasses" (unpublished).
[37]S. H. Risbud, R. J. Kirkpatrick, A. P. Taglialavore, and B. Montez, J. Am. Ceram. Soc. **70**, C-10 (1987).
[38]W. Lowenstein, Am. Mineral. **39**, 92 (1954).
[39]J. F. Stebbins, Nature (London) **330**, 13 (1987).
[40]J. F. Stebbins, E. V. Dubinsky, K. Kanehashi, and K. E. Kelsey, Geochim. Cosmochim. Acta **72**, 910 (2008).
[41]J. S. Wu, M. Potuzak, and J. F. Stebbins, J. Non-Cryst. Solids **357**, 3944 (2011).
[42]K. Kanehashi and J. F. Stebbins, J. Non-Cryst. Solids **353**, 4001 (2007).
[43]Q. J. Zheng, J. C. Mauro, M. M. Smedskjaer, R. E. Youngman, M. Potuzak, and Y. Z. Yue, J. Non-Cryst. Solids **358**, 658 (2012).
[44]M. Moesgaard, R. Keding, J. Skibsted, and Y. Z. Yue, Chem. Mater. **22**, 4471 (2010).
[45]F. F. Foit and D. R. Peacor, Am. Mineral. **58**, 665 (1973).
[46]W. A. Dollase and W. M. Thomas, Contrib. Mineral. Petrol. **66**, 311 (1978).